Computation of NMR shifts for paramagnetic solids: developments and applications

vorgelegt von
M.Sc.
Arobendo Mondal
ORCID: 0000-0002-4714-8083

Von der Fakultät II - Mathematik und Naturwissenschaften
der Technischen Universität Berlin
zur Erlangung des akademischen Grades

Doktor der Naturwissenschaften
– Dr. rer. nat. –

genehmigte Dissertation

Promotionsausschuss:

Vorsitzender:	Prof. Klaus-Peter Straßer
Gutachter:	Prof. Dr. Martin Kaupp
Gutachter:	Prof. Dr. Radek Marek

Tag der wissenschaftlichen Aussprache: 23 Oktober 2018

Berlin 2019

To my mom

Acknowledgements

First and foremost, I would like to express my sincere gratitude towards my advisor Prof. Dr. Martin Kaupp for his continuous support during my Ph.D. study and research, and for his patience, motivation, enthusiasm, as well as supervision. His guidance helped me successfully sail through the time of research and writing of this thesis.

Besides my advisor, I would like to thank the rest of my thesis committee: Prof. Dr. Radek Marek, and Prof. Dr. Klaus-Peter Straßer, for their encouragement, insightful comments, and fruitful discussions.

Thereafter, I would like to express my sincere thanks to Prof. Christophe Copéret (ETH Zürich), Prof. Jürg Hutter (University of Zürich), Prof. Dr. Clare P. Grey (University of Cambridge), Prof. Dr. Claudio Luchinat (Giotto Biotech, CERM Florence) and Prof. Dr. Giacomo Parigi (CERM Florence) for offering me internship (secondment) opportunities in their groups within the framework of pNMR initial training network (EU research grant) and guiding me to learn and work on diverse and exciting projects.

I would also like to acknowledge my colleagues in the Kaupp group, Berlin for helping me during these years of work and for the stimulating scientific and non-scientific discussions. I would cherish our friendship, inside and outside the office/lab. I am also thankful to the administrative and operations staff at the Technical University of Berlin and Zuse Institute Berlin for availing the computational facilities and bureaucratic work. Special thanks to Dr. Christian Tuma, Nadine Rechenberg, and Heidi Grauel. I am also thankful to group members, friends and administrative and operations staff and services at Zürich, Cambridge, and Florence for their hospitality, cooperations, care, enriching scientific discussions and making my visit pleasant and fruitful. I am grateful to all the members of the pNMR-ITN family for everything, without whom the pNMR workshops, meetings, and conferences would not have been so exciting. I would like to especially thank Prof. Dr. Guido Pintacuda, Prof. Dr. Juha Vaara, Prof. Vladimir Malkin, Prof. Olga Malkina, Dr. Jiří Mareš, Dr. Ladislav Benda, Dr. Marcella Iannuzzi, Dr. Andrew J. Pell and Dr. Sebastian Gohr for their discussions, guidance, support and encouragement. I am also thankful to Prof. Dr. Juergen Senker and Dr. Thomas Wittmann for their collaboration.

I am deeply grateful to the pNMR initial training network (Marie Curie Actions, EU Seventh Framework Programme, FP7/2007-2013, REA grant no. 317127) for funding my Ph.D. studies and providing the opportunity to work in an interdisciplinary European

research network. Further support by the UniCat Berlin DFG excellence cluster and HPC resources from the North-German Supercomputing Alliance (HLRN) are gratefully acknowledged.

Finally, I'm deeply thankful to my family and friends for their unfailing support. This work is also their achievement.

Abstract

Nuclear magnetic resonance (NMR) spectroscopy is a powerful tool for studying the structural and electronic properties of paramagnetic solids such as battery materials, metal-organic frameworks, and molecular/ionic crystals. However, the interpretation of paramagnetic NMR spectra is often challenging as a result of the interactions of unpaired electrons with the nuclear spins of interest. In this thesis, we report a novel protocol to compute and analyze NMR chemical shifts for extended paramagnetic solids (pNMR), accounting comprehensively for Fermi-contact (FC), pseudo-contact (PC), and orbital shifts. This approach uses an EPR/NMR parameter-based formalism (hyperfine couplings, g-tensors, zero-field splitting ZFS D-tensors and orbital shieldings) for the computation of pNMR shifts. An incremental cluster model approach applied to the computation of g- and ZFS D-tensors has enabled the use of advanced multireference wave function methods (such as CASSCF or NEVPT2). The Gaussian-augmented plane-wave implementation of the CP2K code was used for periodic calculations whereas ORCA and Gaussian programs were used for more sophisticated molecular calculations. Due to the efficient and highly parallel performance of CP2K, a wide variety of materials with large unit cells can be studied with extended Gaussian basis sets. Using the developed protocol, the computed ^{7}Li pNMR shifts for $Li_xV_2PO_4$ (x=3, 2.5, 2), as well as ^{7}Li and ^{31}P shifts of $LiMPO_4$ (M=Mn, Fe, Co, Ni) /and MPO_4 (M=Fe, Co) cathode materials are in good agreement with available experimental data. Importantly, the ^{7}Li shifts in the high-voltage cathode material $LiCoPO_4$ are dominated by spin-orbit-induced PC contributions, in contrast to previous assumptions, changing fundamentally interpretations of the shifts in terms of covalency. PC contributions are smaller for the ^{7}Li shifts of the related $LiMPO_4$ (M=Mn, Fe, Ni), where FC and orbital shifts dominate. The ^{31}P shifts of all materials finally are almost pure FC shifts. Nevertheless, large ZFS contributions can cause non-Curie temperature dependences for both ^{7}Li and ^{31}P shifts. Similar protocols have been applied to the computation of pNMR shifts for clusters with multiple paramagnetic centers, in particular to ^{1}H and ^{13}C shifts for derivatives of the porous Cr-MIL-101 solid, which contains Cr_3O clusters with magnetically coupled metal centers within the metal-organic framework. Taking a step further, ab initio molecular dynamics simulations have been combined with the ^{1}H and ^{13}C shift computations for a dinuclear iron complex to include the conformational dynamics of the ligands. The developments described pave the way towards a more-widespread computational treatment of NMR shifts for paramagnetic materials.

Zusammenfassung

Kernspinresonanzspektroskopie (NMR) ist ein machtvolles Werkzeug für die Untersuchung von strukturellen und elektronischen Eigenschaften paramagnetischer Festkörper wie zum Beispiel Batteriematerialien, metallorganische Gerüststrukturen oder molekularer oder ionischer Kristalle. Die Interpretation paramagnetischer NMR-Spektren stellt allerdings aufgrund der Wechselwirkung ungepaarter Elektronen mit dem zu untersuchenden Kernspin, oftmals eine Herausforderung dar. In dieser Arbeit stellen wir ein neues Protokoll für die Berechnung und Analyse chemischer Verschiebungen für ausgedehnte paramagnetische Festkörper vor (pNMR), welches Fermikontakt- (FC), Pseudokontakt- (PC), und Orbitalverschiebungen vollständig berücksichtigt. Dieser Ansatz verwendet einen auf EPR- und NMR-Parametern basierenden Formalismus (Hyperfeinkopplungen, g-Tensoren, Nullfeldaufspaltungs-D-Tensoren ZFS-D-Tensoren und Orbitalabschirmungen). Die Verwendung eines inkrementellen Clustermodell-Ansatzes für die Berechnung von g-Tensoren und ZFS-D-Tensoren ermöglicht die Verwendung fortschrittlicher multi-Referenz-Wellenfunktionsmethoden wie zum Beispiel CASSCF oder NEVPT2. Eine Gaussian-augmented-plane-wave (GAPW) Implementierung wurde für Berechnungen mit periodischen Randbedingungen verwendet, für molekulare Rechnungen wurden ausserdem die Programme ORCA und Gaussian verwendet. Auf Grund des effizienten und hoch parallelisierten Programms CP2K kann eine große Bandbreite von Materialien unter Verwendung großer Einheitszellen mit Hilfe erweiterter Gauß-Basissätzer untersucht werden. Die mit dem entwickelten Protokoll berechneten ^{7}Li-Verschiebungen von $Li_xV_2PO_4$ (x=3, 2.5, 2) sowie die ^{7}Li- und ^{31}P-Verschiebungen in den Kathodenmaterialien $LiMPO_4$ (M=Mn, Fe, Co, Ni) und MPO_4 (M=Fe, Co) stimmen gut mit den verfügbaren experimentellen Daten überein. Bemerkenswert ist, dass die ^{7}Li-Verschiebung im Hochspannungs-Kathodenmaterial $LiCoPO_4$, entgegen bisheriger Annahme, von Spin-Bahn-vermittelten PC-Beiträgen dominiert wird, was die Interpretation der Verschiebungen im Hinblick auf Kovalenz fundamental verändert. Die PC-Beiträge zu den ^{7}Li-Verschiebungen in den erwähnten $LiMPO_4$ (M=Mn, Fe, Ni) Materialien sind kleiner. In ihnen dominieren FC- und Orbitalverschiebungen. Die ^{31}P-Verschiebungen aller Materialien sind nahezu ausschließlich FC-Verschiebungen. Nichtsdestotrotz können große ZFS-Beiträge nicht-Curie-Temperaturabhängigkeiten für ^{7}Li- und ^{31}P-Verschiebungen verursachen. Vergleichbare Protokolle wurden zur Berechnung der pNMR-Verschiebungen von Clustern mit mehreren paramagnetischen Zentren verwendet, insbesondere für ^{1}H- und ^{13}C-Verschiebungen von Derivaten des porösen Cr-MIL-101 Festkörpers, der Cr_3O-Cluster mit magnetisch gekop-

pelten Metallzentren innerhalb der metall-organischen Gerüstverbindungen beinhaltet. Desweiteren wurde für zweikernige Eisenkomplexe ab-initio molekulardynamische Simulationen mit der Berechnung von ^{1}H- und ^{13}C-Verschiebungen kombiniert, um die Konformationsdynamik der Liganden zu berücksichtigen. Die in dieser Arbeit beschriebenen Entwicklungen ebnen den Weg zu einer breiteren Anwendung computergestützter Methoden auf die NMR-Verschiebungen paramagnetischer Materialien.

Contents

List of publications

1. A. Mondal and M. Kaupp, *Quantum-chemical study of ^{7}Li NMR shifts in the context of delithiation of paramagnetic lithium vanadium phosphate, $Li_3V_2(PO_4)_3$ (LVP),* ***Solid State Nucl. Magn. Reson.***, **2019**, 101, 89-100. (https://doi.org/10.1016/j.ssnmr.2019.05.008) [Chapter 6, preprint version in part]

2. A. Mondal and M. Kaupp, *Computation of NMR shifts for paramagnetic solids including zero-field-splitting and beyond-DFT approaches. Application to $LiMPO_4$ (M = Mn, Fe, Co, Ni) and MPO_4 (M = Fe, Co),* ***J. Phys. Chem. C***, **2019**, 123, 8387–8405. (https://doi.org/10.1021/acs.jpcc.8b09645) [Chapter 5, preprint version in part]

3. A. Mondal and M. Kaupp, *Quantum-chemical approach to NMR chemical shifts in paramagnetic solids applied to $LiFePO_4$ and $LiCoPO_4$,* ***J. Phys. Chem. Lett.***, **2018**, 9, 1480–1484. (https://doi.org/10.1021/acs.jpclett.8b00407) [Chapter 5, preprint version in part]

4. T. Wittmann, A. Mondal, C. B. L. Tschense, J. J. Wittmann, O. Klimm, R. Siegel, B. Corzilius, B. Weber, M. Kaupp and J. Senker, Probing interactions of N-donor molecules with open metal sites within paramagnetic Cr-MIL-101: A solid-state NMR spectroscopic and density functional theory study, ***J. Am. Chem. Soc.***, **2018**, 140, 2135–2144. (https://doi.org/10.1021/jacs.7b10148) [Chapter 7, preprint version in part]

5. A. Mondal, M. W. Gaultois, A. J. Pell, M. Iannuzzi, C. P. Grey, J. Hutter and M. Kaupp, *Large-scale computation of nuclear magnetic resonance shifts for paramagnetic solids using CP2K,* ***J. Chem. Theory Comput.***, **2018**, 14, 377–394. (https://doi.org/10.1021/acs.jctc.7b00991) [Chapter 4, preprint version]

6. S. Biswas, E. Mani, A. Mondal, A. Tiwari and S. Roy, *Supramolecular polyelectrolyte complex (SPEC): pH dependent phase transition and exploitation of its carrier properties,* ***Soft Matter.***, **2016**, 12, 1989–1997. (https://doi.org/10.1039/c5sm02732b) [not included in the thesis]

Copyright

- Chapter 4 *(pre-print)* as well as tables and graphics within are reproduced with permission from A. Mondal, M. W. Gaultois, A. J. Pell, M. Iannuzzi, C. P. Grey, J. Hutter and M. Kaupp, Large-scale computation of nuclear magnetic resonance shifts for paramagnetic solids using CP2K, *J. Chem. Theory Comput.*, **2018**, 14, 377–394. (https://doi.org/10.1021/acs.jctc.7b00991). Copyright 2018 American Chemical Society.

- Chapter 5 *(pre-print)* as well as tables and graphics within are reproduced in part with permission from A. Mondal and M. Kaupp, Quantum-chemical approach to NMR chemical shifts in paramagnetic solids applied to $LiFePO_4$ and $LiCoPO_4$, *J. Phys. Chem. Lett.*, **2018**, 9, 1480–1484. (https://doi.org/10.1021/acs.jpclett.8b00407) and A. Mondal and M. Kaupp, Computation of NMR shifts for paramagnetic solids including zero-field-splitting and beyond-DFT approaches. Application to $LiMPO_4$ (M = Mn, Fe, Co, Ni) and MPO_4 (M = Fe, Co), *J. Phys. Chem. C*, **2019**, 123, 8387–8405. (https://doi.org/10.1021/acs.jpcc.8b09645). Copyright 2018 American Chemical Society.

- Chapter 6 as well as tables and graphics within are reproduced in part with permission from A. Mondal and M. Kaupp, Quantum-chemical study of ^7Li NMR shifts in the context of delithiation of paramagnetic lithium vanadium phosphate, $Li_3V_2(PO_4)_3$ (LVP), *Solid State Nucl. Magn. Reson.*, **2019**, 101, 89-100. (https://doi.org/10.1016/j.ssnmr.2019.05.008). Copyright 2019 ELSEVIER.

- Chapter 7 *(pre-print)* as well as tables and graphics within are reproduced in part with permission from T. Wittmann, A. Mondal, C. B. L. Tschense, J. J. Wittmann, O. Klimm, R. Siegel, B. Corzilius, B. Weber, M. Kaupp and J. Senker, Probing interactions of N-donor molecules with open metal sites within paramagnetic Cr-MIL-101: A solid-state NMR spectroscopic and density functional theory study, *J. Am. Chem. Soc.*, **2018**, 140, 2135–2144. (https://doi.org/10.1021/jacs.7b10148). Copyright 2018 American Chemical Society.

- Appendixes A and B *(pre-print)* with all tables and graphics therein are reproduced with permission from A. Mondal, M. W. Gaultois, A. J. Pell, M. Iannuzzi, C. P. Grey, J. Hutter and M. Kaupp, Large-scale computation of nuclear magnetic resonance shifts for paramagnetic solids using CP2K, *J. Chem. Theory Comput.*, **2018**, 14,

377–394. (https://doi.org/10.1021/acs.jctc.7b00991). Copyright 2018 American Chemical Society.

- Appendix C *(pre-print)* with all tables and graphics therein are reproduced in part with permission from A. Mondal and M. Kaupp, Quantum-chemical approach to NMR chemical shifts in paramagnetic solids applied to $LiFePO_4$ and $LiCoPO_4$, *J. Phys. Chem. Lett.*, **2018**, 9, 1480–1484. (https://doi.org/10.1021/acs.jpclett.8b00407) and A. Mondal and M. Kaupp, Computation of NMR shifts for paramagnetic solids including zero-field-splitting and beyond-DFT approaches. Application to $LiMPO_4$ (M = Mn, Fe, Co, Ni) and MPO_4 (M = Fe, Co), *J. Phys. Chem. C*, **2019**, 123, 8387–8405. (https://doi.org/10.1021/acs.jpcc.8b09645) Copyright 2018 American Chemical Society.

List of abbreviations

- AMFI : atomic mean-field integrals
- APW : augmented-plan-wave
- B3LYP : Becke, 3-parameter, Lee and Yang and parr
- BOA : Born-Oppenheimer approximation
- BOMD : Born-Oppenheimer molecular dynamics
- BP : Breit-Pauli
- CAS : complete active space
- CASPT2 : complete active space second-order perturbation theory
- CASSCF : complete active space self-consistent field
- CC : coupled-cluster
- CCSD : coupled-cluster single and double
- CCSD(T) : coupled-cluster single, double, and (triple)
- CGO : common gauge origin
- CHF : coupled Hartree-Fock
- CI : configuration interaction
- CSA : complete active space
- CSFs : configuration state functions
- CSGT : continuous set of gauge transformation
- DFT : density functional theory
- EFG : electric field gradient
- EMO-CC : equation of motion coupled-cluster
- EPR : electron paramagnetic resonance
- ESR : electron spin resonance
- EXX : exact-exchange
- FC : Fermi-contact
- FFT : Fast Fourier Transformation
- GAPW : Gaussian and augmented-plan-wave
- GGA : generalized gradient approximation
- GIAO : gauge-including atomic orbital
- GIPAW : gauge including projected augmented wave
- GPW : Gaussian and plan-wave
- GTH : Goedecker-Teter-Hutter
- GTO : Gaussian type orbital
- HDVV : Heisenberg–Dirac–Van Vleck

- HF : Hartree-Fock
- HFC : hyperfine coupling
- HK : Hohenberg-Kohn
- IGAIM : individual gauge for atoms in molecules
- KS : Kohn-Sham
- LCAO : linear combination of atomic orbitals
- LDA : local density approximation
- MCSCF : multi-configurational self-consistent field
- MD : molecular dynamics
- MO : molecular orbital
- MOF : metal-organic framework
- MP : Møller-Plesset perturbation theory
- MP2 : second-order Møller-Plesset perturbation theory
- MRCC : multi-reference coupled-cluster
- MRCI : multi-reference configuration interaction
- MRI : magnetic resonance imaging
- MS-CASPT2 : multi-state CASPT2
- MS-MRCI : multi-state MRCI
- NEVPT2 : n-electron valence state perturbation theory
- NMR : nuclear magnetic resonance
- OPT : optimized
- PBC : periodic boundary conditions
- PBE : Perdew Burke Ernzerhof (functional)
- PBE0 : see PBE (global hybrid functional)
- PC : pseudo-contact
- PK : Pederson-Khanna
- pNMR : nuclear magnetic resonance spectroscopy for paramagnetic systems
- ppm : parts per million
- PRE : paramagnetic relaxation enhancement
- PW : plan-wave
- QDPT : quasi-degenerate perturbation theory
- QZVP : quadruple-zeta valence plus polarization function (basis set)
- RASSCF : restricted active space self-consistent field
- RI : resolution of the identity
- SCF : self-consistent field
- SO : spin-orbit

- SOC : spin-orbit coupling
- SOMF : spin-orbit mean-field
- SOO : spin-other orbit
- SSO : spin-same orbit
- TMS : tetramethylsilan
- TZVP : triple zeta valence plus polarization and diffuse functions (basis set)
- TZVPD : triple zeta valence plus polarization function (basis set)
- VTZ : valence triple zeta (basis set)
- XC : exchange-correlation
- XRD : X-ray diffraction
- ZFS : zero-field splitting

Chapter 1.

Introduction

In present time, diamagnetic solution phase nuclear magnetic resonance (NMR) has become a conventional method for characterizing compounds of different complexities to such a great degree that it is hard to imagine analyzing substances without it.[1–9] NMR spectroscopy provides detailed information about the structure, dynamics, reaction state, and chemical environment of molecules.[1,8,9] NMR has proven to be a highly sensitive and reliable technique and as a result, it is now routinely applied in chemistry, physics, biology, materials science and medical imaging.[10–13] NMR is a technique that gives insight into the structure and bonding in materials by exploiting the sensitivity of nuclear spin to its atomic and molecular environment.[14] Thus, it helps to reveal useful information about the compounds, such as their chemical, physical, electrical and magnetic properties.[14,15] In 1922, Stern and Gerlach discovered nuclei possess their own intrinsic magnetic moment (nuclear spin).[16] Continuing with their molecular beam experiments along with Estermann and Frisch, they succeeded in measuring the magnetic moment of the proton a few years later.[17–20] A turning point in the development of the technique came with Rabi's contributions. In 1938, consolidating the contributions of Stern and others,[21] Rabi and coworkers successfully measured the resonance of lithium atoms in a beam of LiCl molecules.[22]. Moving a step ahead, they measured the magnetic resonances of ^{6}Li, ^{7}Li and ^{19}F in LiCl, LiF, ^{6}Li and NaF molecules.[23] As a result of his significant contributions, Rabi received the 1944 Nobel Prize in Physics.[24] In 1946, Felix Bloch and Edward Mills Purcell expanded the technique for use in liquids and solids, for which they shared the Nobel Prize in Physics in 1952.[24] All the developments made in the magnetic resonance technique in this era have been elaborated in a review by Ramsay, which describes its journey (right from its inception to its developments).[25] Additionally, a brief historical

account of four other Nobel Laureates in the field of magnetic resonance clearly shows the track of the discovery, development, and applications of NMR spectroscopy.[24]

NMR spectra can be easily analyzed for small molecules, and at the same time, they also provide "finger print" regions for complex molecules.[1–3,8,9,26] Thus, this technique has made the identification of new as well as complex molecules fairly accurate.[9] However, in case of very large molecules, which are also often overcrowded with a myriad of different functional groups, the interpretation of NMR spectra becomes quite challenging. This is mainly due to overlapping signals corresponding to similar functionalities.[9] However, even though solution phase NMR analysis is occasionally complicated, solid phase NMR analysis poses an even bigger challenge.[27] This is because the inherent anisotropy of solids leads to a high degree of broadening of the peaks about the resonance frequencies, which makes it harder to distinguish them.[28]

In case of paramagnetic compounds, the unpaired electrons give rise to strong local magnetic fields that influence the spectroscopic properties, such as chemical shift values, line shapes of resonances, and their relaxation times.[29–37] Usually, the presence of paramagnetic centers (atoms with unpaired electrons) in solids is not desirable, particularly for accurate structural studies of materials by NMR. On the other hand, the influence of paramagnetic centers will obviously depend on their concentrations and electron relaxation times.[38] Therefore, an optimal combination can lead to a number of "positive" effects, like increased NMR sensitivity by optimized relaxation, by dynamic nuclear polarization, or by applications of the so-called contrast media in magnetic resonance imaging (MRI) experiments.[38,39] However, in case of a significant presence of paramagnetic centers, or in general for paramagnetic solids (for example: battery materials with paramagnetic centers), acquiring high resolution NMR signals requires further development.[40–42] There are a number of approaches now available to improve resolution (and, concomitantly, sensitivity), many involving specialist hardware or complex pulse sequences, opening up a range of potential opportunities for the characterization of solid materials.[43–47] Even when high-resolution approaches are used, solid-state NMR spectra may still contain complicated or overlapped spectral line shapes, particularly as the structural complexity of the materials studied increases, and it can remain difficult both to assign signals to chemically or crystallographically distinct species and to extract the structural information available.[10,48,49] This problem can be specifically pronounced for inorganic materials, where a range of less commonly studied nuclear species are typically investigated, many of which have an inherently low natural abundance or low sensitivity, and there is often relatively little information available in the literature to aid spectral acquisition or interpretation.[47–50] There is

an increasing interest in paramagnetic NMR as an experimental tool to study the atomic and electronic structure of electronically open-shell systems, for example, metal-containing biomolecules, local magnetic properties of materials, and molecular magnetism.[30,33,37,51,52] As compared to the standard diamagnetic NMR of closed-shell systems, the interaction of magnetic nuclei with the large magnetic moment of the unpaired electron(s) produces large chemical shift values, which could increase the resolution.

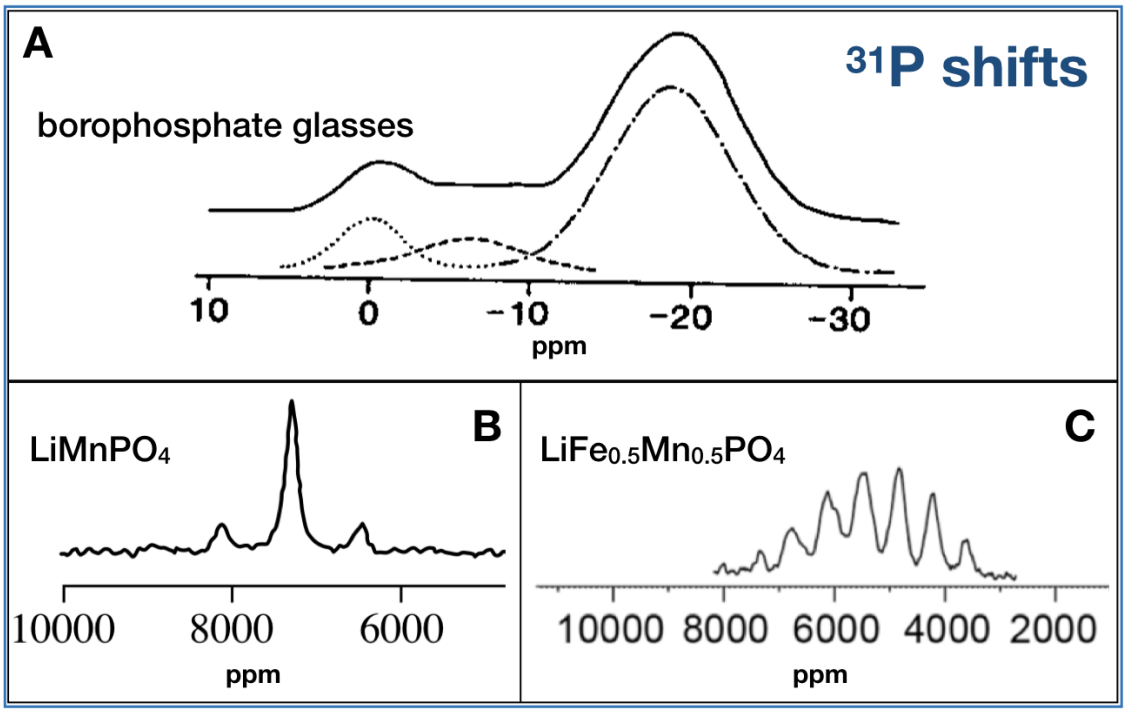

Figure 1.1.: Comparison of ^{31}P shifts for diamagnetic and paramagnetic materials. A) phosphorus shifts of diamagnetic borophosphate glasses with in -30 to 10 ppm.[53] B) phosphorus shift of paramagnetic lithium manganese phosphate 7200 ppm.[41] C) phosphorus shifts of paramagnetic lithium iron-manganese phosphate from 2500 ppm to 8000 ppm.[54] Figure 1.1A reproduced and adapted from Villa, M.; Carduner, K. R.; Chiodelli, G. *J. Solid State Chem.* **1987**, *69*, 19-23. Copyright 1987 Elsevier. Figure 1.1B reproduced and adapted from Wilcke, L.S.; Lee, Y.-J.; Cairns, J. E.; Reimer, A. J. *Appl. Magn. Reson.* **2007**, *32*, 547-563. Copyright 2007 Springer-Verlag. Figure 1.1C reproduced and adapted from Clément, R. J.; Pell, A. J.; Middlemis, D. S.; Strobridge, F. C.; Miller, J. K.; Whittingham, M. S.; Emsley, L.; Grey, C. P.; Pintacuda, G. *J. Am. Chem. Soc.* **2012**, *134*, 17178-17185. Copyright 2012 American Chemical Society.

While in NMR of diamagnetic systems the ^{31}P chemical shift range is about a few ppm, shifts of thousands of ppm can be observed in NMR spectra of paramagnetic systems

(pNMR) (see Figure 1.1).[41,53,54] As compared to electron paramagnetic resonance (EPR) spectroscopy, pNMR is valuable particularly in obtaining information about small electron spin densities.[30] Besides structural information, pNMR can be used to investigate the dynamical properties of molecules and ion dynamics within solids. In MRI, the application of contrast agents is based on the paramagnetic relaxation enhancement (PRE) of water around a paramagnetic center.[30,55]

In recent years, these challenges have resulted in a growing interest of the experimental solid-state NMR community in the use of first-principles calculations, i.e., the computational prediction of NMR parameters for a specified structural model.[44,47–50,54,56–68] Since the resonance of nuclear spins is a fundamentally quantum mechanical phenomenon, the calculations are based on solving the quantum mechanics of the system. Such calculations would not have been possible in practice were it not for theoretical advances such as density functional theory (DFT), the development of algorithms as implemented in modern codes, and high performance computers.[69–78] Computation of a vast range of structural, chemical, optical, spectroscopic, magnetic, elastic, vibrational and thermodynamic properties are possible. Nowadays it is even possible to compute NMR shifts for relatively large diamagnetic systems (both molecules and periodic solids having few hundreds of atoms).[28,77,79–87] The ability to predict structure-property-relationships has revolutionized experimental fields, since studies are no longer restricted to known crystallographic structures. Many material properties are governed by their electronic structure, yet only relatively recently has it become possible to simulate chemical shifts with predictive accuracy.

In the early 1950s, the theories of basic parameters of NMR for diamagnetic systems, the nuclear shielding tensor, and the spin-spin coupling tensor between two nuclei were established by Ramsey.[88–90] After the efficient implementation of the gauge-including atomic orbitals (GIAO) method[91,92] and extension of the analytical derivative techniques to many standard levels of theory, the feasibility of quantum-chemical calculations of nuclear shielding tensor increased rapidly.[93–95] Large molecular systems can be investigated at Hartree-Fock or DFT levels,[96] high accuracy can be obtained by coupled cluster methods,[97] and molecules containing heavy elements can be investigated by various approximate methods regarding the inclusion of relativistic effects in calculations of NMR parameters for diamagnetic systems.[98–106] Efficient implementations of such methods in solid-state codes, using periodic boundary conditions (PBC) and increasing computational power, provides the possibility to compute NMR parameters for diamagnetic solids.[69,76–78]

In contrast, theory and calculations of pNMR parameters have not reached a similar level of popularity. pNMR observables involve averaging hyperfine and Zeeman interactions in an ensemble of thermally accessible levels, arising from a manifold of 2S + 1 states (where S the electronic spin quantum number), the degeneracy of which is lifted in the presence of the external magnetic field of the spectrometer. This complicates the theoretical treatment as compared to the standard NMR of diamagnetic systems, which is mainly concerned with a nondegenerate, pure quantum ground state. The shielding tensor is denoted by $\boldsymbol{\sigma}$, and in case of paramagnetic systems it can be separated into three contributing terms as:

$$\boldsymbol{\sigma} = \boldsymbol{\sigma}_{\mathrm{orb}} + \boldsymbol{\sigma}_{\mathrm{FC}} + \boldsymbol{\sigma}_{\mathrm{PC}}, \tag{1.1}$$

where $\boldsymbol{\sigma}_{\mathrm{orb}}$ is the diamagnetic orbital shielding whereas $\boldsymbol{\sigma}_{\mathrm{FC}}$ and $\boldsymbol{\sigma}_{\mathrm{PC}}$ are explicitly temperature-dependent hyperfine terms arising from the electron spin-dependent Fermi-contact (FC) and pseudo-contact (PC) interactions. For S (generally) >1/2, one needs additionally to take into account the zero-field splitting (ZFS) interaction between the unpaired electrons.[107] Due to the many contributing mechanisms and computational challenges, the accuracy attainable in pNMR shift calculations is not yet at the same level as is customary in diamagnetic NMR.

In 1958, the contact shift was formulated by McConnell and Chesnut as an average of the isotropic hyperfine interaction in the spin-polarized Zeeman manifold in the electronic ground state.[108] In a similar way averaging the dipolar hyperfine interaction leads to the fully anisotropic contribution. These formulae are still predominantly used in computations of pNMR shieldings and comparisons of the associated chemical shifts with experimental data. An important ingredient in the analysis of pNMR shifts has been the concept of the PC shift,[108–110] an isotropic contribution resulting from the long-range dipolar interaction of the nuclear and electronic spins mediated by the spin–orbit-induced magnetic anisotropy of the metal center (which may be parametrized by the g- and ZFS D-tensors, see below). In particular, this shift contribution includes the relative position of the unpaired spin distribution and the NMR nucleus in question. Hence, the PC shift provides a handle on the molecular structure and has been used in the structure determination of, for example, metalloproteins.[65] A new development of magnetic property calculations began in the early 2000s. Pickard and Mauri established methods to compute orbital shieldings and g-tensors for periodic solids when using PBC.[76,77] Bertini *et al.*[56] extended the chemical shift formalism based on the magnetic susceptibility tensor[108–111] for structure determination of metalloproteins using NMR parameters.

Explicit quantum-chemical calculations of pNMR shifts initially were restricted to just the FC term, extracted from quantum-chemically computed hyperfine couplings (HFCs).[112–116] More complete treatments have a somewhat shorter history.[57,59,60,63,117–127] Rinkevicius et al.[115] formulated the pNMR shift of a doublet spin system at the nonrelativistic limit. At this level of theory, the shielding tensor consists of the contact and dipolar terms in addition to the Ramsey orbital terms. The latter are calculated for the paramagnetic system of interest, thus avoiding the use of an equivalent diamagnetic molecule. In 2004, Moon and Patchkovskii presented a framework for systematically extending the pNMR shift theory for computations, still for doublet systems but now including, for example, PC shifts by accounting for the deviation of the g-tensor from the isotropic free-electron value.[117] This deviation arises primarily due to the spin–orbit (SO) interaction. Pennanen and Vaara introduced a consistent implementation of the Moon and Patchkovskii theory in a quantum-chemistry program and extended the approach by including SO corrections to HFCs.[128] This scheme promoted pNMR shift calculations for doublet systems having light nuclei. To include the relativistic effects arising from heavy atoms within the molecule, only scalar relativistic and SO pseudopotentials could be incorporated. But still pNMR theory was lacking the incorporation of higher-order spin interactions occurring in systems with more than one unpaired electron, primarily the ZFS interaction that manifests in a self-coupling term of the effective electron spin in the EPR Hamiltonian.[107] For systems having negligible ZFS, Hrobařik et al.[129] extended the doublet pNMR formalism to higher S values. They added ad hoc ZFS corrections for axial cases only. Keeping the framework of Moon and Patchkovskii theory intact, in 2008 Pennanen and Vaara[57] managed to generalize it for $S \geq 1/2$, with S being the total spin of the systems of general spatial symmetry. In this approach, ZFS is taken systematically into account from the very beginning in the electron spin- and temperature-dependent hyperfine shielding terms. An essential ingredient of this pNMR theory is the recognition that the additional problem of the unpaired electron(s) in the magnetic field necessarily involves statistical thermodynamic averaging of the hyperfine and Zeeman interactions in a manifold of energy levels that are, in the presence of ZFS, nonlinearly dependent on the magnetic field. An underlying approximation of their method is that the spin–orbit coupling is relatively weak and that the higher-order ZFS and Zeeman interactions can be neglected.[120] In addition, it does not reproduce the correct low-temperature limiting behavior of the pNMR shifts.[121] Soncini and Van den Heuvel,[60,120] made significant progress by deriving a general formulation for pNMR shifts in systems with arbitrary degeneracy of the electronic state in terms of the generalized g- (parametrizing the Zeeman interaction) and HFC tensors. This framework not only includes the ground-state 2S + 1 multiplet of 2S+1 state (S is the spin quantum number of the

effective electronic spin) but also the contribution of excited multiplets, and it is applicable to systems having strong spin–orbit couplings.[120] Based on Kurland and McGarvey[110] nuclear shielding theory for paramagnetic systems, Vaara *et al.*[123] extended the Pennanen-Vaara model by treating the thermal occupations of the substates properly. In particular, this method incorporated the contributions of the lowest electronically excited states and produced the correct temperature dependence of the shielding parameters.[123,127] The present work strongly relies on this formulation. Incorporation of relativistic effects, such as the inclusion of scalar relativity in all-electron calculations by Autschbach *et al.*[118,122,124,130] and the 4-component formulation by Komorovský *et al.*[59] were further improvements in the computation of pNMR shifts. An extension to include ZFS at four-component level has also recently presented.[131]

It is now less than a decade that the first computations of pNMR shifts for solids have started to become feasible. Limited options of solid-state computational packages and implemented methods, demanding computational resources and insufficient numerical accuracy hindered the development for a long time. In 2010, Kim and coworkers[44] derived and applied a Curie-Weiss-based formulation for the DFT-calculated hyperfine parameters from the ferromagnetic into the experimentally relevant paramagnetic state, providing quantitative finite-temperature Fermi-contact shifts for phosphate based battery materials having negligible spin–orbit couplings and thus PC shifts. This development opened a wide range of possibilities to compare the experimental pNMR shift values (only FC shifts) with computed values for various materials.[44,47,48,54,58] The first attempts to include PC shifts for extended solids using g-tensors obtained in DFT calculations have been published recently. Mali et al.[45] included g-tensors obtained from gauge-including projected-augmented wave (GIPAW)[76,77] calculations in Quantum Espresso[132] to compute PC shifts in a study of Li_2FeSiO_4 polymorphs.[45] Pigliapochi et al.[68] combined GIPAW g-tensors from Quantum Espresso within the generalized gradient approximation (GGA) with hyperfine couplings obtained at hybrid-DFT levels with the CRYSTAL package[72] for a number of olivine-type $LiMPO_4$ materials.

The condensed-phase quantum-chemical package CP2K[69] has been used for the solid-state calculations in this thesis work. It provides a broad range of models and simulation methodologies, suitable for large molecular and condensed-phase systems, and it is capable of exploiting the most advanced computer hardware efficiently. CP2K has had a large impact in the field of DFT-based molecular dynamics (MD) simulations, particularly with its ability to describe the dynamics of systems containing hundreds of atoms with relative ease. Apart from this, CP2K has a broad range of functions several of which are

of interest regarding our goal to compute pNMR shifts for solids. In particular, the highly efficient Gaussian-augmented plane-wave (GAPW)[133,134] implementation of the CP2K code includes all-electron basis sets for the calculations. GAPW combines the advantages of GTOs (Gaussian type orbitals) LCAO-basis sets (linear combination of atomic orbitals) for the orbitals with those of an augmented plane-wave basis for the density.[135,136] One advantage of CP2K is that it has fewer limitations regarding the permitted GTO basis sets compared to CRYSTAL, and it permits efficient computations with hybrid functionals and large basis sets for the hyperfine couplings. In fact, the extremely efficient parallelization of CP2K makes the code particularly suitable for highly parallel large-scale computations on supercomputers and allows us to address large unit cells.[78] g-Tensor calculations with CP2K using GGA functionals are available and have been reported.[137,138]

The ambition of this thesis work has been to advance the pNMR shift computation formalism for solids by including orbital and PC shift terms in addition to FC terms. A detailed discussion about the developments is provided in Chapter 2. To achieve chemical accuracy of computed values, it is not enough to just extend the formalism but we also need to analyze the specific technical aspects of the methods used for calculating the various contributing quantities. Chapter 3 provides an overview of all methods used in this thesis work. Chapter 4 is about validating the implementation of orbital shielding, g-tensor and HFC modules in CP2K for molecules and solids, and gives the foundation to perform such calculations for periodic solids. Furthermore, the application of a doublet-like pNMR formalism to the ^{7}Li shifts of the $Li_3V_2(PO_4)_3$ solid is discussed, combining orbital, PC, and FC terms. In addition, a systematic approach to build cluster models to compute unit-cell g-tensors for solids is also discussed here. Chapter 5 provides a detailed discussion on the application of the extended pNMR formalism to ^{7}Li and ^{31}P shifts of important lithium-metal-phosphate battery materials, the importance of higher level methods for g-tensor- and ZFS-calculations, and the larger significance of the cluster-model approach for computing g- and ZFS-tensors for solids. Chapter 6 extends the applications to partially delithiated $Li_xV_2(PO_4$ (x = 2.0, 2.5, 3.0) solids for pNMR shift computations. Chapter 7 focuses on an application of some of the developed methodologies to compute ^{13}C and ^{1}H pNMR shifts for derivatives of the Cr-MIL-101 derivatives metal-organic framework material (MOF), which contains Cr_3O clusters with magnetically coupled metal centers. Chapter 8 provides a protocol to combine ab initio MD simulations with chemical-shift computations of dinuclear iron complex to account for the statistical distribution of conformations due to the motion of the ligands. Chapter 9 provides conclusions and an outlook.

Chapter 2.

Theory

2.1. Basics of nuclear magnetic resonance

All nucleons that are protons and neutrons, composing any atomic nucleus, have the intrinsic quantum property of spin. The overall spin of the nucleus is determined by the nuclear spin quantum number I. If the numbers of both the protons and neutrons in a given nucleus are even, then I = 0, i.e. there is no overall spin (as for the ^{12}C nucleus). However, in some atoms (e.g. ^{1}H and ^{13}C) the nucleus does possess an overall spin (I > 0), which is associated with a magnetic moment, because of which the nucleus interacts with a magnetic field. A nucleus of spin I will have 2I + 1 possible spin orientations. In the absence of an external magnetic field, these orientations are of equal energy. However, in the presence of a magnetic field, the energy levels split (nuclear Zeeman interaction). Transitions can be induced between these states by appropriate electromagnetic radiation, usually in the radio frequency range.[1,139] Above zero Kelvin, populations in different nuclear spin states, are not the same, leading to population differences and thus a net nuclear magnetization. Electrons, similar to the nucleus, are also charged and rotate with a spin to produce a magnetic field opposite to the magnetic field produced by the nucleus. The electronic environment of the nucleus affects the local magnetic field at the site of the nucleus and thus the energy differences between the nuclear states. This gives rise to a chemical shift associated with each nucleus, which carries information about the electronic structure around the nucleus and thus the chemical environment around it.

2.2. NMR spin Hamiltonian

Experimental NMR spectra are analyzed based on an effective spin Hamiltonian which contains explicit second rank tensor expressions, describing those interactions that affect the spectrum.[1,2] The actual spectral parameters are specific combinations of the tensor elements as dictated by the nature of molecular orientation and motion under the experimental conditions. Spin Hamiltonians link the energy to experimental variables (such as spin and magnetic field) by including the measured quantities (such as the shielding tensor) as parameters. Implicit degrees of freedom, such as the position of the nuclei and electrons, are included in the parameters. The NMR spin Hamiltonian for a system of nuclei K in frequency units can be written as:[1]

$$H^K_{\mathrm{NMR}} = -\frac{1}{2\pi}\sum_K \gamma_K \mathbf{I}_K \cdot (\mathbf{1} - \boldsymbol{\sigma}_K) \cdot \mathbf{B_0} + \frac{1}{2}\sum_{K<L} \mathbf{I}_K \cdot (\mathbf{D}_{KL} + \mathbf{J}_{KL}) \cdot \mathbf{I}_L + \sum_K \mathbf{I}_K \cdot \mathbf{Q}_K \cdot \mathbf{I}_K. \quad (2.1)$$

Here, γ_K and $\boldsymbol{\sigma}_K$ are the nuclear gyromagnetic ratio and shielding tensor for nucleus K, respectively. $\mathbf{I}_K$ and $\mathbf{I}_L$ are the nuclear spins for nucleus K and L, respectively. $\mathbf{B}_0$ is the external magnetic field, $\mathbf{1}$ is the 3×3 unit matrix. $\mathbf{D}_{KL}$, $\mathbf{J}_{KL}$, and $\mathbf{Q}_K$ are the direct dipole-dipole coupling tensor, the indirect spin-spin coupling tensor and the quadrupole coupling tensor, respectively.[88,90,140]

The first term in eq. 2.1 is the nuclear Zeeman interaction term describing the direct Zeeman interaction between the bare nucleus and the external magnetic field and the modification of this interaction due to the electron cloud through the shielding tensor (see the orbital shielding section below). Nuclear shielding results from the local magnetic field, i.e., the combined effect of the external magnetic field and the secondary field generated by the induced electronic currents around the nucleus.

The second term in eq. 2.1 contains the coupling tensors D_{KL} and J_{KL}. The direct dipole-dipole coupling tensor D_{KL} arises from the direct through-space magnetic interaction between the nuclear spins I_K and I_L. The indirect spin-spin coupling tensor J_{KL} measures the electronic coupling energy between the spins of two nuclei and results from the electron-mediated, indirect magnetic interaction between I_K and I_L. Analogous to σ_K and the direct Zeeman interaction of the bare nucleus, J_{KL} modifies the dipole-dipole interactions represented by D_{KL}. Unlike D_{KL}, J_{KL} depends both on the distance between the nuclei and the electronic structure of the molecule. In isotropic media, the direct couplings average to zero while the indirect couplings average to isotropic coupling constants J_{KL}.[2]

The fine structure of NMR spectra in isotropic systems results from the spin-spin coupling constant. The last remaining parameter in eq. 2.1 is the quadrupole coupling tensor Q_K that arises from the interactions between the nuclear electric quadrupole moment and electric field gradient (EFG) of nucleus K. It appears only if the nuclear quantum number $\mathrm{I}_K > 1/2$.

The focus of the studies in this thesis is on the nuclear shielding for paramagnetic solids.

2.3. EPR spin Hamiltonian

Electron paramagnetic resonance (EPR), also known as electron spin resonance (ESR), spectroscopy is a prominent technique used to study materials with at least one unpaired electron,[141] particularly for metal complexes or organic radicals. The basic concepts of EPR are analogous to those of NMR, but electronic spins are excited instead of the spins of atomic nuclei. An electron can possess both an intrinsic spin and an orbital angular momentum. Its magnetic moment ($\mathbf{m}_\mathrm{e}$) is directly proportional to the effective spin $\mathbf{S}$ as

$$\mathbf{m}_\mathrm{e} = -\mu_B \mathbf{g} \cdot \mathbf{S}. \tag{2.2}$$

Here, μ_B the Bohr magneton, $\mathbf{S}$ the effective spin and $\mathbf{g}$ the g-tensor. The g-tensor (g) defines the Zeeman interaction with the external magnetic field.[107] The interaction of an external magnetic field with an electron spin depends on the magnetic moment associated with the spin, and the nature of an isolated electron spin is such that two and only two orientations are possible. The application of the magnetic field then provides magnetic potential energy, which splits the spin states by an amount proportional to the magnetic field (Zeeman effect). Microwave frequency radiation of the appropriate frequency can cause a transition from one spin state to the other. To interpret experimental EPR spectra, parameters from the EPR effective spin Hamiltonian are fitted to the data, e.g.

$$H_\mathrm{EPR} = \mu_B \mathbf{B}_0 \cdot \mathbf{g} \cdot \mathbf{S} + \sum_K \mathbf{S} \cdot \mathbf{A}_K \cdot \mathbf{I}_K + \mathbf{S} \cdot \mathbf{D} \cdot \mathbf{S}, \tag{2.3}$$

where $\mathbf{A}$ is the hyperfine coupling (HFC) tensor and $\mathbf{D}$ is the zero-field splitting (ZFS) tensor (for $\mathrm{S} > 1/2$). The first term describes the directional dependence of the electron Zeeman interaction through the g-tensor. The second term in H_EPR is the hyperfine interaction term bilinear in S and the nuclear spin I_K. $\mathbf{A}$ describes the interaction between

the nuclear magnetic moment and that of the unpaired electrons, and it gives rise to the hyperfine structure in EPR spectra. Both $\mathbf{g}$ and $\mathbf{A}^I$ are general 3×3 Cartesian matrices composed of a scalar (rank zero tensor), a true anisotropic symmetrical second-rank tensor (g- and A-tensor anisotropies) and an asymmetric (rank 1) tensor (the latter is zero for the nonrelativistically computed $\mathbf{A}^I$ used here).[37] The third term in H_{EPR} is the ZFS interaction, which is quadratic in $\mathbf{S}$. The ZFS interaction term gives rise to a fine structure of the energy levels by removing the degeneracy of the ground state, even in the absence of B_0. The ZFS tensor is symmetric. The g-tensor can be written as $\mathbf{g} = \mathrm{g_e}\mathbf{1} + \Delta\mathbf{g}$, where $\mathrm{g_e}$ = 2.0023193043617... is the isotropic free-electron g-value.[142] Δg is often called "g-shift." It is the deviation from $\mathrm{g_e}$ and has an isotropic and anisotropic part. The g-tensor can be written as a 3×3 Cartesian matrix:

$$\mathbf{g} = \begin{pmatrix} \mathrm{g}_{xx} & \mathrm{g}_{xy} & \mathrm{g}_{xz} \\ \mathrm{g}_{yx} & \mathrm{g}_{yy} & \mathrm{g}_{yz} \\ \mathrm{g}_{zx} & \mathrm{g}_{zy} & \mathrm{g}_{zz} \end{pmatrix}. \tag{2.4}$$

For experiments in liquid solution, only an isotropic g-value is observed due to the free motion of the molecules. However, in frozen solution or for crystalline materials, the principal components (g_{11}, g_{22}, and g_{33}) of the g-tensor can be obtained, neglecting the asymmetric part. The isotropic g-value

$$\mathrm{g_{iso}} = \frac{1}{3}\mathrm{Tr}(\mathbf{g}) = \frac{1}{3}(\mathrm{g}_{11} + \mathrm{g}_{22} + \mathrm{g}_{33}). \tag{2.5}$$

2.4. NMR shifts of paramagnetic molecules

Traditionally, the experimental isotropic pNMR shift is decomposed into three parts: orbital shift (δ_{orb}), Fermi-contact shift (δ_{FC}), and pseudo-contact shift (δ_{PC}):

$$\delta_{\mathrm{exp}} = \delta_{\mathrm{orb}}^{\mathrm{exp}} + \delta_{\mathrm{FC}}^{\mathrm{exp}} + \delta_{\mathrm{PC}}^{\mathrm{exp}}. \tag{2.6}$$

The orbital shift is often approximated by the shift of a diamagnetic analogue to the paramagnetic molecule or solid in question, assuming a similar shift. The orbital shifts are approximately temperature-independent whereas Fermi-contact (FC) shifts and pseudo-contact (PC) shifts are temperature-dependent Conversion from orbital shieldings (σ_{orb}) to relative orbital shifts is done in the usual way by subtracting the shielding from that of a suitable reference compound (see below). In molecules, nuclei are surrounded by other nuclei and electrons. This changes the resonance energy difference, and the nucleus is said to be shielded (for a resonance at a lower frequency than for a bare nucleus) or de-shielded (for a resonance at a higher frequency). The electronic structure around the nucleus responds to the external field, creating its own field, and the nucleus experiences the effective magnetic field (B_K)[143]

$$\mathbf{B}_K = (1 - \boldsymbol{\sigma}_K) \cdot \mathbf{B}_0. \tag{2.7}$$

Here, $\boldsymbol{\sigma}_K$ is the nuclear shielding tensor of nucleus K, usually measured in parts per million (ppm) of the bare nucleus resonance frequency, and $\mathbf{B}_0$ is the external magnetic field. The nuclear magnetic shielding tensor ($\boldsymbol{\sigma}$), is composed of a scalar (rank zero tensor), a true anisotropic symmetrical second-rank tensor (σ-tensor anisotropies) and an asymmetric (rank one) tensor. $\boldsymbol{\sigma}$ is in the Cartesian basis represented by a 3×3 matrix with nine independent components as:

$$\boldsymbol{\sigma} = \begin{pmatrix} \sigma_{xx} & \sigma_{xy} & \sigma_{xz} \\ \sigma_{yx} & \sigma_{yy} & \sigma_{yz} \\ \sigma_{zx} & \sigma_{zy} & \sigma_{zz} \end{pmatrix}. \tag{2.8}$$

In an isotropic environment, such as liquid or gas, the shielding tensor averages to the isotropic shielding constant which is one-third of the trace of $\boldsymbol{\sigma}$ (diagonalization procedure neglects the asymmetric part of the shielding tensor),

$$\sigma_{\mathrm{iso}} = \frac{1}{3}\,\mathrm{tr}(\boldsymbol{\sigma}) = \frac{1}{3}(\sigma_{11} + \sigma_{22} + \sigma_{33}). \tag{2.9}$$

σ_{11}, σ_{22} and σ_{33} are the diagonal values of $\boldsymbol{\sigma}$ (symmetric σ tensor). In an isotropic medium, the frequency of resonance is (cf. eq. 2.1)

$$\nu = \frac{\gamma_K B_0(1-\sigma_{\text{iso}}^K)}{2\pi}. \tag{2.10}$$

The absolute shielding constant σ_{iso}^K is challenging to obtain by experiment because of the difficulties in getting accurate values for ν/B_0.[144] The quantity usually reported is the chemical shift (δ), which is defined as

$$\delta_K = \frac{\sigma_{\text{ref}}^K - \sigma^K}{1-\sigma_{\text{ref}}^K} \approx \sigma_{\text{ref}}^K - \sigma^K, \tag{2.11}$$

where σ_{ref}^K and σ^K are the shielding of a reference nuclei and of the sample nuclei, respectively. They both refer to the same isotope though belonging to different molecules. The approximate expression for δ (r.h.s) is reasonably accurate for small shielding constants ($\sigma^K < 10^{-3}$). The Ramsey orbital shielding tensor is usually expressed in two parts, a diamagnetic part ($\boldsymbol{\sigma}^d$), which is an expectation value of the ground state electronic wavefunction and a paramagnetic part ($\boldsymbol{\sigma}^p$), which can be expressed as a linear response property. The nonrelativistic orbital shielding tensor is, therefore, a sum of two contributions

$$\boldsymbol{\sigma}_{\text{orb}} = \boldsymbol{\sigma}^d + \boldsymbol{\sigma}^p. \tag{2.12}$$

The diamagnetic part is defined as:

$$\sigma_{ij}^d = \frac{e^2\hbar}{2m_{\text{e}}}\frac{\mu_0}{4\pi}\langle\psi_0|\sum_k \frac{\mathbf{r}_k\cdot\mathbf{r}_{kN}\delta_{ij} - \mathbf{r}_{kNi}\mathbf{r}_{kNj}}{r_{kN}^3}|\psi_0\rangle\,, \tag{2.13}$$

where σ_{ij}^d is an element ij $(i,j=x,y,z)$ of the diamagnetic orbital shielding tensor, ψ_0 is the ground-state wave function, δ_{ij} is the Kronecker delta function and $\mathbf{r}_{kN}$ is the distance of electron k relative to nucleus N. Contributions of all k electrons are considered, and the origin of the magnetic vector potential (i.e., the gauge origin) is taken at the nucleus of interest.

The paramagnetic part is defined as:

$$\sigma_{ij}^p = \frac{e^2\hbar}{2m_{\text{e}}}\frac{\mu_0}{4\pi}\sum_n \frac{1}{E_n-E_0}\left[\langle\psi_0|\sum_k \widehat{L}_{ki}|\psi_n\rangle\langle\psi_n|\sum_k \frac{\widehat{L}_{kNj}}{r_{kN}^3}|\psi_0\rangle + c.c.\right], \tag{2.14}$$

where σ_{ij}^{p} is element ij of the paramagnetic orbital shielding tensor, E_n and E_0 are the eigenvalues associated with an excited and the ground electronic state, respectively, $\widehat{L}_{ki}$ and $\widehat{L}_{kNj}$ are angular momentum operators with respect to the magnetic field and nuclear position, respectively, and c.c. represents the complex conjugate. A summation is made over all electrons and electronic states to calculate the paramagnetic shielding contributions. The representation of the magnetic interaction operators corresponding to the external magnetic field depends on the choice of the gauge origin for the magnetic vector potential. For an exact wavefunction or a Hartree-Fock wavefunction with a complete basis set, the gauge origin would not cause any trouble, but in practice, approximate calculations with incomplete basis sets give results that depend on the chosen origin.[145] The Gauge-Including Atomic Orbitals (GIAO) method[91,92] eliminates the problem by introducing a magnetic-field dependence to the basis functions through the inclusion of a complex phase factor. While the GIAO approach may be considered most accurate, CP2K features the individual gauge for atoms in molecules (IGAIM), and continuous set of gauge transformations (CSGT) approaches because of the greater simplicity of the implementation in a solid-state code of these two approaches compared to GIAOs (see Chapter 4).

In 1958, the basic formulation for the FC shift and the PC shift were given by McConnell and Chesnut.[108,109] The result of the Fermi-contact interaction between the nuclear magnetic moment and the average spin density at the location of the nucleus gives the FC shift (δ_{FC}). In the simplest case, it is given by[108,109] *

$$\delta_{\mathrm{FC}} = \frac{\mu_B S(S+1)\mathrm{gA}_{\mathrm{iso}}^{I}}{3k_B T \mathrm{g}_N^I \mu_N}. \tag{2.15}$$

Here, μ_B and μ_N are the Bohr and nuclear magnetons, respectively. S is the spin quantum number, g is the rotationally averaged electronic g-value, g_N^I is the g-factor of nucleus I and $\mathrm{A}_{\mathrm{iso}}^{I}$ is the isotropic hyperfine coupling constant. T is the absolute temperature and k_B the Boltzmann constant.

The long-range dipolar interaction between the induced magnetic moment at the paramagnetic center and the nuclear magnetic moment gives the PC shift (δ_{PC}). In the simplest form, it is given by[108,109]

$$\delta_{\mathrm{PC}} = \frac{\mu_B S(S+1)}{3k_B T} \frac{(3cos^2\Omega - 1)}{R^3} F(g). \tag{2.16}$$

*In all the pNMR shielding and shift equations, K is replaced by I for representing nuclei and k_B is used for representing the Boltzmann constant.

Here, Ω is the angle between the principal symmetry axis, and the direction to the nucleus of interest, keeping the paramagnetic center at the origin of the coordinate system. R is the distance between the induced magnetic moment and the nucleus. F(g) is an algebraic function of the g-tensor components, which subsumes the relative magnitudes of various relaxation times. The pseudo-contact term could also show a T^{-2} temperature dependence in the presence of ZFS.[110,146] Eq. 2.16 is an early, very approximate expression involving a point-dipole approximation, and that more up-to-date and accurate expressions will be given later in this chapter (see below).

A quantum-chemical approach including orbital shifts, FC shifts, and PC shifts was introduced in 2004 by Moon and Patchkovskii[117] to compute NMR shifts for molecules having only one unpaired electron (doublet electronic state). In this framework, the hyperfine shielding is expressed via a matrix product of g- and A-tensors, and the pNMR shielding (σ) is given as:

$$\boldsymbol{\sigma}^I = \boldsymbol{\sigma}^I_{\text{orb}} - \frac{\mu_B}{4k_B T \mathrm{g}^I_N \mu_N} \mathbf{g} \cdot \mathbf{A}^I. \tag{2.17}$$

The total chemical shift is given by $\delta^I = \sigma^I_{\text{ref}} - \sigma^I$ and the orbital shift is $\delta^I_{\text{orb}} = \sigma^I_{\text{ref}} - \sigma^I_{\text{orb}}$ (see above for details). For the analysis of the pNMR shifts, it is useful to consider the isotropic and traceless parts of the g and A tensors separately.

$$\mathrm{g}_{\text{iso}} = \frac{1}{3} \mathrm{Tr}(\mathrm{g}) \tag{2.18}$$

$$\tilde{\mathbf{g}} = \mathbf{g} - \mathrm{g}_{\text{iso}} \mathbf{1} \tag{2.19}$$

$$\mathrm{A}_{\text{iso}} = \frac{1}{3} \mathrm{Tr}(\mathbf{A}) \tag{2.20}$$

$$\mathbf{A}_{\text{dip}} = \mathbf{A} - \mathrm{A}_{\text{iso}} \mathbf{1} \tag{2.21}$$

Inserting these into the pNMR shielding eq. 2.17 gives:

$$\boldsymbol{\sigma}^I = \boldsymbol{\sigma}^I_{\text{orb}} - \frac{\mu_B}{4k_B T \mathrm{g}^I_N \mu_N} \left(\mathrm{g}_{\text{iso}} \mathrm{A}^I_{\text{iso}} \mathbf{1} + \mathrm{A}^I_{\text{iso}} \tilde{\mathbf{g}} + \mathrm{g}_{\text{iso}} \mathbf{A}^I_{\text{dip}} + \tilde{\mathbf{g}} \cdot \mathbf{A}^I_{\text{dip}} \right). \tag{2.22}$$

The first term in the parentheses is equivalent to McConnell's FC shift (eq. 2.15) for S = 1/2. The second term represents the anisotropic contribution of the FC shift.[110,147] The

fourth term ($\tilde{\mathbf{g}} \cdot \mathbf{A}^I_{\mathrm{dip}}$) arises because of the interaction between the anisotropic parts of $\mathbf{g}$ and $\mathbf{A}$ tensors containing an isotropic part, resulting in the PC shift. The second and third terms ($\mathrm{A}^I_{\mathrm{iso}}\tilde{\mathbf{g}}$, $\mathrm{g}_{\mathrm{iso}}\mathbf{A}^I_{\mathrm{dip}}$) are traceless.

Eq. 2.17 is found to be extendable beyond doublet states when the ZFS is negligible, and the pNMR shielding is given for arbitrary spin as:[129]

$$\boldsymbol{\sigma}^I = \boldsymbol{\sigma}^I_{\mathrm{orb}} - \frac{\mu_B S(S+1)}{3k_B T \mathrm{g}^I_N \mu_N} \mathbf{g} \cdot \mathbf{A}^I. \tag{2.23}$$

In 2008, following the framework of Moon and Patchkovskii theory,[117] Pennanen and Vaara[57] generalized the pNMR shielding equation by systematically accounting for ZFS from the very beginning in the electron spin- and temperature-dependent hyperfine shielding terms. This approach also involves statistical thermodynamic averaging of the hyperfine and Zeeman interactions in a manifold of energy levels that are, in the presence of ZFS, nonlinearly dependent on the magnetic field, which leads to the pNMR shielding as[57]

$$\boldsymbol{\sigma}^I_{\varepsilon\tau} = \boldsymbol{\sigma}^I_{\varepsilon\tau,\mathrm{orb}} - \frac{\mu_B}{k_B T \mathrm{g}^I_N \mu_N} \sum_{a,b=x,y,z} \mathrm{g}_{\varepsilon a} \langle S_a S_b \rangle_0 \mathrm{A}^I_{b\tau}. \tag{2.24}$$

In particular, the above equation couples the Zeeman interactions of the electrons with the magnetic field as parameterized by the g-tensor and the hyperfine interactions with the magnetic nucleus (the $\mathbf{A}$ tensor) via the thermal average of the dyadic $\langle \mathbf{SS} \rangle$ of the effective electron spin. For a general spin state S, $\langle \mathbf{SS} \rangle$ is obtained in the manifold of the eigenstates $|n\rangle$ by diagonalizing the magnetic field and nuclear spin-independent energy term $\mathbf{S} \cdot \mathbf{D} \cdot \mathbf{S}$ with each state weighted by the corresponding eigenvalues. The matrix $\langle S_a S_b \rangle_0$ is symmetric in its a,b indices, with the trace $\mathrm{Tr} \langle \mathbf{SS} \rangle_0 = \mathrm{S(S+1)}$.

In 2013, Soncini and Van den Heuvel,[120] pointed out that the above equation is only applicable for systems having relatively weak spin–orbit couplings and at not too low temperatures. They presented a general equation for pNMR shielding expressed in terms of generalized Zeeman and hyperfine tensors, valid in the strong spin–orbit coupling limit. The equation is

$$\boldsymbol{\sigma}^p_{\alpha\beta} = -\frac{\mu_B}{k_B T \mathrm{g}^I_N \mu_N} \frac{1}{2S+1} \sum_{kq} \mathrm{g}^{(k)}_{q\alpha} \mathrm{A}^{(k)*}_{q\beta} \frac{\langle S || S^{(k)} || S \rangle^2}{2k+1}. \tag{2.25}$$

The authors further discussed a more general formalism than eq. 2.25, accounting for a time-even perturbation that weakly splits the 2S +1 degeneracy (see ref. 120 for detailed derivation and discussions).

Applying Kurland–McGarvey theory[110] for the NMR shielding of paramagnetic molecules, in 2015 Vaara et. al[123] presented an extension of eq. 2.24 by treating the thermal occupations of the substates properly and incorporating the contributions of the lowest electronically excited states. This formalism produces the correct temperature dependence of the shielding parameters.[123] The expression for the Cartesian $\varepsilon\tau$ component of the pNMR shielding tensor of nucleus I is[123]

$$\sigma^I_{\varepsilon\tau} = \sigma^I_{\mathrm{orb},\varepsilon\tau} - \frac{\mu_B}{k_B \mathrm{g}^I_N \mu_N} \sum_{ab} \mathrm{g}_{\varepsilon a} \langle S_a S_b \rangle \mathrm{A}^I_{b\tau} \tag{2.26}$$

$$\langle S_a S_b \rangle = \frac{\sum_{qp} Q_{pq} \langle q|S_a|p\rangle \langle p|S_b|q\rangle}{\sum_q \exp(-E_q/k_B T)}, \quad a,b = \{x,y,z\} \tag{2.27}$$

$$Q_{pq} = \begin{cases} e^{-E_q/k_B T} & E_q = E_p \\ -\frac{k_B T}{E_p - E_q}\left[e^{-E_p/k_B T} - e^{-E_q/k_B T}\right] & E_q \neq E_p \end{cases}, \tag{2.28}$$

$\langle \mathbf{SS} \rangle$ is a spin dyadic with the components $\langle S_\epsilon S_\tau \rangle$ evaluated in the manifold of eigenstates $|q\rangle$ with eigenenergies E_q of the ZFS Hamiltonian, H_{ZFS}.[63,123] The off-diagonal elements of the symmetric matrix Q_{pq} incorporate magnetic couplings between the eigenstates of the ZFS Hamiltonian, necessary for the correct behavior when going to low temperatures.[60,122,123] Eq. 2.26 corresponds to the hyperfine shielding formula (eq. 2.25) given by Soncini and Van den Heuvel[120] (see detailed derivation, discussion, and applications in refs. 120,123).

2.5. NMR shifts of paramagnetic solids

In 2002, based on the work of McConnell and Chesnut[108] and Kurland and McGarvey,[110] Bertini *et al.*[56] have provided an extensive list of terms for FC and PC shifts based on the magnetic susceptibility:

$$\delta^{\mathrm{iso}}_{FC} = \frac{1}{3}\left(\frac{1}{\mu_0}\frac{A}{\hbar}\frac{1}{3\gamma_I \mu_B}\left(\frac{\tilde{\chi}_{xx}}{\mathrm{g}_{xx}} + \frac{\tilde{\chi}_{yy}}{\mathrm{g}_{yy}} + \frac{\tilde{\chi}_{zz}}{\mathrm{g}_{zz}}\right)\right), \tag{2.29}$$

$$\delta_{\mathrm{PC}}^{\mathrm{iso}} = \frac{1}{3}\,\mathrm{Tr}\big(\Delta\chi \cdot C^{\mathrm{dip}}\big), \tag{2.30}$$

$$C^{\mathrm{dip}} = \frac{3R_iR_j - R^2\delta_{ij}}{4\pi R^5} \tag{2.31}$$

where $\tilde{\chi}_{ii}$ and g_{ii} are the principal components of the molecular susceptibility and **g**-tensors, respectively. In ref. 56 the authors provided a very detailed discussion on all the shift terms for FC and PC shifts. It is important to mention that the goal was to use NMR parameters as constraints for structure determination of metalloproteins. Benda et. al[65] have discussed the relation of such a magnetic susceptibility-based theory and a pNMR shift theory based on EPR spin-Hamiltonian parameters, pointing out the inconsistency of having the square of the g-tensor in the susceptibility equation. This has led to a still ongoing discussion of the choice of $\mathrm{g_e}\mathbf{g}$ or $\mathbf{g}\cdot\mathbf{g}^{\mathrm{T}}$ in the susceptibility-based equation (see ref. 65 for details).

The computation of FC shifts using a magnetization scaling factor for solids having small spin–orbit couplings was introduced by Kim and coworkers.[44] In this approach, a the magnetization scaling factor $\Phi = \mathrm{M_{para}}/\mathrm{M_{sat}}$ relates to the saturated ferromagnetic magnetization, $\mathrm{M_{sat}}$, and the much weaker paramagnetic magnetization, $\mathrm{M_{para}}$. $\mathrm{M_{sat}}$ is obtained by DFT calculations while $\mathrm{M_{para}}$ is relevant the NMR experiments. The resulting equations were

$$\delta_{iso} = \frac{A_{\mathrm{iso}}\Phi}{2h\nu_0}, \tag{2.32}$$

$$\Phi(B_0, T, \Theta, S, \mu_{\mathrm{eff}}) = \frac{B_0\mu_{\mathrm{eff}}^2}{3k_B\mathrm{g}_e\mu_B S(T-\Theta)}, \tag{2.33}$$

where ν_0 denotes the single quantum resonance frequency of the observed nucleus, $\mathrm{B_0}$ is the applied static magnetic induction, and μ_{eff} the experimental effective magnetic moment. See ref. 44 for details on the derivation and applications.

Following the doublet-state framework proposed by Moon and Patchkovskii[117] (eq. 2.17), found to be extendable beyond doublet states when the ZFS is negligible,[129] and including the residual exchange couplings of the solids in the Curie–Weiss temperature regime,[44] one arrives at a pNMR shielding equation for solids,[148]

$$\boldsymbol{\sigma}^I = \boldsymbol{\sigma}^I_{\mathrm{orb}} - \frac{\mu_B S(S+1)}{3k_B\mathrm{g}_N^I\mu_N}\left(\frac{1}{T-\Theta}\right)\left(\mathbf{g}\cdot\mathbf{A}^I\right). \tag{2.34}$$

Here, $\mathbf{g}$ is the unit-cell g-tensor (which may be expressed as $\mathbf{g} = \frac{1}{m}\sum_i^m \mathbf{g}_i$, where $\mathbf{g}_i$ is the g-tensor of paramagnetic center i and m is the number of paramagnetic centers in the unit cell). Compared to eq. 2.23, the above equation (eq. 2.34) replaces T by T - Θ in the denominator of the hyperfine shift term to account for the residual exchange couplings of extended solids, assuming Curie–Weiss behavior at the temperatures probed experimentally.[149,150] Such a temperature dependence is also observed for the paramagnetic shifts in exchange-coupled systems and thus introduced into eq. 2.34.[43,44,54,58] (see below and Chapter 4 for further details)

Extension of eq. 2.34 to NMR shielding for paramagnetic solids to include ZFS can be obtained by including ZFS and taking the g-tensor and ZFS contributions from the neighboring spin centers into account (see below) based on eq. 2.26,[123,151]

$$\boldsymbol{\sigma}^I = \boldsymbol{\sigma}^I_{\mathrm{orb}} - \frac{\mu_B}{k_B \mathrm{g}^I_N \mu_N}\left(\frac{1}{T-\Theta}\right)\left(\frac{1}{n}\sum_i^n \mathbf{g}_i \cdot \langle \mathbf{SS}\rangle_i \cdot \mathbf{A}^I\right). \tag{2.35}$$

Here, $\mathbf{g}_i$ and $\langle \mathbf{SS}\rangle_i$ are the g-tensor and spin dyadic of paramagnetic center i, respectively (see eq. 2.27 and eq. 2.28 for details). The sum on the right-hand side of eq. 2.35 (normalized by the number of paramagnetic centers n interacting with nucleus I, Figure 2.1) allows us to assemble the magnetic anisotropy in the solid from local g- and ZFS D-tensors of the individual paramagnetic centers. An incremental cluster model approach could be used for obtaining such individual tensors for each paramagnetic center. This procedure is based on the assumption that single-ion anisotropies are much larger than anisotropic exchange interactions, which is clearly expected to hold true for the materials studied in this work, where the transition-metal sites are separated by at least four bonds. Otherwise, the approach would have to be extended to include anisotropic exchange.

Compared to earlier paramagnetic shift formalisms for quantum-chemical computations for solids, eq. 2.35 is different in five respects, a) it includes orbital shielding which is the temperature-independent diamagnetic contribution to the total chemical shift, b) isotropic and anisotropic parts of the g-tensor are included, c) it includes ZFS for the NMR shift calculations of paramagnetic solids (as suggested in ref. 123 for the molecular pNMR formalism), d) in contrast to ref. 110, eq. 2.35 replaces T by $T - \Theta$ to account for the residual exchange couplings of the extended solid-state systems in question, assuming Curie–Weiss behavior at the temperatures probed experimentally. e) It accounts for the averaged individual contributions to the chemical shielding from each spin center, which could be different depending on the nature and local chemical environment of the spin

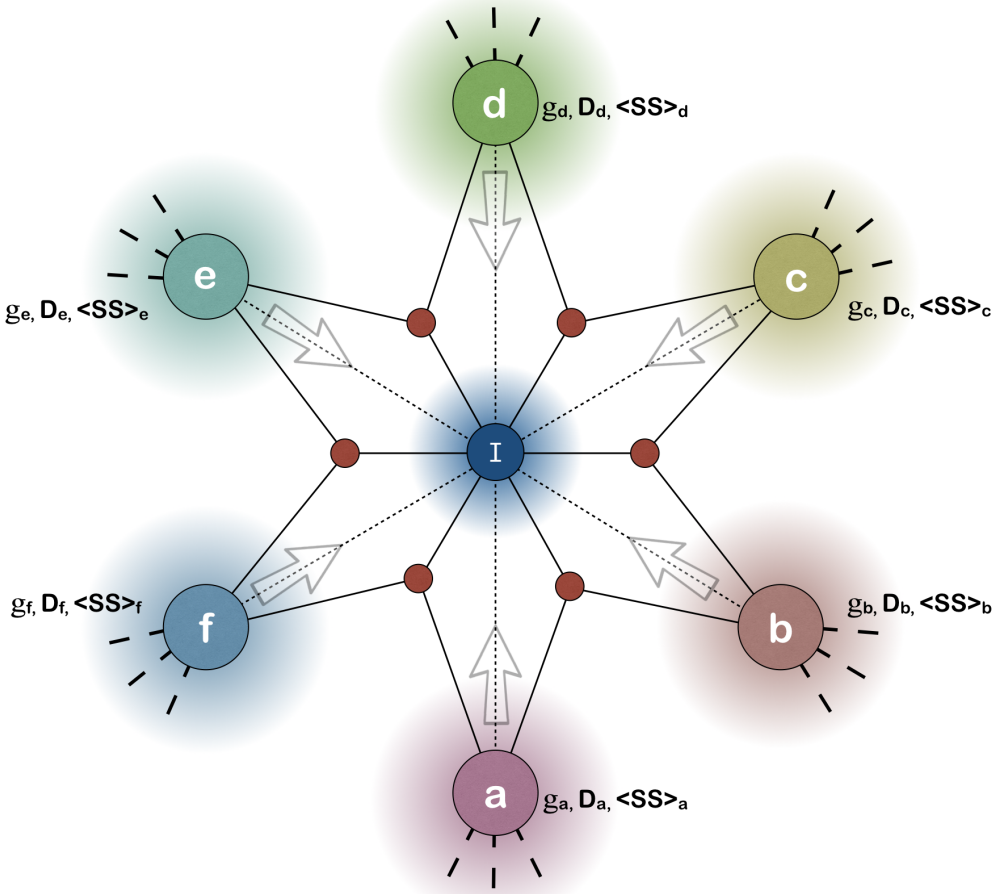

Figure 2.1.: Visual representation of the influence on the shielding of nucleus I by the surrounding paramagnetic centers (a, b, c, d, e, f). In eq. 2.35 the normalized summation accounts the contributions from all the neighboring paramagnetic centers.

centers (see Figure 2.1). These developments in the pNMR formalism for solids have resulted in significant improvements for the computed chemical shift values for cases where PC shifts are important (see Chapters 5 and 6).

In eq. 2.35 the Weiss constant accounts for the contributions of ferromagnetic or antiferromagnetic couplings to the magnetic behavior of the material as present in the high-temperature paramagnetic regime. The FC shift formalism derived by Kim and coworkers[44] for solids introduces a magnetization scaling factor Φ which is the ratio of magnetization of the paramagnetic state, M_{para}, relative to the saturated magnetization, M_{sat}, of a ferromagnetic state given as $\Phi = M_{para}/M_{sat}$. Saturated magnetization can be achieved at low temperature in the limit of high magnetic fields. In this situation all

spin centers are aligned in the direction of the applied magnetic field, which corresponds to the ferromagnetic state. At higher temperature (e.g. room temperature) and low magnetic field, a paramagnetic state with a statistical distribution of the site spins is obtained, which is expected to be probed by the pNMR experiments. Considering the scaling factor to be independent of spin–orbit effects M_{para}/M_{sat} simplifies to $T/(T - \Theta)$. In eq. 2.35 the spin–orbit couplings and magnetic anisotropy are introduced to the shift via the g-tensor and the ZFS D-tensor. The Weiss constant (Θ) contains information on the strength and type of interactions between the magnetic moments of the neighboring paramagnetic centers known as magnetic exchange. If the paramagnetic centers are spatially well separated, the interaction is weak or negligible; hence Θ will be close to zero. A positive Θ indicates ferromagnetic exchange, which tends to align magnetic moments in parallel. A negative Θ indicates antiferromagnetic exchange. The primary magnetic exchange mechanisms include, but are not limited to 1) direct exchange, involving overlap of d-orbitals, 2) superexchange, when ligand orbitals direct spin arrangement at metal ions, 3) weak dipole-dipole interactions, and 4) stronger and longer-range exchange mediated by conducting electrons (see Chapter 4 and the references within for more details). For each material, the Weiss constant obtained experimentally by low-temperature extrapolation of the high-temperature susceptibility curves will be used. All the work regarding this thesis uses experimentally obtained Weiss constants for the computations.

We can also use eq. 2.35 to compute chemical shifts of molecules or molecular clusters where several paramagnetic centers are magnetically coupled. Figure 2.1 shows that the nucleus I is surrounded by six paramagnetic centers. There are two important effects: first nucleus I overall experiences an effective hyperfine interaction from all paramagnetic centers. Second, the paramagnetic centers also interact with the neighboring paramagnetic centers, leading to magnetic couplings among each other. The paramagnetic shifts depend on both effects. In eq. 2.35 the summation accounts for the contribution from each paramagnetic center separately, and the Weiss constant introduces the intrinsic magnetic coupling among the paramagnetic centers.

Robert and coworkers[152] provided similar explanations in ref. 152 to use first-principles computation of magnetic couplings among the paramagnetic centers for computation of FC shifts (excluding spin–orbit and magnetic anisotropy effects) for compounds having several paramagnetic centers. The magnetic coupling introduces the effect of the occurrence of a manifold of states characterized by different total electronic spins S, populated according to Boltzmann's distribution. A Heisenberg–Dirac–Van Vleck spin Hamiltonian (HDVV) describes their energies E_n and eigenfunctions $|S_n\rangle$ after the diagonalization within each

S-manifold:[152–154]

$$H = \sum_{k,l} J_{kl} \cdot \mathbf{s}_k \cdot \mathbf{s}_l, \tag{2.36}$$

where $\mathbf{s}_k$ and $\mathbf{s}_l$ are the electronic spin operators at sites k and l, and J is the exchange constant. Further following ref. 155, Robert and coworkers[152] presented an equation for the hyperfine shift of a given nucleus whose electronic spin density is polarized by the paramagnetic center M_i, as[152]

$$\delta_{\mathrm{M}_i,\mathrm{para}}(T) = \frac{\mathrm{g}\mu_B}{\mathrm{g}_N\mu_N} \frac{A_{\mathrm{M}_i}}{3k_BT} \frac{\sum_S \sum_n K_{\mathrm{M}_i}(n) S(S+1)(2S+1) \exp\left(\frac{-E_n}{k_BT}\right)}{\sum_S \sum_n (2S+1) \exp\left(\frac{-E_n}{k_BT}\right)}, \tag{2.37}$$

where $\mathrm{A}_{\mathrm{M}_i}$ is the HFC constant that the resonant nucleus would experience if the paramagnetic center M_i were not involved in the magnetic coupling. The summation runs over all energy levels E_n in each S-manifold. If the nucleus experiences the magnetic influence of several paramagnetic centers M_i, the equation involves a sum over all paramagnetic centers as:[152]

$$\delta_{\mathrm{para}}(T) = \frac{\mathrm{g}\mu_B}{3k_BT\mathrm{g}_N\mu_N} \sum_i A_{\mathrm{M}_i} \frac{\sum_S \sum_n K_{\mathrm{M}_i}(n) S(S+1)(2S+1) \exp\left(\frac{-E_n}{k_BT}\right)}{\sum_S \sum_n (2S+1) \exp\left(\frac{-E_n}{k_BT}\right)}. \tag{2.38}$$

Eq. 2.38 provides a promising framework for further development to include the magnetic coupling parameters into eq. 2.35 from first-principles calculations.

In ref. 50, the authors have presented the computation of the Weiss constant for $NaMnO_2$ by Monte Carlo Simulations (see ref. 46,50 for computational details). The simulations require the structure and the magnetic couplings between the nearby magnetic ions as input, which could be obtained from first-principles calculations.[46,50] A detailed computational procedure and comparison for $NaMnO_2$ are provided in ref. 50 which could lay the foundation for further applications.

Chapter 3.

Computational aspects

The major computational work in this thesis can be separated into three individual parts: a) structure optimizations, b) calculations of EPR-parameters and orbital shifts, and c) assembly of the overall pNMR shifts. Specific details for each problem studied are provided in the respective chapters, more general details are discussed here. The choice of computational methods is broadly driven by system size, desired property to be computed, availability of implemented methods in the quantum-chemical packages and the computational cost. Here, we provide a brief overview of the computational methods and details.

3.1. Theoretical methods

Quantum chemistry offers various methods for electronic-structure calculations by first-principles. The common goal of these methods consists in solving the Schrödinger equation, within the Born-Oppenheimer approximation (possibly augmented by relativistic contributions):

$$\widehat{H}\Psi = E\Psi, \tag{3.1}$$

where $\widehat{H}$ is the Hamiltonian of the system, Ψ is the N-particle wavefunction and E is the total energy of the system. Schrödinger's equation is typically solved using either wavefunction-based methods or Kohn-Sham density functional theory (DFT), or a combination or hybrid of these two approaches. Starting with the wavefunction based methods, Hartree–Fock (HF) theory is one of the most basic approximations for the solution of the time-independent electronic Schrödinger equation, providing a mean-field approximation to electron–electron interactions.[156] The HF method accounts for the kinetic energy of

the nuclei and electrons and for the potential energy of interaction of the nuclei with each other and with the electrons. The electron–electron interaction is approximated via the HF potential, and each electron interacts only with the averaged charge of all electrons. The lack of Coulomb correlation in this model results in too large repulsive electron–electron interaction. The difference between the independent and the correlated motion of electrons is known as electron correlation, where the Fermi correlation (already accounted for in HF theory) incorporates the effects caused by the antisymmetry of the wavefunction, while the Coulomb correlation describes the additional (smaller) correlation for both same- and opposite-spin electrons due to their negative charge. The Coulomb correlation energy includes two types of not completely separable effects, the dynamical and the static correlations.[157] The dynamical correlation refers typically to short-range Coulomb correlation while the static correlation describes near-degeneracy effects between different configurations, leading to strong interactions between them.

In wavefunction theory, including more than a single determinant for the description of the wavefunction can in principle account for both types of correlation. Expanding the wavefunction in terms of excited HF determinants (one reference determinant, see below for multi-reference methods) gives single-reference methods[157] such as Møller-Plesset perturbation theory (MP), configuration interaction (CI) and coupled-cluster theory (CC).[157] The major part of the dynamical correlation can be described by these methods, while CI and CC methods also include parts of the static correlation. It is also worth mentioning that a complete CI or CC expansion leads to a numerically exact solution of the Schrödinger equation and thus covers all correlation effects.

Still, in some cases HF orbitals are not able to provide a good leading-order description for the real system, especially for systems with strong static correlation. The selection of a single Slater determinant according to the *aufbau* principle is then not sufficient because of the near-degeneracy effects. In these cases, which are usually called multi-reference systems, the spin orbitals can be optimized for a multi-determinantal wavefunction. This multi-configurational self-consistent field method (MCSCF)[157] is generally applied within a complete or a restricted space of active orbitals, leading to the CASSCF or RASSCF methods, respectively. In case of the CASSCF method, the orbitals are divided into three-subspaces, a) doubly occupied orbitals, b) active (partially occupied) orbitals and (c) virtual (empty) orbitals. A CASSCF wavefunction can be generated by assigning some fixed number of electrons to the active orbitals, for example, CAS(n, m) represents n electrons in m orbitals. CASSCF is a variational procedure where the energies are made stationary by varying both the molecular orbital (MO) and the CI coefficients.[158–160] The

CASSCF method is fully variational, which makes the calculation of analytical gradients comparatively straightforward. While CASSCF methods already describe a major part of the static correlation, the remaining dynamical correlation has to be determined by methods using the multi-determinantal wavefunction as reference,[157] e.g. complete-active-space second-order perturbation theory (CASPT2),[161,162] N-electron valence state second-order perturbation theory (NEVPT2),[163–169] multi-reference CI (MRCI) or multi-reference CC (MRCC). CASPT2 or NEVPT2 can be considered as generalizations (with different zero-order Hamiltonians) of second-order Møller-Plesset perturbation theory to multireference CAS cases.[170] For many of the methods mentioned, extensions for the description of excited states exist as well, e.g. equation of motion coupled-cluster (EOM-CC),[171] multi-state MRCI (MS-MRCI)[172] and multi-state CASPT2 (MS-CASPT2).[173]

While wavefunction methods can be systematically improved by adding more determinants to the description, the major bottleneck is their increasing calculation cost, which has an unfavorable scaling with respect to system size. Therefore, accurate calculations are often restricted to small or medium-sized molecules.

In this respect, DFT has radically changed the scenario, opening the way for more computationally affordable yet accurate descriptions of electronic structure, and indeed DFT-based applications are sharing a significant part of the computational-chemistry literature.[174] DFT is a way of including electron correlation at lower computational cost than post-HF methods. This provides the major advantage of DFT and makes it a widely used quantum-chemical computational method in physics, chemistry, and materials science to investigate the electronic ground-state structure of many-electron systems, in particular atoms, molecules, and the condensed phases.[174,175] The basic idea of DFT is to replace the complicated N-electron wavefunction by the electron density ρ as a basic local variable. As demonstrated by the theorems of Hohenberg and Kohn (HK),[175] this fundamental change of variable can in principle be done without loss of accuracy. These authors proved, indeed, that the electron density ρ can determine, in a unique way, all the properties of the system. They also demonstrated that the total energy of the system is stationary with respect to the density ρ (i.e., the minimum of the total energy functional $E[\rho]$ is obtained when evaluated using the exact density of the ground state). Unfortunately, the exact form of the total energy functional $E[\rho]$ is unknown. Among the different components of the total energy, the kinetic energy seems to be particularly difficult to be modeled directly as a density functional. To deal more efficiently with kinetic energy, in 1965 Kohn and Sham (KS) introduced a fictitious non-interacting reference system of electrons moving in an effective local potential also known as KS potential, such that it has the

same electron density as the real interacting system.[176] The KS wavefunction is a single Slater determinant constructed from a set of orbitals that are the lowest-energy solutions. The HK-functional is re-divided into three parts: the classical Coulomb repulsion between the orbital densities, the easily obtainable kinetic energy of the KS reference system, and the exchange-correlation functional. The latter describes the nonclassical part of electron repulsion, as well as the difference in the kinetic energy between the reference and the real system ("correlation kinetic energy"). Within the KS approach, the intricacies of the many-body problem are found in the exchange-correlation term of the functional, for which several different levels of approximation have been proposed. The basic one is the local density approximation (LDA), where in each point of the space the exchange-correlation term is the same as that of a uniform electron gas with the same electron density. The LDA severely underestimates the exchange energy, thus preventing its use in most chemical applications. Substantial improvements are obtained by making the exchange-correlation term dependent on the density gradient (generalized gradient approximation, GGA). When the HF exact exchange partially replaces the exchange part of a functional, a hybrid functional[174] is obtained. Hybrid functionals are used to improve DFT results by including some of the self-interaction correction intrinsic in HF, which is incompletely described by semi-local functionals. Perdew et al.[177] described the developments in DFT functionals as a ladder, with each rung representing a seminal development in the field. The first rung, based on the LDA, was not reliable for studying chemical systems.[178] The most important rungs in terms of chemical applications are the second rung, based on the GGA, the third rung, called meta-GGA due to inclusion of the kinetic energy gradient (and/or the Laplacian of the density), and the fourth rung, called hyper-GGA, which includes non-local occupied-orbital-dependent contributions such as exact exchange, e.g. in global, local, or range-separated hybrid functionals.

In this work, we have also used DFT as a basis for CP2K-based[69,78] large-scale condensed phase calculations. The conventional computational approach to DFT is already efficient and thus suitable for reasonably large molecules (few hundreds of atoms). Although, the computation of the Hartree (Coulomb) energy and the orthogonalization of the wave functions are not scaling linearly with system size, and these terms dominate the computational cost for larger systems.[179] The hybrid Gaussian and plane waves (GPW) method[135] provides an efficient way to treat these terms accurately at a significantly reduced cost. In the GPW method, an atom-centered Gaussian-type basis used to describe the wavefunction, and the density is described using an auxiliary plane-wave (PW) basis. The Poisson equations are solved using Fast Fourier Transformation (FFT) which enhances

the efficiency to obtain the Hartree energy scaling linearly with the system size. Generally, an auxiliary basis set is used to represent the density,[179,180] corresponding to a resolution of the identity (RI) method or density-fitting method. The GPW method is similar to methods that employ auxiliary real-space grids, but it differs by choice of localized primary basis functions used to represent the wave functions.[181–186] The GPW method scales linearly for three-dimensional systems with a small prefactor and an early onset. Gaussian-type basis sets with increasing accuracy can be constructed systematically.[187] Furthermore, as Gaussian functions are localized, the representations of the KS, overlap and density matrix in this basis become sparse with increasing system size.[179] This eventually allows for solving the KS equations using computational resources that scale linearly with system size. Starting from the GPW approach, the PW auxiliary basis for the electron density is substituted by an augmented-plane-wave (APW) auxiliary basis which besides plane waves relies on Gaussians. This gives the possibility of separating the electron density, the exchange-correlation (XC) potential, and the Coulomb potential into a smooth nonlocal contribution expanded in PW and local contributions that can be described in Gaussians. Therefore, they can be treated analytically. This also increases the efficiency. The linear scaling feature remains intact when going from GPW to GAPW. The efficient calculation of the nonlocal part of the Hartree functional in the PW representation in reciprocal space is one of the major advantages of GAPW approach. In the GAPW approach, the combination of the Coulomb and the XC potential into the KS potential allows a combined integration of the matrix elements, which is also an additional advantage. Most importantly, GAPW allows condensed-phase all-electron calculations for properties where core electrons are of importance, namely X-ray absorption spectra,[188] NMR shieldings,[137] and g-tensor calculations.[189]

3.2. General computational details

The computational details can be divided into five primary sections: a) condensed-phase unit/super cell and structure optimization (as well as BOMD simulations) using the CP2K package, b) partial or full structure optimization of molecules and cluster models using Turbomole or Gaussian09 packages, c) computation of EPR/NMR parameters (hyperfine tensor, g-tensor, and orbital shielding) using CP2K for solids and molecules in a supercell, d) EPR/NMR parameter computations (including the ZFS D-tensor) for molecules and cluster models using the ORCA,[70] MAG,[73] and Gaussian09[74] packages, e) assembly of pNMR shifts from computed individual EPR/NMR parameters. General calculation

details are provided below, whereas specific details of each calculation are given in the respective chapters.

Condensed-phase unit/super-cell and structure optimization. The cell parameters have been optimized using periodic boundary conditions (PBC), The GPW formalism together with the pseudopotential approximation, at PBE[190] level using the CP2K/Quickstep package.[69,191] Goedecker-Teter-Hutter (GTH) pseudopotentials[192] and double-ζ MOLOPT basis sets (DZVP-MOLOPT-SR-GTH)[193] have been used for all elements. For the expansion of the charge density in plane waves, an energy cutoff of 500 Ry has been used, and the convergence criterion over the maximum component of the wave function gradient was set to 1.0×10^{-7}. Calculations have been carried out on a sufficiently large super-cell to minimize artifacts of the periodic boundary conditions. Keeping the cell parameters fixed, the atom positions were further optimized using the all-electron GAPW[133,134] formulation with the PBE functional and def2-TZVPD and def2-TZVP[194,195] basis sets for 3d transition-metals and main-group elements, respectively. The wave-function convergence criterion was set to 1.0×10^{-6}, and the energy cutoff has been kept at 500 Ry.

Structure optimization for molecules and cluster models. The molecular structures were optimized either using Gaussian09 or Turbomole. Gaussian09 computations were performed at B3LYP[196–198]/6-311++G(d,p)[199,200] level. PBE and PBE0 functionals combined with def2-TZVP and def2-TZVPD basis sets were used for structure optimizations with the Turbomole package. The cluster models were extracted from the optimized and XRD super-cell structures. The valences of the terminating atoms were saturated with additional hydrogen atoms. The hydrogen-atom positions were optimized at PBE/def2-TZVP level using Turbomole (further details are provided in the respective chapters).

Computation of magnetic properties using CP2K. The all-electron GAPW implementation of CP2K is used for computations of HFCs, g-tensors, and orbital shieldings using PBC for solids. Computation of orbital shieldings followed the existing CP2K implementation for diamagnetic systems[137] in its open-shell extension, using IGAIM to treat the gauge. g-Tensor calculations used the related CP2K implementation,[137,201] (see Chapter 4 for a detailed discussion). Both g-tensors and orbital shieldings were obtained at the PBE level. Hyperfine coupling (HFC) tensors were computed using PBE or PBE-based global hybrid functionals, varying the exact-exchange (EXX) admixture from 5% (PBE5) to 40% (PBE40). Main-group elements were treated with IGLO-II basis sets for all the

property calculations. For the HFC calculations, a (14s11p6d)/[8s7p4d] basis was used for the 3d transition metal.[148,202] Only the most-diffuse s-function had to be removed to accommodate limitations of diffuse functions for compact solids in CP2K, reducing the size from [9s7p4d][202] to [8s7p4d].[148] For the computation of g-tensors and orbital shieldings transition metal atoms were described by def2-TZVP and Ahlrichs-VTZ basis sets, respectively.

Computation of EPR/NMR parameters for molecules and cluster models. To validate the CP2K computation of the different EPR/NMR parameters against standard quantum-chemical codes, orbital shieldings, HFC tensors, and g-tensors for molecules have been computed in a large cubic supercell of size 30 Å×30 Å×30 Å, using def2-QZVP basis sets.[194] For comparison of CP2K results with molecular codes, computation of HFCs and orbital shieldings were done using Gaussian09, g-tensors using ORCA[70] and MAG,[73] also with def2-QZVP basis sets. Orbital-shielding and g-tensor comparisons were done with the BLYP functional,[196,203] while HFCs were computed with both BLYP and PBE0[204] functionals.

DFT-level D-tensors at PBE level were computed using the Pederson-Khanna (PK) second-order perturbation approach[205] with van Wüllen's prefactors,[206] using the ORCA program. Additionally, PBE0 calculations (with a coupled-perturbed extension of the PK approach for hybrid functionals) and the wave-function-based CASSCF and NEVPT2[163,165] methods have been evaluated. The latter has been done using quasi-degenerate perturbation theory (QDPT)[207] for the dominant spin–orbit part. The RI technique was applied to the orbital transformation step of NEVPT2. The reference wave function was obtained at the state-averaged CASSCF level.[158,208]

The HFC calculations were performed with the ORCA code using the modified PBE40 functional (PBE0 with EXX admixture increased to 40%) (see Chapter 7). The orbital shielding tensor is computed either at the PBE or PBE0 level using the Gaussian software. All magnetic-resonance parameters have been computed using appropriate NMR-9s7p4d[202] metal and IGLO-II[209] main-group element basis sets.

Computation of pNMR shifts. Computations of pNMR shifts have been done with "Osprey," an in-house script written in the Python programming language, which has been developed as a part of this thesis. Osprey has implementations of several of the pNMR formalisms described in Chapter 2. It can read the output files from various electronic-structure packages, extract the required data (Cartesian coordinates, spin, orbital shielding, HFCs, g-tensor, D-tensor) and uses them further for the computation of pNMR shifts.

Chapter 4.

Large-scale computation of NMR shifts for paramagnetic solids using CP2K*

4.1. Introduction

The underlying physics of NMR shifts in paramagnetic systems is invariably more complex than in diamagnetic ones, due to interactions between electron and nuclear spin moments, which often dominate the observed quantities.[29–37] These "hyperfine shifts," on the other hand, encode important information about the molecular and electronic structure of a system.[30,33,210] It is thus important to be able to compute such NMR shifts in paramagnetic systems ("pNMR shifts") from first principles to complement experimental studies in interpretative, affirmative or even in predictive mode. Consequently, the past 15 years have seen substantial efforts to improve theoretical formalisms and implementations in computer programs for pNMR shifts in molecular systems.[30,57,59,60,117,118,120–126,128,129,206,211,212] Due to the much greater complexity of extended paramagnetic solids, progress in that field has been slower, despite the importance of such materials and the complexity of their NMR spectra. But substantial steps have been made here recently, too.[44–46,48,54,58,61,213,214]

The earliest solid-state DFT calculations that attempted to model the Fermi-contact (FC) contribution to the hyperfine shift used plane-wave pseudopotential calculations.[213] The needed spin density at the NMR nuclei was approximated by an empirical correlation

*Chapter 4 *(pre-print)* as well as tables and graphics within are reproduced with permission from A. Mondal, M. W. Gaultois, A. J. Pell, M. Iannuzzi, C. P. Grey, J. Hutter and M. Kaupp, Large-scale computation of nuclear magnetic resonance shifts for paramagnetic solids using CP2K, *J. Chem. Theory Comput.*, **2018**, 14, 377–394. (https://doi.org/10.1021/acs.jctc.7b00991). Copyright 2018 American Chemical Society.

with the valence-shell spin-density distribution around the atom of interest. It has been shown that all-electron calculations are preferable for a direct computation of the FC-shifts.[44] Consequently, the Grey and Carlier groups subsequently turned to all-electron calculations, either within the projector-augmented wave (PAW)[215] reconstruction of the core density,[216–218] the full-potential PAW implementation in WIEN2k,[75,214] or the linear-combination of atomic orbital (LCAO) implementation in the CRYSTAL code[72,219] (using Gaussian-type orbital basis sets, GTOs). Focusing on lithium transition-metal oxides, phosphates, and silicates, with emphasis on systems of relevance for battery materials, these computations allowed an analysis of the FC contributions in terms of spin-density transfer pathways from the transition-metal centers to the NMR nucleus of interest (e.g. Li, P, O).[44,54,58,61,214]

Notably, in contrast to isolated molecules, such calculations on extended paramagnetic solids need to be adjusted for the ferro- or antiferromagnetic couplings between the spin centers in the Curie–Weiss paramagnetic temperature region that frequently corresponds to the situation of the NMR measurement.[44,58,214]

For molecular systems, several studies[57,59,60,63,65,118,120,122–125,130,220–224] showed contributions beyond the FC-shift to become important, in particular when the former is, for various reasons, small. These additional contributions consist of a) orbital shifts (analogous to the Ramsey-type expression[88,90] of shifts for diamagnetic systems) and what has been termed "pseudo-contact" or "dipolar" shifts.[109,110] The latter arise from interactions that couple anisotropic hyperfine interactions at the nucleus of interest with the magnetic anisotropy at the paramagnetic metal center (encodable by the electronic g-tensor and, for $S > 1/2$, by the zero-field splitting, ZFS). The first attempts to include pseudo-contact (PC) shifts for extended solids using g-tensors obtained in DFT calculations have been published recently. Mali et al.[45] included g-tensors obtained from GIPAW[76,77] calculations in Quantum Espresso,[132] to compute PC-shifts in a study of Li_2FeSiO_4 polymorphs.[45] Pigliapochi et al.[68] combined GIPAW g-tensors from Quantum Espresso within the generalized gradient approximation (GGA, here the PBE functional) with hyperfine couplings obtained at hybrid-DFT levels with CRYSTAL (GTO LCAO) for a number of olivine-type $LiMPO_4$ materials.

Here we report our first systematic studies using a different type of implementation of pNMR shifts using the Gaussian-augmented-plane-wave (GAPW)[133,134] approach available within the CP2K code.[69] GAPW combines the advantages of GTO-type LCAO-basis sets for the orbitals with those of an augmented plane-wave basis for the density.[135,136] A

large advantage of CP2K is, that it has fewer limitations regarding the permitted GTO basis sets compared to CRYSTAL, and it permits efficient computations with hybrid functionals and large basis sets for the hyperfine couplings. In fact, the extremely efficient parallelization of CP2K makes the code particularly suitable for highly parallel large-scale computations on supercomputers and allows us to address large unit cells.[78] g-Tensor calculations with CP2K using GGA functionals are available and have been reported before.[137,138] In addition, here we report inclusion of orbital shifts for extended solids at the same level. Notably, the present report illustrates the bridges between molecular and periodic pNMR shift computations.

The setup of this chapter is as follows: after describing the theoretical background of the computations and providing Computational Details, discussion of the results starts from validation of CP2K computations for various separate contributions and of full pNMR shifts for isolated molecules in a large super-cell against typical computations using molecular quantum-chemical codes. This is then extended to g-tensor computations for extended transition-metal fluorides and lithium vanadium phosphate materials of general composition $Li_xV_2(PO_4)_3$ (x= 3, 2.75, 2.5, 2.25, 2 and 1). Finally, pNMR shifts for different Li sites are validated and analyzed at various computational levels for $Li_3V_2(PO_4)_3$. The choice of this material was partly motivated by the expectation that it exhibits small ZFS (the latter is not included in the present computations, calculations including ZFS will be reported elsewhere), while being closely related to the above mentioned battery materials. For g-tensor computations, we also have compared full computations using periodic boundary conditions against an incremental approach based on cluster models.

4.2. Theory

pNMR Shift theory. Our pNMR shielding calculations follow the doublet-state framework proposed by Moon and Patchkovskii,[117] found to be extendable beyond doublet states when the ZFS is negligible.[129] In this formalism (note ref. 60 for alternatives), the hyperfine shielding is expressed via a matrix product of the g- and A-tensors. eq. 4.1 formulates this for exchange-coupled solids in the Curie–Weiss temperature regime:

$$\boldsymbol{\sigma}^I = \boldsymbol{\sigma}^I_{\mathrm{orb}} - \frac{\mu_B S(S+1)}{3k_B \mathrm{g}^I_N \mu_N (T-\Theta)} \mathbf{g}\cdot\mathbf{A}^I, \tag{4.1}$$

where S is the total electronic spin quantum number, μ_B the Bohr magneton, k_B the Boltzmann constant, g_N^I is the g-factor of nucleus I, μ_N the nuclear magneton, T temperature, Θ the Weiss constant of the system, $\mathbf{g}$ the electronic g-tensor, and $\mathbf{A}^I$ the hyperfine coupling tensor of nucleus I. In contrast to ref. 117, which deals with isolated paramagnetic molecules, Eq. 4.1 replaces T by T - Θ in the denominator of the hyperfine shift term to account for the residual exchange couplings of the extended solid-state system in question, assuming Curie–Weiss behavior at the temperatures probed experimentally.[149,150] Such a temperature dependence is also observed for the paramagnetic shifts in exchange-coupled systems and thus introduced into Eq. 4.1.[43,44,54,58] For each material, the Weiss constant obtained experimentally by low-temperature extrapolation of the high-temperature susceptibility curves will be used. For the moment, this adds an empirical correction to the computations. In the long run, it will be desirable to obtain analogous information from a statistical first-principles treatment of the exchange interactions in the solid. Note, however, that at the simulation temperature (320 K) used, a change in the Weiss constant of 20 K in one or the other direction affects the hyperfine shifts only by about 5%. Both $\mathbf{g}$ and $\mathbf{A}^I$ are general 3 × 3 matrices composed of a scalar (rank zero), a true anisotropic symmetrical second-rank tensor (g- and A-tensor anisotropies) and an asymmetric (rank 1) part (the latter is zero for the nonrelativistically computed $\mathbf{A}^I$ used here).

We may separate the g- and A-matrices into their individual contributions: $\mathbf{g}$ may be written as $(g_e + \Delta g_{iso})\mathbf{1} + \Delta\tilde{\mathbf{g}}$, where g_e is the isotropic free-electron g-value, Δg_{iso} the isotropic deviation, and $\Delta\tilde{\mathbf{g}}$ the traceless anisotropic part. Similarly, the nonrelativistic $\mathbf{A}^I$ is separated into the isotropic Fermi-contact part $A^I_{FC}\mathbf{1}$ and the dipolar tensor $\mathbf{A}^I_{dip}$. Since $\mathbf{A}^I_{dip}$ and $\Delta\tilde{\mathbf{g}}$ are traceless, eq. 4.2 gives only four non-zero contributions to the isotropic shielding:

$$\sigma^I_{iso} = \sigma^I_{orb,iso} - \frac{\mu_B S(S+1)}{3k_B g^I_N \mu_N (T-\Theta)} \left(g_e A^I_{FC}\mathbf{1} + \Delta g_{iso} A^I_{FC}\mathbf{1} + \Delta\tilde{\mathbf{g}}\cdot\mathbf{A}^I_{\mathbf{dip}}\right)_{iso}. \tag{4.2}$$

Four terms from the matrix product $\mathbf{gA}^I$ contribute to the shielding anisotropy, giving

$$\boldsymbol{\sigma}^I_{aniso} = \boldsymbol{\sigma}^I_{orb,aniso} - \frac{\mu_B S(S+1)}{3k_B g^I_N \mu_N (T-\Theta)} \left(g_e \mathbf{A}^I_{dip} + \Delta g_{iso}\mathbf{A}^I_{dip} + \Delta\tilde{\mathbf{g}} A^I_{FC} + \Delta\tilde{\mathbf{g}}\cdot\mathbf{A}^I_{dip}\right)_{aniso}, \tag{4.3}$$

where the subscript aniso indicates the traceless anisotropic part of the sum in parentheses. Traditionally, the experimental isotropic pNMR shift is decomposed into three parts:

orbital shift (δ_{orb}), Fermi-contact shift (δ_{FC}), and pseudo-contact shift (δ_{PC}):

$$\delta_{\mathrm{exp}} = \delta^{\mathrm{exp}}_{\mathrm{orb}} + \delta^{\mathrm{exp}}_{\mathrm{FC}} + \delta^{\mathrm{exp}}_{\mathrm{PC}}. \tag{4.4}$$

Conversion from nuclear shieldings to relative chemical shifts is done in the usual way by subtracting the shielding from that of a suitable reference compound (see Computational Details below). Comparing thus eq. 4.4 to eq. 4.2, obviously $\sigma^I_{\mathrm{orb,iso}}$ corresponds to $\delta^{\mathrm{exp}}_{\mathrm{orb}}$. The sum of the two terms depending on $\mathrm{g}_e\mathrm{A}^I_{\mathrm{FC}}$ and $\Delta\mathrm{g}_{iso}\mathrm{A}^I_{\mathrm{FC}}$ corresponds to $\delta^{\mathrm{exp}}_{\mathrm{FC}}$, whereas in the doublet formalism (i.e. without ZFS) the term depending on the isotropic part of $\Delta\tilde{\mathbf{g}}\cdot\mathbf{A}^I_{\mathrm{dip}}$ gives $\delta^{\mathrm{exp}}_{\mathrm{PC}}$.

The shift tensor can be characterized by the shift anisotropy, $\Delta = \delta_{zz}$ - $\frac{1}{2}(\delta_{xx} + \delta_{yy})$ and by the asymmetry parameter (deviation from axial symmetry), $\eta = \frac{\delta_{yy}-\delta_{xx}}{\delta_{zz}-\delta iso}$, where the components are arranged according to the Haeberlen convention to give $\mid \delta_{zz} - \delta_{iso} \mid \geq \mid \delta_{xx} - \delta_{iso} \mid \geq \mid \delta_{yy} - \delta_{iso} \mid$, where the orientations of the δ_{ii} components correspond to the principal axis frame of the symmetric part of the shift tensor.[225,226]

Hyperfine coupling tensors. Here we so far are restricted to the nonrelativistic formalism, where $\mathrm{A}_{\mathrm{iso}}$ corresponds to the Fermi-contact term and is thus proportional to the electronic spin density $\rho^I_s(0)$ at the position of nucleus I:[107,189,227,228]

$$\mathrm{A}^I_{\mathrm{iso}} = \frac{4\pi}{3}\frac{\mathrm{g}_e\mu_B\mathrm{g}^I_N\mu_N}{\langle S_z\rangle}\rho^I_s(0) = \mathrm{A}^I_{\mathrm{FC}}. \tag{4.5}$$

$\langle S_z\rangle$ is the expectation value of the z component of the total electronic spin.

The components $\mathrm{A}^I_{\mathrm{aniso},ij}$ of the anisotropic part of the hyperfine matrix result from dipole-dipole interactions,[107,189,227,228] We note in passing, that in molecular computations of pNMR shifts, spin–orbit and scalar relativistic corrections to the HFCs have sometimes been included.[57,59,118,124,125,128,129] They are, however, currently not available in solid-state codes and, moreover, are not expected to be important for the lithium HFCs in the present work.

$$\mathrm{A}^I_{\mathrm{aniso},ij} = \frac{1}{2}\frac{\mathrm{g}_e\mu_B\mathrm{g}^I_N\mu_N}{\langle S_z\rangle}\int d\mathbf{r}\rho^I_s(\mathbf{r})\frac{3r_ir_j - \delta_{ij}r^2}{r^5} = \mathrm{A}^I_{\mathrm{dip},ij}. \tag{4.6}$$

Subscripts i, j refer to Cartesian coordinates x, y, and z. While local spin and thus $\langle S_z\rangle$ is easily defined for molecules, it is less straightforward for condensed-phase systems. In fact, the implementation of hyperfine tensors in solid-state codes does not normalize the spin density to the number of unpaired electrons locally, in the way done in eqs. 4.5 and

4.6.[30,72,189,227] We thus have to divide the spin density provided by CP2K by a factor of $2S$, where S is the spin of the paramagnetic center.[44]

Aspects of g-tensor calculations. As the formalism we use for pNMR shielding (cf. eq. 4.1 above) requires computation of g- and A-tensors, it is important to examine aspects that may affect their accuracy. The solid-state g-tensor implementation in CP2K[69] is based on the second-order perturbation treatment by Pickard and Mauri[76] for paramagnetic defects in solids, using periodic boundary conditions (PBCs). The different contributing terms are:

$$\mathbf{g} = \mathrm{g}_e\mathbf{1} + \Delta\mathbf{g}^{\mathrm{ZKE}} + \Delta\mathbf{g}^{\mathrm{SO}} + \Delta\mathbf{g}^{\mathrm{SOO}} = \mathrm{g}_e\mathbf{1} + \Delta\mathbf{g}. \tag{4.7}$$

Deviations $\Delta\mathbf{g}$ from the free-electron g-factor (first term) are provided by the (isotropic) Zeeman-Kinetic Energy (ZKE) contribution (second term), the "standard" spin–orbit (SO) contributions (third term, contains diamagnetic "gauge" and paramagnetic parts), and the spin-other-orbit (SOO) contribution (fourth term). Pickard and Mauri define these terms as:[76,137]

$$\Delta\mathrm{g}_{ij}^{\mathrm{ZKE}} = -\frac{\mathrm{g_e}}{c^2}(T^\alpha - T^\beta)\delta_{ij} \tag{4.8}$$

$$\Delta\mathrm{g}_{ij}^{\mathrm{SO}} = \frac{(\mathrm{g_e}-1)}{c}\int_{\Omega_c}\left[\mathbf{j}_i^\alpha(r)\times\nabla V_{\mathrm{eff}}^\alpha(r) - \mathbf{j}_i^\beta(r)\times\nabla V_{\mathrm{eff}}^\beta(r)\right]_j d^3r \tag{4.9}$$

$$\Delta\mathrm{g}_{ij}^{\mathrm{SOO}} = 2\int_{\Omega_c} B_{ij}^{\mathrm{corr}}(r)\rho^s(r)d^3r. \tag{4.10}$$

Here $\rho^s = \rho^\alpha - \rho^\beta$ is the spin density, α and β denote the spin channels σ, and T^σ, $\mathbf{j}_i^\sigma$, and ρ^σ are the unperturbed kinetic energy, induced current density, and electron density of the spin-σ channel, respectively. The integrals span the volume of the simulation cell, Ω_c. V_{eff}^σ is the effective Kohn-Sham potential for the the spin-σ electrons.

The spin–orbit contributions dominate the g-tensor. Upon reduction of the full Dirac-Coulomb-Breit Hamiltonian for many-electron systems to the Breit-Pauli Hamiltonian, one obtains a) the one electron spin-orbit-nucleus term, b) the two-electron spin–orbit term resulting from Coulomb- and exchange screening of nuclear charge, and c) the spin-other-orbit term arising from the Breit interaction (relativistic corrections to electron repulsion). Disregarding here the fact that relativistic exchange-correlation functionals would be required for a complete DFT computation of SO effects and assuming that we may use the Kohn-Sham determinant to compute SO matrix elements, we nevertheless end up with a large number of two-electron SO integrals. Several approximations have been suggested to simplify matters. Complete replacement of the two-body interactions by the effective

one-electron Kohn-Sham potential (V_{eff}) is the simplest and most often used. However, this neglects contributions arising from antisymmetric (exchange-like) terms, including the SOO term.[229,230] Mean-field approaches including the exchange and SOO terms include the spin–orbit mean-field (SOMF)[229] method, additionally invoking a one-center approximation gives the so-called atomic mean-field integrals (AMFI) method.[231]

CP2K has the Pickard/Mauri[76,137] V_{eff} implementation augmented by an approximation to the SOO term. V_{eff} is obtained by integrating products of the induced current densities and the gradient of the effective potential $V_{\text{eff}}^{\tau}(\alpha,\beta)$[232] over the simulation cell. V_{eff}^{τ} is defined as

$$V_{\text{eff}}^{\tau}(r) = \nu_{\text{ext}}(r) + \nu_H(r) + \nu_{\text{xc}}^{\tau}(r), \tag{4.11}$$

where ν_{ext} is the Coulombic potential from the nuclei, ν_H the Hartree potential, and ν_{xc}^{τ} the exchange-correlation potential. For further elaboration and implementation see Refs. 137 and 233.

In eq. 4.10 for the missing SOO term,[76] B_i^{corr} represents the magnetic field that originates from the corresponding total (self-interaction-corrected) induced current density, $\mathbf{j}_i$,[137] as experienced by the unpaired electron. That is, the SOO contribution to a g-shift tensor component becomes

$$\Delta g_{xy}^{\text{SOO}} = \frac{1}{S}\int B_y^{1,x}(r)[\rho_\alpha - \rho_\beta]dr, \tag{4.12}$$

where $B^{1,x}$ is the magnetic field induced by the electronic currents when a magnetic field with unit magnitude is applied in the x direction (referred to as $V_{\text{eff,PM}}$). This may miss the abovementioned other exchange-like contributions, which is why one may expect a somewhat overestimated overall SO term compared to the more complete treatments.

The vector potential of the external magnetic field is defined up to an arbitrary translation. For computations in a finite basis set, this leads to the well-known gauge dependence. While this is thought to be less pronounced for g-tensors than, for example, for nuclear shieldings, it nevertheless needs to be accounted for. The most refined method for molecular calculations is the use of gauge-including atomic orbitals (GIAO).[234] The individual gauges for atoms in molecules (IGAIM)[235] or the closely related, simplified continuous set of gauge transformation (CSGT) approach[236] have been found to perform almost as well.[237] A common gauge origin (e.g. at the center of electronic charge, the center of nuclear charges or the position of a specific atom) is clearly the crudest possibility. The proper choice of gauge origin becomes important when the g-shifts are very small and/or spin orbit contributions from the atoms in different parts of a rather unsymmetrical molecule

are of similar magnitude.[238,239] CP2K offers extensions of IGAIM and CSGT to periodic boundary conditions. While the CSGT method has higher computational efficiency,[137] in this work we have focussed on using IGAIM. So far solid-state g-tensor codes offer only local or generalized gradient approximation (GGA) implementations, but no hybrid functionals.

The existing implementations of g-tensors in solid-state codes have furthermore been geared towards paramagnetic defects with only one paramagnetic center in the simulation cell. When using larger cells with more than one center, we found an incorrect size dependence, where the individual site g-tensors simply added up (as also mentioned in ref. 68). To calculate the g-tensor for periodic paramagnetic solids with multiple paramagnetic centers n, we thus have to normalize the resulting g-tensor of the simulation cell as

$$\mathbf{g} = \mathrm{g}_e\mathbf{1} + \frac{1}{n}\left(\Delta\mathbf{g}^{\mathrm{ZKE}} + \Delta\mathbf{g}^{\mathrm{SO}} + \Delta\mathbf{g}^{\mathrm{SOO}}\right) = \mathrm{g}_e\mathbf{1} + \frac{1}{n}\Delta\mathbf{g}. \tag{4.13}$$

Orbital shielding tensor. The components $\sigma^I_{\mathrm{orb},ij}$ of the orbital shielding tensor of nucleus I for periodic solids, as implemented in CP2K, are defined as:

$$\sigma^I_{\mathrm{orb},ij} = \frac{1}{c}\int_{\Omega_S}\left[\frac{r - r'}{|r - r'|^3} \times \mathbf{j}_i(r)\right]_j d^3r, \tag{4.14}$$

where c is the speed of light in vacuum, i, j are the indices to represent x, y and z directions, r' is the position of nucleus I, $\mathbf{j}_i$ is the current density induced by a constant external magnetic field applied along the i axis, and Ω_S is the volume of the entire integration domain, including the periodic replicas of the simulation cell. The other tensor components can be obtained by changing the indices accordingly. This corresponds to the open-shell generalization of the previously reported nuclear shielding implementation for diamagnetic systems,[137] and we have used IGAIM gauges with CP2K (GIAOs with the Gaussian09 molecular code for comparison).

4.3. Computational and Experimental Details

General aspects. Calculations with the CP2K/Quickstep package[69,191] used periodic boundary conditions both for molecules (large super-cell) and solids. Optimizations of cell parameters used the hybrid Gaussian and plane waves (GPW) formalism together with the pseudopotential approximation, applying the PBE GGA exchange-correlation functional.[190]

Goedecker-Teter-Hutter (GTH) pseudopotentials[192] and double-ζ MOLOPT basis sets (DZVP-MOLOPT-SR-GTH)[193] have been used for all elements. For the expansion of the charge density in plane waves, an energy cutoff of 500 Ry has been used, and the convergence criterion over the maximum component of the wave function gradient was set to 1.0×10^{-7}. Calculations have been carried out on a $2 \times 2 \times 2$ super-cell to minimize artefacts of the periodic boundary conditions. Note that, while the GAPW *ansatz* in CP2K uses minimal k-point sampling, the code enables the use of extended super-cells to compensate for this and to thus improve accuracy. Keeping the cell parameters fixed, the atom positions were further optimized using the all-electron Gaussian-augmented-plane-waves (GAPW)[133,134] formulation with PBE and def2-TZVPD/def2-TZVP basis sets.[194,195] The wave-function convergence criterion was set to 1.0×10^{-6}, and the energy cutoff has been kept at 500 Ry.

Magnetic-resonance parameter calculations employed the all-electron GAPW implementation of CP2K, which is particularly suitable for the properties needed here. Computation of orbital shieldings followed the existing CP2K implementation for diamagnetic systems[137] (related to GIPAW) in its open-shell extension, using IGAIM. g-Tensor calculations used the related CP2K implementation,[201] with spin–orbit treatments described in the theory section, and IGAIM for the gauge treatment. Both g-tensors and orbital shieldings were obtained at the PBE level. Hyperfine coupling (HFC) tensor computations were based on the implementation of ref. 189. In addition to PBE, PBE-based global hybrids were used, varying the exact-exchange (EXX) admixture from 5% (PBE5) to 40% (PBE40).With minimal k-point sampling, use of larger super-cells is also known to help improve the accuracy for sensitive quantities such as HFCs.[201] Basis sets to be used in the different comparisons of NMR/EPR parameters vary and will be detailed further below.

Experimental determination of the structure of lithium lactate. Solid Li lactate is an excellent standard for Li shift referencing (discussed later), so the crystal structure of Li lactate was determined by X-ray diffraction (XRD) to serve as the input structure for orbital shielding calculations (see below). Lithium L-lactate (Sigma Aldrich, >98%) was dissolved in ethanol, and recrystallization by isopropanol vapor transport produced needles and rectangular plates after several days. X-ray diffraction (XRD) on a rectangular single crystal with dimensions $0.30\,\text{mm} \times 0.08\,\text{mm} \times 0.02\,\text{mm}$ was performed by collecting ω and φ scans with a Bruker D8-QUEST using Cu Kα radiation ($\lambda = 1.5406\,\text{Å}$), and structure solution and refinement was performed with use of the SHELX program package.[240] Material as purchased was lightly ground and powder XRD was performed to confirm the single crystal was representative of the bulk (PANalytical Empyrean, Cu Kα radiation).

The structure was solved using a unit cell in the $P2_1$ space group, with dimensions $a = 4.5412(4)$ Å, $b = 4.8838(4)$ Å, $c = 10.1982(10)$ Å, and $\beta = 98.226(7)$ °; Li^+ ions sit in a LiO_4 tetrahedral environment (see Figure A.1 in Appendix A). H atoms were treated by a mixture of independent and constrained refinement, The absolute structure was assigned from known L-lactate material, with (S)-configuration at C2. Crystallographic details are listed in Table A.1, atomic coordinates are listed in Table A.2, and anisotropic displacement parameters are listed in Table A.3. Our structure determination differs from a previous report by Clough and Poldy, who observed a similar crystal habit of a thin rectangular plate but assigned a $P2_1/c$ space group in their preliminary analysis.[241] Due to symmetry considerations, the $P2_1/c$ space group is unable to support the periodic packing of a single enantiomorph, whereas the $P2_1$ space group determined in the structure solution presented here is a non-enantiogenic Sohncke space group capable of supporting the packing of the L-lactate enantiomorph.

Shift referencing. ^{7}Li shifts of the solid in question are obtained by subtracting its computed absolute shielding from that of lithium lactate ($LiC_3H_5O_3$) , i.e. $\delta^I = \sigma^I_{ref} - \sigma^I$. The orbital shieldings for solid lithium lactate were computed for two cluster models cut out from the XRD supercell structure (see above), to evaluate convergence with cluster size. The smaller cluster has eight units of $LiC_3H_5O_3$ (96 atoms). The second, much larger cluster has 18 units of $LiC_3H_5O_3$ (216 atoms) (see Figure A.2 in Appendix A). We note in passing, that for the large orthorhombic cells of Li lactate, converged PBC-based computations of the orbital shieldings for large super-cells are currently precluded. The shieldings have been computed at PBE/IGLO-II level in a super-cell of size 40 Å× 40 Å× 40 Å and size 60 Å× 60 Å× 60 Å, for the small and the large cluster, respectively. The resulting shieldings are 90.5 ppm and 90.4 ppm for the small and large cluster, respectively (the shieldings of the inner six Li sites were averaged for the large cluster), indicating a converged cluster model. These data should be useful for further analyses of lithium shifts in solids.

Comparisons of CP2K super-cell results for molecules against quantum-chemical codes. To validate the computation of the different ingredients contributing to pNMR shifts obtained with CP2K against standard quantum-chemical codes, orbital shieldings, HFC tensors, and g-tensors for two doublet molecules (cobaltocene and the TEMPO nitroxide radical) have been computed in a large cubic supercell of size 30 Å×30 Å×30 Å, using large def2-QZVP basis sets.[194] This super-cell size ensures negligible interactions with molecules in neighboring cells. These calculations used structures optimized at B3LYP/6-311++G(d,p)[196–200] level with the Gaussian09[74] code.

Comparisons for HFCs and orbital shieldings were done against Gaussian09 results, g-tensors against ORCA[70] and MAG[73] data, using the same def2-QZVP basis sets. While ORCA provided only a common gauge for the external magnetic field (placed at the center of charge), the MAG calculations allowed additionally the use of gauge-including atomic orbitals (GIAOs).[234] This turned out to be of importance for some comparisons (see below). Orbital shielding and g-tensor comparisons were done with the BLYP functional,[196,203] while HFCs were computed with both BLYP and PBE0[204] functionals. Some additional explorations of gauge aspects and SO operators for g-tensors were done for a number of simple trigonal-planar transition-metal trifluoride complexes MF_3 (M=Ti, V, Cr, Mn, Fe), using the PBE functional and def2-TZVP[242] and IGLO-II basis sets for transition metals and fluorine atoms, respectively, based on B3LYP/6-311++G(d,p)-optimized structures.

Evaluation of g-tensor normalization for periodic solids. To validate the normalization of g-tensors for multiple spin-centers in solids according to eq. 4.13, two sets of test calculations were done. The first set has an increasing number of isolated trifluoride complexes in a supercell of dimension 40 Å×40 Å×40 Å, using the B3LYP/6-311++g(d,p) structures for the individual molecules (see above). The second set consists of variation of the super-cell dimension (and thus of the number of spin centers in the cell) for simple periodic solids, based on structures from X-ray crystallography. Here we chose the four extended trifluorides MF_3 (M=Ti, V, Mn, Fe), with the transition metals octahedrally coordinated. The g-tensor calculations were done at PBE level with IGLO-II and def2-TZVP basis sets for main-group and transition elements, respectively.

Calculations on $Li_xV_2(PO_4)_3$ (x=3, 2.75, 2.5, 2.25, 2 and 1). The initial cell optimization (GPW level with PBE, GTH pseudopotentials, DZVP-MOLOPT-SR basis sets) used a 2 × 2 × 2 super-cell, leading to 512-640 atoms per cell, thus minimizing artefacts of the periodic boundary conditions. Subsequent GAPW optimization of atom positions at PBE/def2-TZVPD/def2-TZVP level (the first basis designation holds for vanadium) used either a simple 1 × 1 × 1 unit cell with 72-80 atoms for the comparatively more expensive subsequent g-tensor and orbital shielding calculations or 2 × 2 × 1 super-cells with 288-320 atoms for the more sensitive HFC calculations to ensure convergence with cell size. HFC values provided by CP2K have been normalized properly to the local spin state (see Theory section).

EPR and NMR parameters were computed both for experimental and optimized structures. g-Tensor calculations were done at PBE/def2-TZVP/IGLO-II level. HFC tensors were calculated both at PBE GGA level and using PBE-based global hybrids, varying exact-

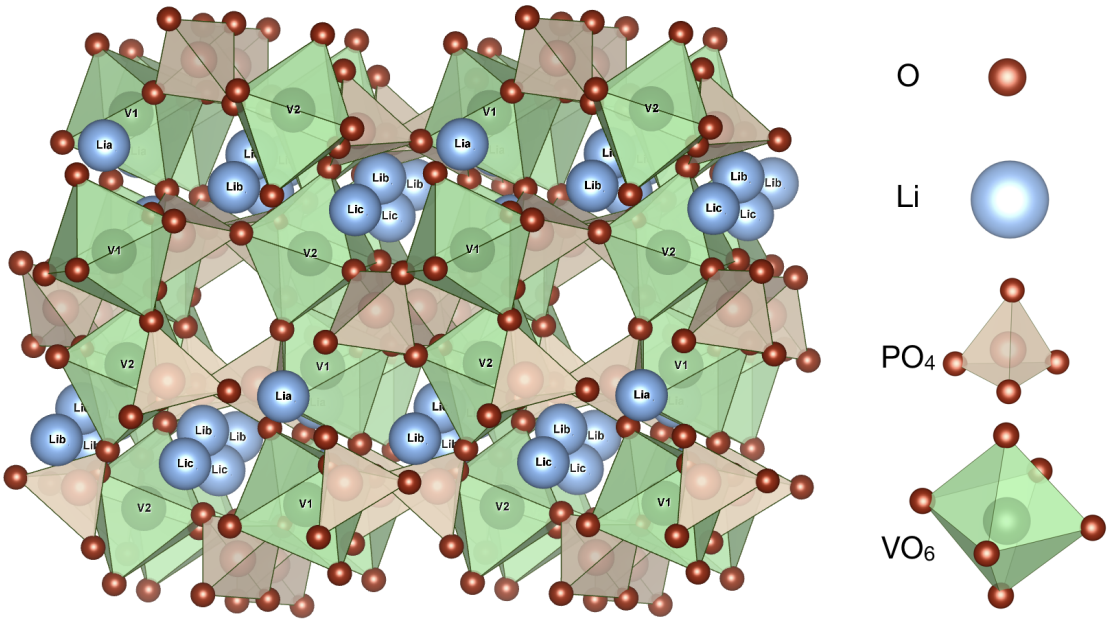

Figure 4.1.: 2 × 2 × 1 Super-cell of nasicon-like lithium vanadium phosphate $Li_3V_2(PO_4)_3$ with 320 atoms (48 lithium atoms with three distinct sites) used for the HFC calculations.

exchange admixture from 5% (PBE5) to 40% (PBE40). This includes the well-known PBE0 functional (25%),[190,204] termed PBE25 in this nomenclature. These computations used basis sets well validated in molecular HFC calculations. A (14s11p6d)/[8s7p4d] basis was used for the transition metal.[202] Only the most diffuse s-function from that work had to be removed to accommodate limitations of diffuse functions for compact solids in CP2K, reducing the size from [9s7p4d] to [8s7p4d]. Unmodified extended Huzinaga-Kutzelnigg-type IGLO-II[209] basis sets were used for the main-group atoms. This possibility to use extended GTO basis sets is a distinct advantage of CP2K over previous FC shift calculations with CRYSTAL.[44]

To finally compute ^{7}Li nuclear shieldings and, thus, NMR shifts of $Li_3V_2(PO_4)_3$, the computed EPR parameters and orbital shieldings were inserted into eq. 4.1, using HFC tensors at various hybrid levels, as well as orbital shieldings and g-tensors at PBE level, as described above. The value of the Weiss constant (Θ = -37 K) has been taken from experiment.[43]

Incremental cluster-model approach to g-tensors for periodic solids. As an alternative to the periodic g-tensor calculations, we have evaluated also the use of an incremental scheme, where the g-tensor of the unit cell is built from clusters around

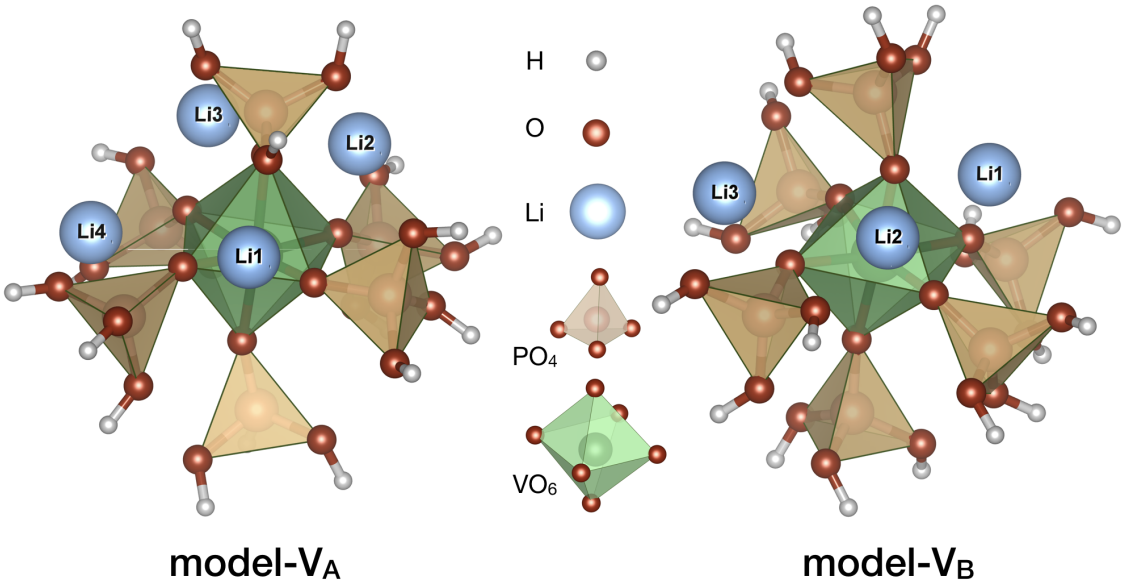

Figure 4.2.: Molecular models of the two distinct vanadium centers of $Li_3V_2(PO_4)_3$ solids, where the terminal oxygens have been saturated with hydrogen atoms. Model A and B has 4 and 3 lithium atoms, respectively.

a given metal center. This exploits the expected locality of g-tensors in insulators or semiconductors and opens the principal possibility to apply more easily higher levels of theory for this property. The approach is analogous to the incremental scheme for electron correlation in solids.[243] The cluster models were extracted from the optimized $Li_3V_2(PO_4)_3$ structures as shown in Figure 4.2. They include the core structure of the metal coordination, i.e. vanadium octahedrally coordinated by six tetrahedral phosphates (PO_4). The oxygen valences of the phosphate groups were saturated with additional hydrogen atoms. The hydrogen-atom positions were optimized at PBE/def2-TZVP level using Turbomole.[71] As $Li_3V_2(PO_4)_3$ has two distinct vanadium environments, two sets of cluster models were constructed. For these, the number of lithium counter-ions was varied, including ions further and further removed from the phosphates. For comparability with the periodic calculations, g-tensors for each of the resulting clusters were computed with CP2K at PBE/def2-TZVP/IGLO-II level in a super-cell of dimension 40 Å × 40 Å × 40 Å. The resulting g-tensors were re-inserted into the solid-state structures in appropriate orientation (using the corresponding rotational matrices), making use of point-group symmetry to replicate identical sites and to thus minimize the number of g-tensor calculations needed. For example, the unit cell of $Li_3V_2(PO_4)_3$ has eight vanadium centers but only two distinct non-equivalent sites. Only two g-tensors thus need to be computed to generate the eight site g-tensors in the cell, which then lead size-consistently to the unit-cell g-tensor by

suitable averaging. We note that the method is somewhat related to the approach in ref. 68, where site g-tensors were obtained from periodic calculations by replacing all but one paramagnetic metal ion in the cell by diamagnetic ions.

4.4. Results and discussion

Validation of CP2K results for isolated molecules against quantum-chemical codes. While CP2K is a well-known computational package,[78] used widely in the solid-state physics and quantum-chemistry community, it has so far not been used to compute NMR shifts for paramagnetic solid-state systems, albeit some experience for g-tensors[137,138] and NMR shifts of diamagnetic systems[87,244,245] exists.

Before delving into explicit solid-state calculations, we thus need to establish the accuracy of the CP2K computations of HFC and g-tensors, as well as orbital shieldings. This is best done by computations on isolated molecules in a sufficiently large super-cell, in comparison with standard molecular quantum-chemical calculations using identical density functionals and basis sets. Let us thus focus on results for the doublet spin molecules TEMPO and cobaltocene (in staggered conformation; see Figure 4.3 and Computational Details), starting with isotropic HFCs, known to be very sensitive to various computational parameters. Figure 4.4 compares relative and absolute deviations of isotropic HFCs (Fermi-contact contribution) for various main-group nuclei in both test molecules with CP2K against Gaussian09 as reference, using either the BLYP GGA or the PBE0 hybrid functional. Relative deviations are generally below 1%, with absolute deviations below 0.05 MHz (ca. 0.1% MHz for the nitroxide nitrogen atom in TEMPO). This confirms that a) use of a super-cell in CP2K does not cause any notable deviations, b) the GAPW *ansatz* in CP2K faithfully reproduces the Gaussian09 results, and c) any deviations due to the different integration grids used in the two codes also remain minor.

Moving on to g-tensors (Table 4.1), in addition to those computational parameters discussed above, the nature of the SO operators comes into play. Comparison is made to calculated g-tensors obtained with ORCA, using the accurate spin-orbit mean-field (SOMF) approximation for the SO matrix elements. In contrast, CP2K utilizes the Mauri/Pickard SO approximations[76] from eq. 4.8. Agreement is good in both cases, but the CP2K results generally give slightly larger deviations from the free-electron g-value than the ORCA data. This is not unexpected, as the treatment of the SOO term is somewhat less complete in CP2K, which is thought to cause a slight overestimate of the SO matrix elements. It is

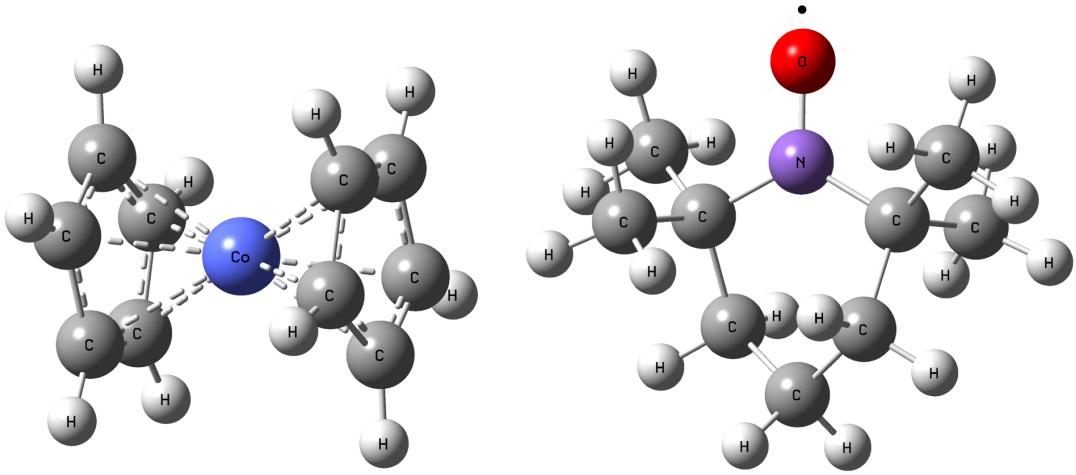

Figure 4.3.: Molecular test cases, a) cobaltocene and b) TEMPO radical, used to validate CP2K super-cell results.

important to point out, however, that previous tests suggest that this overestimate is much smaller than for other solid-state g-tensor implementations.[138] CP2K is thus well-suited to also give us the needed g-tensor, with the current caveat that we cannot yet use hybrid functionals.

Table 4.2 shows the results for triplet-state VF_3, a metal complex reasonably close to a local environment of the solid-state systems in focus in this work (see below). MAG allows the use of a number of different SO operators, ranging from a full treatment (FULL) of the Breit-Pauli SO integrals via the atomic meanfield approximation (AMFI; ORCA's SOMF may be viewed as intermediate between these two treatments) to Koseki's semi-empirical effective one-electron SO operators (1el.-eff.[246–248]) to the bare one-electron SO term (1el.). Focussing on the GIAO-based results, we see that AMFI deviates relatively little from the full treatment (in spite of some known incompatibility between AMFI and GIAO),[238] whereas 1el.-eff. and 1el. overshoot deviations from the free-electron g-value drastically for this system (as two-electron SO contributions diminish the overall SO matrix elements, their incomplete treatment causes an overestimate). The IGAIM-based CP2K results with the eq. 4.8 SO operator are close to the GIAO-based MAG results with AMFI, confirming both the reasonable SO operator of CP2K and the good accuracy of the IGAIM gauge compared to GIAO.

Much larger deviations are apparent for calculations that have a common gauge at the metal center: here the match between ORCA and MAG data is negligible, within the

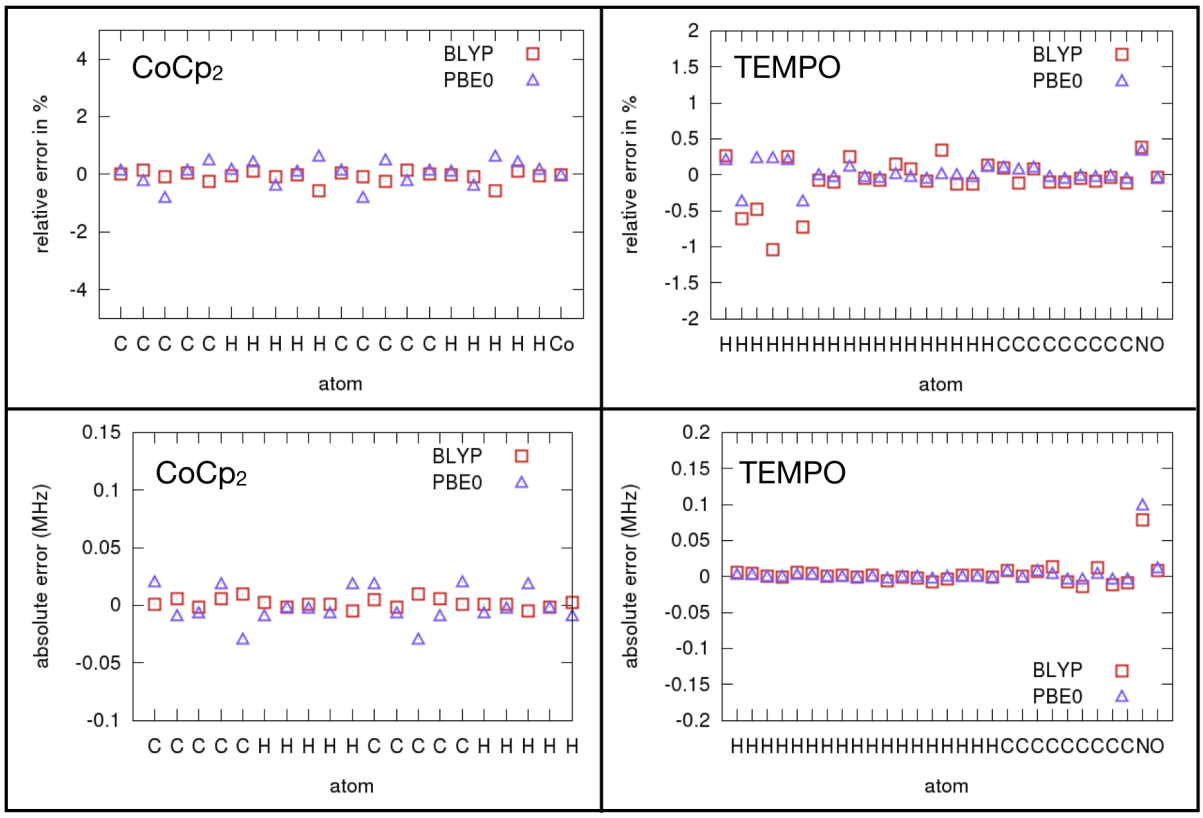

Figure 4.4.: Relative (top) and absolute (bottom) deviations of isotropic HFCs for various main-group nuclei obtained with CP2K compared to Gaussian09 for cobaltocene ($CoCp_2$)(left) and TEMPO (right). Results with def2-QZVP basis set and BLYP or PBE0 functionals.

expected differences between codes, SO-operators, grids, and so on. However, deviations of common-gauge calculations from both GIAO- and IGAIM-based data are notable. This limits the possibility to obtain accurate solid-state g-tensors by inserting molecular model-cluster calculations with ORCA in an incremental scheme, at least for DFT treatments (see below), and points to a need to have a careful eye on the gauge-origin question. Notably, the common-gauge calculations tend to provide smaller deviations from the free-electron value than the GIAO- or IGAIM-based results, an observation we also make for related larger model vanadium complexes (see below). Table A.4 in Appendix A has detailed computed values for other MF_3 (M=Ti, Cr, Mn, Fe) molecules, comparing different codes, gauges and SO operators for g-tensor calculations.

Turning finally to the orbital shieldings, Figure 4.5 shows for both cobaltocene and TEMPO, that IGAIM super-cell calculations with CP2K agree very well with GIAO-based

Table 4.1.: Comparison of g-tensors between CP2K and ORCA for TEMPO and cobaltocene[a]

package	functional	SO-operator	gauge	g_{11}	g_{22}	g_{33}	g_{iso}
TEMPO							
CP2K	BLYP	$V_{\mathrm{eff,PM}}$	IGAIM	2.002	2.007	2.010	2.006
	PBE	$V_{\mathrm{eff,PM}}$	IGAIM	2.002	2.006	2.009	2.006
ORCA	BLYP	SOMF	common	2.002	2.006	2.009	2.006
	PBE	SOMF	common	2.002	2.006	2.009	2.006
	PBE	AMFI	common	2.002	2.006	2.009	2.006
Cobaltocene							
CP2K	BLYP	$V_{\mathrm{eff,PM}}$	IGAIM	1.833	2.018	2.065	1.972
	PBE	$V_{\mathrm{eff,PM}}$	IGAIM	1.831	2.017	2.063	1.970
ORCA	BLYP	SOMF	common	1.858	2.017	2.058	1.977
	PBE	SOMF	common	1.848	2.016	2.057	1.974
	PBE	AMFI	common	1.848	2.016	2.057	1.974

[a] BLYP and PBE results with def2-QZVP basis sets. SOMF operators were used with ORCA, eq. 4.8 with CP2K. The common gauge origin was placed at the center of charge.

calculations using Gaussian09: relative deviations are generally below 1% (slightly above for the small oxygen shielding in TEMPO), absolute deviations are below 1 ppm .

We can thus conclude from these molecular test calculations, that all contributions we need for the doublet-state formalism of pNMR shift calculations (eq. 4.1) are obtainable with CP2K in good accuracy, compared to standard molecular quantum-chemical codes. One possible limitation is the use of only GGA-type functionals for the g-tensor calculations. It is known that such functionals tend to delocalize too much spin density onto the ligands, leading to underestimated SO contributions from the metal center and thus too small g-tensors.[249] This is why we will also explore the use of an incremental scheme based on molecular cluster g-tensor calculations for the different metal sites in the unit cell, as this opens a more facile access to the use of hybrid functionals, or even of post-Hartree-Fock methods.

Validation of g-tensor normalization for more than one spin site in a unit cell. Here we validate the correctness of the normalization to the number of spin centers in eq. 4.13. We first do this by placing an increasing number of molecular metal trifluoride complexes MF_3 (Ti, V, Cr, Mn, Fe) into a large super-cell of 40 Å × 40 Å × 40 Å, so as to minimize interactions between the molecules. Calculations for up to four molecules per

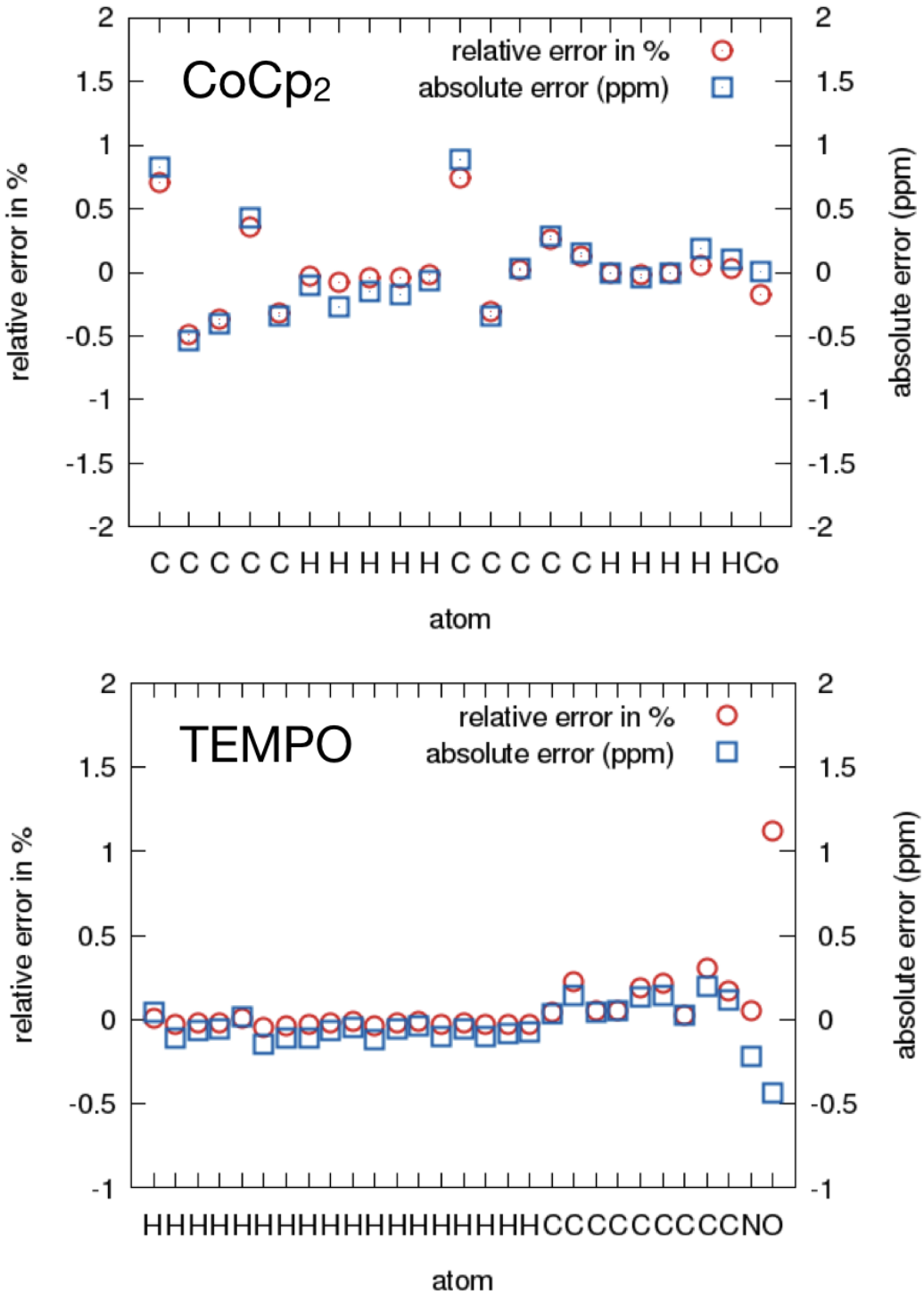

Figure 4.5.: Relative and absolute deviations of CP2K super-cell IGAIM calculations of orbital shieldings from Gaussian09 GIAO data for cobaltocene (left) and TEMPO radical (right), at BLYP/def2-QZVP level.

Table 4.2.: Comparison of different codes, gauges, and SO operators for g-tensor calculations[a] on VF_3

package	**gauge**	**SO-operator**	$\mathbf{g_{11}}$	$\mathbf{g_{22}}$	$\mathbf{g_{33}}$	$\mathbf{g_{iso}}$
CP2K	IGAIM	$V_{eff,PM}$	1.874	1.899	1.976	1.916
MAG	COMMON	FULL	1.975	1.986	1.996	1.986
		AMFI	1.968	1.981	1.994	1.981
		1el.-eff.	1.926	1.958	1.984	1.956
		1el.	1.931	1.960	1.985	1.959
	GIAO	FULL	1.911	1.927	1.982	1.940
		AMFI	1.888	1.909	1.977	1.924
		1el.-eff.	1.751	1.804	1.946	1.834
		1-el.	1.767	1.815	1.950	1.844
ORCA	COMMON	SOMF	1.954	1.963	1.992	1.970
		AMFI	1.954	1.963	1.992	1.970
		1el.-eff.	1.940	1.953	1.990	1.961

[a] PBE results with def2-TZVP and IGLO-II basis sets for vanadium and fluorine, respectively. See text for the abbreviations for SO operators and choices of gauge origin. Super-cell calculations for CP2K, see text.

unit cell at PBE/def2-TZVP/IGLO-II level are given in Table A.5 in Appendix A. Indeed, in spite of the different spin states of the various metal fluorides, normalization renders the g-tensors for the different numbers of spin centers exactly equal, thus confirming the validity of eq. 4.13 for well-separated molecules.

Table 4.3 extends this type of test to extended solids, as exemplified by the solid trifluoride materials, using the same PBE/def2-TZVP/IGLO-II level as for the molecular test. Cell parameters and structures are taken from experimental XRD data,[250–253] which were used to generate super-cells of increasing sizes, having between 24 and 54 spin centers per super-cell. Interaction between the spin centers is now of course more pronounced than for the more or less isolated molecules in the previous test case, and we cannot expect the normalized g-tensors (eq. 4.13) to stay constant as we extend the super-cell size. However, the values vary over only a very small range (super-cell g-tensors exhibit relatively small anisotropy), thus confirming the procedure and providing the necessary setup for g-tensor calculations in super-cells containing more than one spin center.

Table 4.3.: Comparison of normalized solid-state g-tensors for different super-cell sizes of extended MF_3 (M= Ti, V, Mn, Fe) periodic solids using CP2K

solid	**unit**[a]	**n**[b]	$\mathbf{g_{11}}$	$\mathbf{g_{22}}$	$\mathbf{g_{33}}$	$\mathbf{g_{iso}}$[c]
TiF_3	321	36	1.941	1.956	1.951	1.949
	231	36	1.955	1.954	1.954	1.954
	331	54	1.945	1.957	1.954	1.952
VF_3	322	24	1.924	1.900	1.906	1.910
	232	24	1.918	1.903	1.894	1.905
MnF_3	121	24	1.975	1.987	1.987	1.983
	131	36	1.973	1.988	1.987	1.983
	221	48	1.977	1.987	1.989	1.984
FeF_3	221	24	2.026	2.026	2.025	2.025
	321	36	2.025	2.026	2.026	2.026
	231	36	2.026	2.026	2.025	2.025
	331	54	2.024	2.024	2.023	2.024

[a] Digits represent the number of unit-cell replica into the direction of the unit-cell vectors.
[b] Normalization factor reflects the number of paramagnetic spin centers in the super cell.
[c] eq. 4.13 has been used for calculating the normalized g-tensor for periodic solids at PBE/def2-TZVP/IGLO-II level.

Validation for and application to solid lithium vanadium phosphates. Here we focus in particular on g-tensor computations for the series of lithium vanadium phosphates, $Li_xV_2(PO_4)_3$ (x=3, 2.75, 2.5, 2.25, 2, 1), comparing full periodic calculations and the incremental cluster model. Subsequently, the full ^{7}Li pNMR shifts of $Li_3V_2(PO_4)_3$ are analyzed.

Table 4.4 provides results of the PBE/DZVP-MOLOPT-SR-GTH GPW optimizations (cf. Computational Details) of unit-cell parameters in comparison to high-resolution single-crystal XRD data of these phosphate materials.[254] The optimizations were done for a 2 × 2 × 2 super-cell, with dimensions of more than 15 Å in each direction, to minimize artefacts from the periodic-boundary conditions. Agreement to within ca. 1-2% in the cell parameters is generally achieved. Either these optimized or the experimental cell parameters were used subsequently to optimize the atom positions at all-electron GAPW PBE/def2-TZVPD/def2-TZVP level (cf. Computational Details). The same procedure has been used to optimize the structures for the more complicated $Li_{2.75}V_2(PO_4)_3$,

Table 4.4.: Comparison of optimized and XRD unit-cell parameters and volume for $Li_xV_2(PO_4)_3$ (x=3, 2.75, 2.5, 2.25, 2, 1)[a]

material	structure	a (Å)	b (Å)	c (Å)	β(°)	volume (Å^3)
$Li_3V_2(PO_4)_3$	XRD[254]	8.597	8.592	12.001	90.57	886.415
	OPT	8.611	8.606	12.098	90.57	896.448
	% diff	0.16	0.16	0.80	0.00	1.13
$Li_2V_2(PO_4)_3$	XRD[254]	8.461	8.619	11.892	90.00	867.228
	OPT	8.529	8.645	11.965	90.00	882.129
	% diff	0.80	0.30	0.61	0.00	1.72
$LiV_2(PO_4)_3$	XRD[255]	8.301	8.518	11.653	89.61	823.833
	OPT	8.382	8.560	11.745	89.61	842.702
	% diff	0.98	0.49	0.79	0.00	2.29
$Li_{2.75}V_2(PO_4)_3$	OPT	8.624	8.617	12.015	90.57	892.834
$Li_{2.5}V_2(PO_4)_3$	OPT	8.604	8.636	11.956	90.57	888.240
$Li_{2.25}V_2(PO_4)_3$	OPT	8.614	8.654	11.905	90.57	887.288

[a] Cell parameter optimizations at GPW-DZVP-MOLOPT-SR-GTH level for a 2 × 2 × 2 super-cell (monoclinic cell, $P2_1/n$ space group).

$Li_{2.5}V_2(PO_4)_3$, and $Li_{2.25}V_2(PO_4)_3$ systems, for which experimental structural data are lacking. We note in passing the rather large unit-cell sizes and number of atoms (GAPW for atom positions: >300 atoms for 2 × 2 × 1 super-cell; GPW for cell parameters: 2 × 2 × 2 super-cell optimizations, >620 atoms), made possible by the efficient CP2K implementation. Figure 4.6 shows for the example of $Li_3V_2(PO_4)_3$ the excellent agreement between XRD (in yellow) and fully optimized (in blue) structures (similar agreement is found for $LiV_2(PO_4)_3$ and $Li_2V_2(PO_4)_3$, see Figure 4.6). This gives us confidence in the optimized structures for those systems, where XRD data are not available, i.e. $Li_{2.25}V_2(PO_4)_3$, $Li_{2.5}V_2(PO_4)_3$, and $Li_{2.75}V_2(PO_4)_3$. Note the presence of four molecular units in the unit cell for these materials, giving compositions $Li_9V_8(PO_4)_{12}$, $Li_{10}V_8(PO_4)_{12}$ and $Li_{11}V_8(PO_4)_{12}$. This has subtle structural consequences, which need to be taken into account in the NMR/EPR parameter calculations.

Based on these structures we may now compute the various contributions to the pNMR shifts, starting with the g-tensors obtained using the normalization to the number of spin centers in the cell, as discussed above. The PBE/def2-TZVP/IGLO-II-based results for all lithium vanadium phosphate materials studied here are provided in Table 4.5, using both optimized and XRD structures where available, only optimized ones in the remaining cases. While no experimental g-tensors are available for any of these materials, the overall

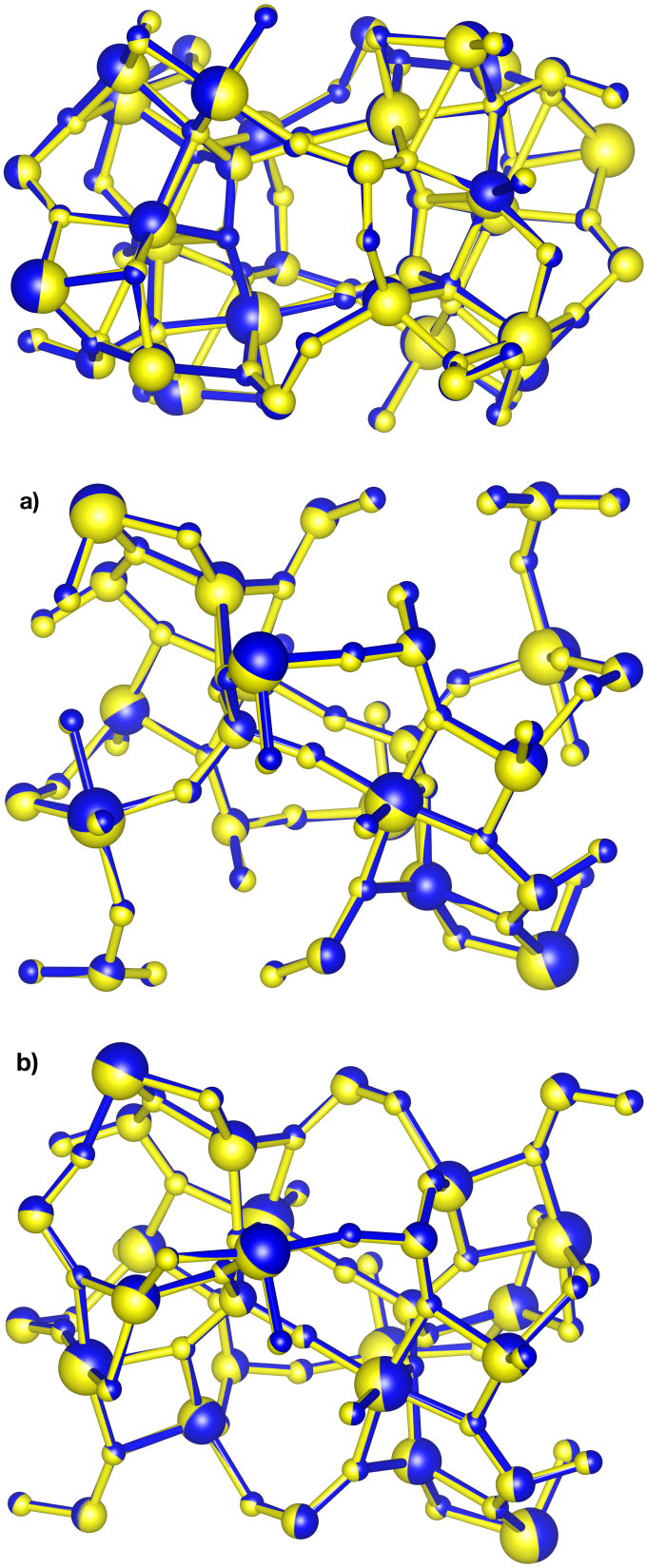

Figure 4.6.: Comparison of XRD (in yellow) and optimized (in blue) structures of $Li_3V_2(PO_4)_3$.

magnitudes compare well to related V^{III}, and V^{IV} sites with octahedral coordination by oxygen atoms (see, e.g., ref. 256), even though we have to assume that the PBE functional underestimates the deviations from the free-electron value (slightly overestimated SO matrix elements may provide some error compensation). Interestingly, the predicted deviations from the free-electron value diminish with an increase of the number of V^{IV} sites (Table 4.5).

Table 4.5.: Computed g-tensors for $Li_xV_2(PO_4)_3$ (x=3, 2.75, 2.5, 2.25, 2, 1) [a,b]

material	**structure**	$\mathbf{V^{+III}}$	$\mathbf{V^{+IV}}$	$\mathbf{g_{11}}$	$\mathbf{g_{22}}$	$\mathbf{g_{33}}$	$\mathbf{g_{iso}}$	$\boldsymbol{\Delta}$[c]	$\boldsymbol{\eta}$[d]
$Li_3V_2(PO_4)_3$	XRD	8	0	1.834	1.870	1.902	1.869	-0.05	0.89
	OPT	8	0	1.864	1.875	1.915	1.885	0.05	0.34
$Li_{2.75}V_2(PO_4)_3$	OPT	7	1	1.875	1.891	1.914	1.894	0.03	0.74
$Li_{2.5}V_2(PO_4)_3$	OPT	6	2	1.871	1.885	1.917	1.891	0.04	0.56
$Li_{2.25}V_2(PO_4)_3$	OPT	5	3	1.880	1.901	1.911	1.897	-0.03	0.58
$Li_2V_2(PO_4)_3$	XRD	4	4	1.897	1.909	1.935	1.914	0.03	0.55
	OPT	4	4	1.895	1.913	1.935	1.914	0.03	0.87
$LiV_2(PO_4)_3$	XRD	0	8	1.877	1.911	1.913	1.901	-0.03	0.09
	OPT	0	8	1.906	1.919	1.919	1.915	-0.01	0.00

[a] Unit-cell g-tensor obtained after normalization (eq. 4.13). Columns V^{+III} and V^{+IV} show the number of vanadium atoms present in the unit cell having oxidation state +III and +IV, respectively (with overall eight vanadium sites present).
[b] Computations on 1 × 1 × 1 cells at PBE/def2-TZVP/IGLO-II level.
[c] g-Tensor anisotropy, $\Delta = g_{zz} - \frac{1}{2}(g_{xx} + g_{yy})$ the components ordered as $| g_{zz} - g_{iso} | \geq | g_{yy} - g_{iso} | \geq | g_{xx} - g_{iso} |$, $g_{iso} = \frac{g_{11}+g_{22}+g_{33}}{3}$ and $g_{11} \leq g_{22} \leq g_{33}$.
[d] Asymmetry parameter, $\eta = \frac{g_{xx}-g_{yy}}{g_{zz}-g_{iso}}$.

In view of these limitations regarding the functional in PBC-based g-tensor calculations, we evaluate additionally in Table 4.6 the performance of an incremental cluster model for obtaining the g-tensor in $Li_3V_2(PO_4)_3$. That is, for both structurally distinct vanadium centers in the unit cell, we have cut clusters with one vanadium site and the six coordinated phosphates (terminated by hydroxy functions) from the solid (Figure 4.2). To include the effect of the lithium counterions, a variable number of ions were included (within 2.2 Å from the oxygen atoms in the direct vanadium coordination sphere). Up to four lithium ions had to be considered for model-V_A, up to three lithium ions for model-V_B (Figure 4.2). To be able to compare directly g-tensor results for the unit cell obtained by placing the molecular g-tensors for these models into the solid-state structure against the full periodic calculations, we used the same PBE functional and the same basis sets and did the cluster

Table 4.6.: Comparison of calculated[a] site g-tensors for clusters,[b] unit-cell g-tensors obtained from cluster models[c] and PBC unit-cell g-tensors[d] for $Li_3V_2(PO_4)_3$

	no. of Li atoms[e]	**Li-O distance**[f] **(Å)**	$\mathbf{g_{11}}$	$\mathbf{g_{22}}$	$\mathbf{g_{33}}$	$\mathbf{g_{iso}}$
model-V_A	0	-	1.792	1.832	1.929	1.851
	1	1.94	1.788	1.847	1.931	1.855
	2	1.96	1.828	1.856	1.933	1.873
	3	1.97	1.821	1.844	1.926	1.864
	4	2.09	1.820	1.852	1.936	1.870
model-V_B	0	-	1.839	1.839	1.945	1.874
	1	1.97	1.834	1.857	1.962	1.884
	2	1.94	1.843	1.856	1.956	1.885
	3	2.02	1.838	1.860	1.943	1.881
unit-cell model	0 (0-0)	-	1.822	1.836	1.929	1.862
	3 (1-2)	-	1.825	1.848	1.936	1.870
	5 (3-2)	-	1.858	1.868	1.896	1.874
	7 (4-3)	-	1.848	1.874	1.901	1.875
PBC results	unit cell	-	1.864	1.875	1.915	1.885

[a] PBE/IGLO-II/def2-TZVP results.
[b] Cluster model with variable number of Li counter-ions, see Computational Details.
[c] g-Tensor for unit cell obtained by replacing the cluster-model g-tensors into the solid-state structure after averaging.
[d] Full calculation of unit-cell g-tensor from periodic calculations (using proper normalization).
[e] Number of Li counter-ions included in cluster model.
[f] Shortest Li-O distance from the VO_6 octahedron.

computations in a large super cell in CP2K. Starting with the individual site g-tensors (Table 4.6), we see that for model-V_A the overall deviations from the free-electron value (cf. g_{iso}) diminish slightly upon inclusion of more Li counterions, while the opposite effect holds true for model-V_B. Generation of the overall unit-cell g-tensor shows a clearer effect of the counterions: as more of them are added, g_{11} and g_{22} increase, and g_{33} decreases somewhat. Overall, agreement with the full PBC result is good, suggesting the cluster modelling to be an adequate alternative that opens avenues towards improved electronic-structure levels from molecular computations. Likely, protonation of phosphate oxygen atoms and addition of Li ions as a means of saturating valencies in the clusters is a sufficiently small perturbation to the central part of the cluster to still provide accurate local g-tensors.

The second, arguably most important individual aspect contributing to the pNMR shifts in the lithium vanadium phosphates are the ^{7}Li HFCs. The isotropic HFCs enter the

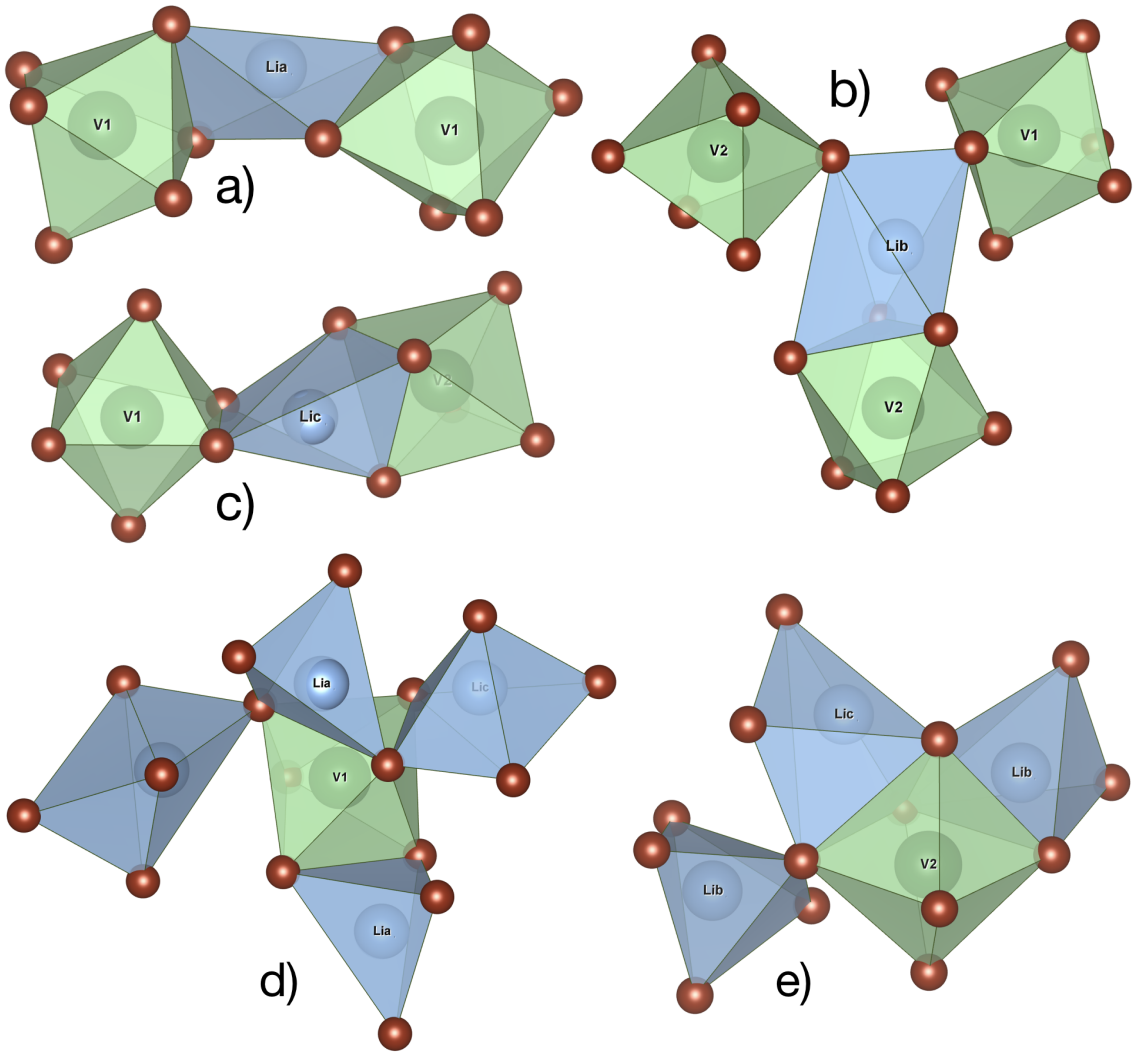

Figure 4.7.: Local environment of three Li and two V sites in $Li_3V_2(PO_4)_3$. a) Li_a, b) Li_b, c) Li_c, d) V_1 and e) V_2, see text.

often dominant FC term, whereas the HFC anisotropies influence not only the shift anisotropies but also the isotropic shift via the PC term. It is the isotropic HFCs that tend to be most sensitive to the computational level, however. Here the strength of CP2K is the possibility to use extended Gaussian-type all-electron basis sets within the GAPW scheme (see Computational Details), together with hybrid functionals. Using IGLO-II and 8s7p4d basis sets for main-group elements and vanadium, respectively (see Computational Details), we thus evaluate the influence of EXX admixture for PBE-based hybrids with EXX admixtures between 5% and 40% for the $2 \times 2 \times 1$ supercell from both XRD and DFT-optimized structures. As shown in Figure 4.7, there are three distinct lithium sites in the structure, Li_a, Li_b, and Li_c, and two distinct vanadium sites, V_1 and V_2, contributing

to the hyperfine shifts. Li_a is in a tetrahedral site sharing edges with two V_1 octahedra, Li_b is in a distorted trigonal bipyramidal site sharing a face with V_2 octahedra and two corners with V_1 and V_2 octahedra, and Li_c is also in a distorted trigonal bipyramidal site sharing a face with V_2 octahedra and an edge with V_1 octahedra.[257,258]

Isotropic (A_{FC}) and dipolar (A_{dip}) HFCs for all three lithium sites are provided in Tables B.1 and B.2 in Appendix B. The A_{FC} values decrease as $A_{FC}(Li_a) > A_{FC}(Li_c) > A_{FC}(Li_b)$ for both XRD and optimized structures. In all cases the computed A_{FC} decreases almost linearly from PBE5 to PBE40, consistent with more localized spin density around the metal center. We will see below from the pNMR shift analyses, that significant EXX admixtures are needed for "best" agreement with experiment. Thus, while the computation of HFCs with hybrid functionals is appreciably more expensive than with the PBE GGA, this is clearly warranted by the results (see below). A_{FC} for the Li_a and Li_b sites is larger when computed at the XRD rather than at the optimized structure, while matters are reversed for Li_c. The A_{dip} tensor is not only less sensitive to the EXX admixture, as expected, but also depends less on structure (XRD vs. optimized). The asymmetry parameter η (see Computational Details) remains almost constant with functional, and structural effects are also small.

The orbital shifts are directly taken relative to the lithium lactate reference (PBE/Ahlrichs-VTZ/IGLO-II level with IGAIM; cf. Table B.3 in Appendix B). They are less affected by the nature of the spin centers but are characteristic of the overall structure of the solid. While they are usually small compared to the FC-shifts, they may play an important role when the latter are small. Remembering the small differences between XRD and optimized structures (cf. Figure 4.6 above), we nevertheless see effects of these changes on the orbital shifts: while for the XRD structure $\delta(Li_a^{orb}) < \delta(Li_c^{orb}) < \delta(Li_b^{orb})$, for the optimized structure we see $\delta(Li_a^{orb}) < \delta(Li_b^{orb}) < \delta(Li_c^{orb})$, i.e. a switch between Li_b and Li_c. The fact that the Li_a orbital shift is less affected reflects its more rigid environment, while the other two Li positions vary more. Indeed, in the delithiation process of $Li_3V_2(PO_4)_3$, the first lithium atoms are removed from the Li_c site followed by the Li_b sites.[258]

Having thus now everything needed for the ^{7}Li pNMR shieldings and shifts within the doublet formalism (lacking ZFS and currently also SO contributions to HFCs, which, however, are expected to be small) we may now proceed to discuss the total lithium shifts for $Li_3V_2(PO_4)_3$. This then also allows an evaluation of the relative importance of the different terms, of the importance of the functional on the HFC contributions, and a comparison of PBC-based and cluster-model based g-tensor calculations. For comparison

with experiment,[258] we report shifts at 320 K temperature (a value slightly higher than room temperature being used to account for frictional heating due to magic-angle spinning). The vanadium ions exhibit the +III oxidation state (d^2 configuration with local triplet spin), and an approximately octahedral coordination. We obtain seven terms contributing to the shift tensor, four to the isotropic part (eq. 4.2). $\delta \mathrm{g}_e \mathrm{A}_{\mathrm{FC}}$ and $\delta \Delta \mathrm{g}_{\mathrm{iso}} \mathrm{A}_{\mathrm{FC}}$ make up the Fermi-contact shift, $\delta \Delta \tilde{\mathbf{g}} \mathbf{A}_{\mathrm{dip}}$ the pseudocontact shift, and we have δ_{orb} as the orbital shift.

Figures 4.9, 4.10, 4.11 illustrates the contributions to the isotropic ^{7}Li-shifts at various levels, comparing the total shifts with experiment[258] for the three lithium sites (Tables B.4, B.5 in Appendix B provide detailed numerical comparisons of all terms). For better contrast, Figure 4.8 (bottom) compares the total isotropic shifts for both XRD and optimized structures. Assignment of the shifts to the corresponding sites is clearly possible, giving the order $\delta^{\mathrm{Li}_a} > \delta^{\mathrm{Li}_c} > \delta^{\mathrm{Li}_b}$. Just by visual inspection of the structure, it would appear difficult to make this assignment, pointing to the usefulness of explicit computations. The almost linear dependence of A_{FC} on EXX admixture in the functional (see above) translates into a similar dependence of the total isotropic shifts, dominated by the $\delta \mathrm{g}_e \mathrm{A}_{\mathrm{FC}}$ term. Deviations of the isotropic g-value from the free-electron value combine with A_{FC} to give in most cases the second-largest contribution (only when $\delta \mathrm{g}_e \mathrm{A}_{\mathrm{FC}}$ is clearly the largest, see below), $\delta \Delta \mathrm{g}_{\mathrm{iso}} \mathrm{A}_{\mathrm{FC}}$, which is still part of the FC-shift. Obviously, this second term should not be neglected for materials with significant g-shifts.

In the absence of ZFS, the PC-shift is represented by the third term, $\delta \Delta \tilde{\mathbf{g}} \mathbf{A}_{\mathrm{dip}}$. It reflects the trace of the interaction between the anisotropic parts of the HFC and g-tensors. As A_{dip} depends little on the functional (see above), and the g-tensor has been obtained at PBE level, this term remains almost constant for a given site. While it may seem small at first sight, it may become relevant for cases of small FC-shifts. The difference between PC-shifts for $\mathrm{Li_b}$ and $\mathrm{Li_c}$ is 7.1 ppm and 4.9 ppm for XRD and optimized structures, respectively. Considering more complex systems with lower symmetry like $\mathrm{Li}_{2.75}\mathrm{V}_2(\mathrm{PO}_4)_3$ (see ^{7}Li MAS NMR in Figure 7 of ref. 258), shift separations may be less than 20 ppm, and inclusion of PC-shifts may be crucial for assigning the NMR signals. As we saw already above, the orbital shifts (fourth term) may differ between sites and for different structures. They can be negative or positive (for the given reference). While in the present case they are also smaller than the FC-shifts, it is clear that their inclusion may become important when FC-shifts are small. The question which functional used for A_{FC} provides the best agreement of total pNMR shifts with experiment depends somewhat on the input structure, and results also differ between the three Li sites (Figures Figures 4.9, 4.10, 4.11,

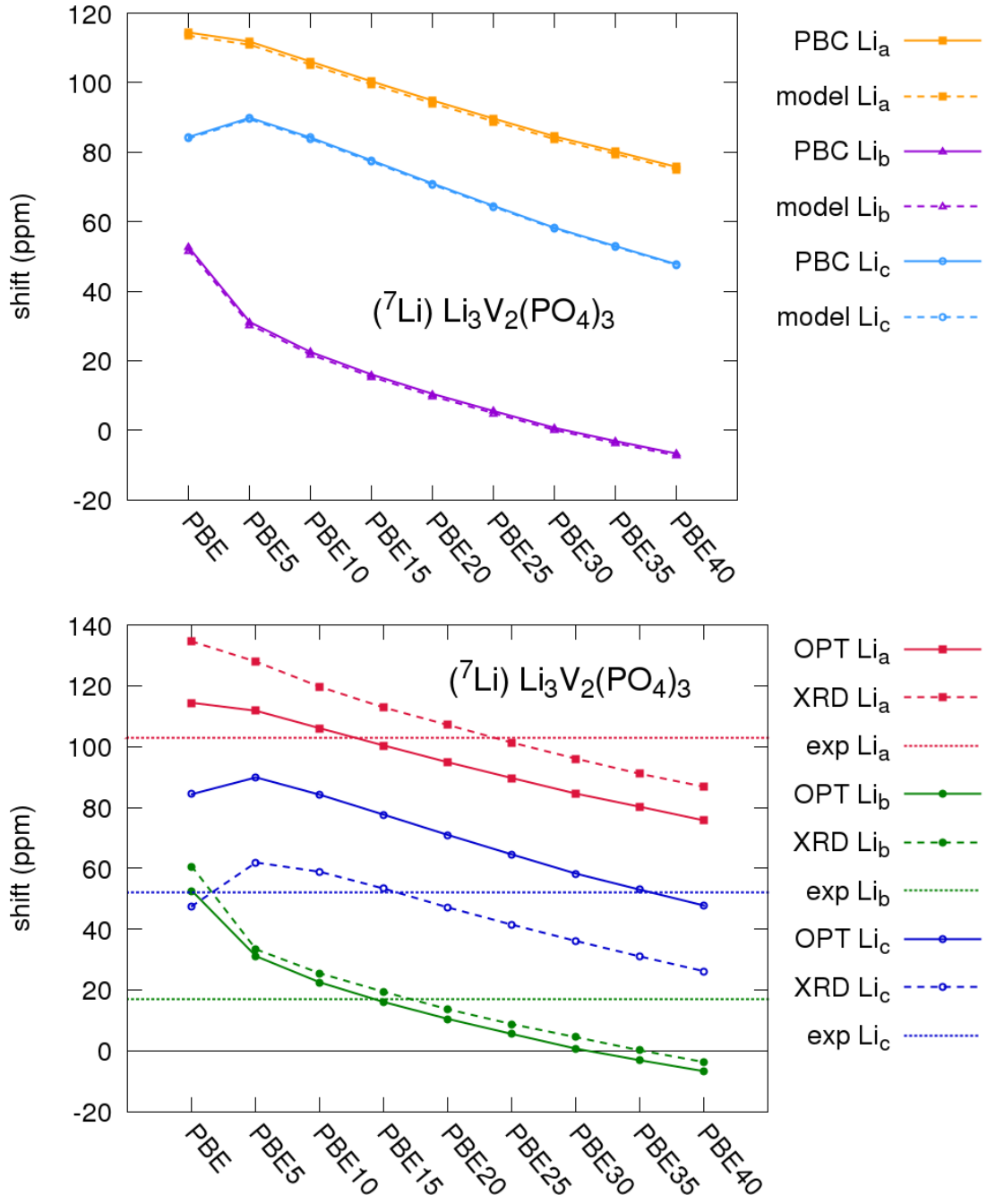

Figure 4.8.: Comparison of computed total ^{7}Li chemical shifts for $Li_3V_2(PO_4)_3$ as function of EXX admixture to the functional for the HFC tensors. Top: comparison of results with g-tensors computed within PBC (solid line) or obtained from cluster models (dashed line). Bottom: the effect of the input structure (XRD vs. optimized) is probed. g-Tensor and orbital shielding at PBE level. Shifts relative to solid lithium lactate ($LiC_3H_5O_3$). Experimental values from ref. 258 (see Tables B.4, B.5, B.6 in Appendix B for numerical values).

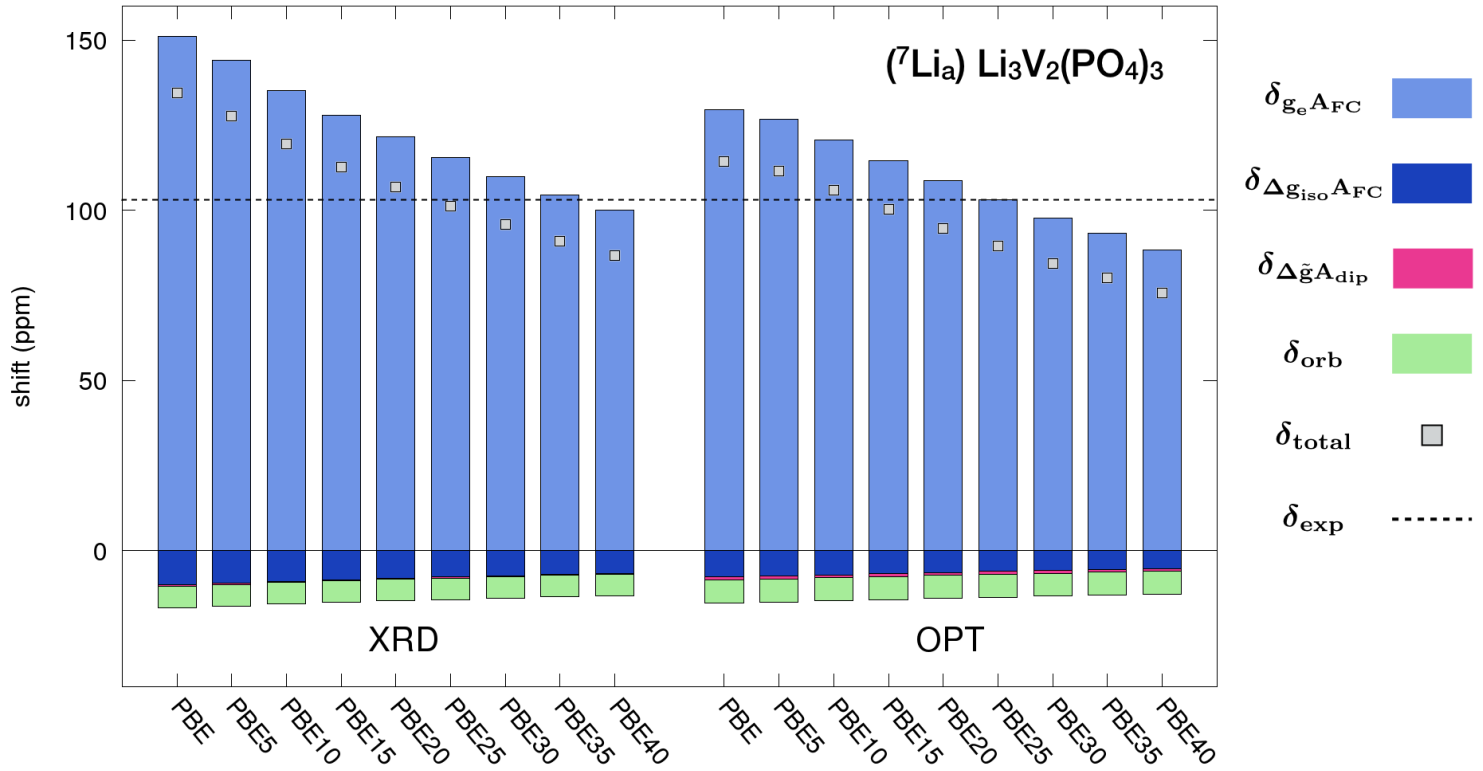

Figure 4.9.: Comparison of ^{7}Li chemical shifts of three distinct lithium sites, Li_a (Figure 4.9), Li_b (Figure 4.10) and Li_c (Figure 4.11) for $Li_3V_2(PO_4)_3$ computed for both XRD and optimized (OPT) structures. Variations with EXX admixture to PBE-based functionals for the HFC tensors are shown. g-Tensor and orbital shielding obtained at PBE level. Shieldings converted to shifts relative to solid lithium lactate ($LiC_3H_5O_3$). Experimental values from ref. 258 (see Tables B.4, B.5 in Appendix B for numerical values).

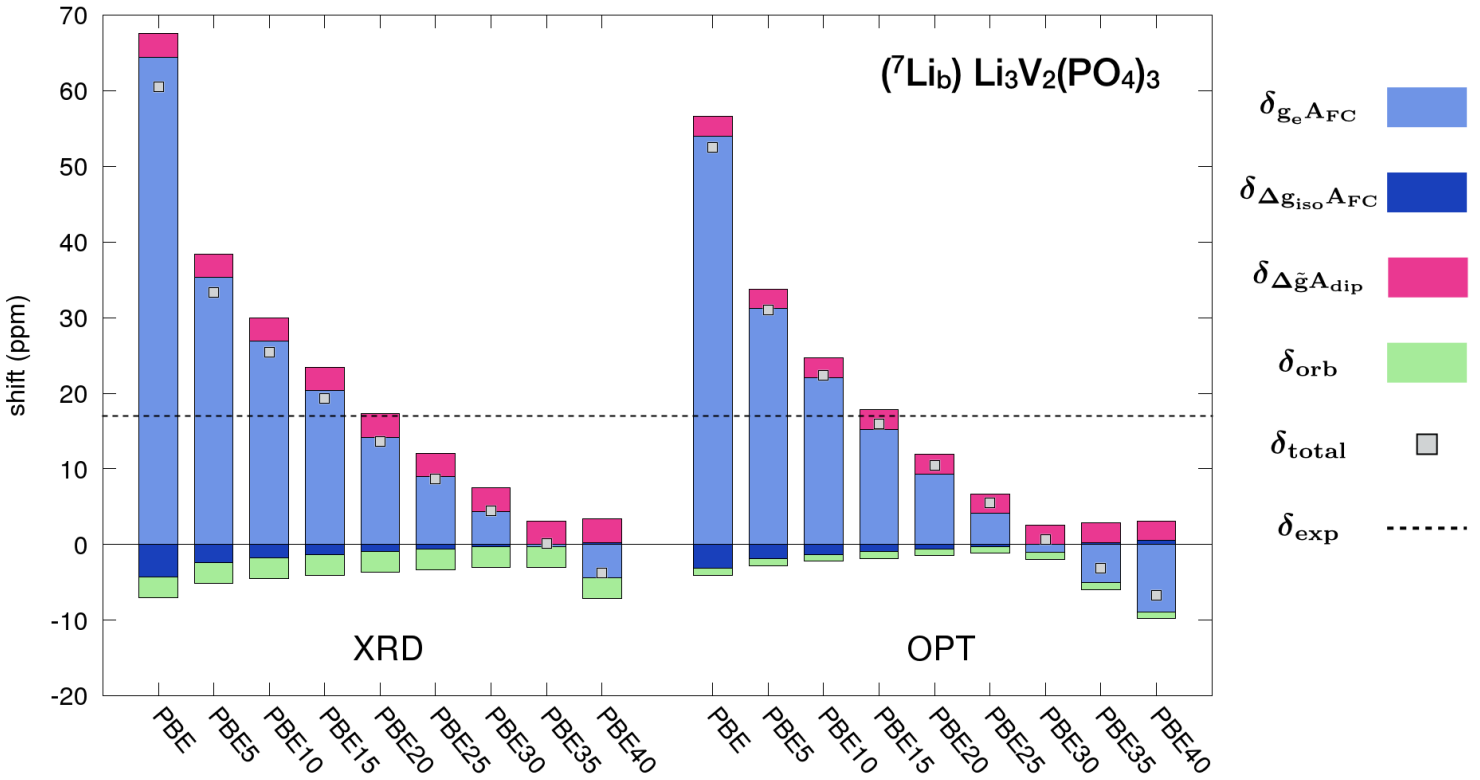

Figure 4.10.: Comparison of ^{7}Li chemical shifts of three distinct lithium sites, Li_a (Figure 4.9), Li_b (Figure 4.10) and Li_c (Figure 4.11) for $Li_3V_2(PO_4)_3$ computed for both XRD and optimized (OPT) structures. Variations with EXX admixture to PBE-based functionals for the HFC tensors are shown. g-Tensor and orbital shielding obtained at PBE level. Shieldings converted to shifts relative to solid lithium lactate ($LiC_3H_5O_3$). Experimental values from ref. 258 (see Tables B.4, B.5 in Appendix B for numerical values).

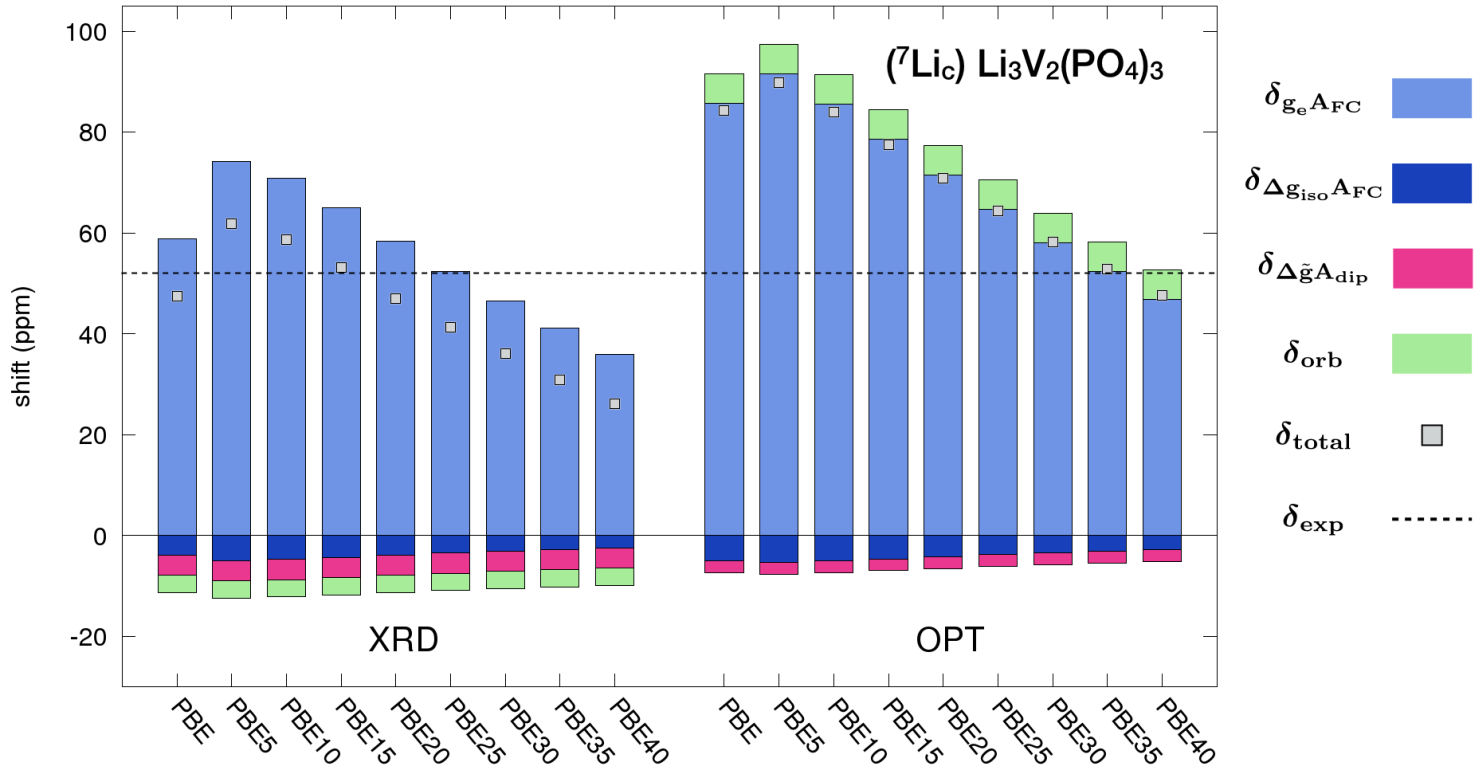

Figure 4.11.: Comparison of ^{7}Li chemical shifts of three distinct lithium sites, Li_a (Figure 4.9), Li_b (Figure 4.10) and Li_c (Figure 4.11) for $Li_3V_2(PO_4)_3$ computed for both XRD and optimized (OPT) structures. Variations with EXX admixture to PBE-based functionals for the HFC tensors are shown. g-Tensor and orbital shielding obtained at PBE level. Shieldings converted to shifts relative to solid lithium lactate ($LiC_3H_5O_3$). Experimental values from ref. 258 (see Tables B.4, B.5 in Appendix B for numerical values).

4.8). For example, for Li_a use of the XRD structure would suggest best performance of PBE25 (PBE0, 25% EXX admixture), while 15% EXX admixture might be indicated upon using the optimized structure. A similar dependence holds for Li_b, but with a shift to lower optimum EXX admixtures (Figures 4.9, 4.10, 4.11). Finally, matters appear reversed for Li_c, where use of the XRD structure would suggest 15% to 20% EXX admixture as optimal, while use of the optimized structure requires 35% to 40% for best agreement. This shows the subtle interdependence between structure, functional and further aspects of the computations (e.g. the level used for g-tensor and orbital shift, SO operators, etc.). Taking, for the sake of argument, PBE25 (PBE0, 25% EXX admixture) as functional used for HFC computations, we arrive at the conclusion that with the XRD structure the shift for Li_a is described well, whereas those for Li_b and Li_c are underestimated by 5-10 ppm. Using instead the optimized structure, the shifts for Li_a and Li_b are somewhat low (by approximately 10 ppm), and that for Li_c 10 ppm too large. In any case, it can be stated clearly that with essentially all hybrid functionals the order of shifts between the three sites is reproduced faithfully.

Comparison of ^{7}Li-shifts with PBC-based and cluster-model based g-tensors shows essentially negligible differences (Figure 4.8, top), suggesting the incremental cluster scheme as a viable alternative (also for our ongoing efforts towards including ZFS contributions). Further information on isotropic shifts and shift anisotropies are found in Tables B.5 and B.6 in Appendix B.

Five terms contribute to the shift-tensor anisotropies (see eq. 4.3). Detailed numerical results are provided in Tables B.7, B.8, B.9 in Appendix B. Interestingly, the shift anisotropy (Δ) and asymmetry parameter (η) depend much less on the choice of XRD vs. optimized structures, likely because they are dominated by the less sensitive $\mathbf{A}_{\mathrm{dip}}$. In general, the clear trends $\Delta_{\mathrm{Li}_a} < \Delta_{\mathrm{Li}_b} < \Delta_{\mathrm{Li}_c}$ and $\eta_{\mathrm{Li}_a} \approx \eta_{\mathrm{Li}_b} > \eta_{\mathrm{Li}_c}$ are found. As $\mathbf{A}_{\mathrm{dip}}$ depends also much less on EXX admixture than the isotropic HFC, it is not surprising that the shift anisotropies, which tend to be dominated by the HFC anisotropies, also show a small dependence on the functional. For all three lithium sites use of 15% to 40% EXX admixture provides good agreement with experiment. We keep in mind that the g-tensor was computed at PBE level (it appears in the anisotropic terms and is also included in the determination of the Weiss constant, see above). Other choices might affect shift anisotropies to some extent.

4.5. Conclusions

This work shows that the spin Hamiltonian terms needed to compute NMR shifts for paramagnetic solids based on density functional theory can be obtained in an efficient way from the CP2K program package. In fact, the extensive parallelization, general computational efficiency, the possibility to use extended Gaussian basis sets including relatively diffuse functions, the possibility to use hybrid functionals efficiently for the computation of hyperfine tensors, as well as the availability of g-tensors (with reasonable spin–orbit operators) and orbital shieldings with distributed gauges (IGAIM, CSGT) for paramagnetic solids make CP2K a very valuable tool for future work in the field. Limitations apply currently to the use of only semi-local functionals for g-tensors and orbital shifts, and the absence of zero-field splittings and spin–orbit corrections to hyperfine couplings.

We also found that current standard solid-state implementations of g-tensors are geared towards one isolated defect per unit cell. Application to extended solids with more than one open-shell site per cell requires thus a suitable normalization of g-tensors. We could furthermore show that an incremental cluster model, that constructs the g-tensor of the simulation cell from individual molecular g-tensors, is a viable and accurate alternative to computations using periodic boundary conditions. This opens the possibility of using advanced molecular electronic-structure methods to construct a suitable g-tensor for a solid (insulator or semiconductor), making use of its relative locality. Similar approaches seem attractive to obtain zero-field-splittings. We note that the gauge of the magnetic vector potential for g-tensors had a larger impact on the present results than anticipated. This also has to be kept in mind for future work.

This paper has established the basis for reliable computations using CP2K by first comparing the various contributions to pNMR shifts (hyperfine and g-tensors, orbital shieldings) for molecules (computed in a super-cell) against well-established quantum-chemical codes. Second, the various computational parameters have been evaluated for simple extended solid-state fluorides, and third for more complex ternary lithium vanadium phosphates. We have furthermore provided an accurate ^{7}Li NMR shift standard for solid-state computations by modelling the absolute shieldings in solid lithium lactate. Finally, all relevant contributions to the ^{7}Li pNMR shifts of the three lithium sites in $Li_3V_2(PO_4)_3$ have been examined in detail. While the Fermi-contact shifts dominate, it is clear that pseudo-contact and orbital shifts may not be negligible for accurate calculations (in particular if contact shifts are small), and deviations of the isotropic g-value from g_e may affect even the

contact terms. The interrelation between input structure (XRD vs. DFT-optimized) and computation of the pNMR parameters (exact-exchange admixture for hybrid functionals used for the hyperfine couplings) has been clearly exposed. Differences between the shifts of the three individual lithium sites are sufficient to get a clear computational assignment. The computations furthermore provide the entire shift tensor for comparison with suitable experimental data, at levels that go beyond previous approaches by including more of the relevant contributions. Our ongoing work focuses on the inclusion of zero-field splitting, which is expected to appreciably affect the pNMR shifts of systems with high-spin ions, in particular for later 3d-elements like Co or Ni.

Chapter 5.

Computation of NMR shifts for paramagnetic solids including zero-field-splitting and beyond-DFT approaches*

5.1. Introduction

Development of environmentally friendly, sustainable and renewable energy sources are essential to serve the increasing energy demand.[259–261] As reversible energy storage devices, lithium-ion batteries show high power density, high energy density, and lightweight compared with traditional batteries.[262–264] Lithium-ion batteries are not only extensively used in compact electronic gadgets (Bluetooth speakers, drones, cameras, laptops, smartphones), but also to power emerging largescale applications such as electric bikes, electric cars, robots, hybrid vehicles.[263–266] The choice of cathode material plays an essential role in the life cycle, cost, and energy density in lithium-ion batteries.[262,267,268] Olivine-type lithium transition-metal phosphates $LiMPO_4$ (M = Fe, Mn, Co, or Ni) have attracted significant attention as cathode materials for rechargeable lithium-ion batteries because

* Chapter 5 *(pre-print)* as well as tables and graphics within are reproduced in part with permission from A. Mondal and M. Kaupp, Quantum-chemical approach to NMR chemical shifts in paramagnetic solids applied to $LiFePO_4$ and $LiCoPO_4$, *J. Phys. Chem. Lett.*, **2018**, 9, 1480–1484. (https://doi.org/10.1021/acs.jpclett.8b00407) and A. Mondal and M. Kaupp, Computation of NMR shifts for paramagnetic solids including zero-field-splitting and beyond-DFT approaches. Application to $LiMPO_4$ (M = Mn, Fe, Co, Ni) and MPO_4 (M = Fe, Co), *J. Phys. Chem. C*, **2019**, 123, 8387–8405. (https://doi.org/10.1021/acs.jpcc.8b09645). Copyright 2018 American Chemical Society.

of their thermal stability, high energy density, high theoretical specific capacities, low cost, and environmental friendliness.[262,264,269–275] For the further developments of cathode materials, it is essential to have a better understanding of their physical and chemical properties.[276] In this respect, NMR spectroscopy of battery materials is currently gaining an enormous boost due to, on the one hand, substantial instrumental developments such as fast magic-angle spinning (MAS) combined with high-field instruments and, on the other hand, improved computational methods providing analysis and even prediction.[37,44,54,58,277]

The role of NMR spectroscopy in lithium-ion batteries can hardly be overestimated; it allows even in situ studies under charging or discharging conditions.[278] The ^{7}Li NMR shifts of such paramagnetic electrode materials, including phosphates like those studied here, have been interpreted extensively in terms of hyperfine-coupling (HFC) pathways as well as M-O and O-Li covalency in attempts to aid the analysis of electronic structure and properties.[40,41,54,58] In general, the discussions and computations of pNMR shifts, for lithium-ion battery materials and related extended solids, have so far centered on the so-called Fermi-contact (FC) shifts, which are directly related to the isotropic HFCs and thus to spin-density delocalization from the various neighboring transition-metal sites onto the Li atoms. It is known for molecular systems, however, that magnetic anisotropy around specific metal sites, induced by spin–orbit (SO) coupling, may give rise to so-called pseudo-contact (PC) shifts that relate to the HFC anisotropy and may be parametrized using the electronic g-tensor and the zero-field splitting (ZFS) D-tensor.[57,110,123] Long-range PC shifts are used widely, for example, in the structure refinement of metalloproteins.[279] Benda and coworkers[65] have recently demonstrated the successful *ab initio* simulation of long-range PC shifts for an entire (cobalt-substituted) metalloprotein domain.[65]

In the regime of extended paramagnetic solids, the treatment of such PC contributions is still in its infancy. The first attempts to incorporate them via the electronic g-tensor in a doublet state formalism were restricted to semilocal DFT functionals, and the effects on the overall shifts were moderate.[45,68] In Chapter 4, we have also added the relevant orbital shifts to such solid-state calculations, and we found that the periodic g-tensor calculations may be replaced by an incremental cluster approach, making use of the essential locality of the g-tensor in such materials.[148] So far, however, pNMR shift calculations on extended solids had neglected entirely the potentially important ZFS effects. In Chapter 4, we have shown explicit computations of all pNMR shift terms within a doublet-state formalism for the Li sites in the lithium vanadium phosphate material $Li_3V_2(PO_4)_3$.[148] Agreement with experimental shifts was reasonable, and the computations allowed a detailed analysis of the shift contributions for the different Li sites. However the limitations in that work were

the following: 1) The doublet formalism was used, and thus any effects of ZFS for systems with $S > 1/2$ (thought to be small for the particular vanadium material studied but not for many other important materials, see below) were neglected. 2) The g-tensors and orbital shieldings could only be computed at the GGA level, while hybrid functionals could be evaluated for the HFC contributions. It is known that g-tensors for typical transition-metal sites tend to be somewhat underestimated at GGA levels, due to exaggerated delocalization of spin density from the metal site to the ligands and consequently spin–orbit contributions from the metal center were underestimated.[249] We could also show, however, that the locality of the g-tensor can be utilized by constructing the unit-cell g-tensor in the solid from a superposition of site g-tensors obtained from molecular cluster models cut from the solid. Agreement between the results of this incremental cluster treatment and full periodic g-tensor calculations with the same functional and basis set (and treatment of the gauge of the magnetic vector potential) were excellent. This suggests an extension of the treatment of ref. 148 in the following way: a) We could obtain the g-tensor of such clusters at higher computational levels using molecular codes than currently possible for solids within periodic boundary conditions (PBC), going even beyond DFT approaches. b) The same locality as for g-tensors should also apply to the ZFS D-tensor. This fact has recently been used in the context of modelling the long-range PC shifts of an entire metalloprotein domain.[65] Moreover, it is known that currently, available DFT approaches may be inadequate for treating ZFS and g-tensors for highly correlated transition-metal centers (such as quartet Co^{II}), and multireference ab initio wave function approaches may be required.[280,281]

Here, we provide the first pNMR shift calculations of extended solids that go beyond the doublet-state formalism by explicitly including ZFS effects (and g-tensors), using an incremental cluster approach. This has allowed us to treat these two contributions at multireference wave-function levels (complete-active-space self-consistent field, CASSCF, and the N-electron valence-perturbation theory, NEVPT2), which turns out to be crucial for several systems studied. We thus provide an extended NMR shift formalism for paramagnetic solids within the Curie–Weiss regime that for the first time includes ZFS. Combining the wave-function cluster modelling of g- and D-tensors with periodic (hybrid) DFT computations of the hyperfine tensors of the solid and GGA-based computations of the orbital shifts, we evaluated lithium and phosphorus shifts for the series of olivine-type $LiMPO_4$ (M = Mn, Fe, Co, Ni) materials studied previously at the FC-shift-only level[44,54,58,61,214] or within the doublet formalism[68] (i.e. with GGA g-tensors but without

ZFS, and also without orbital shifts), as well as for the related binary phosphates MPO_4 (M = Fe, Co).[58]

5.2. Computational Details

General aspects. Calculations with the CP2K/Quickstep package[69,191] used periodic boundary conditions (PBC) both for molecules (large super-cell) and solids. The initial cell optimization of $LiMPO_4$ (M = Mn, Fe, Co, Ni) and MPO_4 (M = Fe, Co) solids starting from the XRD structures used the hybrid Gaussian and plane waves (GPW) formalism together with the pseudopotential approximation, applying the PBE GGA exchange-correlation functional.[190] Goedecker-Teter-Hutter (GTH) pseudopotentials[192] and double-ζ MOLOPT basis sets (DZVP-MOLOPT-SR-GTH)[193] were used for all elements. For the expansion of the charge density in plane waves, an energy cutoff of 500 Ry was used, and the convergence criterion over the maximum component of the wave function gradient was set to 1.0×10^{-7}. Calculations were carried out on a $2 \times 4 \times 4$ super-cell (768-896 atoms) to minimize artefacts of the periodic boundary conditions. Keeping the cell parameters fixed, the atom positions were further optimized using the all-electron Gaussian-augmented-plane-waves (GAPW)[133,134] formulation with PBE and def2-TZVP and def2-TZVPD basis sets[194,195] for main group elements and transition elements, respectively. These optimizations used $2 \times 2 \times 2$ super-cells (see Figure 5.1) with 192-224 atoms. The wave-function convergence criterion was set to 1.0×10^{-6}, and the energy cutoff was kept at 500 Ry.

Magnetic-resonance parameter calculations (in particular HFCs and orbital shieldings, but also g-tensors where needed for comparison) with PBC employed the all-electron GAPW implementation of CP2K, which is particularly suitable for the properties needed here, using the same $2 \times 2 \times 2$ super-cells as the optimization of atom positions. Computation of orbital shieldings[148] used the PBE GGA functional, Ahlrichs' VTZ basis sets[242] for the metal centers, and unmodified extended Huzinaga-Kutzelnigg-type IGLO-II[209] basis sets for the main-group atoms. Orbital shieldings were obtained with the open-shell extension of the existing CP2K implementation for diamagnetic systems[137] (related to GIPAW), using "individual gauges for atoms in molecules" (IGAIM[235]). The PBC g-tensor calculations used the related CP2K implementation,[201] at PBE/def2-TZVP/IGLO-II level, also with IGAIM. spin–orbit matrix elements were computed using the effective Kohn-Sham potential ($V_{\mathrm{eff,\,PM}}$ level) and an approximation for the spin-other-orbit term.[76,137]

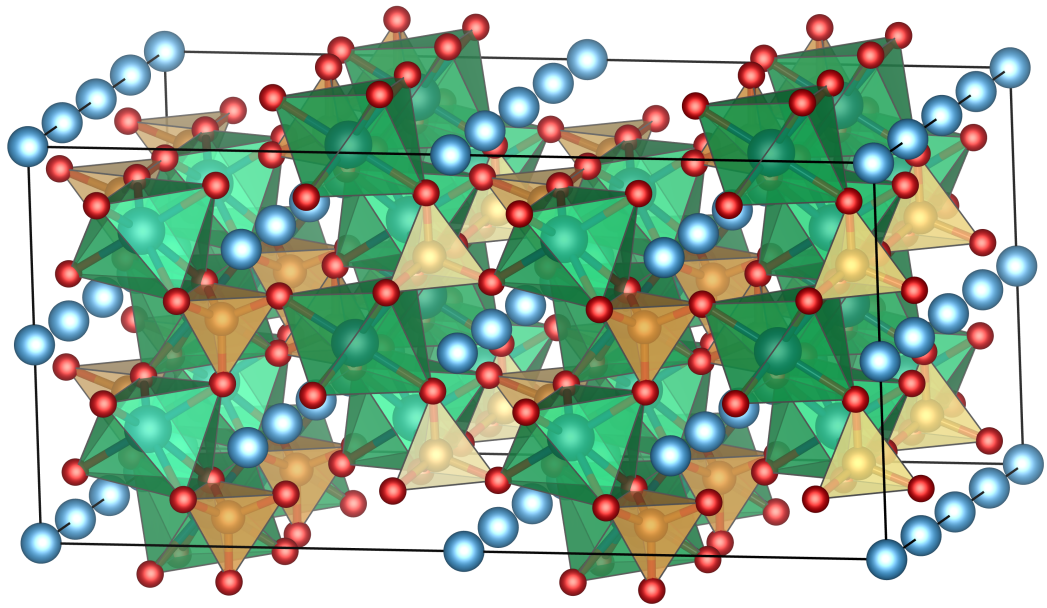

Figure 5.1.: 2 × 2 × 2 supercell of olivine-type $LiMPO_4$ used in the periodic calculations.

Hyperfine coupling (HFC) tensor computations were based on the nonrelativistic implementation of ref. 189. In addition to PBE, PBE-based global hybrids[190,204] were used, varying the exact-exchange (EXX) admixture from 5% (PBE5) to 40% (PBE40). Note that, while the GAPW *ansatz* in CP2K uses minimal k-point sampling, the code enables the use of extended super-cells to compensate for this and to thus improve accuracy (see ref. 148 and references within for detailed theory and discussion). These computations used basis sets well validated in molecular HFC calculations. A (14s11p6d)/[8s7p4d] basis was used for the transition metal (with only the most diffuse s-function removed[148] from the original [9s7p4d] basis designed specifically for HFC computations[202]), and IGLO-II main-group basis sets. HFC values provided by CP2K were normalized properly to the local spin state.[148]

Incremental cluster-model approach for g- and D-tensors. To be able to include the ZFS D-tensor into solid-state calculations, and to obtain both D- and g-tensors at higher quantum-chemical levels than currently available in solid-state codes, we exploited the expected locality of these quantities for insulators or semiconductors and computed them using an incremental cluster model introduced for g-tensors in ref. 148. The approach is analogous to the incremental scheme for electron correlation in solids.[243] That is, we constructed the unit-cell g- and D-tensors of the solid incrementally from the tensors computed in molecular calculations on molecular complexes cut out from the $LiMPO_4$ (M=Mn, Fe, Co, Ni) and MPO_4 (M=Fe, Co) structures (see Figure 5.3).

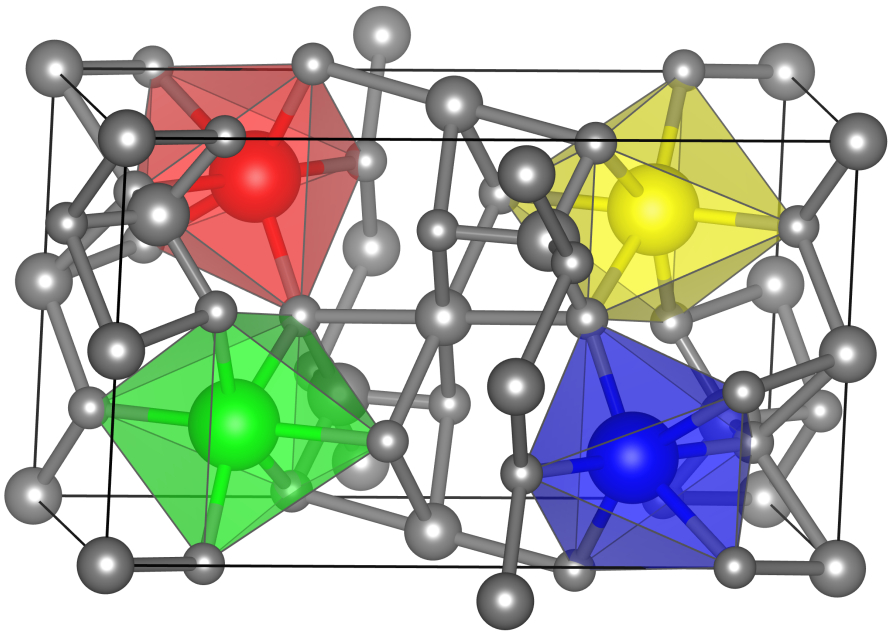

Figure 5.2.: Unit cell of $LiMPO_4$ depicting the orientation of the four spin-centers within the structure

The core structures of the model clusters for $LiMPO_4$ and MPO_4 materials are similar for the different metal centers studied (only with differences in the distances), leading to only two types of cluster models, one with and the other without lithium atoms (see Figure 5.3 for $LiFePO_4$ and $FePO_4$). Figure C.1 in Appendix C shows the cluster models for all materials. In the cluster models, the transition-metal site is surrounded by five tetrahedral PO_4 units. The oxygen valences of the phosphate groups were saturated with additional hydrogen atoms. The hydrogen-atom positions were optimized at PBE/def2-TZVP level using Turbomole.[71] For $LiMPO_4$ the six nearest lithium atoms were included, which is important to reproduce the local chemical environment of the spin center.[148] While the clusters extracted from the XRD or optimized solid-state structures differ only slightly, we give results for both sets of structures. As $LiMPO_4$ has only one distinct transition-metal environment, we only need one cluster in each case to construct the unit-cell tensors. In each case, the molecular g- and D-tensors are re-inserted in the correct orientations at the various metal sites within the solid-state structure (Figure 5.2), making use of point-group symmetry.

To be able to validate the cluster model against full PBC calculations, we also ran them for g-tensors at PBE/def2-TZVP/IGLO-II level in CP2K (with IGAIM and $V_{\text{eff, PM}}$ SO operators) using a super-cell of dimension 40 Å × 40 Å × 40 Å. However, as calculations

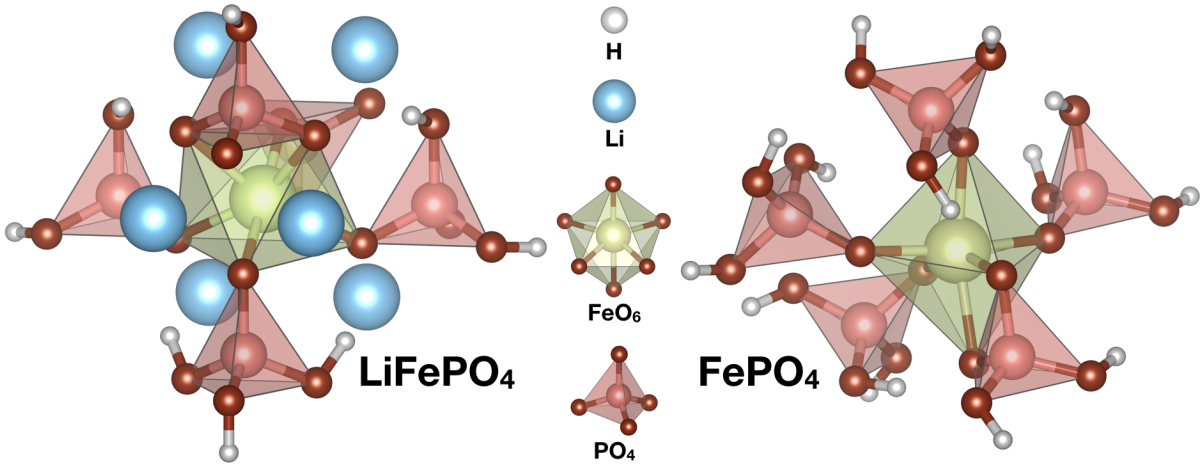

Figure 5.3.: Molecular cluster models of the local environment of the transition-metal sites for $LiFePO_4$ and $FePO_4$, with the terminal oxygen valencies saturated by hydrogen atoms (Figure C.1 in Appendix C provides the cluster models for all materials considered in this work).

of ZFS are currently not feasible with CP2K, and we suspect[65,168] that DFT may not be sufficient to provide accurate D-tensors (and likely g-tensors as well) for all of the materials of interest, we focus on molecular quantum-chemistry packages, such as ORCA[70,282] to do the cluster calculations. For comparison with the CP2K g-tensor results, we initially did PBE-based computations, using SOMF (spin–orbit mean-field)[229] SO operators in ORCA. Only a common gauge origin is currently available for g-tensor calculations in ORCA (chosen here at the metal center). While this may introduce significant errors at DFT levels,[148] a common gauge is expected to provide much more accurate results at CASSCF and NEVPT2 levels. While in the DFT computations the dominant second-order contributions are expanded in the virtual MO space, in the wave-function calculations the excited states are computed explicitly. This is expected to reduce the imbalance between "paramagnetic" and "diamagnetic" contributions to the perturbational treatment compared to a single-determinantal approach. CASSCF and NEVPT2 g-tensor calculations used the effective Hamiltonian approach.[283]

ZFS D-tensors were also obtained with the ORCA program and SOMF operators. DFT-level D-tensors at PBE level were computed using the Pederson-Khanna (PK) second-order perturbation approach[205] with van Wüllen's prefactors.[206] Additionally, PBE0 calculations (with a coupled-perturbed extension of the PK approach for hybrid functionals) and the wave-function-based CASSCF and NEVPT2[163,165] methods were evaluated. The latter was done using quasi-degenerate perturbation theory (QDPT)[207] for the dominant SO

part. The less important[280,284–286] spin-spin part was also included. The RI technique was applied to the orbital transformation step of NEVPT2. The reference wave function was obtained at the state-averaged CASSCF level.[158,208] An active space that treated the electrons in the five 3d-orbitals was chosen. The state-averaging involved 1 sextet and 24 quartet roots for $LiMnPO_4$, CAS(5,5), 5 quintet and 45 triplet roots for $LiFePO_4$, CAS(6,5), 10 quartet and 40 doublet roots for $LiCoPO_4$, CAS(7,5), 10 triplet and 15 singlet roots for $LiNiPO_4$, CAS(8,5), 1 sextet and 24 quartet roots for $FePO_4$, CAS(5,5), and 5 quintet and 45 triplet roots for $CoPO_4$, CAS(6,5), all were equally weighted. Further details on the number of roots and multiplicity are given in Table C.1 in Appendix C.

Shift referencing. Finally, the computed pNMR shieldings were converted to shifts to compare with experimental values. The phosphorus chemical shifts were referenced to 85% H_3PO_4 using gaseous PH_3 as a secondary standard,[287]

$$\delta^{\mathrm{P}} = \sigma^{\mathrm{P}}_{\mathrm{PH_3}} - \sigma^{\mathrm{P}} - 266.1 \text{ ppm}. \tag{5.1}$$

The orbital shielding for PH_3 was computed at PBE/IGLO-II/IGAIM level in a super-cell of size 40 Å× 40 Å× 40 Å (on a structure optimized at the same level). Similarly, ^{7}Li chemical shifts were referenced to aq. LiCl using solid LiCl as a secondary standard,

$$\delta^{\mathrm{Li}} = \sigma^{\mathrm{Li}}_{\mathrm{LiCl,solid}} - \sigma^{\mathrm{Li}} - 1.1 \text{ ppm}. \tag{5.2}$$

The lithium orbital shielding for LiCl was computed at PBE/IGLO-II/IGAIM level in a 3 × 3 × 3 super-cell constructed from the XRD structure.[288] The resulting absolute reference shieldings are 279.5 ppm and 89.2 ppm for ^{31}P and ^{7}Li, respectively ($\sigma^{\mathrm{P}}_{\mathrm{PH_3}}$ = 545.6 ppm, $\sigma^{\mathrm{Li}}_{\mathrm{LiCl,solid}}$ = 90.3 ppm; the Li-shift of $LiCl_{solid}$ with respect to aq. LiCl is 1.1 ppm[289]).

Setup for pNMR shift computation. To compute the target ^{7}Li and ^{31}P nuclear shieldings and, thus, pNMR shifts of $LiMPO_4$, both PBC and cluster-model g-tensors and spin dyads (obtained from cluster-model D-tensors) were contracted directly with the HFC tensors computed at PBC (hybrid) DFT levels in eq. 2.34 (see Chapter 2 for details), The values of the Weiss constants (Θ_{LiMnPO_4} = -65 K,[290] Θ_{LiFePO_4} = -82 K,[291] Θ_{LiCoPO_4} = -75 K,[292] Θ_{LiNiPO_4} = -74 K,[293] Θ_{FePO_4} = -120 K[294] and Θ_{CoPO_4} = -100 K[295]) were taken from experiment. The orbital shielding was then added at PBE DFT (PBC) level. These calculations were all done using Osprey, an in-house program written in the Python programming language. For comparison with experiment,[40,41,61,296] we report

shifts at 320 K. This value is slightly above room temperature, which has usually been reported in the experimental work, to account for frictional heating due to magic-angle spinning.

We may separate the g- and A-matrices into their individual contributions: $\mathbf{g}$ may be written as $(\mathrm{g_e} + \Delta\mathrm{g_{iso}})\mathbf{1} + \Delta\tilde{\mathbf{g}}$, where $\mathrm{g_e}$ is the isotropic free-electron g-value, $\Delta\mathrm{g_{iso}}$ the isotropic deviation, $\Delta\tilde{\mathbf{g}}$ the traceless anisotropic part and $\mathbf{1}$ is 3×3 identity matrix. Similarly, the nonrelativistic $\mathbf{A}^I$ is separated into the isotropic Fermi-contact part $\mathrm{A}^I_{\mathrm{FC}}\mathbf{1}$ and the dipolar tensor $\mathbf{A}^I_{\mathrm{dip}}$. Since $\mathbf{A}_{\mathrm{dip}}$, and $\Delta\tilde{\mathbf{g}}$ are traceless, the contributions to the isotropic shielding (using eq. 2.34 from Chapter 2) up to the order of α^4 in the fine structure constant α are given as[57,63,123]

$$\begin{aligned}\sigma^I = \sigma^I_{\mathrm{orb}} - \frac{\mu_B}{k_B \mathrm{g}^I_N \mu_N}\left(\frac{1}{T-\Theta}\right)\Bigg(&\frac{1}{n}\sum_i^n \mathrm{g_e}\langle\mathbf{SS}\rangle_i \mathrm{A}^I_{\mathrm{FC}} + \frac{1}{n}\sum_i^n \Delta\mathrm{g}_{\mathrm{iso},i}\langle\mathbf{SS}\rangle_i \mathrm{A}^I_{\mathrm{FC}} \\ &+\frac{1}{n}\sum_i^n \Delta\tilde{\mathbf{g}}_i\cdot\langle\mathbf{SS}\rangle_i\cdot\mathbf{A}^I_{\mathrm{dip}} + \frac{1}{n}\sum_i^n \mathrm{g_e}\langle\mathbf{SS}\rangle_{\mathrm{i}}\cdot\mathbf{A}^I_{\mathrm{dip}} \\ &+\frac{1}{n}\sum_i^n \Delta\mathrm{g}_{\mathrm{iso},i}\langle\mathbf{SS}\rangle_i\cdot\mathbf{A}^I_{\mathrm{dip}} + \frac{1}{n}\sum_i^n \Delta\tilde{\mathbf{g}}_i\cdot\langle\mathbf{SS}\rangle_i \mathrm{A}^I_{\mathrm{FC}}\Bigg).\end{aligned} \tag{5.3}$$

Traditionally, the experimental isotropic pNMR shift is decomposed into three parts: the orbital shift (δ_{orb}), the Fermi-contact shift (δ_{FC}), and the pseudo-contact shift (δ_{PC}):

$$\delta_{\mathrm{exp}} = \delta^{\mathrm{exp}}_{\mathrm{orb}} + \delta^{\mathrm{exp}}_{\mathrm{FC}} + \delta^{\mathrm{exp}}_{\mathrm{PC}}. \tag{5.4}$$

Conversion from nuclear shieldings to relative chemical shifts is performed in the usual way by subtracting the shielding from that of a suitable reference compound (see Computational Details below). Comparing thus eq. 5.4 to eq. 5.3, obviously $\sigma^I_{\mathrm{orb,iso}}$ corresponds to $\delta^{\mathrm{exp}}_{\mathrm{orb}}$. The sum of the three terms depending on $\mathrm{g_e}\langle\mathbf{SS}\rangle\mathrm{A}^I_{\mathrm{FC}}$, $\Delta\mathrm{g_{iso}}\langle\mathbf{SS}\rangle\mathrm{A}^I_{\mathrm{FC}}$ and $\Delta\tilde{\mathbf{g}}_i\cdot\langle\mathbf{SS}\rangle_i\mathrm{A}^I_{\mathrm{FC}}$ corresponds to $\delta^{\mathrm{exp}}_{\mathrm{FC}}$. The other three terms in the parentheses of eq. 5.3 sum up to provide the PC shift.

5.3. Results and discussion

Structure optimization. Table C.2 in Appendix C provides results of the PBE/DZVP-MOLOPT-SR-GTH GPW optimizations (cf. Computational Details) of unit-cell parameters in comparison to high-resolution single-crystal XRD data of $LiMPO_4$ (M=Mn, Fe, Co, Ni) and MPO_4 (M=Fe, Co).[295,297–301] The optimizations were done for a $2 \times 4 \times 4$ super-cell with dimensions of more than 15 Å in each direction, to minimize artifacts from the periodic-boundary conditions. Agreement to within ca. 1-2% in the cell parameters was generally achieved. Subsequent optimization of the atom positions at all-electron GAPW PBE/def2-TZVPD/def2-TZVP level ($2 \times 2 \times 2$ super-cell) gave excellent agreement with the XRD structures (Figure 5.4 shows the level of agreement for $LiFePO_4$ and $FePO_4$. Figure C.2 in Appendix C gives similar comparisons for all $LiMPO_4$ and MPO_4 structures). That is, we could use optimized structures in cases where high-quality XRD structures are not available.

g-Tensors: comparisons of PBC and cluster-model computations at different levels. Following the procedure from ref. 148, we first validated the correctness of the cluster-model computations of the unit-cell g-tensors against PBC calculations at PBE/def2-TZVP/IGLO-II/IGAIM level in CP2K. A graphical comparison for $LiFePO_4$ is seen in the middle part of Figure 5.5 (CP2K/PBE/$V_{\mathrm{eff,\,PM}}$/IGAIM entries). Similar comparisons for $LiCoPO_4$ and $LiNiPO_4$ are provided in Figures 5.6 and 5.7, respectively. In Appendix C, Figures C.3 and C.4 show a similar comparison for $LiMnPO_4$, $FePO_4$, and $CoPO_4$. The numerical values are provided in Tables C.3-C.8.

Agreement between PBC and cluster-model unit-cell g-tensors at the given level is good, confirming the incremental cluster model to be an adequate alternative to periodic calculations of this property. In general, this approach is expected to work well, when the electronic structure is sufficiently localized, and we can assign well-defined spin centers (for example, we do not expect such an approach to handle the Knight shifts well in metallic materials).

The good performance of the cluster model opens the door towards using more sophisticated and computationally expensive quantum-chemical methods to compute g-tensors. Figure 5.5 provides a comparison of computations using different molecular codes (ORCA, MAG), choices of gauge origin, exchange-correlation functionals or wave-function methods, and SO operators. First, we see that at DFT levels the choice of gauge origin has an unexpectedly large effect: a common gauge leads to an underestimation of the deviations from the

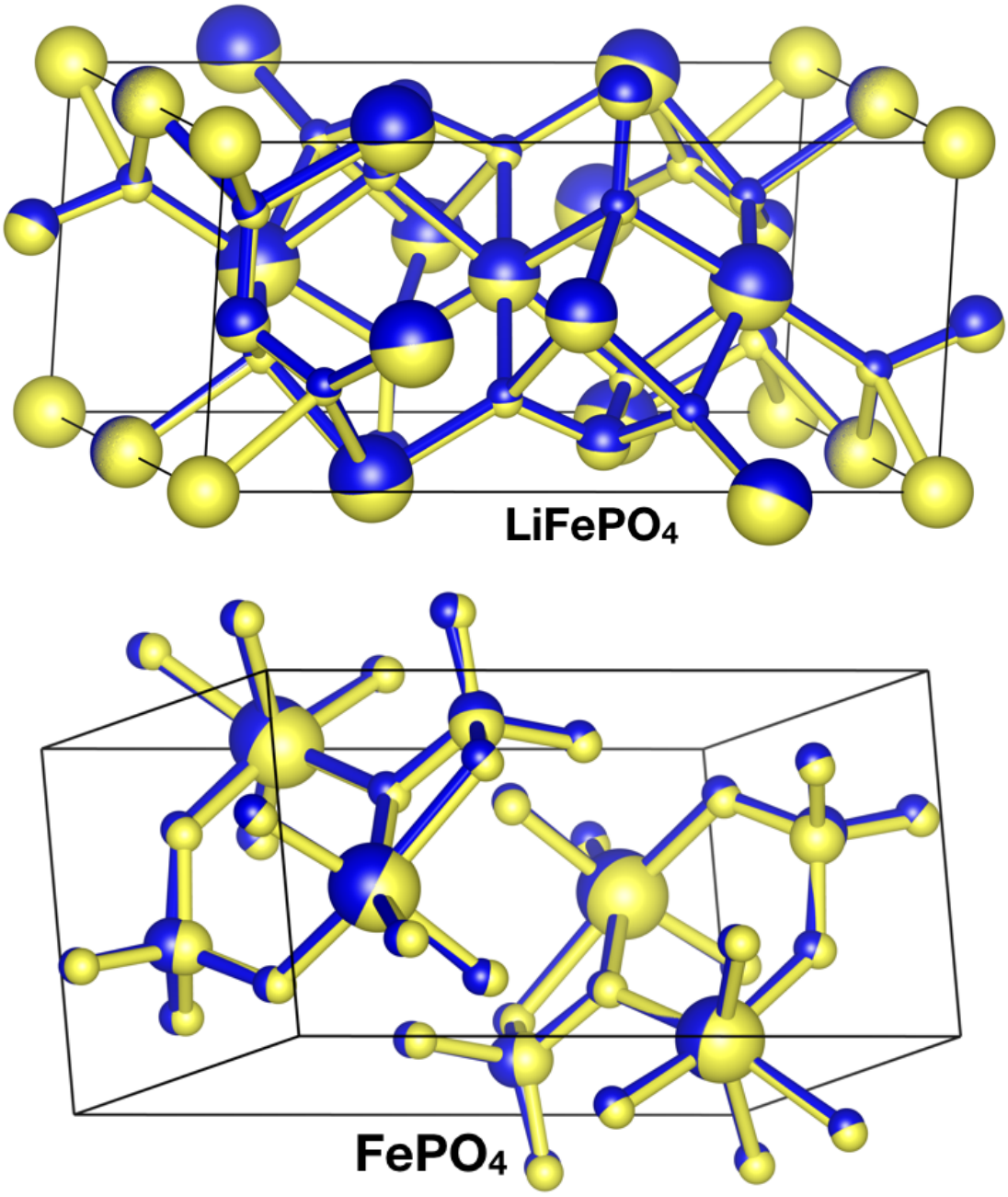

Figure 5.4.: Comparison of XRD (in yellow) and optimized (in blue) structures of $LiFePO_4$ and $FePO_4$. Table C.2 and Figure C.2 in Appendix C provides the numerical values of cell parameters and comparison of XRD and optimized structures of all the phosphate materials considered in this work respectively. (See Computational Details above)

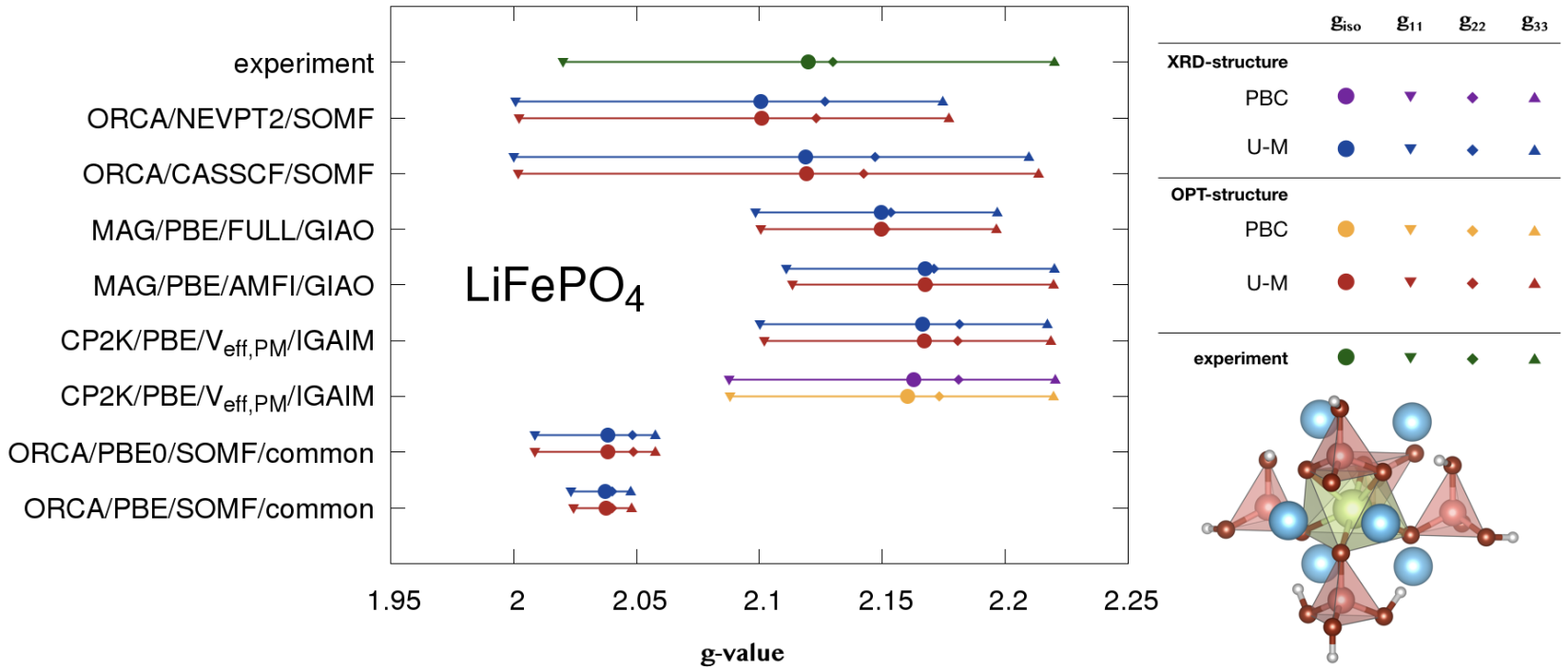

Figure 5.5.: Comparison of computed unit-cell g-tensors obtained from cluster models (U-M) and from PBC calculations for $LiFePO_4$ at various computational levels. (see Table C.3 in Appendix C for numerical values.)

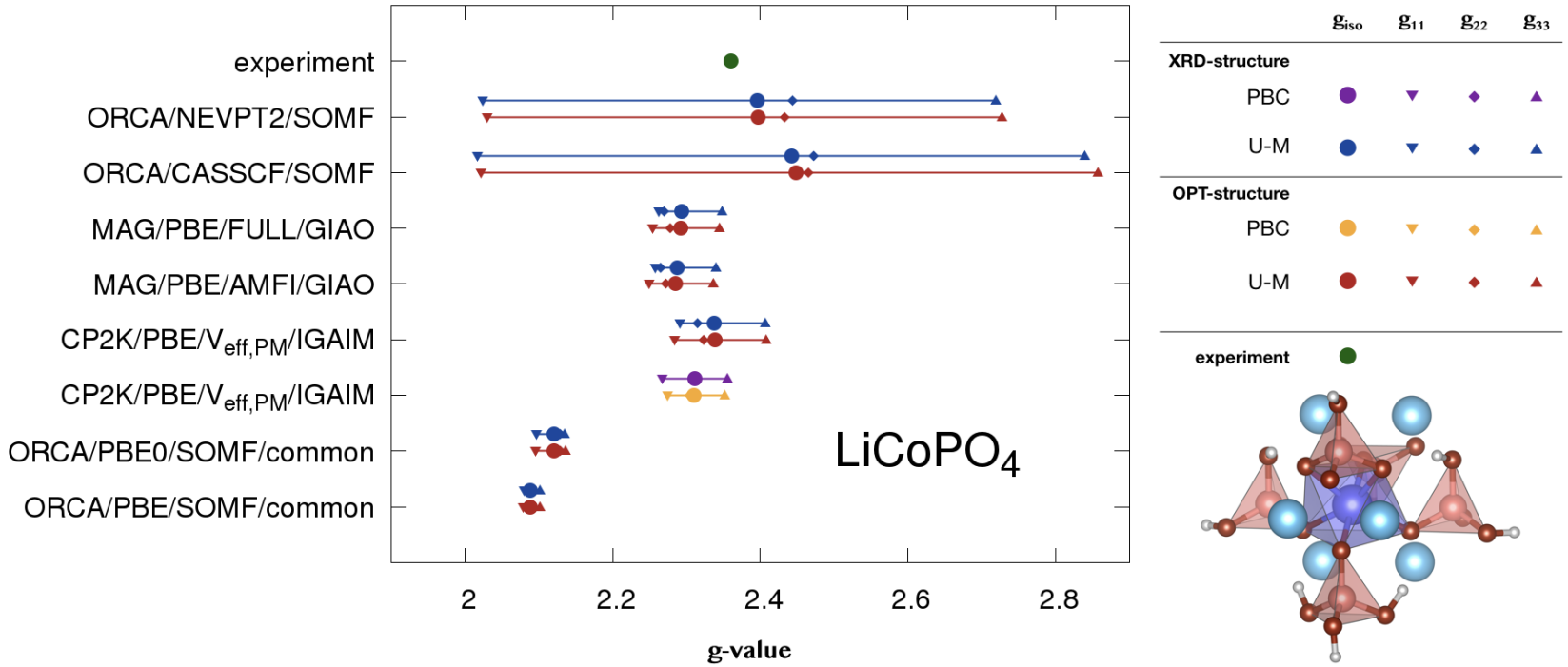

Figure 5.6.: Comparison of computed unit-cell g-tensors obtained from cluster models (U-M) and from PBC calculations for $LiCoPO_4$ at various computational levels. (see Table C.4 in Appendix C for numerical values.)

Overall, the g-anisotropies of the common-gauge results are strongly underestimated. We observed this behavior already in ref. 148. On the other hand, we found there that GIAO and IGAIM results agree well. Figure 5.5 shows that these choices lead to much larger g-shift components. Taking the "FULL" SO operators of MAG and the "SOMF" SO operators in ORCA as the best choice, we see that the AMFI approximation works well, and the $V_{\mathrm{eff,\,PM}}$ approximation in CP2K is doing almost as well (the SO splittings tend to be overestimated by these SO operators, leading to somewhat larger g-anisotropies), as also found previously.[138,148]

Use of the PBE0 hybrid functional in ORCA somewhat increases the g-anisotropy, likely moving the results in the right direction. However, due to the common gauge used, the g-shifts nevertheless appear still far too small. Matters are different with the wave-function-based approaches: in CASSCF and NEVPT2 computations, the "paramagnetic contribution" (more precisely the SO-orbital Zeeman cross-term dominating the g-tensor) is not expanded in the virtual orbital space of a single-determinantal perturbation approach. That is, here the contributing excited states are computed explicitly, and the effect of the choice of the gauge should thus be substantially diminished compared to DFT computations.

Therefore we expect that the CASSCF and NEVPT2 results should be particularly realistic, despite the common gauge origin (at the metal nucleus) used in these calculations. Indeed, the CASSCF calculations give the largest g-anisotropies (Figures 5.5-5.7, Figures C.3-C.4, Tables C.3-C.8), which are reduced upon the inclusion of dynamical correlation at the NEVPT2 level. For the case of $LiFePO_4$ shown in Figure 5.5, the effects of dynamical correlation brought in at NEVPT2 level are only moderate. In this case, an experimental g-tensor from single-crystal work[291] is available, and both CASSCF and NEVPT2 data agree very well with experimental values ($g_{11} = 2.22$, $g_{22} = 2.13$, $g_{33} = 2.02$, $g_{iso} = 2.12$). DFT data with suitable gauge treatment overall perform overall reasonably as well in this case, but they tend to have a too large g_{11} value and thus a too small spread. Moreover, the CP2K results with the $V_{\mathrm{eff,\,PM}}$ approximation for the SO operator also tend to give a too axial tensor.

Turning to $LiCoPO_4$, the direct comparison with experimental g-tensors is somewhat hampered by limited experimental data. Our best NEVPT2 calculations give $g_{11} = 2.728$, $g_{22} = 2.4334$, $g_{33} = 2.030$, and $g_{iso} = 2.397$ (at the optimized structure, cf. Tables C.4 and C.12). This may be compared to experimental estimates from neutron diffraction $g_{iso} = 2.36$, $(g_{33} - g_{11})/g_{iso} \approx 0.3$.[302,303] We can also extract an effective g-tensor for the lowest Kramers

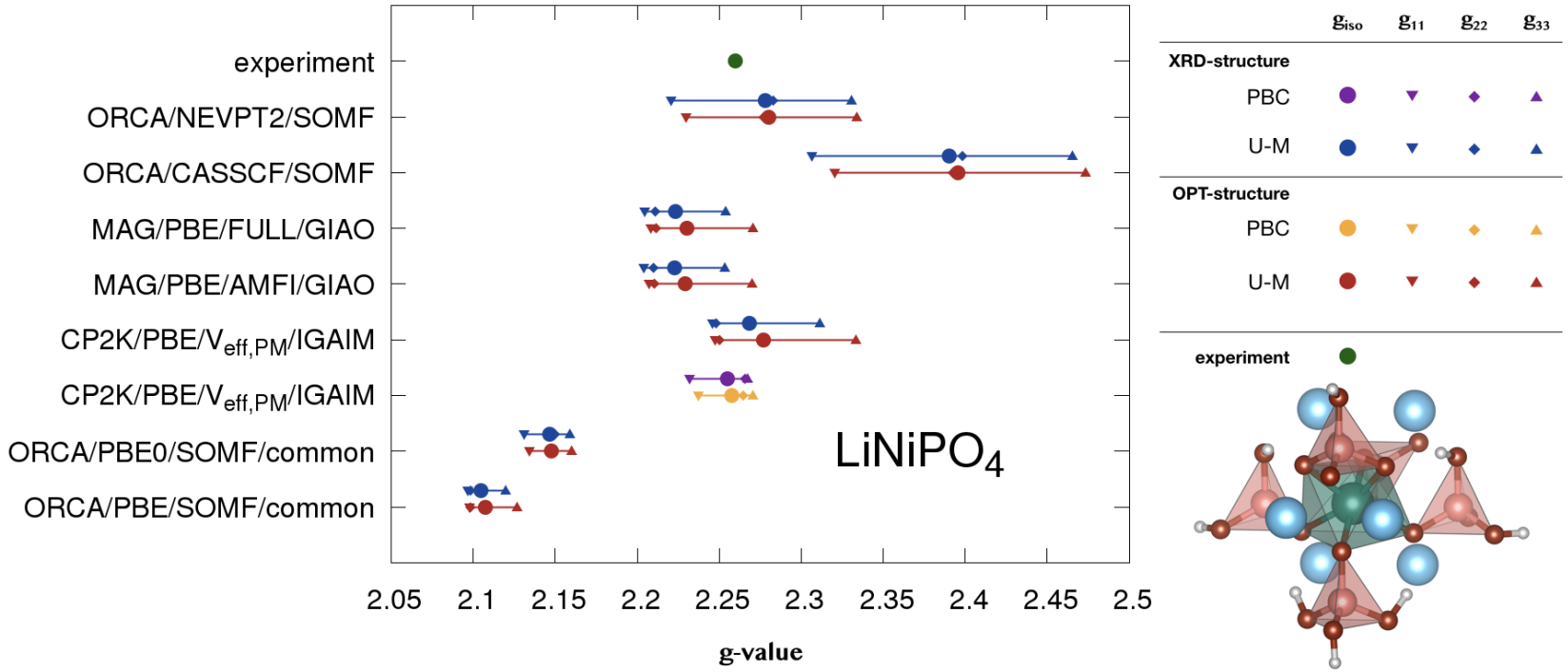

Figure 5.7.: Comparison of computed unit-cell g-tensors obtained from cluster models (U-M) and from PBC calculations for $LiNiPO_4$ at various computational levels. (see Table C.5 in Appendix C for numerical values.)

doublet of the system and compare it with EPR data (see Table C.24).[304] Differences between DFT and wave-function results and the effects of dynamic correlation tend to be more pronounced for $LiCoPO_4$ and $LiNiPO_4$, as expected (Figures 5.6-5.7, Tables C.4-C.5). Starting with $LiCoPO_4$ (Figure 5.6), we see that DFT results vastly underestimate the presumably most accurate NEVPT2 data for the g-anisotropy. Here CASSCF clearly overshoots. In the case of $LiNiPO_4$ (Figure 5.7), also the range of the CASSCF values is shifted upwards notably compared to the NEVPT2 data. DFT also gives a too small range and overall too low values, albeit not as dramatically as for the Co system. These observations are consistent with experience for the related (SO-dominated) ZFS tensors for molecular Co and Ni complexes[63,65,284] (see also below). Different experimental isotropic g-values of 2.25 and 2.36 have been reported for $LiNiPO_4$.[293,304] NEVPT2 reproduces the lower one, whereas CASSCF data are close to the higher one. Interestingly, while the overall deviations of the g-shift components of $LiNiPO_4$ are more significant than those of $LiFePO_4$, the anisotropy is smaller (Tables C.5, C.3). This will play a role below for the calculation of hyperfine shifts.

Figure C.3 in Appendix C shows similar comparisons of computed g-tensors for $LiMnPO_4$ and $FePO_4$. As Mn and Fe are in their +II and +III oxidation states, respectively, both with a d^5 configuration, the experimental[290,305] g-value for $FePO_4$ is very close to 2, (for $LiMnPO_4$, g_{iso}=1.98)[290] and the anisotropy should be very small. This is reproduced at all levels. The DFT g-values tend to be too large, while the NEVPT2 and CASSCF values reproduce experiment well.

Zero-field splitting tensors. Here we have no possibility to compare with PBC results, as currently CP2K and other solid-state codes seem to lack appropriate perturbational treatments of ZFS. Based on the excellent agreement between the PBC and cluster-based results for the g-tensor (see above), we expect a similarly good performance of the cluster model also for the ZFS calculations. In this case, there is no gauge issue. We will mainly concentrate on CASSCF, and NEVPT2 results obtained with ORCA but have also evaluated some DFT approaches with the same code. Starting with $LiMnPO_4$ and $FePO_4$ featuring a d^5 configuration (see above), we see that these materials exhibit not only negligible deviations of the g-tensor from the free-electron value (see above) but also negligibly small ZFS (Tables C.9, C.10 in Appendix C). We may thus view these materials as reference points, where anisotropy vanishes, and we thus expect the pNMR shifts to be entirely dominated by the FC shieldings (augmented by orbital shieldings).

Table 5.1.: Comparing computed[a] and experimental[b] D-tensor

Material		**Structure**	$\mathbf{D}_{11}$ (cm^{-1})	$\mathbf{D}_{22}$ (cm^{-1})	$\mathbf{D}_{33}$ (cm^{-1})	**D** (cm^{-1})	**E/D**
$LiMnPO_4$	cal	XRD	0.001	0.023	-0.023	-0.035	0.315
		OPT	0.008	0.025	-0.034	-0.051	0.169
	exp[306]		0.010	0.023	-0.034	-0.051	0.191
$LiFePO_4$	cal	XRD	-1.532	-5.093	6.626	9.938	0.179
		OPT	-1.282	-5.240	6.521	9.782	0.202
	exp[303]		-0.807	-5.807	6.775	10.082	0.248
$LiCoPO_4$	cal	XRD	-13.662	-34.199	47.862	71.793	0.143
		OPT	-12.961	-34.329	47.290	70.935	0.151
$LiNiPO_4$	cal	XRD	0.814	8.188	-9.002	-13.502	0.273
		OPT	1.457	7.264	-8.721	-13.082	0.222
	exp[307]		-3.073	-5.807	8.872	13.312	0.103
$FePO_4$	cal	XRD	0.076	0.179	-0.254	-0.381	0.135
		OPT	0.040	0.118	-0.159	-0.229	0.134
$CoPO_4$	cal	XRD	-0.344	-5.744	6.088	9.133	0.296
		OPT	1.408	4.174	-5.582	-8.373	0.165

[a] Computed at NEVPT2/EFFECTIVE/SOMF level

[b] Experimental values have been transformed from full ZFS tensor to traceless tensor and further used for obtaining experimental D and E/D values.

The case is already different for $LiFePO_4$, which exhibits not only significant g-anisotropy (see above) but also sizeable ZFS. Taking the NEVPT2 data as the reference (Table C.11 in Appendix C), CASSCF slightly overshoots, whereas DFT data with the PBE functional give only about one-third of the NEVPT2 value, and the PBE0 hybrid functional improves this only slightly. This is consistent with experience for the calculation of ZFS for molecular complexes,[63,65,284] where DFT is known to underestimate the ZFS, in particular towards the right side of the 3d series. We, therefore, expect this trend to be even more significant for $LiCoPO_4$. The DFT-computed D-value, in this case, is more than two orders of magnitude too small compared to the NEVPT2 data (Table C.12 in Appendix C), consistent with the dramatically underestimated g-tensor (see above). For this material, use of beyond-DFT approaches is thus expected to be crucial for the non-contact contributions to the hyperfine shifts (see below). The (NEVPT2) ZFS for this material is thus by far largest of all the systems studied here, as is the g-anisotropy. Overestimation at CASSCF level is also

more pronounced than for $LiFePO_4$. In contrast, the high-spin d^6 material $CoPO_4$ shows a smaller underestimation of DFT and overestimation of CASSCF (Table C.14) than even the related $LiFePO_4$ (likely due to the reduction of local symmetry in the latter material due to the presence of the Li counterions). Finally, the differences between the computational levels are again substantial (but slightly smaller than for $LiCoPO_4$) for $LiNiPO_4$ (Table C.13 in Appendix C). This material also presents a typical multi-reference case and benefits significantly from including both static and dynamic correlation at NEVPT2 level. DFT data at PBE level are about a factor 3-4 too small. The absolute (NEVPT2) D-value is comparable to that for $LiFePO_4$. For all systems, the differences between results obtained for XRD and optimized structures are only moderate. Table 5.1 provides a comparison of computed ZFS D-tensor parameters for XRD and optimized structures and experimental data.

Hyperfine coupling tensors. The hyperfine couplings are essential both for FC and PC contributions to the shifts, both for ^{7}Li and ^{31}P. The isotropic HFCs enter the often dominant FC term, whereas the HFC anisotropies influence not only the shift anisotropies but also the isotropic shift via the PC contributions. It is the isotropic HFCs that tend to

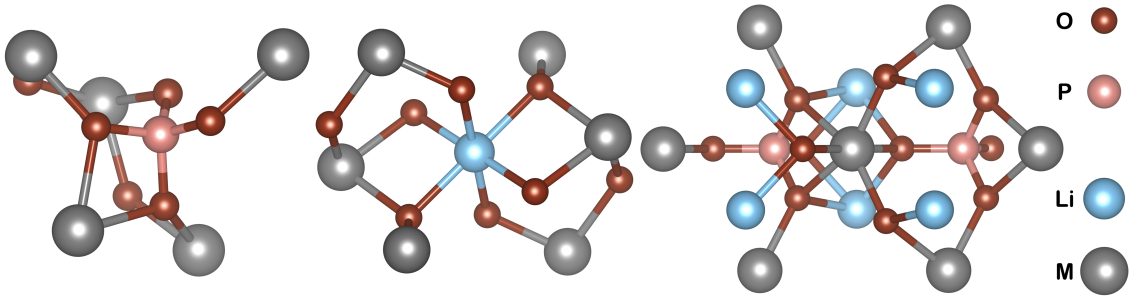

Figure 5.8.: Local environment of lithium, phosphorus and transition metal sites in $LiMPO_4$ (M=Mn, Fe, Co, Ni) and MPO_4 (M=Fe, Co), see text

be most sensitive to the computational level. An incremental cluster-model treatment for the HFCs is made more difficult than for g- and D-tensors due to the need to describe the important spin delocalization and polarization mechanisms involving several transition-metal centers. Even in molecular calculations of HFCs, the exchange, as well as extensive static and dynamic correlation effects involved in subtle spin-polarization mechanisms render a quantitative post-Hartree-Fock treatment challenging. For the present systems, we have to rely on DFT approaches with PBC. In this context, an advantage of CP2K is the possibility to use extended Gaussian-type all-electron basis sets within the GAPW scheme (see Computational Details), together with hybrid functionals.[148] As an *a priori*

prediction of the best functional is difficult. We thus evaluated the influence of EXX admixture for PBE-based hybrids with EXX admixtures between 0% and 40% for the 2 × 2 × 2 supercell from both XRD and DFT-optimized structures. As shown in Figure 5.8, lithium and phosphorus sites are connected to six and five transition-metal centers, respectively, via oxygen bridges. Comparison of relevant Li-O, and P-O bond lengths and O-Li-O, O-P-O bond angles for all materials is given in Table C.15 in Appendix C.

Detailed information for both the ^{7}Li and ^{31}P HFC tensors for all materials in dependence on the EXX admixture is provided in Tables C.16-C.20 in Supporting Information. Closer scrutiny allows us not only to relate the HFCs to the electronic structure but also to predict better the importance of FC and PC terms for the pNMR shifts to be discussed below. Starting with the ^{7}Li HFCs, we first note the mostly dipolar nature of the HFC tensors, within most cases very small isotropic HFCs and significantly larger anisotropies (in stark contrast to the ^{31}P HFCs discussed below). Provided we have significant magnetic anisotropy around the metal centers (as parametrized by the g- and D-tensors, see above), this makes us expect the non-negligible importance of the PC contributions to the ^{7}Li pNMR shifts. The only materials, for which the absolute value of A_{FC} can be above 0.10 MHz, are $LiMnPO_4$ (but only slightly so for the smallest EXX admixtures, Table C.16), and particularly $LiNiPO_4$ (increasing from -0.41 MHz at PBE level to -0.35 MHz at PBE40 level; Table C.19). A_{FC} decreases significantly with EXX admixture (trends are shown in Figure C.5 in Appendix C), except for $LiNiPO_4$, where an increase is observed. A_{FC} is generally positive and small for $LiMnPO_4$, negative and small for $LiCoPO_4$, more notably negative for $LiNiPO_4$, and changing sign from small positive to small negative for $LiFePO_4$. Moving from XRD to optimized structures increases the values, except for $LiNiPO_4$, where the structural effect is negligible.

In contrast to A_{FC}, the ^{7}Li A_{dip} values are almost independent of EXX admixture (suggesting only small effects of spin polarization). Most notably, the A_{dip} also varies very little for the different materials, and it generally remains between +3.25 MHz ($LiMnPO_4$, Table C.16) and +4.07 MHz ($LiNiPO_4$, Table C.19). Even the asymmetry parameter remains in a relatively narrow range between 0.14 and 0.27 (only for $LiNiPO_4$ it is smaller and varies between 0.06 and 0.11). This suggests already that the magnitude of the ^{7}Li PC shifts for the various $LiMPO_4$ materials is determined less by variations in A_{dip} but more by those of the spin-orbit-induced contributions parametrized by the g- and D-tensors.

Matters are very different for the ^{31}P HFC tensors. Here A_{FC} is much larger, in fact roughly an order of magnitude larger than A_{dip} (Tables C.16-C.19). This tells us already

that likely the ^{31}P pNMR shifts will generally be dominated strongly by the FC term. A_{FC} is generally positive (roughly between +7 MHz and +20 MHz) and decreases with increasing EXX admixture, suggesting a lowering of the spin delocalization from the metal centers to the phosphate ligands with the more exact exchange in the functional.For a given functional the magnitude of A_{FC} follows roughly (with some crossings, Figure S5) the order: $FePO_4 \approx LiMnPO_4 > LiNiPO_4 \approx CoPO_4 > LiCoPO_4 \approx LiFePO_4$. That is, delithiation from $LiFePO_4$ to $FePO_4$ almost doubles A_{FC}, whereas the increase appears more moderate from $LiCoPO_4$ to $CoPO_4$ (with a larger negative slope for $CoPO_4$, Figure C.5). The overall differences between the materials appear to be reduced somewhat with larger EXX admixture. Comparisons between XRD and optimized structures indicate that the changes can be positive ($LiMnPO_4$), negative ($LiNiPO_4$, $FePO_4$, $CoPO_4$) or negligible ($LiFePO_4$, $LiCoPO_4$; Figure C.5 in Appendix C). In the absence of experimental ligand HFC data for the materials studied here, we may judge the "best" A_{FC} (and thus the optimal EXX admixture and structure) only indirectly from the comparison of computed and experimental pNMR shifts (see below), assuming that errors for the other contributions (g-tensors, D-tensors, Weiss constants, orbital shieldings) are small. While the ^{31}P HFC anisotropies and asymmetries are less relevant in the present context, due to the dominance of A_{FC}, we nevertheless note that in some cases they depend somewhat more on the functional than in the ^{7}Li case (see above). For example, while A_{dip} increases with EXX admixture for $LiFePO_4$ (Table C.17), the asymmetry parameter increases most notably for $LiCoPO_4$ and $LiNiPO_4$ (Tables C.18, C.19).

Orbital shifts. For orbital shifts in extended solids, we are currently more restricted regarding the available computational methodologies (see Computational Details). While the orbital-shift contributions to the overall pNMR shifts are small for ^{31}P, they can be important for ^{7}Li (see below). It is thus important that we understand not only the relation of the orbital shifts to the electronic structure but can also identify possible sources of error. Table C.21 reports the PBC orbital shifts (PBE/Ahlrich-VTZ/IGLO-II/IGAIM level) for all materials studied directly relative to the $LiCl_{aq.}$ and 85% aq. H_3PO_4, respectively (via secondary referencing).

The orbital shifts are less affected by the nature of the spin centers but are characteristic of the overall molecular and electronic structure of the solid.[148] Below in the pNMR shift discussion we will see that for phosphorus shifts, orbital shift contributions to the total chemical shift are less than 1%, while it can go up to 30% for lithium shifts. Therefore, inclusion of orbital shifts may be important for comparison with experiment for the lithium shifts, (where the FC-shifts may be of the same order of magnitude as the orbital shifts).

Even though differences between XRD and optimized structures were small (cf. Figure 5.4 above and Figure C.2 in Appendix C), we nevertheless see effects of these changes on the orbital shifts. For both XRD and optimized structures the lithium orbital shifts increase as $\delta(\mathrm{Li^{orb}})_{\mathrm{LiMnPO_4}} < \delta(\mathrm{Li^{orb}})_{\mathrm{LiFePO_4}} < \delta(\mathrm{Li^{orb}})_{\mathrm{LiCoPO_4}} < \delta(\mathrm{Li^{orb}})_{\mathrm{LiNiPO_4}}$. There is no implementation in CP2K for computing orbital shielding using hybrid functionals. Even if implementations become available, they will likely be computationally rather demanding. The improvement may also turn out to be moderate compared to the magnitude of other contributions to the overall pNMR shifts.

Putting together the pNMR shifts. We are now in a position to put together the overall ^{7}Li and ^{31}P pNMR shifts for all systems. For the first time in the case of solid-state materials, we use a full formalism for arbitrary spin multiplicities, accounting for the SO-induced anisotropies around the metal centers arising from g-tensors and zero-field splittings (as well as orbital shifts). While above we have already been able to anticipate to some extent the relative importance of the different terms for the different nuclei and materials from the magnitude of the EPR parameters and orbital shieldings, a more detailed analysis along the lines of eq. 2.34 (see Chapter 2 for details) will now be carried out. In the following discussion, we will not evaluate the different methods for the computation of the g- and D-tensors anymore but will use the best level (NEVPT2/def2-TZVP/IGLO-II) throughout. For the orbital shifts, we are restricted to the PBE-based periodic results, and we will stick to the "best" Weiss constants we could identify from various experimental studies (see Computational Details). The only variation in the following results will thus be a) the EXX admixture in the PBE-based hybrid functionals for the HFC calculations and b) the choice of XRD or DFT-optimized input structures. These two aspects may be identified as the main possible error sources, together with the chosen Weiss constants, the orbital shifts, and possibly the choice of temperature. Given the above evaluations, we expect the large isotropic HFCs for phosphorus to likely make the FC shifts dominant for ^{31}P, while ^{7}Li shifts should more likely show the importance of non-contact terms. In the latter case, $LiCoPO_4$ is the system for which we expect the PC terms to be particularly important, due to the large ZFS and g-anisotropy (see above).

^{7}Li shifts for $LiFePO_4$ and $LiCoPO_4$. We start with a detailed discussion on the computation of ^{7}Li shifts for $LiFePO_4$ and $LiCoPO_4$. Figure 5.9 shows the ^{7}Li shifts obtained with the help of these g- and D-tensor data for $LiFePO_4$ (see also Tables C.22 and C.23), dependent on the EXX admixture of the hybrid functionals used for the periodic HFC calculations (relative to 1 M aqueous LiCl, cf. Computational Details). The sign of the FC shifts, and thus of the total shifts, even changes with increasing EXX

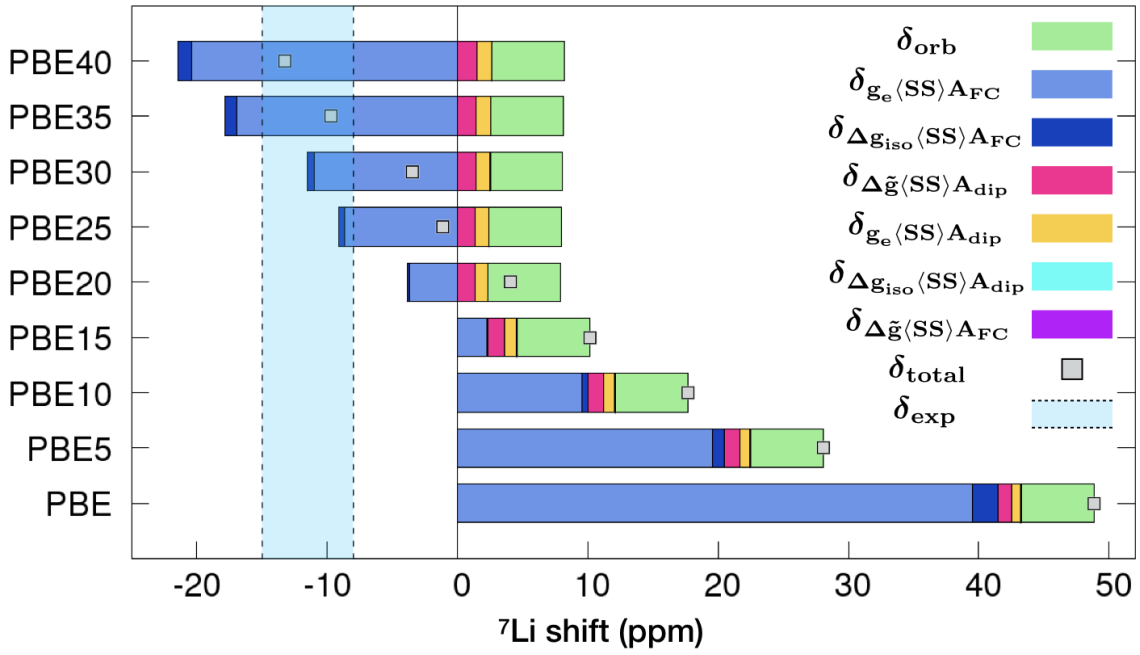

Figure 5.9.: Isotropic ^{7}Li shifts (relative to $LiCl_{aq}$) computed for $LiFePO_4$ as function of EXX admixture in the PBE-based hybrid functional used for the HFC calculations. g- and D-tensors obtained at NEVPT2 level, orbital shifts at PBE level, at optimized structure, Θ = -82 K. The shifts are broken down into individual contributions (see eq. 5.3).[57,123] See Table C.22 for further details and Table C.23 and Figure 5.13 for results at the XRD structure.

admixture, as the (small) isotropic HFCs also change sign (Table C.17). At 25–30% EXX admixture, the total shifts are still somewhat too high compared with experiment; at 35–40% the values are within the experimental range (Figure 5.9). Figure 5.9 also provides a color-coded breakdown into different contributions to the isotropic shifts, as detailed in eq. 5.3:[110] the terms dominated by A^I_{FC} that make up the FC shift δ_{FC} (depending in the numerator of eq 5.3 on, respectively, $\mathbf{g}_e \langle \mathbf{SS} \rangle \mathbf{A}^I_{FC}$ (light blue), $\Delta\mathbf{g}_{iso} \langle \mathbf{SS} \rangle \mathbf{A}^I_{FC}$ (dark blue), $\Delta\tilde{\mathbf{g}} \langle \mathbf{SS} \rangle \mathbf{A}^I_{FC}$ (magenta)), those accounting for the PC shift δ_{PC} ($\Delta\tilde{\mathbf{g}} \langle \mathbf{SS} \rangle \mathbf{A}^I_{dip}$ (red), $\mathbf{g}_e \langle \mathbf{SS} \rangle \mathbf{A}^I_{dip}$ (yellow), $\Delta\mathbf{g}_{iso} \langle \mathbf{SS} \rangle \mathbf{A}^I_{dip}$ (cyan)), as well as δ_{orb} (green). In contrast with $LiCoPO_4$ (see below), the PC shift contributions are relatively small, summing up to only ca. 2–4 ppm (depending on input structure). At the chosen computational levels, the orbital shifts (PBE results) of ca. 6–8 ppm (Tables C.22 and C.23) are larger here than the overall PC contributions.

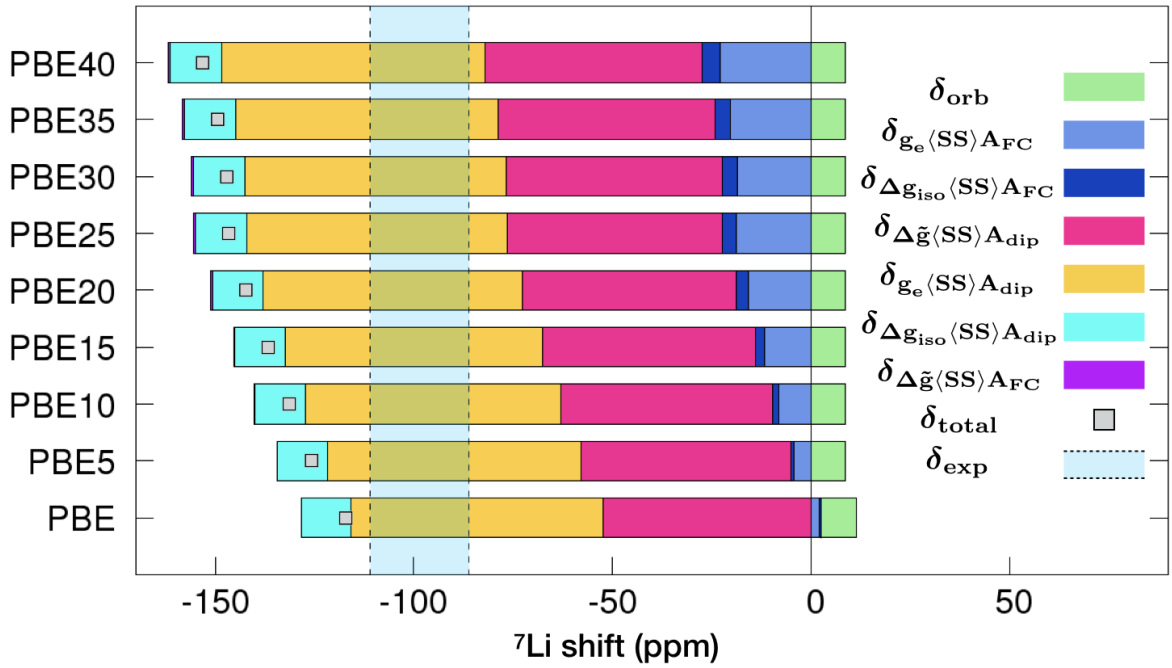

Figure 5.10.: Isotropic ^{7}Li shifts (relative to $LiCl_{aq}$) computed for $LiCoPO_4$ as function of EXX admixture in the PBE-based hybrid functional used for the HFC calculations. g- and D-tensors obtained at NEVPT2 level, orbital shifts at PBE level, at optimized structure, Θ = -75 K. The shifts are broken down into individual contributions (eq. 5.3).[57,123] See Table C.25 for further details and Table C.26 and Figure 5.14 for results at the XRD structure.

Inserting our currently best D- and g-tensor results (NEVPT2 level) into eq 2.34 (see Chapter 2) to compute ^{7}Li NMR shifts for $LiCoPO_4$ as a function of the EXX admixture in the HFC computations, we obtain the ^{7}Li shifts shown in Figure 5.10 (Tables C.25 and C.26). The three PC terms (eq 5.3), except the one depending on $\Delta\tilde{\mathbf{g}}\,\langle\mathbf{SS}\rangle\,\mathbf{A}^I_{dip}$ (red), for which preliminary DFT attempts have been reported in a doublet-state formalism,[45,148,308] had so far not been considered for extended solids. For $LiCoPO_4$, the PC terms dominate the overall negative Li shifts. Even at 40% EXX admixture for the HFC calculations and taking into account a computed ca. +10 ppm orbital shift (Table C.25), we would arrive at best at around -20 ppm for the overall shift when neglecting the PC shifts (the larger FC shifts of $LiCoPO_4$ compared with $LiFePO_4$ reflect opposing trends between a larger A_{FC} (Tables C.18 and C.17) and a lower spin multiplicity, S = 3/2 versus S = 2, entering the spin dyadic, leading to a factor 3.75/6 between the shifts for Co versus Fe.) This falls significantly short of the observed experimental range of -86 to -111 ppm.[41,296,309]

The PC shift contributions overall account for about -133 ppm and would thus let us overshoot to about -140 to -160 ppm at realistic EXX admixtures of 20–35% for the HFCs (Figure 5.10, Tables C.25 and C.26). Apart from possible remaining error sources regarding δ_{orb}, HFCs, Θ, and simulation versus measurement temperature, we regard the likely $\sim$20% too large g-shift- and D-tensors at the chosen computational level (see above) as the main suspects for this discrepancy. It seems that the cluster model accounts for about half of the errors in the g- and D-tensors (see above), and the accurate but not perfect NEVPT2 computations account for the other half. Scaling those two quantities down by a corresponding amount provides shifts close to the experimental range (Figure C.7). Even after scaling them down in this way, the previously neglected PC shift contributions are clearly decisive for the overall much more negative ^{7}Li shifts in $LiCoPO_4$ compared with $LiFePO_4$, consistent with the appreciable importance of single-ion anisotropy also for the low-temperature magnetoelectric properties of this material.[292]

The ca. 100 ppm negative, previously neglected PC shifts for $LiCoPO_4$ significantly affect the interpretation of the ^{7}Li shifts in terms of hyperfine couplings and covalency. If one would extract ^{7}Li HFCs and thus lithium spin-density values from the overall shifts, after correcting for the temperature-independent contributions[278] one would obtain a far too negative HFC for $LiCoPO_4$ (Table C.18) and a much more reasonable value for $LiFePO_4$ (Table C.17). Importantly, inclusion of the orbital shifts, which so far have not been considered in most pNMR shift calculations for extended solids,[148] is also crucial when trying to quantitatively account for the lithium shifts.

Application of the same computational levels to the ^{31}P shifts shows a clear dominance of the FC shifts (Figures 5.13 and 5.14 and Tables C.22, C.23, C.25, and C.26) due to the much larger delocalization of spin density (Tables C.17 and C.18) onto the phosphorus atoms. For $LiFePO_4$, the PC shift terms now account for less than + 5 ppm out of ca. + 3400 ppm (at 25% EXX admixture, with an orbital shift of about +10 ppm). For $LiCoPO_4$, the various ^{31}P PC shift contributions have opposite signs and together account for less than -10 ppm (with orbital shifts of about -20 ppm), also negligible compared with the ca. + 2400 ppm FC shifts at the 25% EXX level. About +400 ppm of the FC shifts are contributed by the spin–orbit-induced deviation of the isotropic g-value from the free-electron one via the term depending on $\Delta\mathbf{g}_{\mathrm{iso}} \langle \mathbf{SS} \rangle \mathbf{A}^I_{\mathrm{FC}}$ compared with about +160 ppm for $LiFePO_4$.

Figure 5.11 shows the inverse temperature dependence of the computed ^{7}Li shift contributions for $LiCoPO_4$. Deviations from a linear Curie behavior arise from the dominant

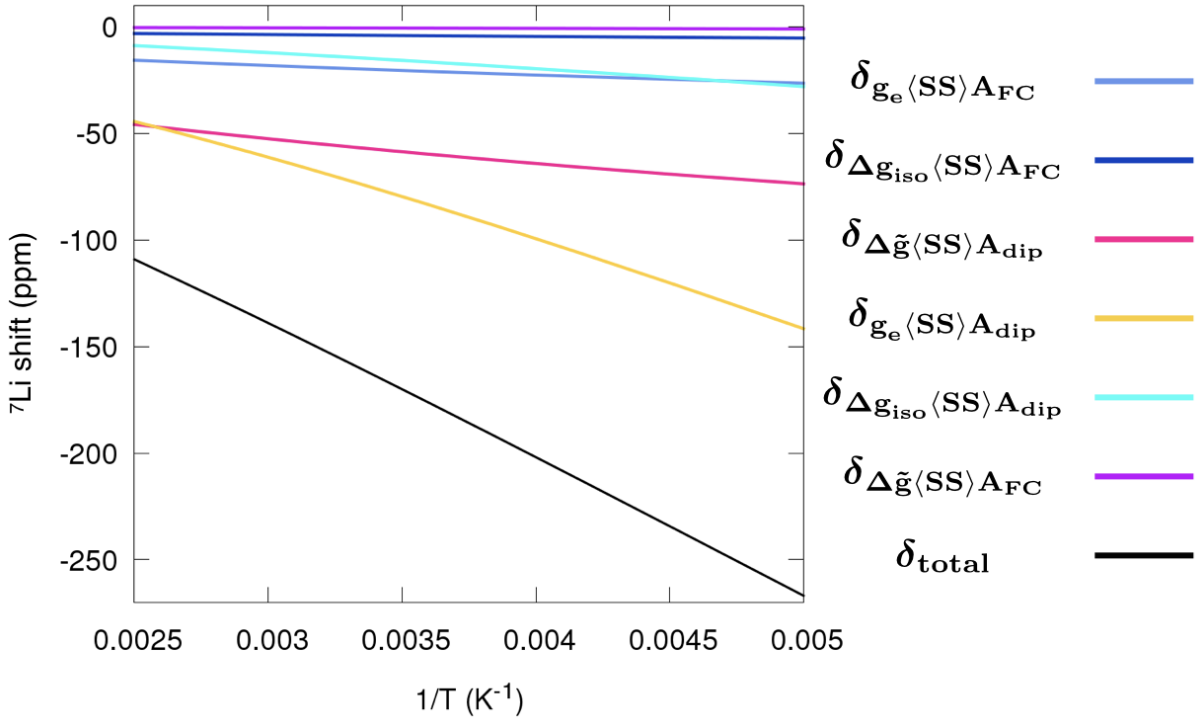

Figure 5.11.: Inverse temperature dependence of the computed ^{7}Li shifts and individual shift contributions for $LiCoPO_4$ (at optimized structure). HFC tensor obtained at PBE0 level (25% EXX), g-Tensor and D-tensor at NEVPT2 level. Shieldings converted to shifts relative to aq. lithium chloride (LiCl). Deviations from linearity indicate deviations from a Curie 1/T behavior.

ZFS-derived contributions (in particular, the one depending on $\Delta\mathbf{g}_e \langle\mathbf{SS}\rangle \mathbf{A}^I_{FC}$). Deviations from Curie behavior are also apparent from experimental ^{7}Li shift plots.[40] Interestingly, even the ^{7}Li shifts in $LiFePO_4$ (Figure C.8) and the ^{31}P shifts in both materials (Figures C.9 and C.10) exhibit some deviations from Curie behavior, despite being clearly dominated by FC terms. This is due to significant deviations of $\langle\mathbf{SS}\rangle_i$ from the S(S + 1)/3 expected in a doublet-state formalism due to an appreciable influence of ZFS even for those terms we consider to be FC shifts.

Extension to the entire set of chemical shifts for $LiMPO_4$ (Mn, Fe, Co, Ni) and MPO_4 (Fe, Co). Here we extend the discussion to a comparison of the shifts (^{7}Li and ^{31}P) for the entire series of materials. This then also allows us to evaluate the relative importance of the different terms, and the overall importance of the functional on the HFC contributions. The transition metal ions exhibit the +II oxidation state for $LiMPO_4$ (M=Mn, Fe, Co, Ni, having d^5, d^6, d^7, d^8 configuration with local sextet, quintet, quartet and triplet spin states, respectively) and +III oxidation state for MPO_4 (M=Fe,

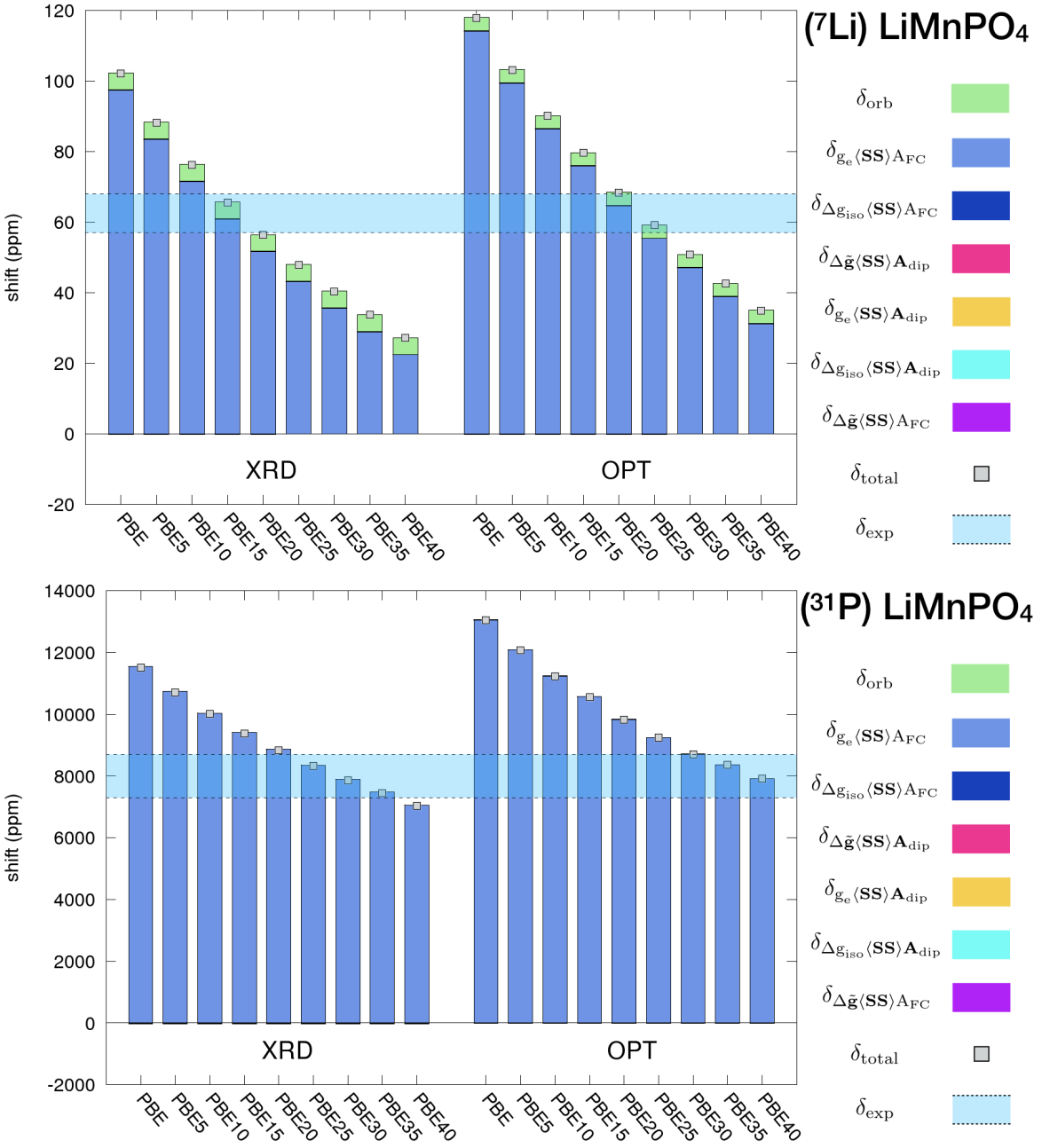

Figure 5.12.: Comparison of ^{7}Li and ^{31}P chemical shifts for $LiMnPO_4$ computed for both XRD and optimized (OPT) structures. Variations with EXX admixture to PBE-based functionals for the HFC tensors are shown. g-Tensor and D-tensor obtained at NEVPT2 level. Orbital shielding obtained at PBE level. Shieldings converted to shifts for Li and P relative to aq. lithium chloride (LiCl) and 85 % aq. phosphoric acid (H_3PO_4), respectively. Experimental range shown according to refs. 40,41 (see Tables C.27, C.28 for numerical values).

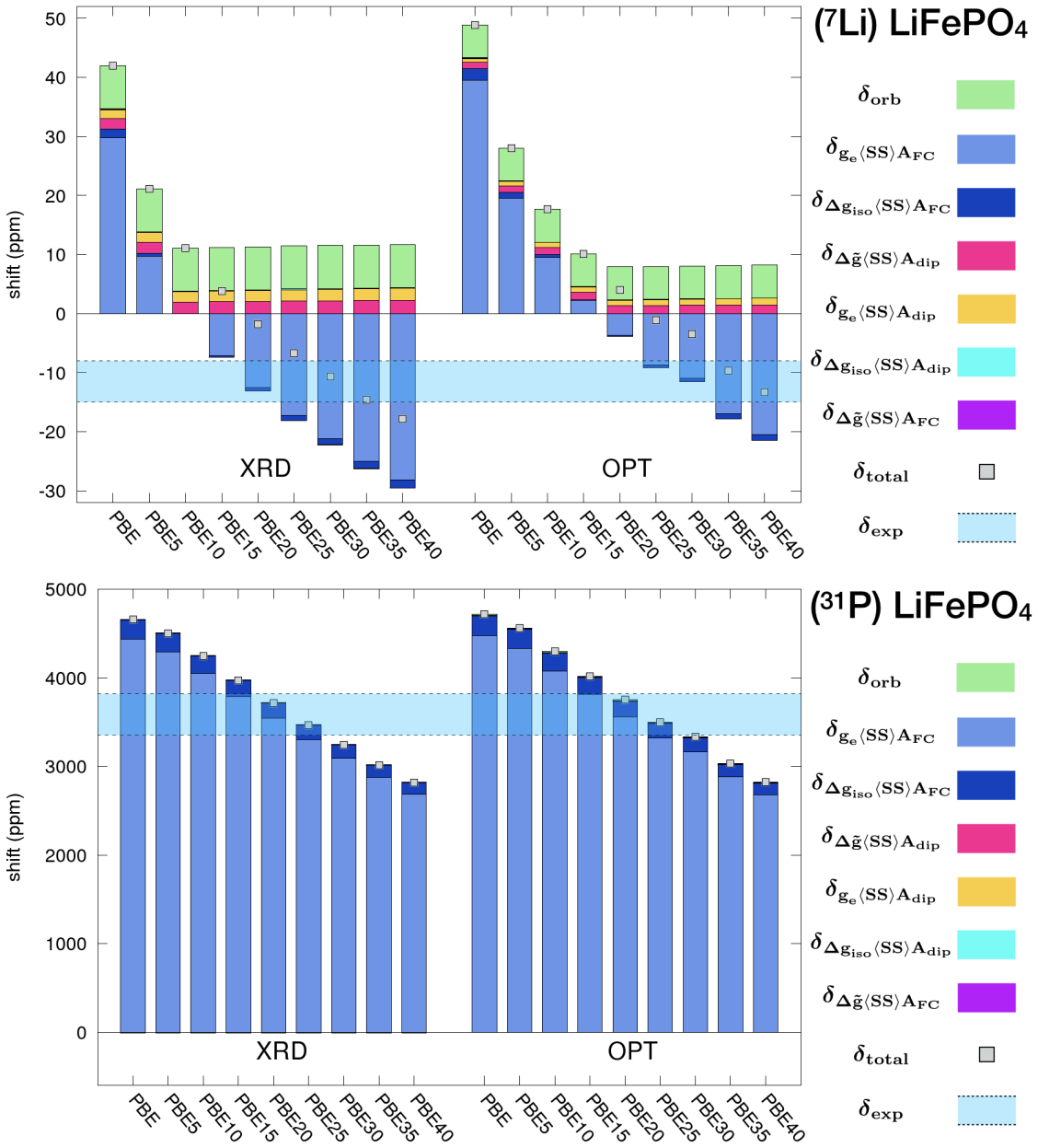

Figure 5.13.: Comparison of ^{7}Li and ^{31}P chemical shifts for $LiFePO_4$ computed for both XRD and optimized (OPT) structures. ^{7}Li shifts for the XRD structure (top-left) are repeated from Figure 5.9 to compare the magnitudes of the different terms. Variations with EXX admixture to PBE-based functionals for the HFC tensors are shown. g-Tensor and D-tensor obtained at NEVPT2 level. Orbital shielding obtained at PBE level. Shieldings converted to shifts for Li and P relative to aq. lithium chloride (LiCl) and 85 % aq. H_3PO_4, respectively. Experimental range shown according to refs. 40,41,61,296 (see Tables C.22, C.23 for numerical values).

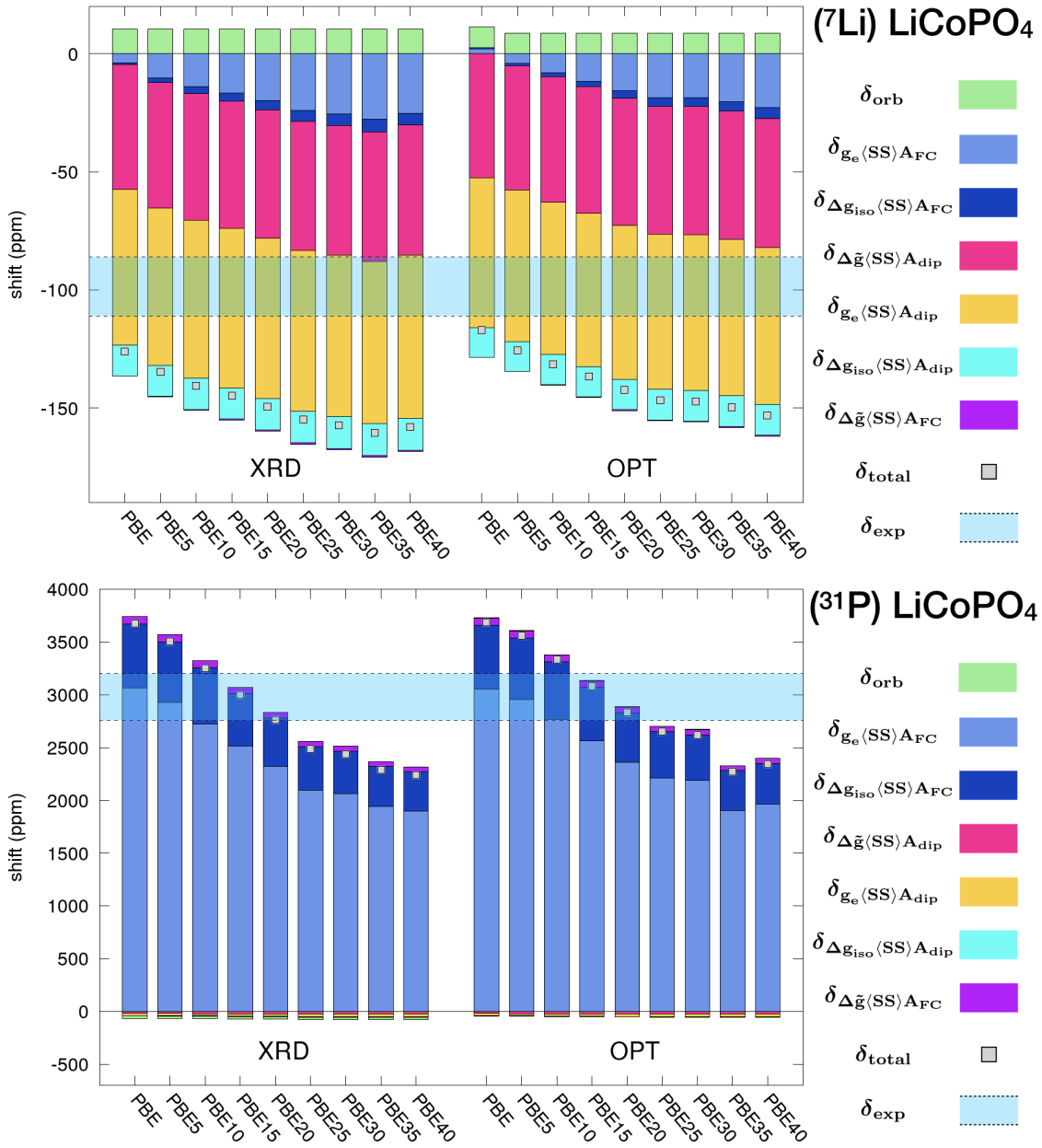

Figure 5.14.: Comparison of ^{7}Li and ^{31}P chemical shifts for $LiCoPO_4$ computed for both XRD and optimized (OPT) structures. ^{7}Li shifts for the XRD structure (top-left) are repeated from Figure 5.10 to compare the magnitudes of the different terms. Variations with EXX admixture to PBE-based functionals for the HFC tensors are shown. g-Tensor and D-tensor obtained at NEVPT2 level. Orbital shielding obtained at PBE level. Shieldings converted to shifts for Li and P relative to aq. lithium chloride (LiCl) and 85 % aq. phosphoric acid (H_3PO_4), respectively. Experimental range shown according to refs. 40,41,61,296 (see Tables C.25, C.26 for numerical values).

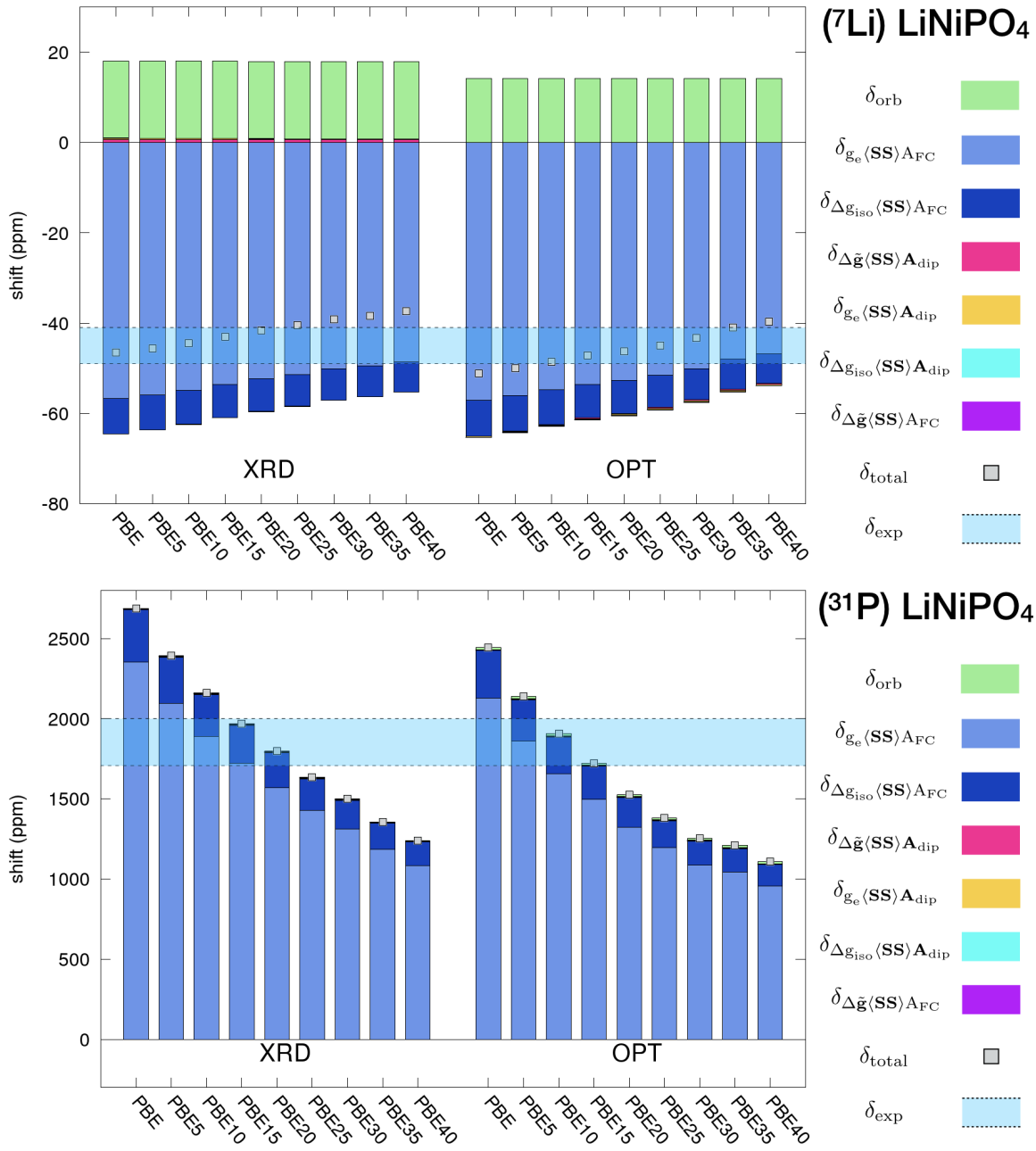

Figure 5.15.: Comparison of ^{7}Li and ^{31}P chemical shifts for $LiNiPO_4$ computed for both XRD and optimized (OPT) structures. Variations with EXX admixture to PBE-based functionals for the HFC tensors are shown. g-Tensor and D-tensor obtained at NEVPT2 level. Orbital shielding obtained at PBE level. Shieldings converted to shifts for Li and P relative to aq. lithium chloride (LiCl) and 85 % aq. phosphoric acid (H_3PO_4), respectively. Experimental range shown according to refs. 40,41 (see Tables C.29, C.30 for numerical values).

Co, having d^5, d^6 configuration with local sextet and quintet spin states, respectively), and an approximately octahedral coordination for the lithium site and tetrahedral coordination for the phosphorus site.

As expected from the very small SO effects of a d^5 configuration, the ^{7}Li shifts in $LiMnPO_4$ are dominated by the pure FC term ($g_e\langle \mathbf{SS}\rangle A^I_{FC}$), as shown in Figure 5.12 (cf. Tables C.27, C.28 in Appendix C). At 15% EXX and 20% EXX for the HFC computations, the total shifts for the XRD and optimized structure, respectively, turn out to be within the experimental range of about 57 ppm - 68 ppm.[40,41,296] Orbital shifts contribute about 4-5 ppm, all other terms are not visible on the scale of the plot (cf. C.27, C.28 in Appendix C). A large contribution to ^{7}Li shifts in $LiNiPO_4$ comes from pure FC term ($g_e\langle \mathbf{SS}\rangle A^I_{FC} \approx$ -50 ppm) whereas $g_e\langle \mathbf{SS}\rangle A^I_{FC}$ ($\approx$ -7 ppm) and orbital shifts (17.1 ppm) are also significant (see Figure 5.15).

As expected, the ^{31}P shifts for all six materials are dominated by the FC contributions. We therefore discuss them more briefly here than the ^{7}Li shifts and provide the graphical comparisons in Figures 5.12-5.15 and Figure C.11 in Appendix C (numerical data are in Tables C.22, C.23, C.25-C.37). SO effects manifest in contributions to the FC shifts via the term $\Delta g_{iso}\langle SS\rangle A^I_{FC}$ in several cases, in particular for $LiCoPO_4$ (Figure 5.14) and $LiNiPO_4$ (Figure 5.15).

Figure 5.16 looks at the overall comparison of computed and experimental isotropic ^{7}Li and ^{31}P shifts for both XRD (dashed lines) and optimized (solid lines) structures for all materials studied here. While the experimental ranges are crossed by the curves in all cases, the optimum EXX admixtures for which this is the case, vary non-negligibly. For the ^{7}Li shifts (top), this is apparent from the rather low optimum EXX admixtures for $LiCoPO_4$ and the much higher ones for $LiFePO_4$. Optimum EXX values for agreement with experiment for the ^{31}P shifts also vary (bottom), e.g. from relatively large values for $LiMnPO_4$ to much lower ones for $LiNiPO_4$. Apart from possible limitations in using global hybrid functionals with a constant EXX admixture for the HFC computations, these differences may well reflect other uncertainties in the calculations, as mentioned above. This points to areas for improvement. In particular, the computation of orbital shifts for solids deserves more attention in the future. Of course, the empirical correction of the shift formalism by measured Weiss constants, and the need to match temperature with experiment, give rise to further uncertainties.

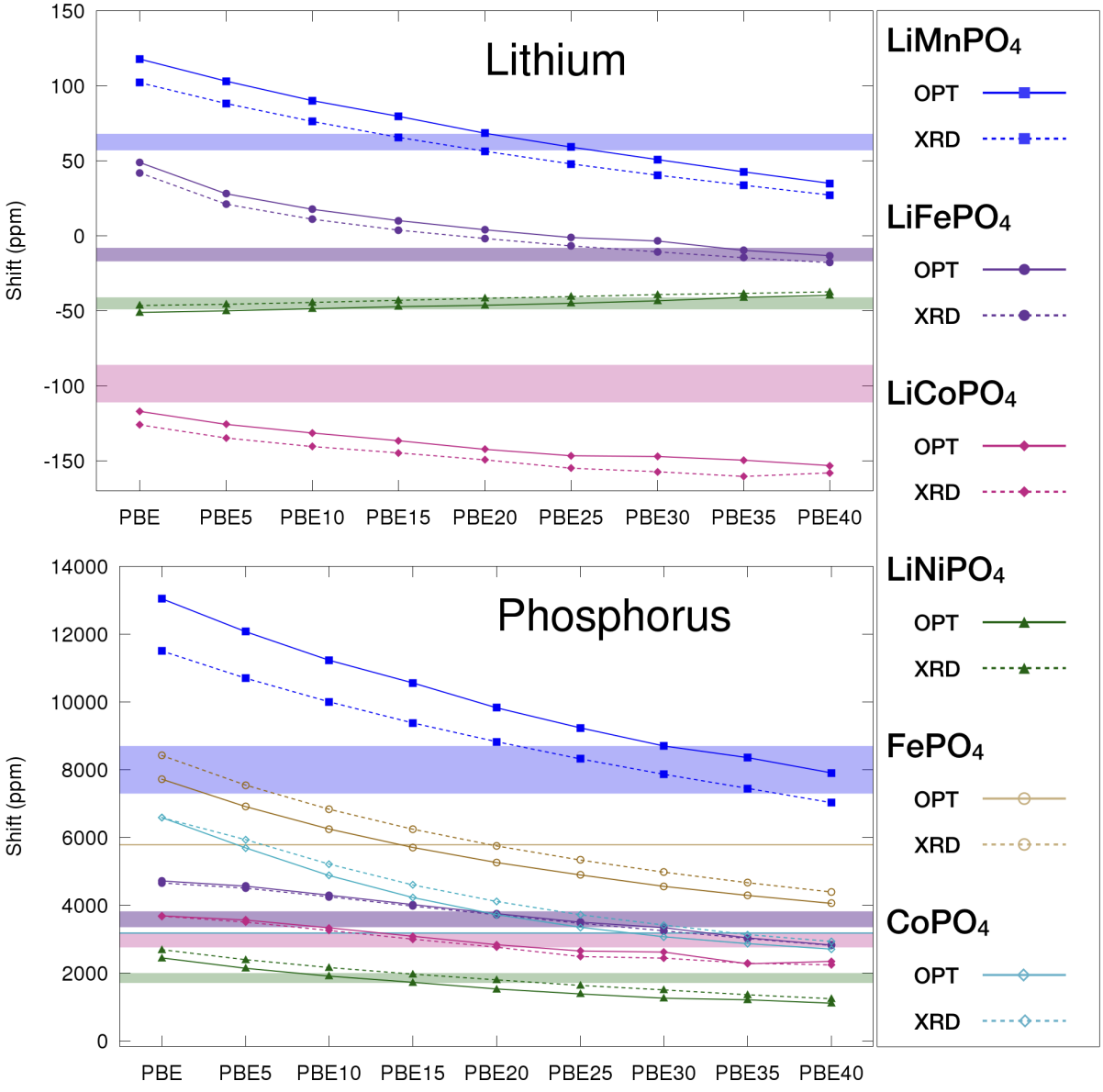

Figure 5.16.: Comparison of computed total ^{7}Li and ^{31}P chemical shifts (relative to $LiCl_{aq.}$ and 85% aq. H_3PO_4, respectively) for both XRD (dashed lines) and optimized (solid lines) structures of $LiMPO_4$ (M=Mn, Fe, Co, Ni) and MPO_4 (M=Fe, Co) as function of EXX admixture in the HFC computations (g-tensor and ZFS obtained at NEVPT2 level in cluster models, orbital shieldings at PBE level with PBC). Experimental ranges from Refs. 40,41,58 (cf. Tables C.22, C.23, C.25-C.37 for numerical values).

5.4. Conclusions

This work shows a new computational methodology that combines high-level ab initio multireference wave-function calculations of g- and D-tensors on clusters with periodic solid-state DFT calculations of hyperfine couplings and orbital shieldings to provide the first access to full NMR shift calculations for paramagnetic solids, including the major spin–orbit-related ("pseudo-contact") contributions arising for magnetically anisotropic metal centers. This work benefits from the extensive parallelization, general computational efficiency of the CP2K package, its possibility to use extended Gaussian basis sets including relatively diffuse functions, and the possibility to use hybrid functionals efficiently for the computation of hyperfine tensors for paramagnetic solids. In CP2K the availability of g-tensors (with reasonable spin–orbit operators) and orbital shieldings with distributed gauges (IGAIM and CSGT) for paramagnetic solids using periodic boundary conditions, provides an excellent benchmark for building incremental cluster models to use advanced molecular electronic-structure methods to construct a suitable g-tensor and ZFS D-tensor for a solid (insulator or semiconductor), making use of its relative locality.

This novel protocol to has been used compute and analyze NMR chemical shifts for extended paramagnetic solids, accounting comprehensively for Fermi-contact (FC), pseudo-contact (PC), and orbital shifts. It has been applied to the important lithium ion battery cathode materials $LiMPO_4$ (M = Mn, Fe, Co, Ni) and MPO_4 (M = Fe, Co). The cell parameters and atomic positions were optimized for each material and a detailed comparison with XRD versus DFT-optimized structure has been given. Throughout the work the computed EPR/NMR parameters for both structures have been discussed, exposing the interrelation between input structures (XRD and DFT-optimized) and computed spectroscopic parameters. We showed that an incremental cluster model that constructs the g-tensor of the simulation cell from individual molecular g-tensors is a viable and accurate alternative to computations using periodic boundary conditions. Using the incremental cluster model approach, g-tensors and ZFS D-tensors computed by ab initio complete active space self-consistent field and N-electron valence-state perturbation theory method showed excellent agreement with experimental data. DFT clearly underestimates ZFS D-tensor values for several materials, and it has been important to use high-level multireference method for accurate calculations. Computation of isotropic HFCs strongly depends on the chosen percentage of exact-exchange admixture of PBE-based global hybrid DFT functionals. Computed isotropic HFCs dominate in determining the Fermi-contact shifts. While the Fermi-contact shifts have major contributions to the total shifts, it is

clear that pseudo-contact and orbital shifts may not be negligible for accurate calculations (in particular if contact shifts are small), and deviations of the isotropic g-value from g_e may affect even the contact terms.

Our computations have shown that the ^{7}Li shifts in the high-voltage cathode material $LiCoPO_4$ are dominated by spin-orbit-induced PC contributions, in contrast to previous assumptions, changing interpretations of the shifts in terms of covalency. PC contributions are smaller for the ^{7}Li shifts of the related $LiMnPO_4$, $LiFePO_4$, and $LiNiPO_4$, where FC and orbital shifts dominate. The ^{31}P shifts of all six materials studied here finally are almost pure FC shifts. Nevertheless, large ZFS contributions can cause non-Curie temperature dependences for both ^{7}Li and ^{31}P shifts. These contributions have been shown to be crucial for the quantitative and even for the qualitative computation and proper interpretation of the ^{7}Li NMR shifts of the important $LiCoPO_4$ material, somewhat less important for the ^{7}Li shifts for the other materials, and comparatively unimportant for the ^{31}P shifts in the same materials (but affecting the temperature dependence). Magnetic anisotropy effects are expected to be similarly crucial for NMR shifts in many other relevant paramagnetic materials, for example, when containing Co or Ni and in cases where FC shifts are small due to various reasons, but also clearly for compounds that incorporate heavier d- or f-metal centers. Inclusion of pseudo-contact as well as orbital shift contributions in computational studies should allow improved interpretations of NMR measurements for paramagnetic solids in various fields of research.

Chapter 6.

Quantum-chemical approach to compute ^{7}Li shifts for partially delithiated lithium vanadium phosphates*

6.1. Introduction

As we had discussed in Chapter 5, the reversible delithiation of lithium metal phosphates is crucial for their function as cathode materials. The study of partially delithiated intermediates in the charging cycle by NMR spectroscopy is thus a central aspect. In Chapter 4 (ref. 148), we had provided computations on the fully lithiated $Li_3V_2(PO_4)_3$ cathode material as an initial test for the doublet formalism of pNMR shift computations for solids. Chapter 5 has extended the formalism to a full treatment for arbitrary multiplicities, including the effects of ZFS, and we have demonstrated the usefulness of cluster models to apply beyond-DFT approaches to the g- and D-tensors.

Here we apply this advanced formalism[148,151,310] to the first systematic studies of partially delithiated vanadium phosphates. In these computations we do not only include the FC shifts arising from isotropic hyperfine-couplings (HFC) but also account for the combined effects of the anisotropic parts of HFC, g-tensor, and D-tensor leading to PC shifts and

* Chapter 6 as well as tables and graphics within are reproduced in part with permission from A. Mondal and M. Kaupp, Quantum-chemical study of ^{7}Li NMR shifts in the context of delithiation of paramagnetic lithium vanadium phosphate, $Li_3V_2(PO_4)_3$ (LVP), *Solid State Nucl. Magn. Reson.*, **2019**, 101, 89-100. (https://doi.org/10.1016/j.ssnmr.2019.05.008). Copyright 2019 ELSEVIER.

for the temperature-independent orbital shifts. We focus on the computation of ^{7}Li shifts for $Li_3V_2(PO_4)_3$, $Li_{2.5}V_2(PO_4)_3$ and $Li_2V_2(PO_4)_3$ solids, where the latter two are partially delithiated materials.

6.2. Computational Details

Condensed-phase calculations were carried out for $Li_3V_2(PO_4)_3$, $Li_{2.5}V_2(PO_4)_3$ and $Li_2V_2(PO_4)_3$, with the CP2K package[69,191] using PBC. The structures were obtained from XRD.[254,258] Magnetic-resonance parameter calculations (in particular HFCs and orbital shieldings) employed the all-electron GAPW implementation of CP2K. Computations of orbital shieldings[148] used the PBE GGA functional, Ahlrichs' VTZ basis sets[242] for the metal centers, and unmodified extended Huzinaga-Kutzelnigg-type IGLO-II[209] basis sets for the main-group atoms. Orbital shieldings were obtained with the open-shell extension of the existing CP2K implementation for diamagnetic systems,[137] using "individual gauges for atoms in molecules" (IGAIM).[235] Hyperfine coupling (HFC) tensor computations were based on the nonrelativistic implementation of ref. 189. In addition to PBE, PBE-based global hybrids[190,204] were used, setting the exact-exchange (EXX) admixture to 20 % (PBE20) or 40 % (PBE40). These computations used basis sets that were well validated in molecular HFC calculations. A (14s11p6d)/[8s7p4d] basis was used for the transition metal (with only the most diffuse s-function removed[148] from the original [NMR_9s7p4d] basis designed specifically for HFC computations[202]), and IGLO-II main-group basis sets. HFC values provided by CP2K have been properly normalized to the local spin state.[148] For the expansion of the charge density in plane waves, an energy cutoff of 600 Ry was used, and the convergence criterion over the maximum component of the wave function gradient was set to 1.0×10^{-6}. Calculations were carried out on a unit cell (76-80 atoms).

In order to be able to include the ZFS D-tensor into solid-state calculations, and to obtain both D- and g-tensors at higher quantum-chemical levels than currently available in solid-state codes we followed the incremental cluster model approach introduced for g-tensors in refs. 148 (see Chapter 4 above), and further used for $LiFePO_4$ and $LiCoPO_4$ in ref. 151 (Chapter 5). Figure 6.1 shows the cluster models constructed for $Li_3V_2(PO_4)_3$, $Li_{2.5}V_2(PO_4)_3$, and $Li_2V_2(PO_4)_3$. In all cluster models, the transition-metal site is surrounded by six tetrahedral PO_4 units. The oxygen valences of the phosphate groups have been saturated by additional hydrogen atoms. At PBE/def2-TZVP level the hydrogen atom positions were optimized using Turbomole.[71] Three to four nearest lithium

atoms were included for $Li_xV_2(PO_4)_3$, which is important to reproduce the local chemical environment of the spin center.[148]

Using ORCA, the wave-function-based CASSCF and NEVPT2[163,165] methods were used to compute g- and ZFS D-tensors. These computations used the effective Hamiltonian approach[283] for the g-tensor and quasi-degenerate perturbation theory (QDPT),[207] for the dominant SO part of the D-tensor. These computations used SOMF SO operators. The less important[280,284–286] spin-spin part was also included. The RI technique was applied to the orbital transformation step of NEVPT2. The reference wave function was obtained at the state-averaged CASSCF level.[158,208] An active space that treated the electrons in the five 3d-orbitals was chosen. The state-averaging involved a CAS(2,5) space and 10 triplet and 15 singlet roots for cluster models a) and b) of $Li_3V_2(PO_4)_3$, as well as for cluster models c) and e) of $Li_{2.5}V_2(PO_4)_3$. A CAS(2,5) and 5 doublet roots were used for cluster models d) and f) of $Li_{2.5}V_2(PO_4)_3$, a CAS(1,5), and 10 triplet and 15 singlet roots for cluster model g) a CAS(2,5) and 5 doublet roots for cluster model h), and a CAS(1,5) of $Li_2V_2(PO_4)_3$, all equally weighted. See Figure 6.1 for the corresponding cluster models.

Our approach to the computation of g- and ZFS D-tensors follows ref. 148. The cluster models were extracted from the XRD structures of $Li_3V_2(PO_4)_3$, $Li_{2.5}V_2(PO_4)_3$ and $Li_2V_2(PO_4)_3$ as shown in Figure 6.1. They include the core structure of the metal coordination, i.e., vanadium octahedrally coordinated by six tetrahedral phosphates (PO_4). The phosphates have been saturated by hydrogen atoms, conserving the right oxidation states of the metal centers and phosphorus atoms. The hydrogen-atom positions were optimized at the PBE/def2-TZVP level using Turbomole. Since $Li_3V_2(PO_4)_3$ has two distinct vanadium environments (both V_a and V_b have the V^{+III} oxidation state), two sets of cluster models were constructed. Similarly, for $Li_2V_2(PO_4)_3$ two sets of cluster models were constructed having oxidation state V^{+IV} and V^{+III} for V_a and V_b, respectively. For $Li_{2.5}V_2(PO_4)_3$, four sets of cluster models were constructed with combinations of V^{+IV} and V^{+III} oxidation states for both V_a and V_b. NEVPT2 was applied to the g- and D-tensor computations on the resulting complexes, using the ORCA code. The cluster models with vanadium in its +4 oxidation state have only one unpaired electron, leading to vanishing single-ion ZFS. Using point-group symmetry, g-tensors and D-tensors were generated for all vanadium sites within the unit cell from the cluster models.

To compute the target ^{7}Li nuclear shieldings and, thus, pNMR shifts of lithium-vanadium-phosphates, cluster-model g-tensors and spin dyads (obtained from cluster-model D-tensors) were contracted directly with the HFC tensors computed at PBC (hybrid) DFT levels

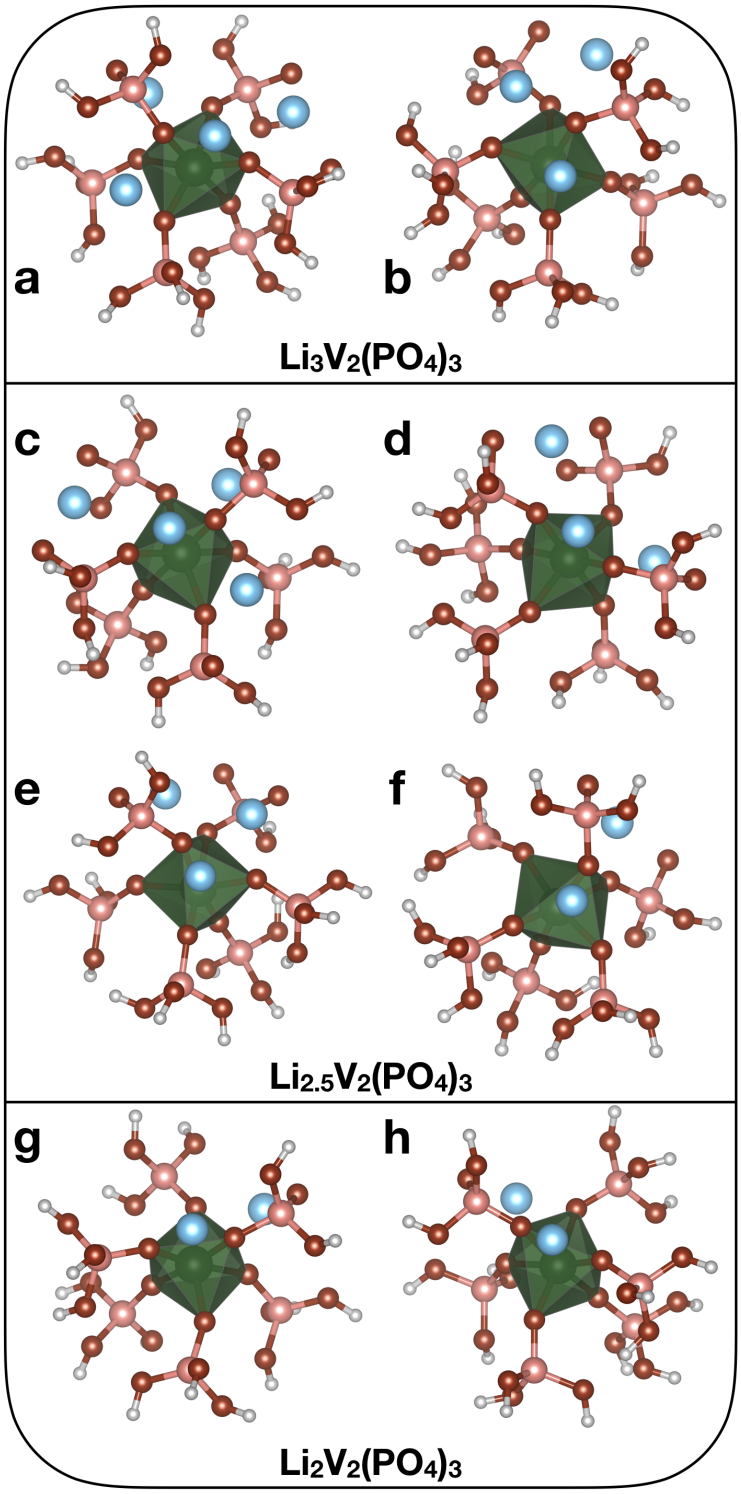

Figure 6.1.: Molecular models of the distinct vanadium centers of $Li_3V_2(PO_4)_3$, $Li_{2.5}V_2(PO_4)_3$ and $Li_2V_2(PO_4)_3$ solids, where the terminal oxygens were saturated with hydrogen atoms.

in eq. 2.34 (see Chapter 2 for details). The value of the Weiss constant Θ = -37 K for $Li_3V_2(PO_4)_3$ was taken from experiment.[43] To the best of our knowledge, there is no report in the literature regarding Weiss constants of $Li_{2.5}V_2(PO_4)_3$ and $Li_2V_2(PO_4)_3$. As the electronic structures and thus the exchange couplings of $Li_{2.5}V_2(PO_4)_3$ and $Li_2V_2(PO_4)_3$ are expected to be similar to those of $Li_3V_2(PO_4)_3$, we have used the same Weiss constant Θ = -37 K for the ^{7}Li shift computations of these two materials. Compared to $Li_3V_2(PO_4)_3$, $Li_{2.5}V_2(PO_4)_3$ and $Li_2V_2(PO_4)_3$ have a smaller number of unpaired electrons, which likely leads to smaller exchange couplings among the paramagnetic centers resulting in slightly smaller absolute values of Weiss constant (-37 K $< \Theta <$ 0 K). Such small differences will not affect computed shifts very much. The orbital shielding was then added at PBE DFT (PBC) level. These calculations were all done using Osprey, an in-house program written in the Python programming language. For comparison with experiment,[40,41,61,296] we report shifts at 320 K. This value is slightly above room temperature, which was usually reported in the experimental work, to account for frictional heating due to magic-angle spinning. ^{7}Li shifts were obtained by subtracting the computed absolute shielding from that of lithium lactate ($LiC_3H_5O_3$), i.e., $\delta^I = \sigma^I_{\text{ref}} - \sigma_{\text{ref}}$. The orbital shieldings for solid lithium lactate were computed for a cluster model cut out from the XRD structure at PBE/IGLO-II level in a supercell of size of 60 Å × 60 Å × 60 Å, resulting in 90.4 ppm.[148]

6.3. Results and discussions

Figure 6.2 compares the XRD structures of $Li_3V_2(PO_4)_3$ (ref. 254), $Li_{2.5}V_2(PO_4)_3$ (ref. 258), $Li_2V_2(PO_4)_3$ (ref. 254) and their overlapped positions. The unit cell of $Li_3V_2(PO_4)_3$ (reddish color) has 12 lithium atoms, which may be grouped into three distinct sites Li_a, Li_b, and Li_c due to point-group symmetry. $Li_2V_2(PO_4)_3$ (bluish color) has only eight lithium atoms in the unit cell, which may be grouped into two distinct lithium sites, Li_a and Li_b. During the delithiation of $Li_3V_2(PO_4)_3$, lithium atoms from the Li_c site are completely removed to obtain $Li_2V_2(PO_4)_3$. In $Li_{2.5}V_2(PO_4)_3$ (greenish color) lithium atoms are partially removed, giving 50 % occupancy at the Li_c site, and overall ten lithium atoms in the unit cell.

The overlapped figure of all three structures shows the comparative changes. In general the positions of atoms other than lithium exhibit only a small variation. Also, lithium atoms at the Li_a site differ slightly. The major changes may be seen at the Li_b and Li_c sites. In the structure of $Li_2V_2(PO_4)_3$, lithium atoms at the Li_b site are moved towards

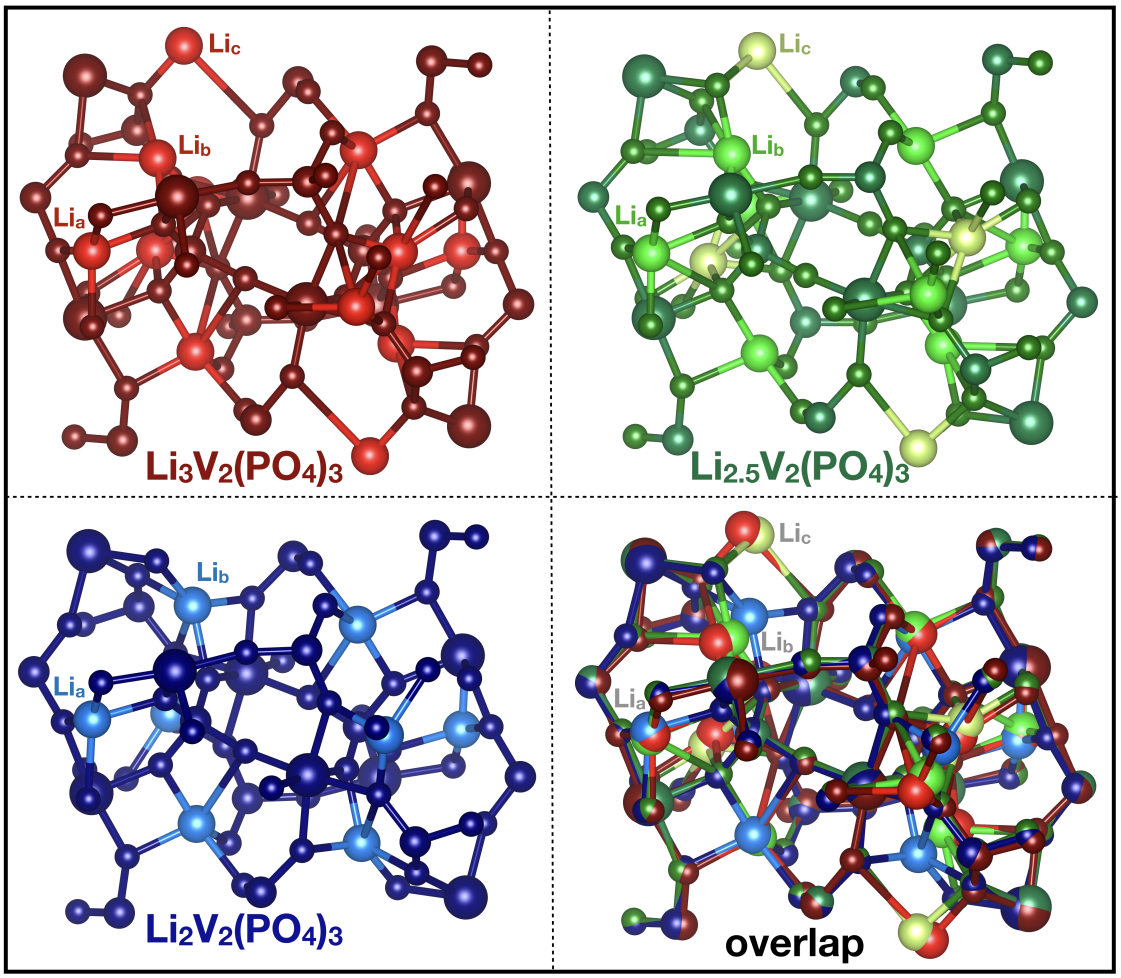

Figure 6.2.: Comparison of unit-cell structures of $Li_3V_2(PO_4)_3$, $Li_{2.5}V_2(PO_4)_3$, $Li_2V_2(PO_4)_3$.

the Li_c site compared to $Li_3V_2(PO_4)_3$. The empty Li_c site in $Li_2V_2(PO_4)_3$ allows the structure to relax and moves the loosely bound Li_b towards the open space. In contrast to $Li_2V_2(PO_4)_3$, Li_b sites in $Li_{2.5}V_2(PO_4)_3$ are moved slightly. This analysis also gives insight on the lithium dynamics during the delithiation of $Li_xV_2(PO_4)_3$.

The unit cell of $Li_3V_2(PO_4)_3$ contains eight vanadium atoms, at two distinct sites V_a and V_b, both in the +3 oxidation state. Table 6.1 shows the connection of lithium atoms to vanadium via a coordinated phosphate oxygen atom. Lithium atoms at the Li_a site have three neighboring vanadium atoms, two from the V_a group and one from the V_b group. Lithium atoms at Li_b and Li_c sites have two neighboring vanadium atoms. Both are from V_b group for Li_b, while Li_c shares one each from V_a and V_b. For the computation of

Table 6.1.: The list of neighboring vanadium atoms connected via phosphate oxygen atoms to specific lithium atoms in the $Li_3V_2(PO_4)_3$ unit cell (see Figure 6.3).

Atom	$\mathbf{V_{a1}^{(+III)}}$	$\mathbf{V_{a2}^{(+III)}}$	$\mathbf{V_{a3}^{(+III)}}$	$\mathbf{V_{a4}^{(+III)}}$	$\mathbf{V_{b1}^{(+III)}}$	$\mathbf{V_{b2}^{(+III)}}$	$\mathbf{V_{b3}^{(+III)}}$	$\mathbf{V_{b4}^{(+III)}}$
Li_{a1}	⊙		⊙		⊙			
Li_{a2}		⊙		⊙		⊙		
Li_{a3}	⊙		⊙				⊙	
Li_{a4}		⊙		⊙				⊙
Li_{b1}					⊙		⊙	
Li_{b2}						⊙		⊙
Li_{b3}					⊙		⊙	
Li_{b4}						⊙		⊙
Li_{c1}	⊙				⊙			
Li_{c2}		⊙				⊙		
Li_{c3}			⊙				⊙	
Li_{c4}				⊙				⊙

pNMR shifts, it is important to have clear insight into the neighboring (coordinating) paramagnetic centers to the nucleus of interest.

Table 6.2.: The list of neighboring metal center sites connected via phosphate oxygen atoms to specific lithium atoms in the $Li_2V_2(PO_4)_3$ unit cell (see Figure 6.4).

Atom	$\mathbf{V_{a1}^{(+IV)}}$	$\mathbf{V_{a2}^{(+IV)}}$	$\mathbf{V_{a3}^{(+IV)}}$	$\mathbf{V_{a4}^{(+IV)}}$	$\mathbf{V_{b1}^{(+III)}}$	$\mathbf{V_{b2}^{(+III)}}$	$\mathbf{V_{b3}^{(+III)}}$	$\mathbf{V_{b4}^{(+III)}}$
Li_{a1}	⊙		⊙					
Li_{a2}		⊙		⊙				
Li_{a3}	⊙		⊙					
Li_{a4}		⊙		⊙				
Li_{b1}					⊙		⊙	
Li_{b2}						⊙		⊙
Li_{b3}					⊙		⊙	
Li_{b4}						⊙		⊙

The unit cell of $Li_2V_2(PO_4)_3$ has eight vanadium atoms. As compared to the unit cell of $Li_3V_2(PO_4)_3$, there are four fewer lithium atoms in $Li_2V_2(PO_4)_3$, half of the vanadium atoms are in a +4 oxidation state. Mulliken spin densities show that vanadium atoms of the V_a group are V^{+IV} sites and those of the V_b group V^{+III} sites, consistent with the analysis in ref. 258. Table 6.2 summarizes the neighboring vanadium atoms of the various lithium sites. Interestingly, Li_a and Li_b have two neighboring vanadium atoms from the V_a and V_b groups, respectively.

The Li_c lithium sites in $Li_{2.5}V_2(PO_4)_3$ unit cell are 50 % occupied, which means for a given unit cell that two Li_c sites are occupied, and two are empty. Within the unit cell, Li_c sites are related by point-group symmetry, which gives three unique occupations of Li_c sites labeled as Set-1, Set-2, and Set-3 unit-cell structures. The two lithium vacancies in the $Li_{2.5}V_2(PO_4)_3$ unit cell are accompanied by two vanadium atoms in V^{+IV} oxidation state (see Table 6.3). Mulliken spin densities indicate the following positions for the V^{+IV} atoms: V_{a3} and V_{a4} for Set-1, V_{b2} and V_{b3} for Set-2, and V_{a2} and V_{b2} for Set-3. The neighboring vanadium atoms for each lithium site are also specified in Table 6.3.

Figure 6.8 provides the experimentally obtained lithium shifts for a) $Li_3V_2(PO_4)_3$, c) $Li_{2.5}V_2(PO_4)_3$, and e) $Li_2V_2(PO_4)_3$, which were reproduced from ref. 258. Three lithium shift values at 17 ppm, 52 ppm and 103 ppm are found for $Li_3V_2(PO_4)_3$, confirming the existence of three unique lithium sites. Similarly, for $Li_2V_2(PO_4)_3$ two signals at 77 ppm and 143 ppm confirm that during the delithiation process only one of the lithium sites vanishes completely, and two kinds of lithium sites remain. Interestingly, for $Li_{2.5}V_2(PO_4)_3$ at least five signals could be resolved at 188 ppm, 121 ppm, 51 ppm, 27 ppm and -9 ppm (see Figure 6.8). With the help of the computed ^{7}Li shifts we now attempt to assign the peaks to their respective lithium sites in three sets of $Li_{2.5}V_2(PO_4)_3$ structures.

Figure 6.9 shows the range of ^{7}Li shifts computed using HFCs obtained, as function of EXX admixture (between 0% and 40%, as indicated by each bar) of the PBE-based hybrid functionals used, for lithium sites of $Li_3V_2(PO_4)_3$, $Li_{2.5}V_2(PO_4)_3$, and $Li_2V_2(PO_4)_3$. Figure 6.9 shows the range of ^{7}Li shifts of three lithium sites for $Li_3V_2(PO_4)_3$ (left), of two lithium sites for $Li_2V_2(PO_4)_3$ (right), and of seven isotropic shifts for $Li_{2.5}V_2(PO_4)_3$ (middle). The small square dots represent the values of isotropic chemical shifts extracted from the experimentally obtained spectra in ref. 258 (see Figure 6.8). The three lithium sites for $Li_3V_2(PO_4)_3$ and two lithium sites for $Li_2V_2(PO_4)_3$ are well defined, and the computed range of ^{7}Li shifts contains the experimental value in almost all cases. The shift of the Li_a site in $Li_2V_2(PO_4)_3$ is slightly below the computed range. This gives us the confidence that our computed shift ranges are appropriate for $Li_3V_2(PO_4)_3$ and $Li_2V_2(PO_4)_3$ solids and can be used for analyzing and assigning the ^{7}Li shifts of the more complex, intermediate $Li_{2.5}V_2(PO_4)_3$ structure. For each lithium site, the range of ^{7}Li shifts was computed for each of the different Li occupations possible, has been grouped depending on the computed range, and has been assigned to one of the seven experimental signals (see Figure 6.9). The agreement of the computed shift range with the experimental values is excellent. The most interesting and important observation is a clear assignment of the signals at 143 ppm and 77 ppm. While it was mentioned in ref. 258 that these

Table 6.3.: The list of neighboring vanadium centers connected via phosphate oxygen atoms to specific lithium sites for three sets of $Li_{2.5}V_2(PO_4)_3$ unit cells (see Figure 6.5, Figure 6.6 and Figure 6.7)

Set-1								
Atom	$\mathbf{V_{a1}^{(+III)}}$	$\mathbf{V_{a2}^{(+III)}}$	$\mathbf{V_{a3}^{(+IV)}}$	$\mathbf{V_{a4}^{(+IV)}}$	$\mathbf{V_{b1}^{(+III)}}$	$\mathbf{V_{b2}^{(+III)}}$	$\mathbf{V_{b3}^{(+III)}}$	$\mathbf{V_{b4}^{(+III)}}$
Li_{a1}	⊙				⊙		⊙	
Li_{a2}		⊙				⊙		⊙
Li_{a3}			⊙		⊙		⊙	
Li_{a4}				⊙		⊙		⊙
Li_{b1}	⊙		⊙					
Li_{b2}		⊙		⊙				
Li_{b3}	⊙		⊙					
Li_{b4}		⊙		⊙				
Li_{c1}	⊙				⊙			
Li_{c2}		⊙				⊙		

Set-2								
Atom	$\mathbf{V_{a1}^{(+III)}}$	$\mathbf{V_{a2}^{(+III)}}$	$\mathbf{V_{a3}^{(+III)}}$	$\mathbf{V_{a4}^{(+III)}}$	$\mathbf{V_{b1}^{(+III)}}$	$\mathbf{V_{b2}^{(+IV)}}$	$\mathbf{V_{b3}^{(+IV)}}$	$\mathbf{V_{b4}^{(+III)}}$
Li_{a1}	⊙				⊙		⊙	
Li_{a2}		⊙				⊙		⊙
Li_{a3}			⊙		⊙		⊙	
Li_{a4}				⊙		⊙		⊙
Li_{b1}	⊙		⊙					
Li_{b2}		⊙		⊙				
Li_{b3}	⊙		⊙					
Li_{b4}		⊙		⊙				
Li_{c1}	⊙				⊙			
Li_{c4}				⊙				⊙

Set-3								
Atom	$\mathbf{V_{a1}^{(+III)}}$	$\mathbf{V_{a2}^{(+IV)}}$	$\mathbf{V_{a3}^{(+III)}}$	$\mathbf{V_{a4}^{(+III)}}$	$\mathbf{V_{b1}^{(+III)}}$	$\mathbf{V_{b2}^{(+IV)}}$	$\mathbf{V_{b3}^{(+III)}}$	$\mathbf{V_{b4}^{(+III)}}$
Li_{a1}	⊙				⊙		⊙	
Li_{a2}		⊙				⊙		⊙
Li_{a3}			⊙		⊙		⊙	
Li_{a4}				⊙		⊙		⊙
Li_{b1}	⊙		⊙					
Li_{b2}		⊙		⊙				
Li_{b3}	⊙		⊙					
Li_{b4}		⊙		⊙				
Li_{c1}	⊙				⊙			
Li_{c3}			⊙				⊙	

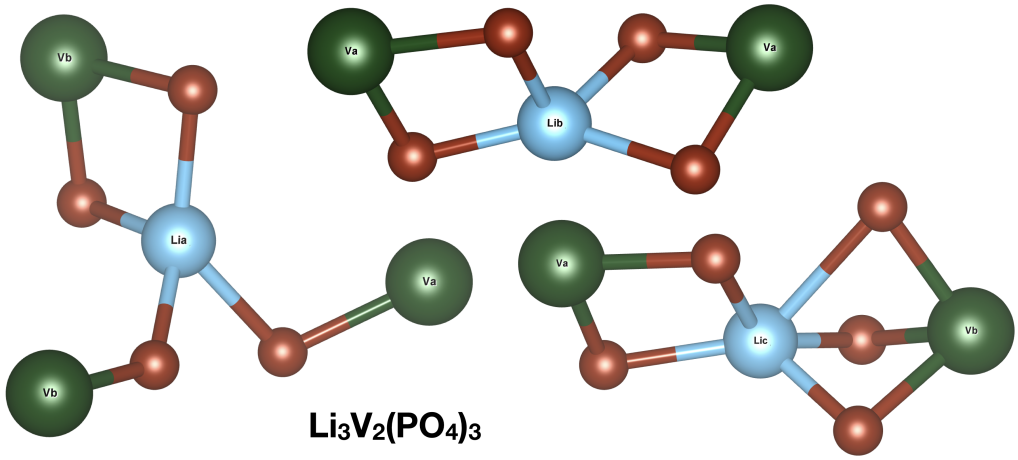

Figure 6.3.: The neighboring vanadium atoms connected via phosphate oxygen atoms to specific lithium atoms in the $Li_3V_2(PO_4)_3$ unit cell (see Table 6.1).

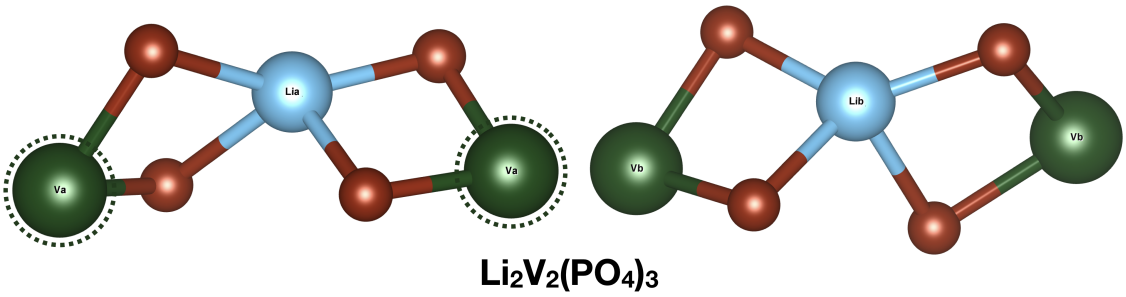

Figure 6.4.: The neighboring vanadium atoms connected via phosphate oxygen atoms to specific lithium atoms in the $Li_2V_2(PO_4)_3$ unit cell (see Table 6.2). The vanadium atoms represented with and without greenish ring are in +4 and +3 oxidation states respectively.

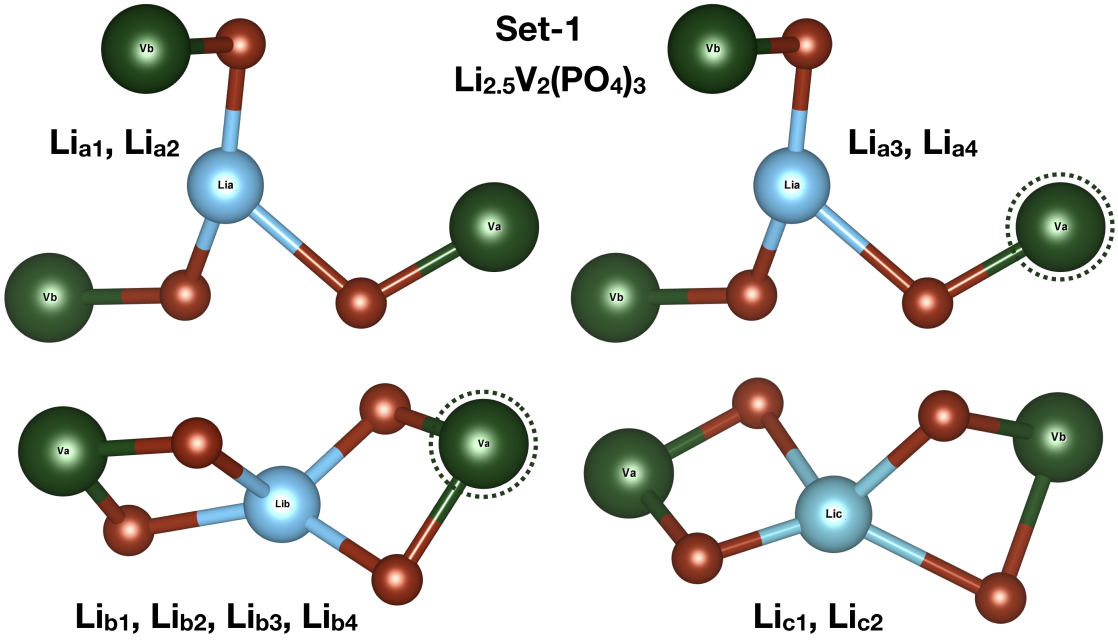

Figure 6.5.: The neighboring vanadium atoms connected via phosphate oxygen atoms to specific lithium atoms in the $Li_{2.5}V_2(PO_4)_3$ unit cell (see Table 6.3). The vanadium atoms represented with and without greenish ring are in the +4 and +3 oxidation states, respectively.

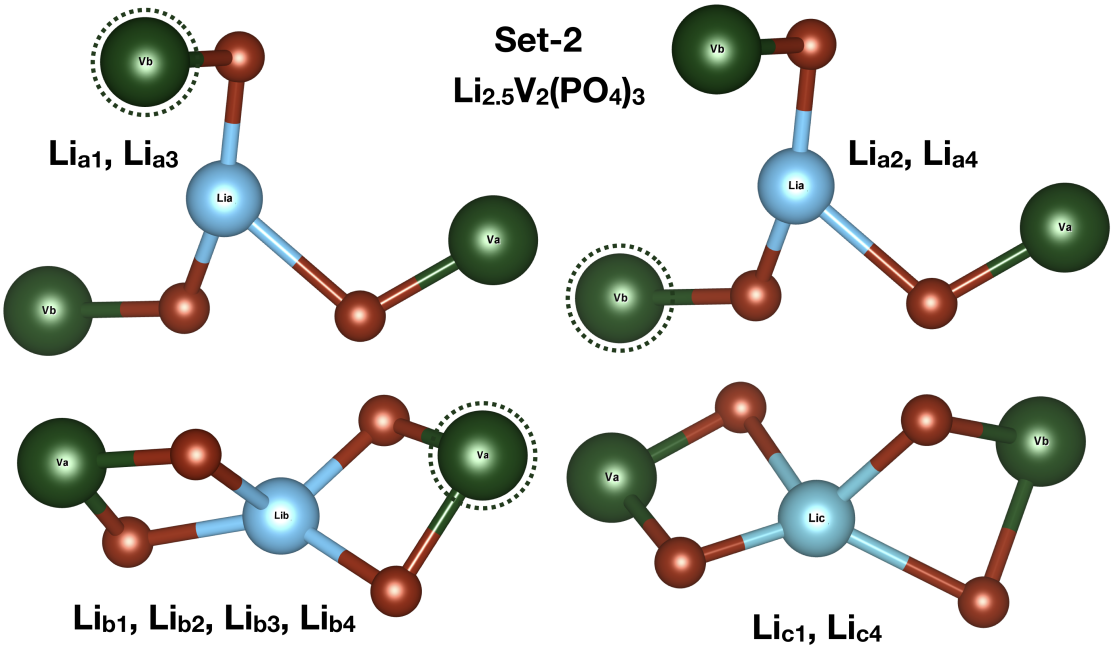

Figure 6.6.: The neighboring vanadium atoms connected via phosphate oxygen atoms to specific lithium atoms in the $Li_{2.5}V_2(PO_4)_3$ unit cell (see Table 6.3). The vanadium atoms represented with and without greenish ring are in the +4 and +3 oxidation states, respectively.

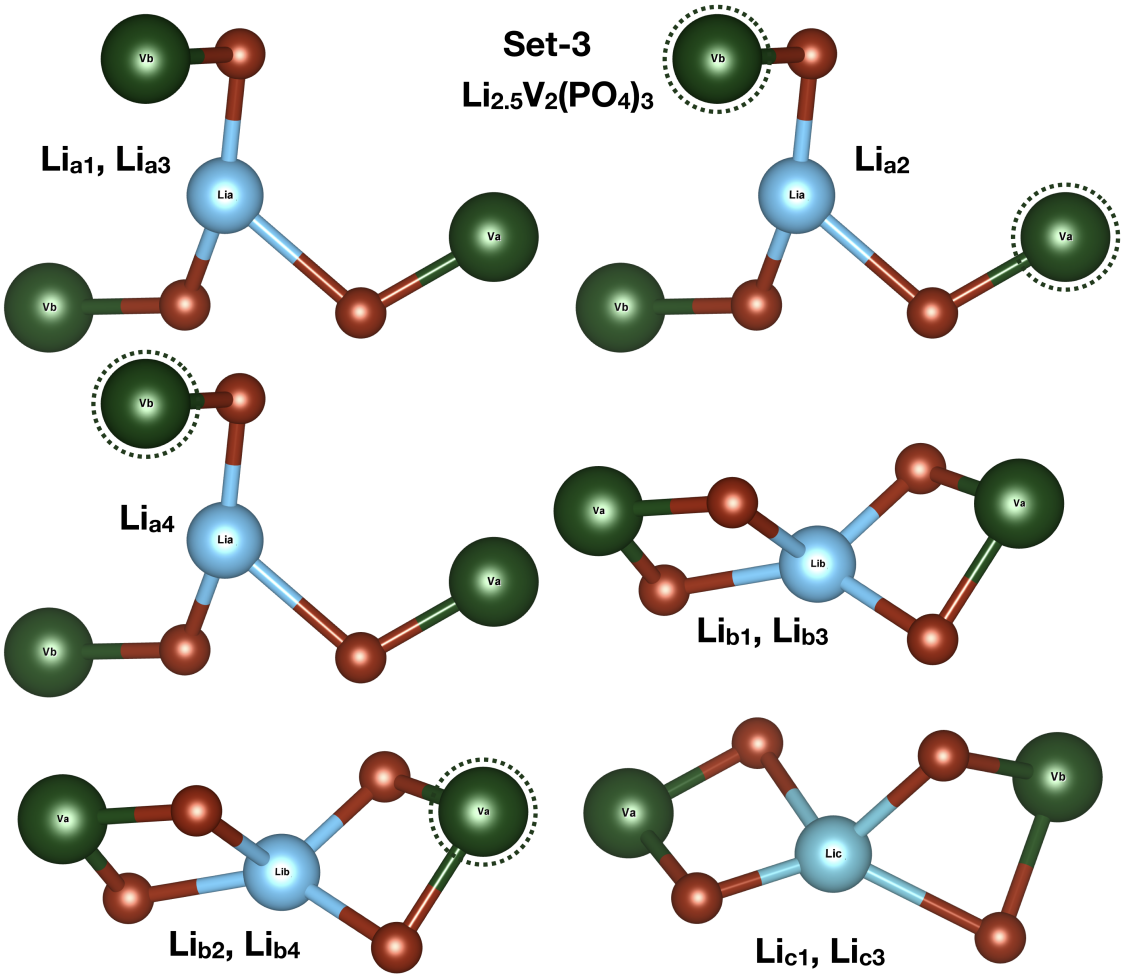

Figure 6.7.: The neighboring vanadium atoms connected via phosphate oxygen atoms to specific lithium atoms in the $Li_{2.5}V_2(PO_4)_3$ unit cell (see Table 6.3). The vanadium atoms represented with and without greenish ring are in the +4 and +3 oxidation states, respectively.

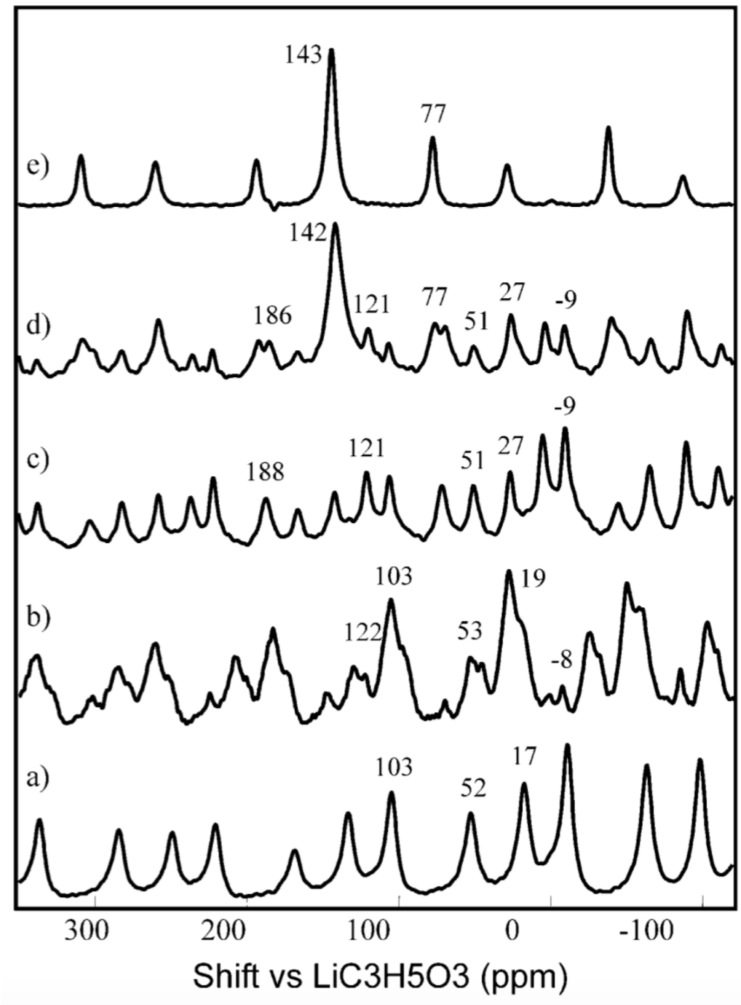

Figure 6.8.: ^{7}Li MAS NMR spectrum of $Li_xV_2(PO_4)_3$ on delithiation from $x = 3 \rightarrow 2$. a) $x = 3.0$; b) $x = 2.75$; c) $x = 2.5$; d) $x = 2.25$; e) $x = 2.0$. The isotropic chemical shifts in each spectrum are labeled (ppm). Figure 6.8 reproduced and adapted with permission from Yin, S.-C.; Grondey, H.; Strobel, P.; Anne, M.; Nazar, L. F. *J. Am. Chem. Soc.* **2003**, *125*, 10402-10411. Copyright 2003 American Chemical Society.

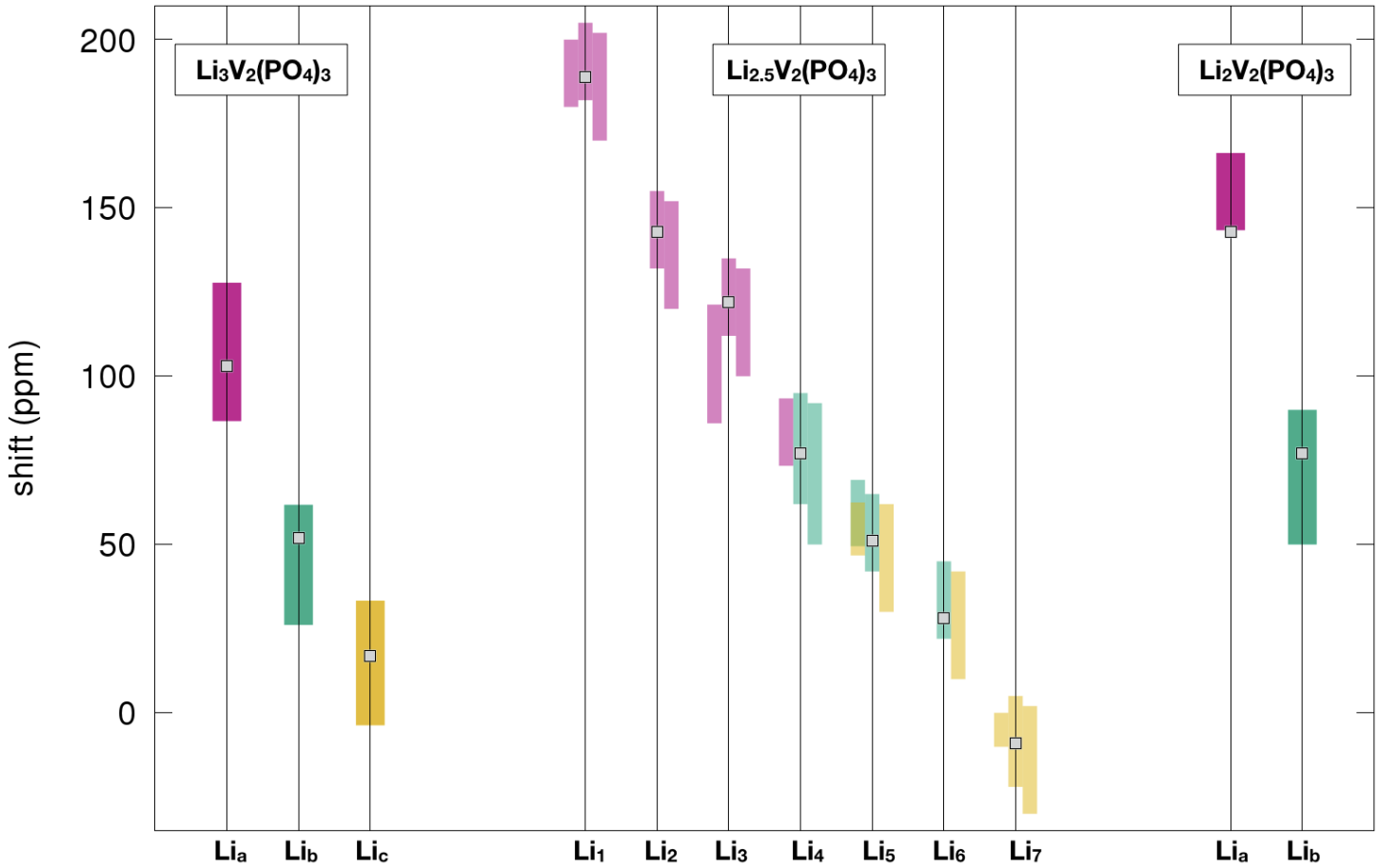

Figure 6.9.: Comparison of computed ^{7}Li shifts for $Li_xV_2(PO_4)_3$ solids (x= 3.0, 2.5, 2.0). Three lithium sites for $Li_3V_2(PO_4)_3$ (left), two lithium sites for $Li_3V_2(PO_4)_3$ (right) and seven sets of signals for $Li_{2.5}V_2(PO_4)_3$ (middle) are shown as function of the range of EXX admixture (0-40%)to PBE-based functionals for HFC. g-Tensors and ZFS D-tensors have been obtained at NEVPT2 level, orbital shieldings obtained at PBE level. Shielding have been converted to shifts relative to solid lithium lactate. The dots represents the experimental values from ref. 258. Each bar represents the specific lithium site in the corresponding unit cell (see Figures 6.3 - 6.7). The lithium sites Li_a, Li_b and Li_c are represented by reddish, greenish and yellowish color bars, respectively. The upper EXX admixture corresponds to the lower end of a given bar.

two signals come from the presence of the $Li_2V_2(PO_4)_3$ phase (see Figure 6 in ref. 258), our computations show that the computed two peaks at 77 ppm and 143 ppm do likely originate from specific lithium sites in $Li_{2.5}V_2(PO_4)_3$. In fact, the computed pNMR shifts allow a rather comprehensive mapping of the lithium sites to the spectral signals. Such a possibility should be very useful in general for characterizing complex pNMR spectra like those in the partially delithiated $Li_{2.5}V_2(PO_4)_3$.

6.4. Conclusions

This chapter shows a representative application of our newly developed computational methodology for pNMR shift calculations in extended solids to the ^{7}Li shifts of a set of complex lithium vanadium phosphates, combining high-level ab initio multi-reference wave function calculations of g- and D-tensors on cluster models with periodic solid-state DFT calculations of hyperfine couplings and orbital shieldings. Apart from the FC shift contributions, these calculations account adequately also for the PC shift and orbital shift contributions. This has enabled us to meaningfully analyze and assign closely spaced lithium shifts, especially for the rather complex $Li_{2.5}V_2(PO_4)_3$, where seven distinct lithium shift signals between -9 ppm to 188 ppm can be seen in the experimental NMR spectra. We have discussed in detail the protocols for constructing the cluster models of $Li_3V_2(PO_4)_3$, $Li_{2.5}V_2(PO_4)_3$, and $Li_2V_2(PO_4)_3$ and for using them to compute g-tensors and ZFS D-tensors by ab initio wave-function methods. The computed pNMR shift ranges (see Computational Details) for all lithium sites in $Li_3V_2(PO_4)_3$, $Li_{2.5}V_2(PO_4)_3$, and $Li_2V_2(PO_4)_3$ are in good agreement with the experimental data. It is important to emphasize that the lithium shifts are small and closely spaced. However, the computed pNMR shift ranges allow the assignment of the lithium signals to their respective sites in all three materials $Li_3V_2(PO_4)_3$, $Li_{2.5}V_2(PO_4)_3$, and $Li_2V_2(PO_4)_3$. This work clearly shows the usefulness of our newly developed methodology for pNMR shift calculations from saturated lithium phosphates to more complex delithiated lithium vanadium phosphate materials, providing a strong foundation for applying them to more complex materials such as lithium-nickel-cobalt-manganese-oxides.

Chapter 7.

Quantum-chemical computation of ^{1}H and ^{13}C shifts for paramagnetic Cr-MIL-101 derivatives*

7.1. Introduction

Porous materials with regular, large, accessible tunnels and cages are increasingly in demand for applications in sensors, electronics, gas storage,[311] separations,[312] recognition,[313,314] catalysis[315–318] and drug delivery.[319–321] These materials allow only molecules of specific shapes and sizes to enter the pores, depending on their structures and pore sizes. Moreover, large pores generate confined volume which may provide an ideal environment to act as nanoreactors, or as nanomolds for calibration and monodisperse nanomaterials.[322] Various kinds of porous materials with large pore sizes provide a more extensive range of reactants that can be combined or stored. These applications fundamentally rely on selective interactions between the target molecules and the host. Depending on the topology of metal-organic frameworks (MOFs), these interactions are mediated either by the organic linkers[313,323,324] or by strong coordinative interactions.[325–327] However, the architecture of the MOFs with large pores carries the risk of the interpenetration of the structures. Accurate structural characterization of such solids with large unit cells is

* Chapter 7 *(pre-print)* as well as tables and graphics within are reproduced in part with permission from T. Wittmann, A. Mondal, C. B. L. Tschense, J. J. Wittmann, O. Klimm, R. Siegel, B. Corzilius, B. Weber, M. Kaupp and J. Senker, Probing interactions of N-donor molecules with open metal sites within paramagnetic Cr-MIL-101: A solid-state NMR spectroscopic and density functional theory study, *J. Am. Chem. Soc.*, **2018**, 140, 2135–2144. (https://doi.org/10.1021/jacs.7b10148). Copyright 2018 American Chemical Society.

possible when single crystals are available.[328] To have a reliable chemical understanding of the interaction of the guest molecules with the host, it becomes essential to use several techniques for characterization. Adsorption isotherms, calorimetric measurements, and thermogravimetric experiments coupled to an infrared (IR) or a mass spectrometer allow for the determination of adsorption enthalpies and binding preferences.[329–332] With the combination of microscopic techniques like fluorescence,[333] UV–vis,[334] and Raman/IR[335] spectroscopy as well as solid-state NMR spectroscopy on diamagnetic MOFs,[336,337] considerable progress was made on unraveling active binding sites, and first insights into the microscopic interaction mechanism were provided.

There are various MOFs with paramagnetic transition metal cations which serve as hosts such as Cu^{2+} in HKUST-1,[338] Ni^{2+} and Co^{2+} in CPO-27,[330,339] and Cr^{3+} and Fe^{3+} in MIL-100,[340] and in MIL-101.[319,341] Solid-state NMR provides additional insight into the adsorption processes and the local chemical environment close to metal centers. The study of paramagnetic MOFs using NMR spectroscopy is so far rare. However, this method is well developed for structure determination of biomolecules in the liquid state.[116,342–346] Guest molecules coordinated at the metal sites can experience large hyperfine shifts leading to differences of up to several hundreds of ppm compared to non-coordinated and diamagnetic guest molecules.[56] While individual resonances might be severely broadened, large shift dispersions still result in excellent resolution. Additionally, it should be possible to distinguish species directly coordinated to the metal site against those physisorbed in the periphery of the framework. This helps to determine and separate various active binding sites, as well as to derive binding affinities, leading to an improved understanding of host-guest interactions, in particular for competitive adsorption processes.

In addition to the combination of several experimental NMR/EPR techniques such as fast magic angle spinning,[347] spin–lattice relaxations and REDOR (rotational echo double resonance),[347–349] together with computed chemical shifts helps in the assignment of the NMR spectra.[148,151] Our computations are based on newly developed protocols to compute, and analyze NMR chemical shifts for solids, clusters and molecules having multiple paramagnetic centers.[148,151] The formalism not only includes all contributions to orbital, Fermi-contact (FC), and pseudo-contact (PC) shifts but also accounts for the magnetic couplings between the paramagnetic metal sites within the Curie–Weiss regime (see Chapter 2 for details).[44]

7.2. Computational details

DFT computations of the ^{13}C and ^{1}H shifts were done for structures of the four model clusters optimized at PBE0-D3/def2-TZVP level,[190,194,195,204,350] using the Turbomole program.[71] Subsequently, the magnetic-resonance parameters have been computed using appropriate 9s7p4d metal[202] and IGLO-II main-group element[209] basis sets. In these calculations, a ferromagnetically coupled spin arrangement within the cluster was chosen. The HFC and g-tensor calculations with the ORCA code[70] used a modified PBE40 hybrid functional (PBE0 with increased 40% exact-exchange admixture) that we recently found to perform well for solid-state pNMR shift calculations,[148] and which is also known to give excellent HFCs and g-tensors in relativistic computations for molecules.[224] The computed HFCs have been normalized to the number of spin centers present.[351] ZFS tensors were computed using the PBE exchange-correlation functional[190] and the Pederson-Khanna second-order perturbation approach[205] with van Wüllen's prefactors.[206] For both g-tensors and ZFS, the necessary spin–orbit matrix elements were computed within the spin–orbit mean-field approximation[229] implemented in ORCA. Orbital shieldings were obtained with the PBE40 functional using Gaussian09 (for both open- and closed-shell cases).[74] All pNMR computations were performed for T = 325 K. The Weiss constant (Θ = –102 K) obtained by extrapolation of the high-temperature part of the magnetic susceptibility for H_2O@Cr-MIL-101 was used.[310] We noted that a change of 20 K in Θ affects the computed hyperfine shifts at most by 5%, which renders our use of the same Weiss constant for the other derivatives a reasonable approximation. Both ^{1}H and ^{13}C shifts were referenced to tetramethylsilane (TMS) at the same level (using a PBE/def2-TZVP structure for TMS; the values are σ^{C}_{ref} = 189.23 ppm and σ^{H}_{ref} = 31.68 ppm). The pNMR shifts were computed using eq. 2.35 (see Chapter 2 for detailed discussion about the theory).

7.3. Results and discussion

Figure 7.1 shows the cage structure of Cr-MIL-101 which has a large cell volume, surface area (5900 m^2g^{-1}), a hierarchy of extra-large pore sizes ($\sim$ 29 to 34 Å), and few thousand atoms in the unit cell.[341] Even with the significant development of computational algorithms and computation facilities, the computation of the required EPR/NMR parameters is still limited to a few hundreds of atoms in both condensed-phase and molecular calculations.[78,137,138,148,151] The EPR/NMR properties are influenced mostly by the local nature of

the chemical environment, which gives the possibility to construct cluster models for MOFs.

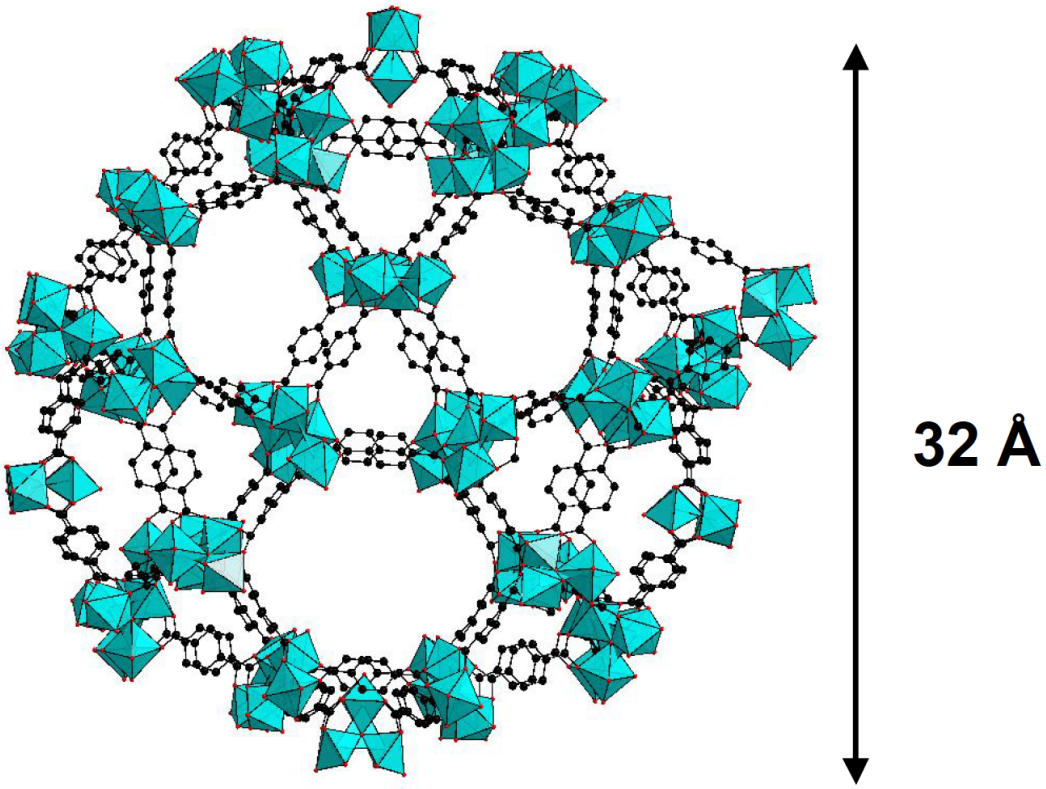

Figure 7.1.: Mesoporous cage structure of Cr-MIL-101 metal-organic frameworks.[352]

Cluster models were prepared keeping the Cr_3O center intact and including the neighboring ligands and saturating the valency of terminal oxygen atoms with hydrogen atoms. Figure 7.2 shows the cluster models of four Cr-MIL-101 derivatives with a) water (H_2O), b) 2-aminopyridine (2-AP) c) 3-aminopyridine (3-AP) and d) diethylamine (DEA) having 208, 123, 123 and 126 atoms, respectively. H_2O@Cr-MIL-101 contains two sets of Cr_3O centers for the appropriate chemical environment on the bridging terephthalic acid group. The other three have only one Cr_3O unit in the cluster model. The clusters were fully optimized at PBE0-D3/def2-TZVP level using the Turbomole program. The optimized structures were used further for the computation of magnetic-resonance parameters. All the computations were done with the Cr_3O unit in a ferromagnetically coupled state.

Table 7.1 provides the principal and isotropic value of the g-tensor computed for Cr-MIL-101 derivatives at the PBE40/9s7p4d/IGLO-II level using the ORCA code (see Computational Details).The g-value of 1.985 extracted from magnetic susceptibility measurements and EPR data for H_2O@Cr-MIL-101 agree well with the computed values. The experimental g-tensor obtained from EPR experiments for H_2O@Cr-MIL-101 (axial fit) is $g_{\|} = 1.988$,

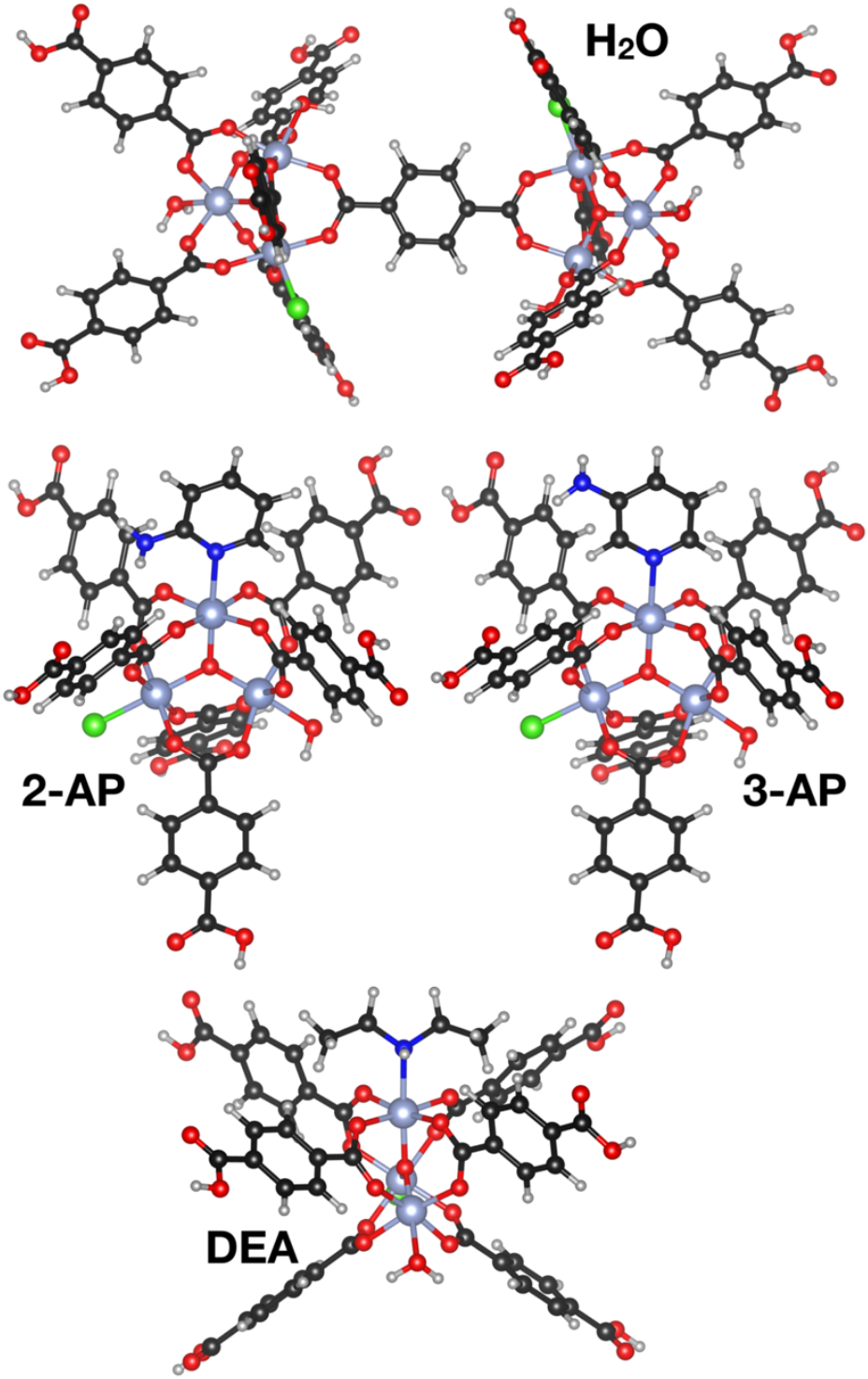

Figure 7.2.: DFT-optimized fragment clusters used for the computational studies: a) H_2O@Cr-MIL-101, b) 2-AP@Cr-MIL-101, c) 3-AP@Cr-MIL-101, and d) DEA@Cr-MIL-101.

Table 7.1.: Comparison of computed[a] g-tensors of the Cr-MIL-101 derivatives.

compound	$\mathbf{g_{11}}$	$\mathbf{g_{22}}$	$\mathbf{g_{33}}$	$\mathbf{g_{iso}}$
H_2O@Cr-MIL-101	1.98155	1.98318	1.98443	1.98306
2-AP@Cr-MIL-101	1.98134	1.98269	1.98408	1.98270
3-AP@Cr-MIL-101	1.98134	1.98358	1.98412	1.98268
DEA@Cr-MIL-101	1.98141	1.98277	1.98409	1.98276

[a] The cluster-model computations were done at PBE40/IGLO-II/9s7p4d level (see Computational Details).

$g_\perp$ = 1.980, g_{iso}= 1.985 (see ref. 310) also is in good agreement with the computed values. In ref. 310, magnetic susceptibility measurements for H_2O@Cr-MIL-101 show that χ^{-1}(T) above 50 K obeys the Curie–Weiss law with an effective magnetic moment μ_{eff} of 3.566 μ_B per Cr^{3+} and a Weiss temperature Θ of -102 K. μ_{eff} is low compared to the "spin-only" value for Cr^{3+} (μ_{eff} = 3.87 μ_B), which agrees well with values observed for isolated Cr_3O clusters.[353] These results hint to an antiferromagnetic interaction between the three Cr^{3+} ions at low temperatures, mediated via superexchange through the μ_3-oxygen atom and to a lower extent by the carboxylate groups, each of which bridges two Cr^{3+} ions.[354,355] Table 7.2 shows the computed ZFS D-tensors for the cluster models at PBE/9s7p4d/IGLO-II level. The experimental value[310] for H_2O@Cr-MIL-101 is D = 0.01 cm^{-1}, agreeing well with the computed value.

Table 7.2.: Comparison of computed D-tensor components of the Cr-MIL-101 derivatives.

compound	$\mathbf{D_{11}(cm^{-1})}$	$\mathbf{D_{22}(cm^{-1})}$	$\mathbf{D_{33}(cm^{-1})}$	$\mathbf{D(cm^{-1})}$	**E/D**
H_2O@Cr-MIL-101	-0.0018	-0.0045	0.0063	0.0094	0.1443
2-AP@Cr-MIL-101	-0.0045	-0.0076	0.0121	0.0181	0.0856
3-AP@Cr-MIL-101	-0.0058	-0.0065	0.0123	0.0185	0.0198
DEA@Cr-MIL-101	-0.0016	-0.0101	0.0117	0.0176	0.2423

[a] The cluster-model computations were done at PBE40/IGLO-II/9s7p4d level (see Computational Details).

Figure 7.3 reproduced from ref. 310 shows the ^{13}C NMR spectra of H_2O@Cr-MIL-101, 2-AP@Cr-MIL-101, 3-AP@Cr-MIL-101, and DEA@Cr-MIL-101 (right column) and corresponding signals of the carbon atoms in the cluster models (left column). A wide range of shift values from -350 ppm to +468 ppm indicates hyperfine shifts.

For systems with isolated paramagnetic centers, quantum-chemical shift calculations could help in characterizing complicated NMR spectra and could provide further microscopic

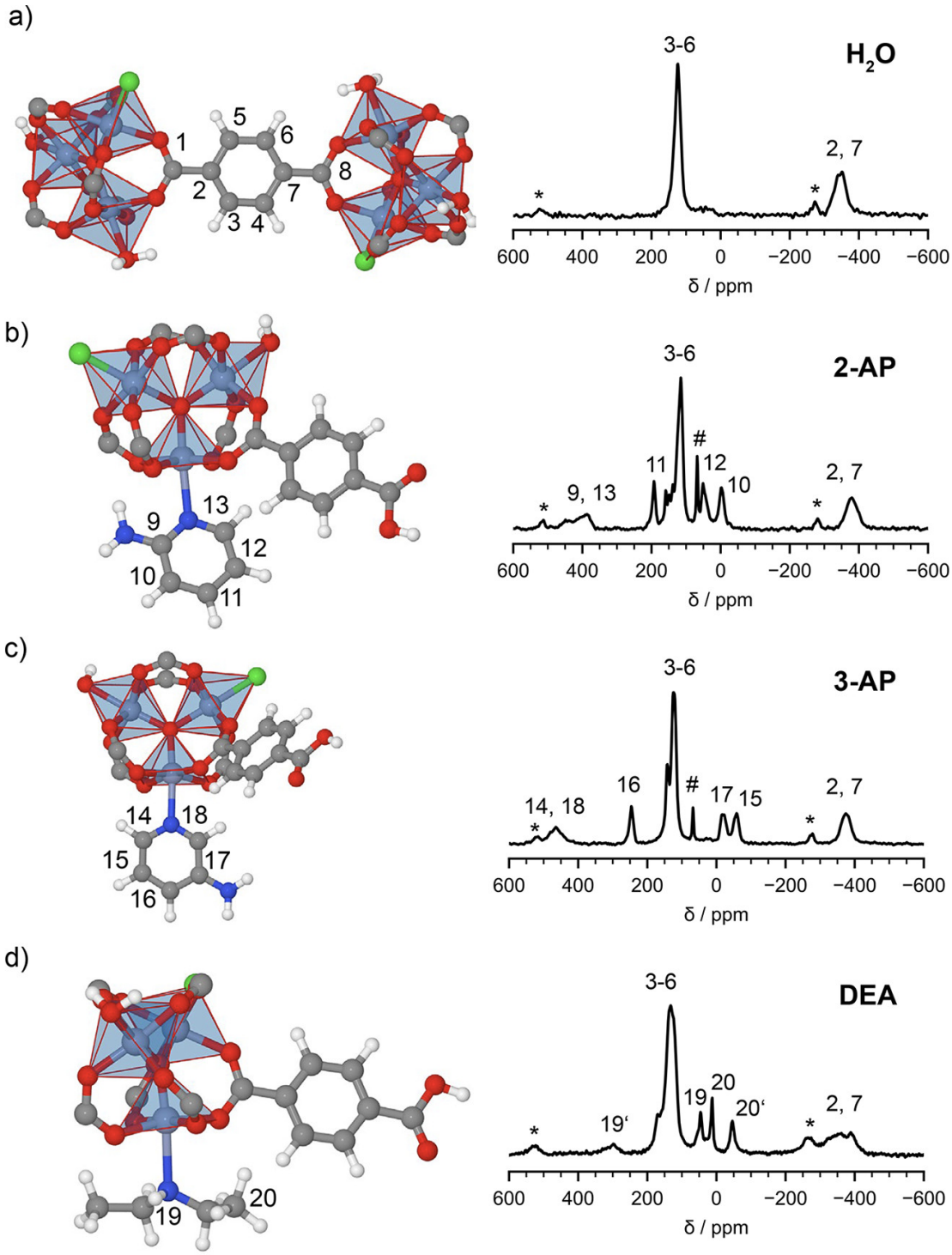

Figure 7.3.: DFT-optimized structural fragments (left column) and ^{13}C MAS NMR spectra (right column) of (a) H2O@Cr-MIL-101, (b) 2-AP@Cr-MIL-101, (c) 3-AP@Cr-MIL-101, and (d) DEA@Cr-MIL-101, including assignments. (reproduced from ref. 310)

Table 7.3.: Comparison of calculated[a] and observed isotropic ^{13}C chemical shifts.

	^{13}C calculated (ppm)				**^{13}C observed (ppm)**	
signal	δ_{orb}	δ_{FC}	δ_{PC}	δ_{total}	δ_{FC}	δ_{total}
X = H_2O						
1, 8	180.62	1502.72	0.04	1683.38	—	—
2, 7	140.41	-552.08	0.03	-411.65	-523	-350
3, 4, 5, 6	134.92	-6.44	0.03	128.51	0	130
X = 2-AP						
9	164.08	231.37	0.05	395.50	251	415
10	111.85	-145.45	0.00	-33.60	-116	-4
11	145.62	89.72	0.01	235.35	46	192
12	113.56	125.81	-0.03	-12.28	-65	49
13	156.47	288.08	-0.07	444.48	251	415
X = 3-AP						
14	143.92	313.56	-0.03	457.45	324	468
15	127.98	-254.68	-0.03	-126.92	-187	-59
16	125.38	164.77	0.02	290.17	121	246
17	146.84	-226.92	0.00	-80.09	-167	-20
18	141.84	316.82	0.06	458.71	324	468
X = DEA						
19′	51.77	193.81	-0.01	245.57	248	300
20′	18.00	-18.48	-0.01	0.49	-59	-46

[a] All cluster-model computations were done using IGLO-II/9s7p4d basis sets. Orbital shielding, HFC and g-tensor were computed with the PBE40 hybrid functional, ZFS contributions with the PBE functional (see Computational Details). Eq. 2.35 was used with a temperature of 325 K and a Weiss constant Θ = -102 K taken from experiment.[310] ^{13}C shifts were referenced to tetramethylsilane (TMS) computed at the same level (σ^{c}_{ref} = 189.23 ppm).

insight.[65,356–359] The applicability of eq. 2.35, that includes the Weiss constant to account for residual magnetic couplings in the Curie–Weiss temperature regime for spin-coupled clusters (see refs. 44 and 360 for related applications to solid-state calculations), still needs careful validation, which is possible with the available experimental NMR data. We thus applied the full formalism of eq. 2.35 at DFT level (see Chapter 2) to the cluster models displayed in Figure 7.2 and compared the results with the experimental assignment.[310] While we have computed all terms in eq. 2.35 (see Chapter 2), in the following discussion we will focus only on the FC contributions. The reason is that our computations confirm the expectation of small g- and ZFS-anisotropies (see g-tensor and ZFS data in Tables

Table 7.4.: Comparison of calculated[a] and observed isotropic ^{1}H chemical shifts.

	^{1}H calculated (ppm)				^{1}H observed (ppm)	
signal	δ_{orb}	δ_{FC}	δ_{PC}	δ_{total}	δ_{FC}	δ_{total}
X = H_2O						
1	8.22	-4.56	0.03	3.69	-5.22	3.00
X = 2-AP						
2	8.41	-41.91	0.00	-33.50	—	—
3	6.49	3.42	0.00	9.91	4.01	10.50
4	7.64	-14.37	0.00	-6.73	-11.64	-4.00
5	6.43	-5.29	0.00	1.14	-4.38	2.05
X = 3-AP						
6	8.35	-62.12	0.04	-53.73	-49.35	-41.00
7	7.21	7.24	-0.01	14.43	6.03	13.24
8	7.18	-24.86	0.00	-17.68	-19.83	-12.65
9	8.25	-61.43	-0.10	-53.28	-49.25	-41.00
X = DEA						
10	3.00	-19.21	0.00	-16.22	-18.50	-15.50
10′	2.45	-26.87	-0.01	-24.27	-29.45	-27.00
10″	3.54	-11.56	0.00	-8.01	—	—
11	1.54	0.55	0.00	2.09	—	—

[a] All cluster-model computations were done using IGLO-II/9s7p4d basis sets. Orbital shielding, HFC and g-tensor were computed with the PBE40 hybrid functional, ZFS contributions with the PBE functional (see Computational Details). Eq. 2.35 with a temperature of 325 K and a Weiss constant Θ = -102 K taken from experiment.[310] ^{13}C shifts were referenced to tetramethylsilane (TMS) at the same level (σ^{H}_{ref} = 31.68 ppm).

7.1 and 7.2, which are in perfect agreement with the measured EPR spectrum.[310] As a consequence, the PC contributions to the isotropic ^{13}C shifts (Table 7.3 and 7.4) are small. Comparison of computed and observed ^{13}C and ^{1}H shifts are provided in Tables 7.3 and 7.4 respectively. The orbital shifts reflect the chemical environment of the nucleus in question in a similar way as for diamagnetic analogues (Table 7.3 and 7.4) and will also not be discussed in details.

The total computed ^{13}C shifts given in Table 7.3 thus reflect particularly the FC contribution and therefore the delocalization of spin density over the ligand framework, as well as to some extent spin polarization effects. The sign and magnitude of the computed ^{13}C (Table 7.4) and ^{1}H (Table 7.4) hyperfine shifts agree well with experimental data, and the computed data were helpful in the signal assignment.[310] Notably, the reduction

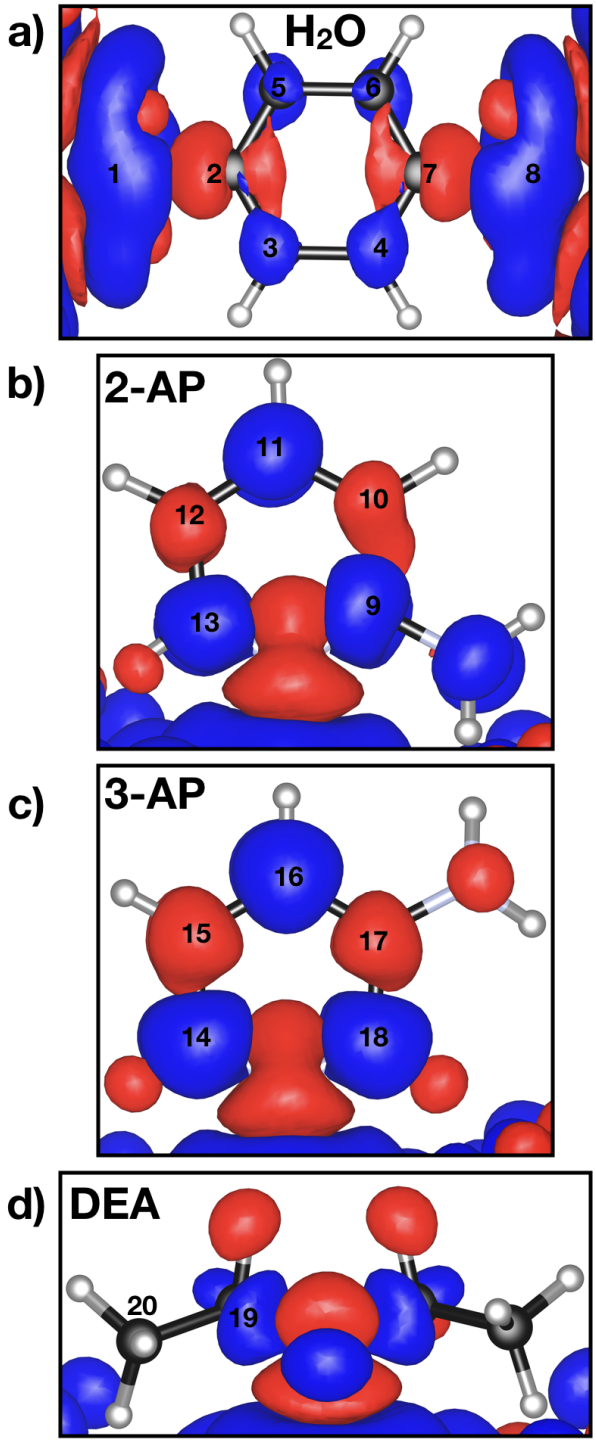

Figure 7.4.: Spin-density plots of a) H_2O@Cr-MIL-101, b) 2-AP@Cr- MIL-101, c) 3-AP@Cr-MIL-101, and d) DEA@Cr-MIL-101. The blue and red colors represent positive and negative spin-density isosurfaces (± 0.0001 au), respectively.

of hyperfine shifts due to the Curie–Weiss correction by a factor $T/(T - \Theta) = 0.761$ for H_2O@Cr-MIL-101 brings computed and experimental shifts into significantly better agreement. We used the experimentally determined reduction factor for all X@Cr-MIL-101 derivatives, since we do not expect large differences in their magnetic susceptibilities compared that of H_2O@Cr-MIL-101 (experimental data are not available).[310] This expectation is based on the magnetic properties for molecular compounds with isolated Cr_3O clusters with H_2O and pyridine-based ligands.[354,355,361] The corresponding exchange constants are similar to the one observed for H_2O@Cr-MIL-101 and vary only between 10 cm^{-1} and 13 cm^{-1}. Additionally, for a simulation temperature of 325 K, a change of Θ by 20 K only affects the hyperfine shifts by less than 5%. We note that the negative deviations of the g-tensor from the free-electron value only reduce the computed shifts additionally by about 1%.

The shifts may be rationalized to a great extent by the spin-density plots for the cluster models (Figure 7.4). For H_2O@Cr-MIL-101, ^{13}C nuclei 1–8 split into two sets: carbons 2 and 7 have negative spin densities, while the others exhibit positive spin densities. 2-AP@Cr-MIL-101 and 3-AP@Cr-MIL-101 exhibit additionally alternating positive and negative spin densities within the aminopyridine ring. For carbon atoms 9–18 we may distinguish negative spin densities for atoms 10, 12, 15, and 17, and positive spin densities for the remaining atoms. For DEA@Cr-MIL-101, carbons 19′ and 20′ for the DEA molecules attached to the metal-site have positive and negative spin densities, respectively, while the non-coordinated ones (carbons 19 and 20) exhibit the diamagnetic shifts only.

In all cases, the sign of the assigned hyperfine shifts (see Table 7.3) agrees perfectly with these spin-density analyses. We note that the extremely large positive spin densities at the carboxyl carbon atoms 1 and 8 in H_2O@Cr-MIL-101 (Figure 7.4a) give rise to very large positive computed shifts at around +1683 ppm. However, the large positive π-spin density also causes very short transverse (T_2) relaxation times that result in severe signal broadening.[310] As a consequence, the signal disappears in the noise level. In all cases, negative spin densities, and thus negative hyperfine shifts, are due to $\pi-\sigma$-spin polarization mechanisms. Positive spin-delocalization and negative spin-polarization contributions may also partly compensate. Carbon atoms of the linkers 3–6 in H_2O@Cr-MIL-101 are examples of such a cancellation (Figure 7.4a), giving rise to signals near the positions expected for such nuclei in diamagnetic samples (Table 7.3).[323]

7.4. Conclusions

This chapter shows an illustrative application of our newly developed computational methodology to the computation of pNMR shifts for clusters with multiple paramagnetic centers. Using such a procedure, ^{1}H and ^{13}C shifts have been computed for derivatives of the porous Cr-MIL-101 solid, which contain Cr_3O clusters with magnetically coupled metal centers within the metal-organic frameworks. The computed ^{13}C and ^{1}H shifts for all the Cr-MIL-101 derivatives are in good agreement with the NMR spectra obtained from experiment and characterized using various experimental approaches. The computed hyperfine shifts are dominated by the FC term, which in turn accurately reflects the computed spin-density distributions within the clusters. The Curie–Weiss scaling brings the computed shifts to within about $\pm 20\%$ of the experimental values, also allowing shifts to be predicted in cases where paramagnetic line broadening did not allow detection. This chapter demonstrates the potential of the modified cluster approach to obtain accurate chemical shifts also for exchange-coupled systems like the present MOFs. Our results show that both the experimental and computational approaches present equivalent assignment strategies and might be used independently or together in the future.

Chapter 8.

Including dynamical effects in the computation of paramagnetic NMR shifts for iron-silica-surface-grafted catalysts

8.1. Introduction

A significant number of reactions in the chemical industry uses silica-supported metal ions as active catalysts.[362–364] For example, since the 1960s, the Cr/SiO_2 Phillips catalyst is well known for manufacturing linear polyethylenes with different grades, and it accounts for more than one-third of the worldwide polyethylene supply.[365] The Ziegler-Natta catalyst is widely used in alkene polymerization and is used to produce a total volume of plastics, elastomers, and rubbers that exceeds one million tons per year worldwide.[366,367] Despite the extensive use of these systems, the structures of the active species in their silica-supported form are still elusive, and thus the effective catalytic mechanism is still not completely understood. The design and characterization of heterogeneous catalysts remain a crucial challenge for modern chemistry,[368–370] which limits the possibilities of further improvement in catalytic efficiency, and the extension of the range of applicability. Developments in this area rely on the detailed and accurate determination of the molecular structure of the catalytically active sites.[368,370] NMR experiments accompanied by quantum-chemical calculations could provide details of the local structure and chemical environment, which would be helpful for the subsequent development of structure-reactivity relationships to

facilitate the design and synthesis of catalysts with improved activity and selectivity for a particular reaction.

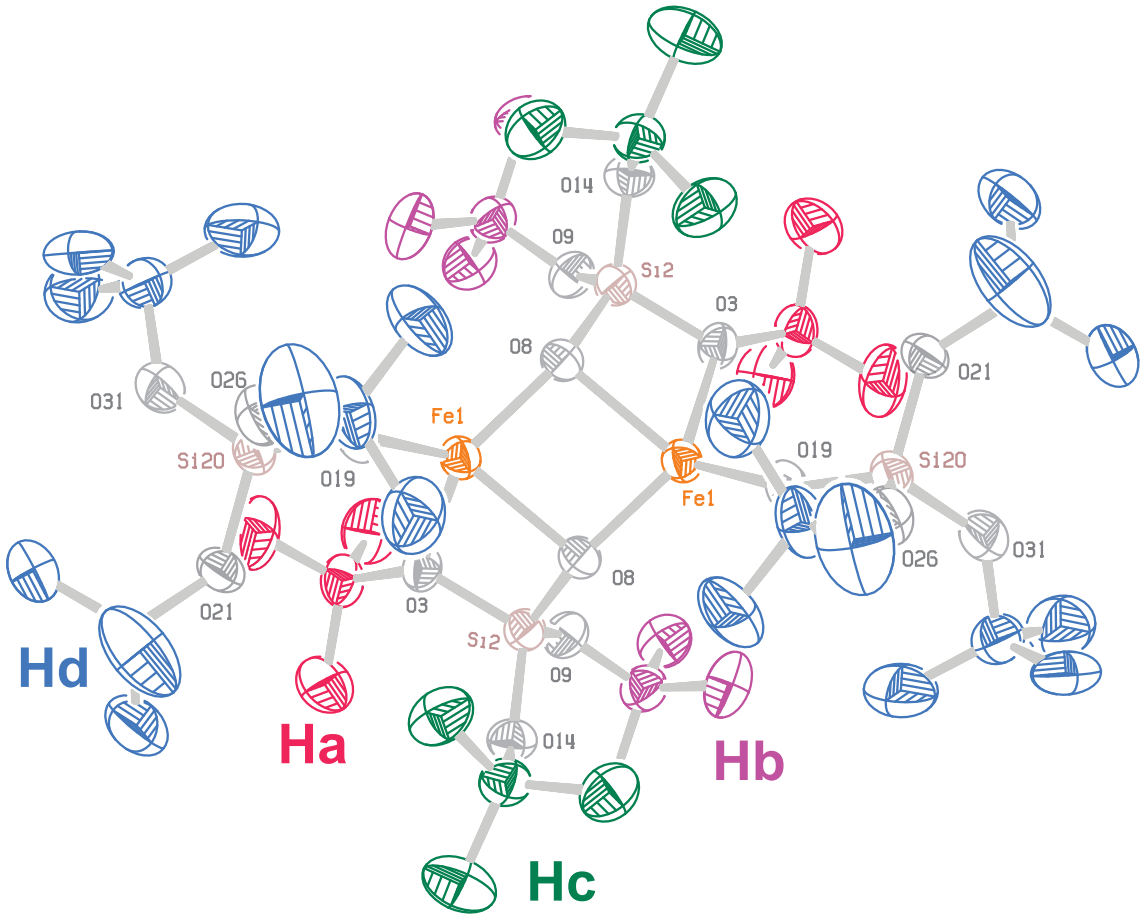

Figure 8.1.: XRD structure of dinuclear Fe(II) complex having 178 atoms. The four colors red, purple, green and blue represent four kinds of tertiary butyl groups. The position of 108 hydrogen atoms are not shown here.[371]

One promising class of materials for the catalysis of selective oxidation reactions comprises molecules that contain iron centers, supported on a silica surface. The underlying molecules form crystalline solids, which gives the possibility to obtain solid-state NMR data on those molecules in that state, even before grafting them on the silica surface providing insight about their intrinsic structure in advance. Here we will focus in particular on a dinuclear Fe(II) complex (see Figure 8.1 for the crystal structure obtained from experiments[371]), having 108 hydrogen atoms. This complex has been grafted on a silica surface (iron-silica-surface-grafted catalysts). Figure 8.2 shows the preliminary ^{1}H shifts obtained experimentally for the crystalline iron dimer complexes.[371] This work is an ongoing collaboration started within the pNMR ITN-Network with the groups of Guido Pintacuda

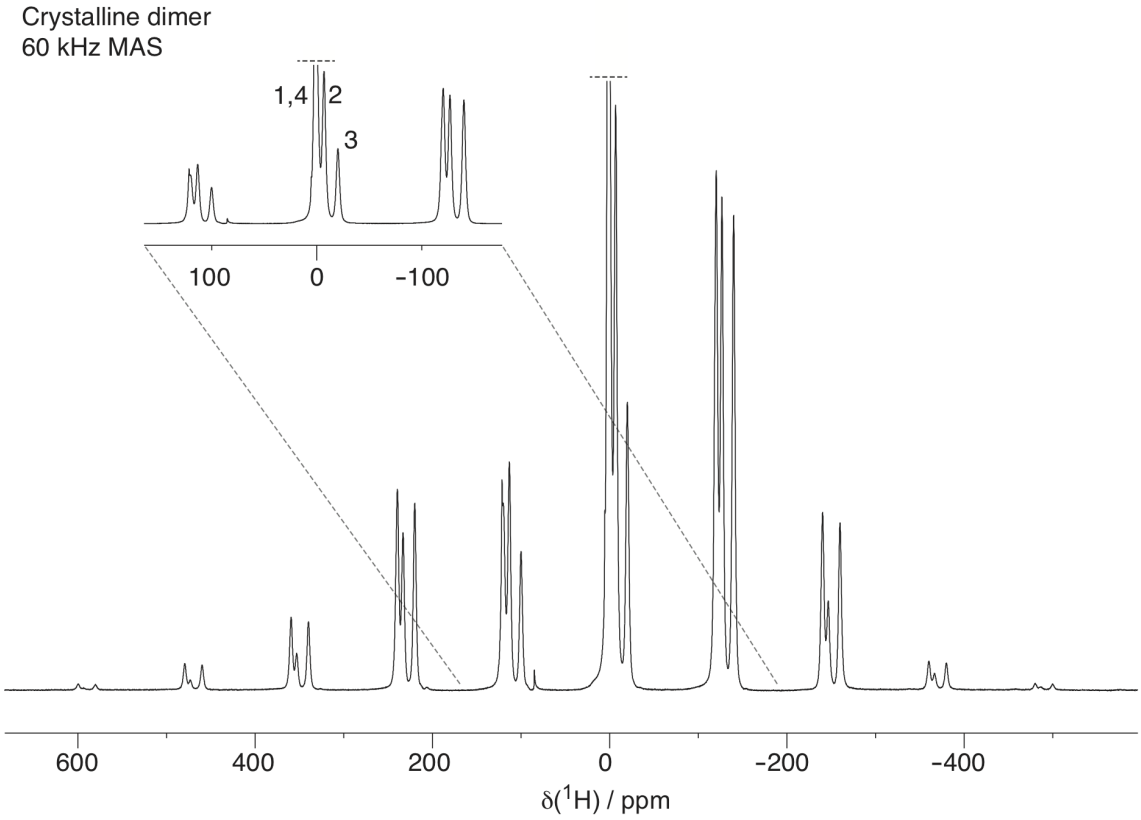

Figure 8.2.: ^{1}H MAS NMR spectra of the dinuclear iron complex (see Figure 8.1 for the crystal structure).[371]

(CNRS, ESN Lyon) and Christophe Copéret (ETH Zürich). It aims at a combined experimental-computational analysis of carbon and proton shifts.[371] Figure 8.2 shows the preliminary ^{1}H shifts obtained experimentally for the iron dimer in the solid state. The dynamics of the ligand groups result in averaged NMR signals for each group, showing only four distinct spectral lines, see Figure 8.2 and Figure 8.1). Figure 8.1 shows the crystal structure obtained from XRD. The cluster has four distinct chemical environments for hydrogen atoms (see Figure 8.2 and Figure 8.1) labeled with red (a), purple (b), green (c) and blue (d). Advanced experimental NMR techniques will be used to gain more insight into the dynamics of the individual groups. Meanwhile, we proceed with the computations of the paramagnetic NMR shifts to support available experimental data and confirm the assignment of the signal for each group. Theoretical simulations of such flexible paramagnetic systems are challenging since the paramagnetic chemical shifts in metal complexes are sensitive to structure and spin state of the molecule. Often elaborate dynamical sampling techniques are needed to achieve sufficient agreement with experiments.[87,372] To assess the importance of dynamical effects in the specific

dinuclear Fe(II) complex, we sampled several degrees of freedom using ab initio molecular dynamics (AIMD) methods. Paramagnetic chemical shifts were calculated for each of the conformers, applying the theory of paramagnetic NMR shielding developed by Vaara and coworkers,[57,123] which includes the effects of zero-field splitting and is hence appropriate for systems of arbitrary multiplicity (see eq. 2.26 in Chapter 2 for details). To include dynamical effects, in this study we performed AIMD simulations of the periodic infinite solid with CP2K to obtain a more realistic description.

8.2. Computational details

Starting from the XRD-structure of the Fe-dimer cluster (see Figure 8.1) having 178 atoms (2 Fe, 4 Si, 16 O, 48 C and 108 H atoms), the atomic positions of the hydrogen atoms were further optimized with BP86 functional,[190,203] including D3 corrections,[350] using def2-TZVP and def2-SVP basis-sets[242,373] for Fe and main group elements (Si, O, C, H), respectively, using the high-spin electronic configuration (S = 4) using the Turbomole program[71] (see Figure 8.3).

The unit-cell of the iron-dimer crystal contains cluster of four units with a total of 712 atoms. The XRD cell parameters are a = 14.0995 Å, b = 14.0995 Å, c = 34.5177 Å and $\alpha = \beta = \gamma = 90°$. The cell parameters were further optimized using the hybrid Gaussian and plane waves[135] (GPW) formalism together with the pseudopotential approximation, applying the PBE GGA exchange-correlation functional.[190] In the periodic calculations, D3 corrections were not included because they resulted in an unrealistic Fe-Fe distance and overall the unit cell shrank compared to the XRD data. Goedecker–Teter–Hutter (GTH) pseudopotentials[192] and double-ζ MOLOPT basis sets[193] were used for all elements. For the expansion of the charge density in plane waves, an energy cutoff of 500 Ry was used, and the convergence criterion over the maximum component of the wave function gradient was set to 1.0×10^{-7}. The optimized unit-cell vectors a = 14.540 Å, b = 14.540 Å and c = 35.546 Å and angles $\alpha = \beta = \gamma = 90°$ were further used for the molecular dynamics calculations.

AIMD calculations within the Born–Oppenheimer framework were performed to obtain the molecular dynamics trajectory. The electronic structure and nuclear forces were calculated using the PBE functional at DFT level of theory, applying the Gaussian augmented plane wave (GAPW) method,[133,191] as implemented in CP2K,[78] with periodic boundary conditions. Ahlrichs-pTZV Gaussian basis sets[133,373] were used for all atoms. We truncated

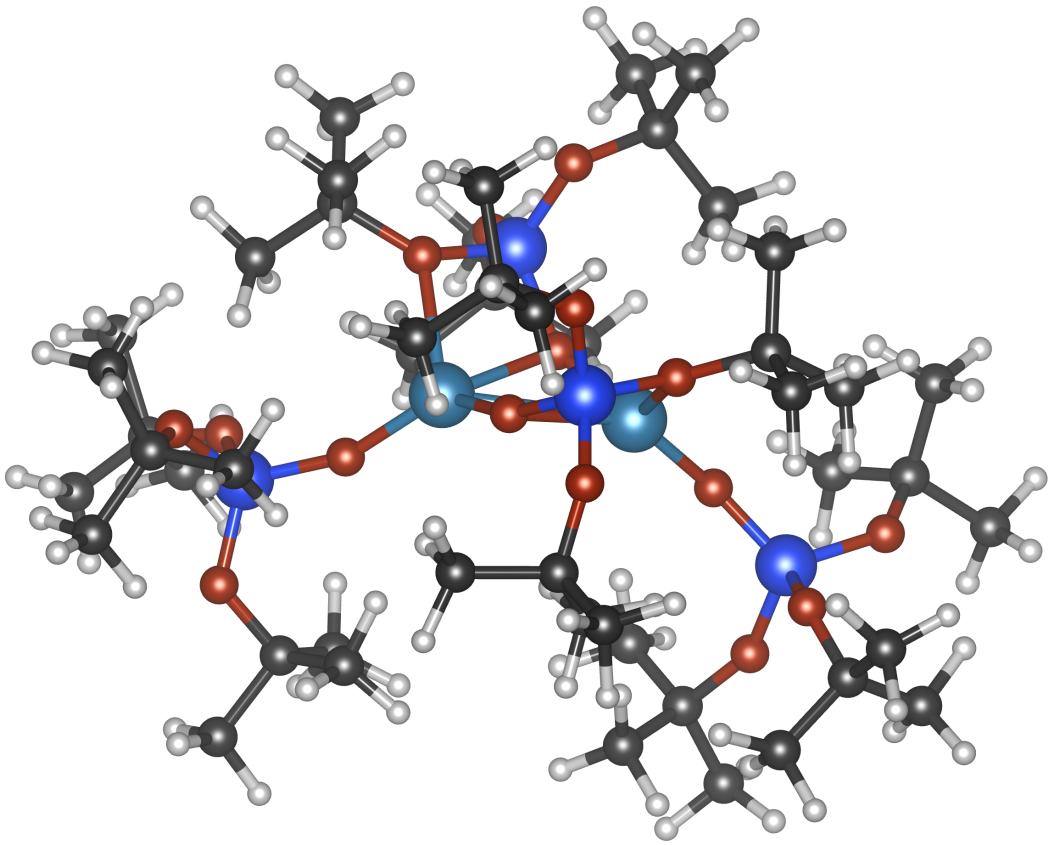

Figure 8.3.: Optimized position of hydrogen atoms, starting from the XRD structure of the dinuclear Fe(II) complex, keeping the core structure frozen.

the plane-wave basis set at 600 Ry. The Hamiltonian equations of motion were numerically integrated using the velocity Verlet algorithm and a time step of 0.5 fs. The canonical distribution of momenta at 290 K was enforced using a canonical stochastic rescaled velocity (CSVR) thermostat[374] at a time constant of 100 fs. From the AIMD trajectory, 400 Fe-dimer clusters snapshots (without periodic boundary conditions) were sampled for further computation of EPR/NMR parameters.

For the computation of HFCs, g-tensors, ZFS D-tensors and orbital shieldings, NMR-9s7p4d[202] and IGLO-II[209] basis sets were used for iron and the main-group elements, respectively. Within the cluster, a ferromagnetically coupled spin arrangement (S=4) has been used. The HFC, g-tensor, and ZFS tensor calculations were carried out with ORCA code[70] using the BP86 functional. ZFS tensors were computed using the Pederson–Khanna second-order perturbation approach[205] with van Wüllen's prefactors.[206] For both g-tensor and ZFS, the necessary spin–orbit matrix elements have been computed within the spin–orbit mean-field (SOMF) approximation[229] implemented in ORCA. Orbital shieldings

were obtained with the BP86 functional using Gaussian09 (for both open- and closed shell cases).[74] All pNMR computations have been performed keeping the temperature $T = 290$ K. Both ^{1}H and ^{13}C shifts were referenced to tetramethylsilane (TMS) at the same level (using BP86/IGLO-II structures, the values are $\sigma^{\mathrm{C}}_{\mathrm{ref}} = 181.87$ ppm and $\sigma^{\mathrm{H}}_{\mathrm{ref}} = 31.67$ ppm). The pNMR shifts were computed using eq. 2.26 (see Chapter 2 for detailed discussion about the theory).[123]

Molecules and clusters with large ligands and multiple paramagnetic centers show a wide range of chemical shifts. Larger ligands have more possibilities of vibrational and conformational motions, which changes the effective distance and interaction of the nucleus of interest to the paramagnetic center(s). Depending on the amplitude and direction of motion, the chemical shifts may vary considerably. In the case of the dimer, where two paramagnetic centers are close to each other, their effective interaction could influence the chemical shift of other nuclei. To account for the averaged dynamical effects, we have sampled structures from the AIMD trajectories. The generated trajectory is expected to include structures according to their statistical probability under the chosen thermodynamic conditions. In this regard, the MD simulation samples the free energy surface carrying the dynamics of the system of interest and reproduces its normal thermal fluctuations. These sampled structures cover a wide distribution of atomic positions. A trajectory of 21320 steps (10.660 ps) has been obtained keeping temperature at 290 K with a step size of 0.5 fs from the AIMD simulation at PBE/Ahlrichs-pTZV GAPW level. From this particular AIMD trajectory, four trajectories of the Fe-dimer cluster were obtained, as there are four clusters in the unit cell. Among the four individual cluster trajectories, 100 structures from each trajectory were sampled for the shift computations (see Figure D.1 in Appendix D).

8.3. Results and Discussion

The dinuclear Fe(II) cluster contains 178 atoms (2 Fe, 4 Si, 16 O, 48 C and 108 H) (see Figure 8.1 and 8.3). The core contains two iron atoms connected by oxo-bridges. Twelve tertiary butyl groups are present, connected to the iron atom by -O-Si-O- linkages. These groups may be divided into four types, designated by four colors (red, purple, green and blue) in Figure 8.2. The proton shifts acquired experimentally indicate only four distinct signals (see Figure 8.2), suggesting possible dynamics of the proton shifts of the tertiary butyl groups (partial or full rotation around O-C and C-C bonds).

First, we focused on the proton shifts of a statical model cluster. Only the positions of the hydrogen atoms were optimized (see Computational Details and Figure 8.3). Further, the computed, HFCs, g-tensors, ZFS D-tensors and orbital shieldings have been computed. Eq. 2.26 (see Chapter 2) has been used to assemble the ^{1}H pNMR shifts parameters at 290 K.

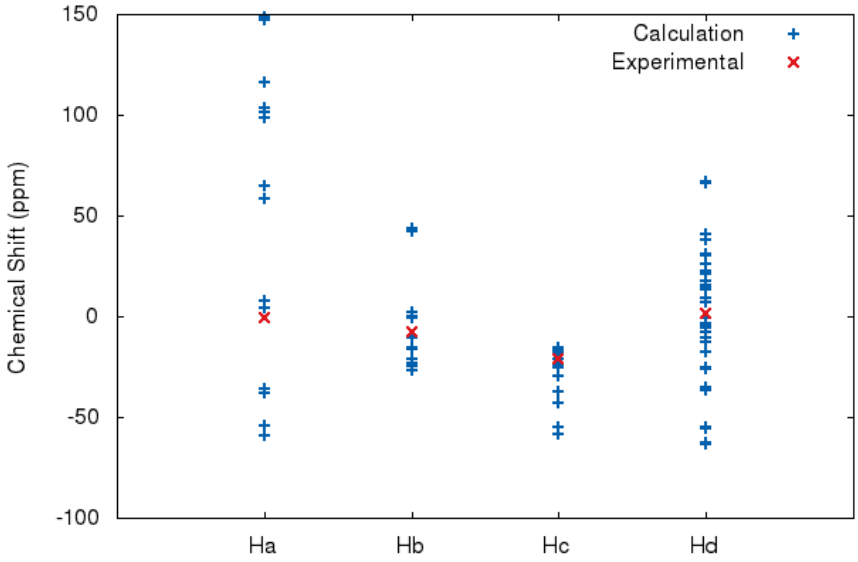

Figure 8.4.: Computed ^{1}H shift for Fe-dimer cluster, separated into the four distinct H_a, H_b, H_c and H_d groups.

Figure 8.4 shows the computed ^{1}H shifts (in blue) of 108 hydrogen atoms present in the cluster, divided into four groups, H_a, H_b, H_c and H_d having 18, 18, 18, and 54 atoms, respectively. The experimental isotropic ^{1}H shifts extracted from Figure 8.2 are shown as red points. The computed ^{1}H shifts of the four groups are spread over a wide range of approximately -65 ppm $< \delta_{H_a} <$ 150 ppm, -25 ppm $< \delta_{H_b} <$ 45 ppm, -60 ppm $< \delta_{H_c} <$ -15 ppm, and -70 ppm $< \delta_{H_d} <$ 65 ppm. Comparing the four groups in figure 8.1, H_a is comparatively closer to the iron atoms and thus exhibits the largest spread of shift values. The spin density is higher in the vicinity of the paramagnetic center and decreases with distance, which influences the Fermi-contact shifts strongly. Groups H_b and H_c are located in similar position and chemical environment, leading to similar chemical shifts. Group H_d, which contains 54 hydrogen atoms and is found over a larger volume in the cluster, also covers a broad ^{1}H shifts range which, however, is more homogeneously distributed due to the large number of hydrogen atoms contained.

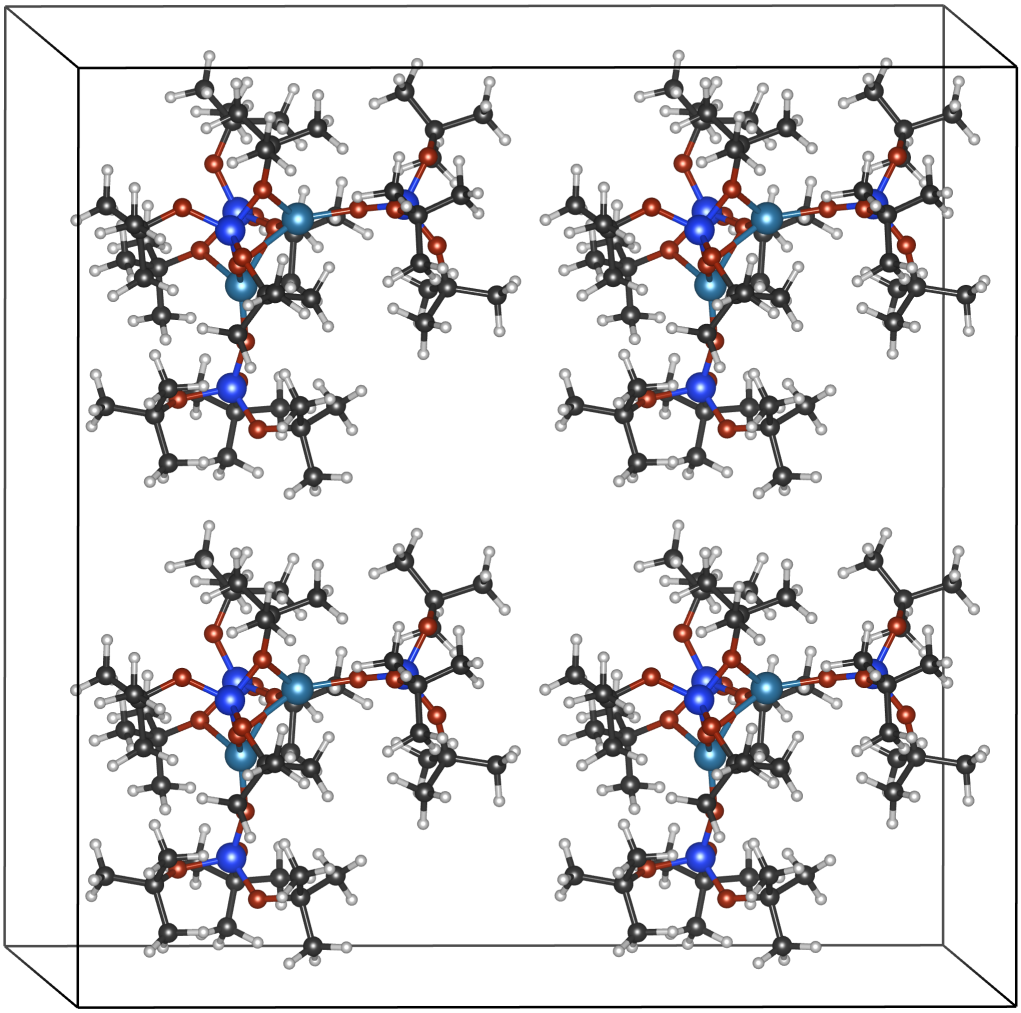

Figure 8.5.: The unit cell structure contains four dinuclear iron complexes having 712 atoms (see Figures 8.2 and 8.3 for the structure of dinuclear iron complex).

For all four groups, the computed ^{1}H shift range overlaps with the experimentally obtained shifts. Conformational dynamics of methyl groups around C-C bonds and that of tertiary butyl groups around C-O bonds clearly may be crucial here. Therefore, AIMD should be useful for sampling various configurations, providing averaged shifts.

Starting from the XRD data of the unit cell of the dinuclear iron complex (total 712 atoms, see Figure 8.5), the unit-cell parameters were optimized, and further used for optimizing the atomic positions (see Computational Details). This optimized structure has been used further as the initial configuration for the AIMD simulations.

The sampled structures were further used for computations of ^{1}H and ^{13}C shifts. HFCs, g-tensor, ZFS D-tensor and orbital shieldings were computed for all 400 sampled structures

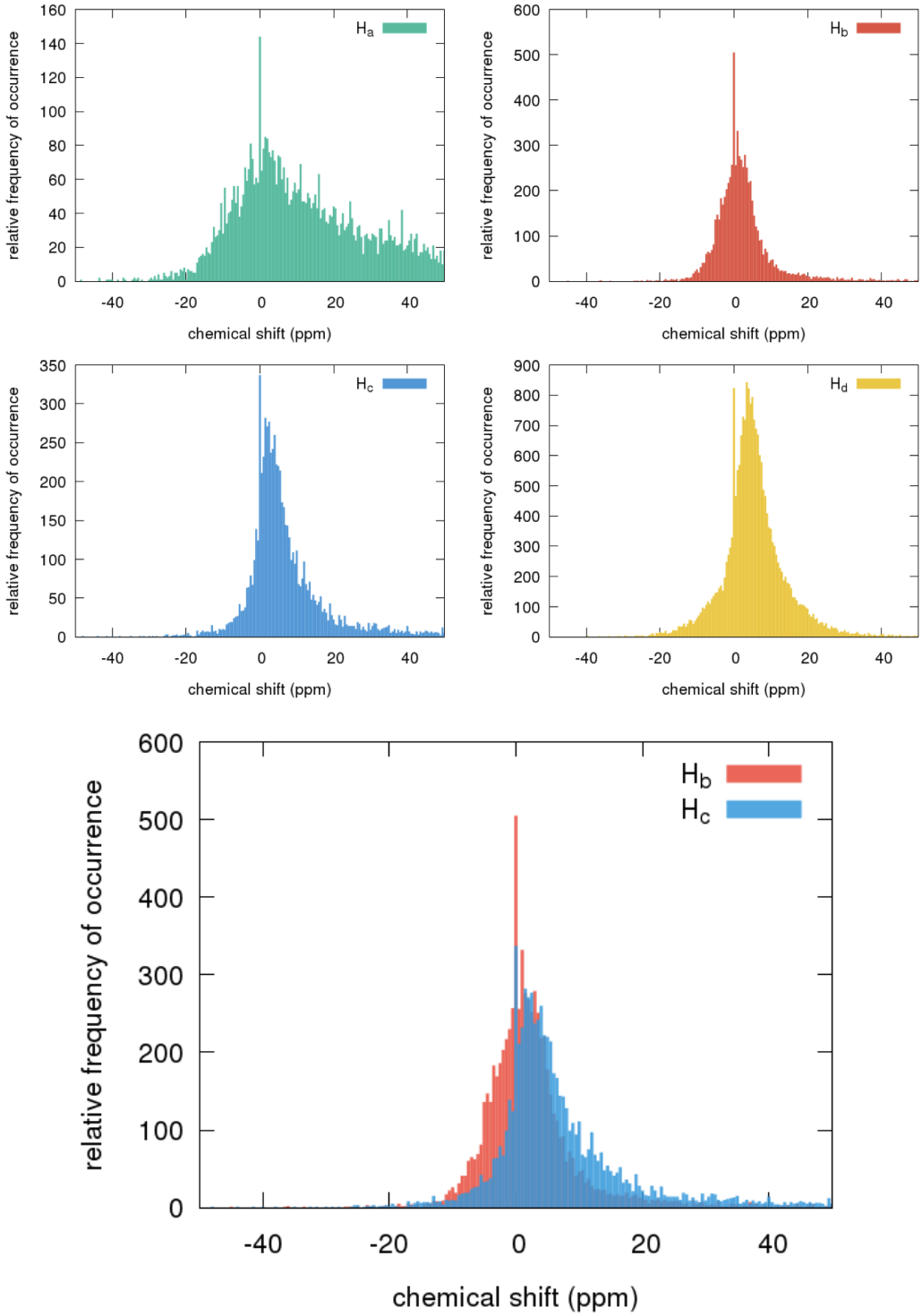

Figure 8.6.: Histogram for the occurrence of ^{1}H shifts (top four) for H_a (green), H_b (red), H_c (blue), and H_d (yellow). Bottom: comparison of distributions for H_b and H_c.

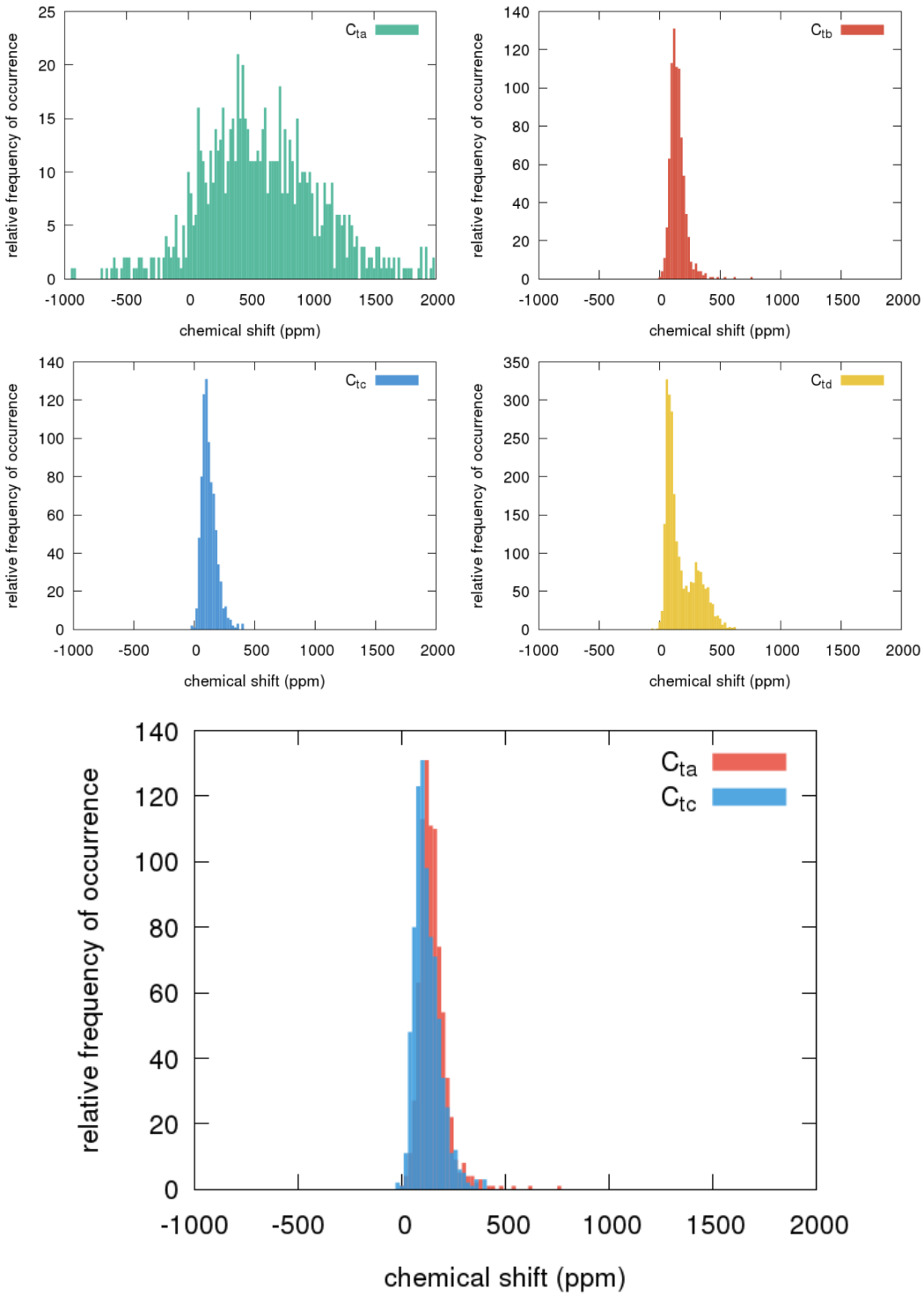

Figure 8.7.: Histograms for the occurrence of ^{13}C shifts (top four) for C_{t_a} (green), C_{t_b} (red), C_{t_c}, and C_{t_d} (yellow). Bottom: comparison of distributions for C_{t_b} and C_{t_c}.

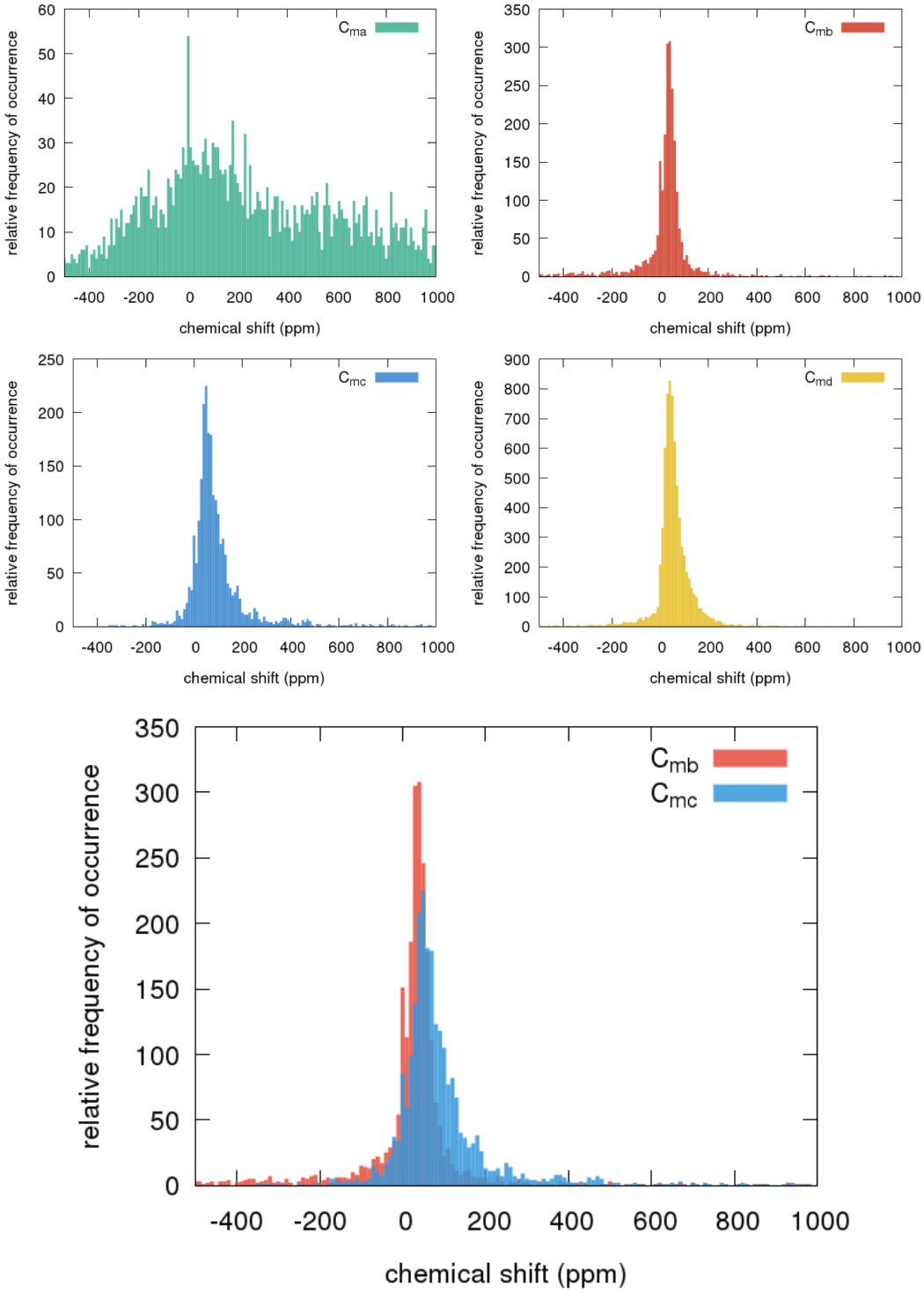

Figure 8.8.: Histogram for the occurrence of ^{13}C shifts (top four) for C_{m_a} (green), C_{m_b} (red), C_{m_c}, and C_{m_d} (yellow). Bottom: comparison of distributions for C_{t_b} and C_{t_c}.

(see Computational Details). Eq. 2.26 (see Chapter 2 for details) has been used for obtaining the ^{1}H and ^{13}C shifts at 290K. From these calculations we generated 43200 data points for ^{1}H shifts, which could be separated into the above mentioned four groups H_a, H_b, H_c and H_d. Similarly, for ^{13}C shifts 19200 data points were generated, which could be divided into eight groups, as each group (a, b, c, d) has two kinds of tertiary-butyl and methyl carbon atoms denoted C_{t_a}, C_{m_a}, C_{t_b}, C_{m_b}, C_{t_c}, C_{m_c}, C_{t_d}, C_{m_d}.

Figure 8.6 compares the distribution of occurring ^{1}H shifts for H_a (red), H_b (green), H_c (blue), and H_d (yellow). Similar to Figure 8.4 the ^{1}H shifts are distributed over a wide range. It is also clear from Figure 8.6 that eventhough the distribution range is overall broad, there is a small region in which the frequency of occurrence is high, particularly for H_b, H_c, and H_d. Further, when considering these small high-frequency occurrence regions for H_b and H_c (see Figure 8.6 bottom), the overall distribution of ^{1}H shifts for H_b is shifted to higher values compared to H_c.

Figure 8.7 and 8.8 shows the ^{13}C shift distributions for tertiary-butyl (C_t) and methyl (C_m) carbon atoms, respectively. The ^{13}C shifts for C_{t_a} (Figure 8.7, green) are distributed over a wide range (from almost -1000 ppm to 2000 ppm), reflecting the large variation of spin-density distributions. The ^{13}C shifts for C_{t_b} (red) and C_{t_c} (blue) are concentrated in a smaller shift range (see Figure 8.7). The ^{13}C shifts of C_{t_d} group (yellow) are distributed over a small range. The overall distribution of ^{13}C shifts for C_{t_b} is shifted to lower values compared to C_{t_b} (see Figure 8.7, bottom). The is opposite to the trend found for the ^{1}H shifts for H_b and H_c. Turning to the methyl groups, the ^{13}C shifts exhibit a comparably smaller range (approximately from -450 ppm to 1000 ppm), than the shifts of tertiary carbon atoms (approximately from -1000 ppm to 2000 ppm). Similar to the proton shifts of H_b and H_c, the overall distribution of ^{13}C shifts for C_{m_b} is shifted to higher values compare to C_{m_c}.

These are preliminary computational data within an ongoing collaboration. A more meaningful analysis will have to wait for completion of the experimental part of the work.

8.4. Conclusions

This work combines the AIMD simulations with NMR shift computations for paramagnetic materials. The AIMD trajectories of a dinuclear iron complex in the molecular solid confirm the conformational dynamics of the ligand groups. Computations of ^{1}H and ^{13}C

shifts were carried out for isolated complexes cut from the solid over 400 sampled structures obtained from the AIMD trajectories to account for the conformational distribution of the positions of hydrogen and carbon atoms and their corresponding paramagnetic shifts. This chapter shows a further development for the computation of pNMR shifts for materials with large ligands exhibiting conformational dynamics.

Chapter 9.

Summary and outlook

9.1. Conclusions

This thesis presents a novel protocol to compute and analyze NMR chemical shifts for extended paramagnetic solids such as battery materials, metal-organic frameworks, and molecular crystals having multiple paramagnetic centers. This approach combines EPR-NMR parameters (hyperfine, g-tensor, ZFS D-tensor and orbital shieldings) for the computation of NMR chemical shifts for paramagnetic materials/clusters accounting comprehensively for Fermi-contact (FC), pseudo-contact (PC), and orbital shifts.

An introductory overview of the previous developments in the computation of NMR shift for diamagnetic and paramagnetic molecules have been presented in Chapter 1. It provided the essential foundation for Chapter 2, where various chemical shift formalisms were discussed, beginning from the parameters involved in those equations. Further, a comparison between various pNMR formalisms provides the insight about their differences, limitations, relations, and advantages. Chapter 3 presents the summary of computational aspects used in the following chapters. Chapter 4 is very crucial, as this chapter established the foundation for reliable computation of pNMR shifts for solids within the doublet framework. Hyperfine, g-tensors and orbital shieldings for molecules computed in a supercell using CP2K compared to well-established quantum-chemical codes, various computational parameters have been evaluated for transition metal trifluorides solids and lithium vanadium phosphates. Using the doublet like formalism (excluding ZFS effects) contributing FC, PC and orbital shifts to the ^{7}Li pNMR shifts of the three lithium sites in $Li_3V_2(PO_4)_3$ were examined in detail. The influence of input structures obtained from XRD or optimized at DFT level and amount of exact-exchange admixture for hybrid functionals used for the hyperfine couplings in

determining the pNMR shifts has been clearly exposed. The current standard solid-state implementations of g-tensors are limited to isolated defect per unit cell, and computation of g-tensors for extended solids having more than one paramagnetic center needs suitable normalization. Further, an alternative to periodic solid-state g-tensors calculations by introducing an incremental cluster model approach that constructs the g-tensor of the simulation cell from individual molecular calculations was validated.

Chapter 5 presents the extended methodology including ZFS as a parameter for computation of pNMR shifts for solids. This approach combines periodic DFT computation of hyperfine and orbital-shielding tensors with an incremental cluster model for g- and ZFS D-tensors. The incremental cluster model allows the computation of g- and ZFS D-tensors by ab initio complete active space self-consistent field and N-electron valence-state perturbation theory methods. Application of this approach shows that the ^{7}Li shifts in the cathode material $LiCoPO_4$ are dominated by spin-orbit-induced PC contributions, in contrast to previous assumptions, changing interpretations of the shifts fundamentally in terms of covalence. PC contributions are smaller for the ^{7}Li shifts of other materials ($LiMnPO_4$, $LiFePO_4$, and $LiNiPO_4$), where FC and orbital shifts dominate. The ^{31}P shifts of all materials $LiMPO_4$ (M=Mn, Fe, Co, Ni) and MPO_4 (M=Fe, Co) finally are almost pure FC shifts. Nevertheless, substantial ZFS contributions can cause non-Curie temperature dependences for both ^{7}Li and ^{31}P shifts.

Chapter 6 presents an extended application of the above mentioned newly developed pNMR shift computations for much complex delithiated lithium vanadium phosphates. The experimental NMR spectra of $Li_{2.5}V_2(PO_4)_3$ have seven signals of lithium shifts from -9 ppm to 188 ppm. The computed range of pNMR shifts makes it possible to assign all the signals to their respective origin of lithium sites. This demonstrates a considerable step forward in the computations of pNMR shifts for solids and possible use of computations for the characterization of complicated NMR spectrums.

Chapter 7 goes even further and presents the applications of the protocols to the computation of pNMR shifts for clusters with multiple paramagnetic centers. Using such a procedure, ^{1}H and ^{13}C shifts have been computed for derivatives of the porous Cr-MIL-101 solid, which contain Cr_3O clusters with magnetically coupled metal centers within the metal-organic frameworks. A combination of experimental and computational methods were used to explore the competitive small-ligand binding to these MOFs.

In Chapter 8, the computations of pNMR shifts were combined with AIMD simulations to incorporate the conformational dynamics of the ligands in the dinuclear iron complex

having 178 atoms (108 hydrogen and 48 carbon atoms). From the AIMD trajectory, 400 structures were sampled and further used for computing ^{1}H and ^{13}C shifts for each structure. These results will be helpful for characterizing the experimental ^{1}H and ^{13}C NMR spectra.

9.2. Subsequent developments and applications

This thesis provides a strong foundation to compute magnetic properties such as hyperfine coupling constants, g-tensors, ZFS D-tensors, orbitals shieldings and paramagnetic NMR shifts for solids, molecular clusters and molecules having multiple paramagnetic metal centers. These insights could be used for further development of protocols and methods for accurate computation of EPR/NMR parameters for more complex materials. In Chapter 2, the further possibilities of computing magnetic coupling parameters such as spin-spin coupling and Weiss constant from first principles and how to include them directly into the pNMR shift equation have been discussed briefly. In principle, methods required for computations for Weiss constant for solids are already known, but further developed and standardized protocols for accurate computations are required to obtain predictive calculations. For metallic solids, the computation of so-called Knight shifts will need further elaboration.

The computational methods and protocols developed in this thesis performed remarkably well for both solids and clusters with multiple paramagnetic centers. The computed ^{7}Li shifts for various lithium transition-metal phosphates were in good agreement with the experimentally observed spectra. This opens the potential applications of these methodologies for more complex lithium-ion battery materials such as lithium manganese iron phosphate, lithium nickel manganese spinel, lithium nickel cobalt manganese oxide and lithium nickel cobalt aluminium oxide. Possible applications are not restricted to only lithium-ion batteries, but the methodology is equally applicable to other promising sodium and magnesium ion battery materials. In this work, only ^{1}H, ^{7}Li, ^{13}C and ^{31}P shifts have been computed, which could be easily extended to other NMR active nuclei like ^{15}N, ^{17}O, ^{23}Na, ^{25}Mg, ^{27}Al, ^{29}Si. Also, the application is not limited to battery materials but a more extensive range of molecular/ionic solids, MOFs and crystals.

In the course of the present developments, protocols for computation of g-tensor and ZFS D-tensors for solids using cluster models were optimized. This not only gave the possibility to use ab initio computation for such parameters but also gives the options to

directly complement experimental data. This will be useful for comparison of experimental and computed values and in some cases explaining the complicated experimental EPR spectra of solids. Similarly computed HFCs for solids could bring even more insight of EPR spectra. The computed ZFS D-tensors could complement neutron scattering studies for magneto-electric phenomena. Therefore the ability to compute magnetic resonance parameters for paramagnetic solids open a wide range of potential applications and will be helpful in also investigating other magnetic properties.

In the course of the present developments, protocols for computation of g-tensor and ZFS D-tensors for solids using cluster models were optimized. This not only gave the possibility to use ab initio computation for such parameters but also gives the options to directly complement experimental data. This will be useful for comparison of experimental and computed values and in some cases explaining the complicated experimental EPR spectra of solids. Similarly computed HFCs for solids could bring even more insight of EPR spectra. The computed ZFS D-tensors could complement neutron scattering studies for magneto-electric phenomena. Therefore the ability to compute magnetic resonance parameters for paramagnetic solids open a wide range of potential applications and will be helpful in investigating also other magnetic properties.

The combination of AIMD simulations with these developments enhances the possible applications to compute the temperature-dependence EPR/NMR parameters. This could also be useful to observe the pNMR shift dependencies during charging and discharging processes of lithium-ion batteries because of the lithium dynamics within the material.

Appendix A.

Unit cell structure and cluster models of lithium lactate and g-Tensor data for transition-metal trifluoride complexes*

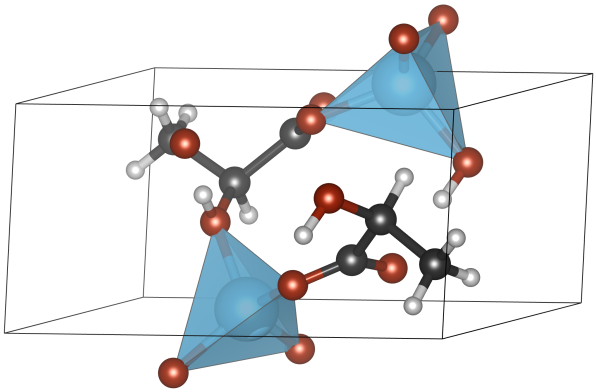

Figure A.1.: Single-crystal XRD structure of the lithium lactate unit cell containing two molecular formula units of $LiC_3H_5O_3$.

*Appendixes A *(pre-print)* with all tables and graphics therein are reproduced with permission from A. Mondal, M. W. Gaultois, A. J. Pell, M. Iannuzzi, C. P. Grey, J. Hutter and M. Kaupp, Large-scale computation of nuclear magnetic resonance shifts for paramagnetic solids using CP2K, *J. Chem. Theory Comput.*, **2018**, 14, 377–394. (https://doi.org/10.1021/acs.jctc.7b00991). Copyright 2018 American Chemical Society.

Table A.1.: Crystallographic data for lithium L-lactate ($LiC_3H_5O_3$).

Crystal data	
Formula	$Li^+C_3H_5O_3^-$
Formula mass	96.01
Space group	Monoclinic, $P2_1$
a (Å)	4.5412(4)
b (Å)	4.8838(4)
c (Å)	10.1982(10)
β (°)	98.226(7)
V (Å^3)	223.85(3)
T (K)	180
Z	2
ρ_{calcd} (g cm^{-3})	1.5588
Crystal dimensions (mm)	0.30 × 0.08 × 0.02
Data collection and refinement	
Radiation type	Cu $K\alpha$
μ(Cu $K\alpha$) (mm^{-1})	1.06
Scan method	ω and φ scans
θ range (°)	4.4−67.0
$(\sin\theta/\lambda)_{\mathrm{max}}$ (Å^{-1})	0.597
Transmission factors	0.514, 0.753
R_{int}	0.053
No. of reflections collected	2423
No. of unique reflections, including $F_o^2 < 0$	769
No. of unique reflections, with $F_o^2 > 2\sigma(F_o^2)$	686
No. of variables	69
No. of restraints	1
$R(F)$ for $F_o^2 > 2\sigma(F_o^2)$[a]	0044
$R_w(F_o^2)$[b]	0.121
Goodness of fit	1.090
$(\Delta\rho)_{\mathrm{max}}$, $(\Delta\rho)_{\mathrm{min}}$ (e Å^{-3})	0.17, −0.20

[a] $R(F) = \frac{\sum||F_o|-|F_c||}{\sum|F_o|}$.

[b] $R_w(F_o^2) = \sqrt{\frac{\sum[w(F_o^2-F_c^2)^2]}{\sum wF_o^4}}$; $w^{-1} = [\sigma^2(F_o^2) + (Ap)^2 + Bp]$ where $p = \frac{\max(F_o^2)+2F_c^2}{3}$.

Table A.2.: Atomic coordinates and equivalent isotropic displacement parameters for lithium L-lactate ($LiC_3H_5O_3$). H atoms treated by a mixture of independent and constrained refinement.

Atom	Wyckoff position	x	y	z	U_{eq} (Å^2)[a]
Li1	2*a* (*x*, *y*, *z*)	1.0453(16)	0.9427(15)	0.5882(7)	0.0241(15)
O1	2*a* (*x*, *y*, *z*)	0.8069(6)	0.6784(5)	0.6656(3)	0.0277(8)
O2	2*a* (*x*, *y*, *z*)	0.8202(6)	0.2753(6)	0.5667(3)	0.0241(7)
O3	2*a* (*x*, *y*, *z*)	0.4041(6)	0.0599(7)	0.7065(3)	0.0268(7)
H3	2*a* (*x*, *y*, *z*)	0.544(16)	-0.076(14)	0.695(7)	0.06(2)
C1	2*a* (*x*, *y*, *z*)	0.7330(8)	0.4300(8)	0.6499(4)	0.0205(9)
C2	2*a* (*x*, *y*, *z*)	0.5355(9)	0.3162(9)	0.7471(4)	0.0241(9)
H2A	2*a* (*x*, *y*, *z*)	0.3721	0.4507	0.7535	0.029
C3	2*a* (*x*, *y*, *z*)	0.7232(13)	0.2922(13)	0.8834(4)	0.0447(13)
H3A	2*a* (*x*, *y*, *z*)	0.5976	0.2300	0.9481	0.067
H3B	2*a* (*x*, *y*, *z*)	0.8086	0.4714	0.9103	0.067
H3C	2*a* (*x*, *y*, *z*)	0.8839	0.1600	0.8793	0.067

[a] U_{eq} is defined as one-third of the trace of the orthogonalized U_{ij} tensor.

Table A.3.: Anisotropic displacement parameters for lithium L-lactate ($LiC_3H_5O_3$).

Atom	U_{11} (Å^2)	U_{22} (Å^2)	U_{33} (Å^2)	U_{23} (Å^2)	U_{13} (Å^2)	U_{12} (Å^2)
Li1	0.027(3)	0.014(3)	0.032(4)	−0.001(3)	0.007(3)	0.001(3)
O1	0.0250(15)	0.0192(17)	0.0394(18)	0.0002(12)	0.0068(12)	−0.0019(12)
O2	0.0257(15)	0.0181(16)	0.0293(15)	0.0014(14)	0.0061(11)	0.0024(12)
O3	0.0223(14)	0.0179(15)	0.0406(17)	−0.0035(14)	0.0061(13)	−0.0031(12)
C1	0.0144(17)	0.014(2)	0.032(2)	0.0017(17)	−0.0006(15)	0.0014(16)
C2	0.023(2)	0.019(2)	0.031(2)	−0.0031(18)	0.0069(16)	−0.0020(17)
C3	0.056(3)	0.051(3)	0.028(2)	−0.001(3)	0.007(2)	−0.018(3)

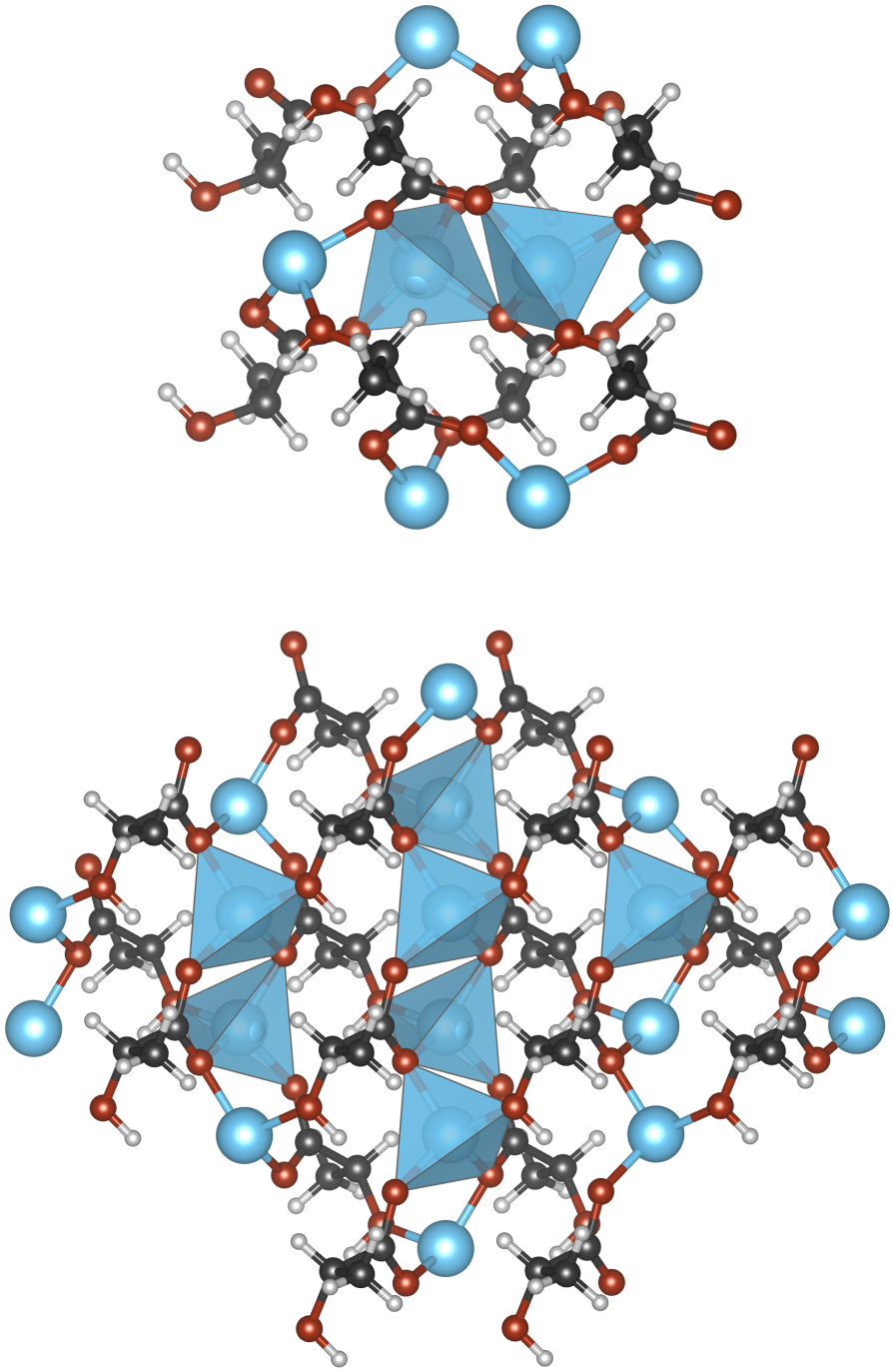

Figure A.2.: Cluster models of solid lithium lactate with a) 8 molecular units and b) 18 molecular units of $LiC_3H_5O_3$, cut from a $2 \times 4 \times 2$ super-cell of the XRD structure (see Computational Details in Chapter 4).

Table A.4.: Validation of eq. 4.13 (Chapter 4) for g-tensors of multiple spin sites per unit cell[a] for up to four MF_3 complexes (M= Ti, V, Cr, Mn, Fe) in a large super-cell

molecule	**n**[b]	$\mathbf{g_{11}}$	$\mathbf{g_{22}}$	$\mathbf{g_{33}}$	$\mathbf{g_{iso}}$
$^{2}TiF_3$	1	1.957	1.957	2.001	1.972
	2	1.957	1.957	2.001	1.972
	3	1.957	1.957	2.001	1.972
	4	1.957	1.957	2.001	1.972
$^{3}VF_3$	1	1.907	1.978	1.884	1.923
	2	1.907	1.978	1.884	1.923
	3	1.907	1.978	1.884	1.923
	4	1.907	1.978	1.884	1.923
$^{4}CrF_3$	1	1.989	1.955	1.955	1.966
	2	1.989	1.955	1.955	1.966
	3	1.989	1.955	1.955	1.966
	4	1.989	1.955	1.955	1.966
$^{5}MnF_3$	1	2.002	1.994	1.950	1.982
	2	2.002	1.994	1.950	1.982
	3	2.002	1.994	1.950	1.982
	4	2.002	1.994	1.950	1.982
$^{6}FeF_3$	1	2.048	2.048	2.052	2.049
	2	2.048	2.048	2.052	2.049
	3	2.048	2.048	2.052	2.049
	4	2.048	2.048	2.052	2.049

[a] Eq. 4.13 (Chapter 4) has been used for calculating the normalized g-tensor, at PBE/def2-TZVP/IGLO-II level, in a super-cell of dimension 40 Å×40 Å×40 Å.
[b] Number of paramagnetic spin centers present in the super-cell.

Table A.5.: Comparison of different codes, gauges, and SO operators for g-tensor calculations[a] on molecular MF_3 (M=Ti, Cr, Mn, Fe)[b]

molecule	**package**	**gauge**	**SO-operator**	$\mathbf{g_{11}}$	$\mathbf{g_{22}}$	$\mathbf{g_{33}}$	$\mathbf{g_{iso}}$
	CP2K	IGAIM	$V_{eff,PM}$	1.953	1.953	2.000	1.969
	MAG	COMMON	FULL	1.981	1.981	2.002	1.988
			AMFI	1.976	1.976	2.002	1.984
$^2TiF_3$			KOSEKI	1.937	1.937	2.001	1.958
		GIAO	FULL	1.967	1.969	2.001	1.979
			AMFI	1.960	1.960	2.001	1.974
			KOSEKI	1.901	1.901	2.000	1.934
	ORCA	COMMON	SOMF	1.966	1.966	2.001	1.977
	CP2K	IGAIM	$V_{eff,PM}$	1.952	1.952	1.988	1.964
	MAG	COMMON	FULL	1.994	1.994	2.001	1.997
			AMFI	1.992	1.992	2.000	1.995
$^4CrF_3$			KOSEKI	1.981	1.981	2.000	1.986
		GIAO	FULL	1.961	1.961	1.994	1.972
			AMFI	1.952	1.952	1.992	1.965
			KOSEKI	1.900	1.900	1.985	1.928
	ORCA	COMMON	SOMF	1.989	1.989	1.999	1.992
	CP2K	IGAIM	$V_{eff,PM}$	1.945	1.994	2.002	1.980
	MAG	COMMON	FULL	1.997	2.002	2.004	2.001
			AMFI	1.995	2.002	2.003	2.000
$^5MnF_3$			KOSEKI	1.984	2.000	2.003	1.996
		GIAO	FULL	1.947	1.993	2.001	1.980
			AMFI	1.922	1.990	1.998	1.970
			KOSEKI	1.818	1.977	1.989	1.928
	ORCA	COMMON	SOMF	1.992	2.001	2.002	1.998
	CP2K	IGAIM	$V_{eff,PM}$	2.050	2.050	2.054	2.051
	MAG	COMMON	FULL	2.010	2.010	2.011	2.011
			AMFI	2.010	2.010	2.012	2.011
$^6FeF_3$			KOSEKI	2.016	2.016	2.017	2.016
		GIAO	FULL	2.038	2.038	2.047	2.041
			AMFI	2.041	2.041	2.051	2.044
			KOSEKI	2.064	2.064	2.079	2.069
	ORCA	COMMON	SOMF	2.011	2.011	2.011	2.011

[a] PBE/def2-TZVP/IGLO-II level. See Chapter 4 for the abbreviations for SO operators and choices of gauge origin. Super-cell calculations for CP2K, see Chapter 4.
[b] The comparison for VF_3 is given in Chapter 4.

Appendix B.

Numerical values of ^{7}Li shifts computed for $Li_3V_2(PO_4)_3$*

* Appendixes B *(pre-print)* with all tables and graphics therein are reproduced with permission from A. Mondal, M. W. Gaultois, A. J. Pell, M. Iannuzzi, C. P. Grey, J. Hutter and M. Kaupp, Large-scale computation of nuclear magnetic resonance shifts for paramagnetic solids using CP2K, *J. Chem. Theory Comput.*, **2018**, 14, 377–394. (https://doi.org/10.1021/acs.jctc.7b00991). Copyright 2018 American Chemical Society.

Table B.1.: Comparison of computed[a] HFC tensors using both PBE and PBE-based global hybrids with varying EXX admixture between 5% (PBE5) and 40% (PBE40) for lithium sites of $Li_3V_2(PO_4)_3$ using the XRD structure

Atom	**Functional**	$\mathbf{A_{FC}}$ (MHz)	$\mathbf{A_{dip}}$ (MHz)			**Anisotropy**[b] (MHz)	**Asymmetry**[c] (MHz)
			A_{11}	A_{22}	A_{33}		
Li_a	PBE	0.93	-1.77	0.28	1.49	-2.66	0.68
	PBE5	0.89	-1.76	0.26	1.50	-2.64	0.71
	PBE10	0.83	-1.76	0.26	1.51	-2.64	0.71
	PBE15	0.79	-1.76	0.26	1.51	-2.65	0.71
	PBE20	0.75	-1.77	0.26	1.51	-2.65	0.70
	PBE25	0.71	-1.77	0.26	1.51	-2.65	0.70
	PBE30	0.68	-1.77	0.26	1.51	-2.66	0.70
	PBE35	0.65	-1.77	0.27	1.51	-2.66	0.70
	PBE40	0.62	-1.77	0.27	1.50	-2.66	0.70
Li_b	PBE	0.40	-1.58	-0.24	1.82	2.73	0.74
	PBE5	0.22	-1.56	-0.22	1.79	2.68	0.75
	PBE10	0.17	-1.56	-0.22	1.78	2.67	0.75
	PBE15	0.13	-1.56	-0.23	1.78	2.67	0.75
	PBE20	0.09	-1.55	-0.23	1.78	2.67	0.74
	PBE25	0.06	-1.55	-0.23	1.78	2.68	0.74
	PBE30	0.03	-1.55	-0.23	1.78	2.68	0.74
	PBE35	-0.00	-1.55	-0.23	1.79	2.68	0.74
	PBE40	-0.03	-1.55	-0.24	1.79	2.68	0.74
Li_c	PBE	0.36	-1.66	-1.23	2.89	4.34	0.15
	PBE5	0.46	-1.66	-1.24	2.90	4.36	0.14
	PBE10	0.44	-1.66	-1.24	2.91	4.36	0.14
	PBE15	0.40	-1.67	-1.25	2.91	4.37	0.14
	PBE20	0.36	-1.67	-1.24	2.91	4.37	0.15
	PBE25	0.32	-1.67	-1.24	2.91	4.37	0.15
	PBE30	0.29	-1.67	-1.24	2.91	4.37	0.15
	PBE35	0.25	-1.67	-1.24	2.91	4.37	0.15
	PBE40	0.22	-1.67	-1.24	2.91	4.37	0.15

[a] All computations were done for a $2 \times 2 \times 1$ super-cell using IGLO-II/8s7p4d basis sets (see Computational Details in Chapter 4).

[b] Anisotropy (Δ) = A_{zz} - $\frac{1}{2}(A_{xx} + A_{yy})$; the components are ordered as $| A_{zz} - A_{iso} | \geq | A_{yy} - A_{iso} | \geq | A_{xx} - A_{iso} |$, $A_{iso} = \frac{1}{3}(A_{11} + A_{22} + A_{33})$ and $A_{11} \leq A_{22} \leq A_{33}$.

[c] Asymmetry (η) = $\frac{A_{xx}-A_{yy}}{A_{zz}-A_{iso}}$.

Table B.2.: Comparison of computed[a] HFC tensors using both PBE and PBE-based global hybrids with varying EXX admixture between 5% (PBE5) and 40% (PBE40) for lithium sites of $Li_3V_2(PO_4)_3$ using the optimized structure

Atom	**Functional**	$\mathbf{A_{FC}}$ (MHz)	$\mathbf{A_{dip}}$ (MHz)			**Anisotropy**[b] (MHz)	**Asymmetry**[c] (MHz)
			A_{11}	A_{22}	A_{33}		
Li_a	PBE	0.80	-1.73	0.22	1.52	-2.60	0.75
	PBE5	0.78	-1.73	0.21	1.52	-2.60	0.76
	PBE10	0.74	-1.74	0.21	1.53	-2.61	0.76
	PBE15	0.71	-1.74	0.22	1.52	-2.61	0.75
	PBE20	0.67	-1.74	0.22	1.52	-2.61	0.75
	PBE25	0.64	-1.74	0.22	1.52	-2.61	0.75
	PBE30	0.60	-1.74	0.22	1.52	-2.62	0.74
	PBE35	0.58	-1.75	0.22	1.52	-2.62	0.74
	PBE40	0.55	-1.75	0.23	1.52	-2.62	0.74
Li_b	PBE	0.33	-1.59	-0.31	1.90	2.85	0.68
	PBE5	0.19	-1.57	-0.31	1.88	2.82	0.67
	PBE10	0.14	-1.57	-0.31	1.88	2.82	0.67
	PBE15	0.09	-1.56	-0.31	1.88	2.81	0.67
	PBE20	0.06	-1.56	-0.32	1.88	2.81	0.66
	PBE25	0.03	-1.56	-0.32	1.88	2.81	0.66
	PBE30	-0.01	-1.56	-0.32	1.88	2.82	0.66
	PBE35	-0.03	-1.56	-0.32	1.88	2.82	0.66
	PBE40	-0.05	-1.55	-0.33	1.88	2.82	0.65
Li_c	PBE	0.53	-1.68	-1.30	2.98	4.47	0.13
	PBE5	0.57	-1.68	-1.31	2.99	4.48	0.13
	PBE10	0.53	-1.68	-1.31	2.99	4.49	0.13
	PBE15	0.49	-1.69	-1.31	2.99	4.49	0.13
	PBE20	0.44	-1.69	-1.31	2.99	4.49	0.13
	PBE25	0.40	-1.69	-1.31	3.00	4.49	0.13
	PBE30	0.36	-1.69	-1.31	3.00	4.49	0.13
	PBE35	0.32	-1.69	-1.31	3.00	4.49	0.13
	PBE40	0.29	-1.69	-1.31	3.00	4.49	0.13

[a] All computations were done for a $2 \times 2 \times 1$ super-cell using IGLO-II/8s7p4d basis sets (see Computational Details in Chapter 4).

[b] Anisotropy (Δ) = A_{zz} - $\frac{1}{2}(A_{xx} + A_{yy})$; the components are ordered as $| A_{zz} - A_{iso} | \geq | A_{yy} - A_{iso} | \geq | A_{xx} - A_{iso} |$, $A_{iso} = \frac{1}{3}(A_{11} + A_{22} + A_{33})$ and $A_{11} \leq A_{22} \leq A_{33}$.

[c] Asymmetry (η) = $\frac{A_{xx} - A_{yy}}{A_{zz} - A_{iso}}$.

Table B.3.: Orbital shift tensors[a] for different lithium sites in $Li_3V_2(PO_4)_3$ using both XRD and optimized structures

Structure	**Atom**	**Orbital shift (ppm)**	**Anisotropic tensor**			**Anisotropy[b] (ppm)**	**Asymmetry[c]**
			δ_{11}^{orb} (ppm)	δ_{22}^{orb} (ppm)	δ_{33}^{orb} (ppm)		
XRD	Li_a	-6.38	29.92	-4.21	-25.71	44.88	0.72
	Li_b	-2.79	23.11	11.84	-34.95	-52.43	0.32
	Li_c	-3.48	36.16	-9.65	-26.51	54.24	0.47
OPT	Li_a	-6.81	30.88	-7.73	-23.15	46.32	0.50
	Li_b	-0.97	11.89	6.11	-18.00	-27.00	0.32
	Li_c	5.86	16.69	2.90	-19.59	-29.39	0.70

[a] Computations on $1 \times 1 \times 1$ cells at PBE/Ahlrichs-VTZ/IGLO-II level (see Computational Details in Chapter 4).

[b] Anisotropy $(\Delta) = \delta_{zz}$ - $\frac{1}{2}(\delta_{xx}+\delta_{yy})$; the components are ordered as $| \delta_{zz}-\delta_{iso} | \geq | \delta_{yy}-\delta_{iso} | \geq | \delta_{xx} - \delta_{iso} |$, $\delta_{iso} = \frac{1}{3}(\delta_{11} + \delta_{22} + \delta_{33})$ and $\delta_{11} \leq \delta_{22} \leq \delta_{33}$.

[c] Asymmetry $(\eta) = \frac{\delta_{xx}-\delta_{yy}}{\delta_{zz}-\delta_{iso}}$.

Table B.4.: Computed[a] ^{7}Li chemical shifts for three distinct lithium sites Li_a, Li_b and Li_c of $Li_3V_2(PO_4)_3$ using the XRD structure, depending on the functional used for the hyperfine calculations.[b] g-Tensor[c] (PBC, Eq. 4.13 in Chapter 4) and orbital shielding[d] obtained at the PBE level.

Atom	**functional**	$\boldsymbol{\delta_{g_e A^{FC}}}$ **(ppm)**	$\boldsymbol{\delta_{\Delta g A^{FC}}}$ **(ppm)**	$\boldsymbol{\delta_{\Delta \tilde{g} A^{dip}}}$ **(ppm)**	$\boldsymbol{\delta_{orb}}$ **(ppm)**	$\boldsymbol{\delta_{total}}$ **(ppm)**
	PBE	151.16	-10.10	-0.34	-6.34	134.39
	PBE5	144.04	-9.62	-0.31	-6.34	127.77
	PBE10	135.15	-9.03	-0.30	-6.34	119.48
	PBE15	127.85	-8.54	-0.30	-6.34	112.67
Li_a	PBE20	121.72	-8.13	-0.30	-6.34	106.95
	PBE25	115.52	-7.72	-0.29	-6.34	101.17
	PBE30	109.87	-7.34	-0.29	-6.34	95.90
	PBE35	104.54	-6.98	-0.29	-6.34	90.93
	PBE40	99.99	-6.68	-0.29	-6.34	86.68
	PBE	64.39	-4.30	3.15	-2.75	60.49
	PBE5	35.32	-2.36	3.10	-2.75	33.32
	PBE10	26.86	-1.79	3.10	-2.75	25.42
	PBE15	20.35	-1.36	3.09	-2.75	19.33
Li_b	PBE20	14.20	-0.95	3.09	-2.75	13.60
	PBE25	8.98	-0.60	3.09	-2.75	8.73
	PBE30	4.38	-0.29	3.09	-2.75	4.44
	PBE35	-0.26	0.02	3.09	-2.75	0.10
	PBE40	-4.34	0.29	3.09	-2.75	-3.71
	PBE	58.80	-3.93	-3.97	-3.43	47.47
	PBE5	74.18	-4.96	-3.99	-3.43	61.80
	PBE10	70.92	-4.74	-4.00	-3.43	58.75
	PBE15	65.00	-4.34	-4.00	-3.43	53.23
Li_c	PBE20	58.36	-3.90	-4.00	-3.43	47.03
	PBE25	52.31	-3.49	-4.00	-3.43	41.38
	PBE30	46.57	-3.11	-4.00	-3.43	36.03
	PBE35	41.13	-2.75	-4.00	-3.43	30.94
	PBE40	35.93	-2.40	-4.00	-3.43	26.10

[a] Equations 4.1-4.2 in Chapter 4 have been used for computing the total shielding tensor. Referenced against solid lithium lactate (cf. Computational Details in Chapter 4).
[b] HFC computations were done for a 2 × 2 × 1 super-cell using IGLO-II/8s7p4d basis sets (see Computational Details in Chapter 4).
[c] g-Tensor (PBC, Eq. 4.13 in Chapter 4) computations were done for a unit cell at PBE/def2-TZVP/IGLO-II level (see Computational Details in Chapter 4).
[d] Calculations of orbital shielding tensor were done for a unit cell at PBE/Ahlrich-VTZ/IGLO-II level (see Computational Details in Chapter 4).

Table B.5.: Computed[a] ^{7}Li chemical shifts for three distinct lithium sites Li_a, Li_b and Li_c of $Li_3V_2(PO_4)_3$ using the optimized structure, depending on the functional used for the hyperfine calculations.[b] g-Tensor[c] (PBC, Eq. 4.13 in Chapter 4) and orbital shielding[d] obtained at the PBE level.

Atom	functional	$\delta_{g_e A^{FC}}$ (ppm)	$\delta_{\Delta g A^{FC}}$ (ppm)	$\delta_{\Delta \tilde{g} A^{dip}}$ (ppm)	δ_{orb} (ppm)	δ_{total} (ppm)
	PBE	129.51	-7.60	-0.90	-6.77	114.24
	PBE5	126.73	-7.44	-0.89	-6.77	111.63
	PBE10	120.62	-7.08	-0.89	-6.77	105.88
	PBE15	114.57	-6.73	-0.88	-6.77	100.20
Li_a	PBE20	108.73	-6.38	-0.88	-6.77	94.70
	PBE25	103.22	-6.06	-0.88	-6.77	89.52
	PBE30	97.79	-5.74	-0.87	-6.77	84.41
	PBE35	93.20	-5.47	-0.87	-6.77	80.09
	PBE40	88.43	-5.19	-0.87	-6.77	75.61
	PBE	54.03	-3.17	2.57	-0.92	52.50
	PBE5	31.26	-1.84	2.54	-0.92	31.05
	PBE10	22.11	-1.30	2.54	-0.92	22.43
	PBE15	15.26	-0.90	2.54	-0.92	15.98
Li_b	PBE20	9.36	-0.55	2.54	-0.92	10.42
	PBE25	4.12	-0.24	2.54	-0.92	5.49
	PBE30	-1.02	0.06	2.54	-0.92	0.66
	PBE35	-5.06	0.30	2.54	-0.92	-3.15
	PBE40	-8.88	0.52	2.54	-0.92	-6.74
	PBE	85.73	-5.03	-2.33	5.90	84.27
	PBE5	91.58	-5.38	-2.34	5.90	89.77
	PBE10	85.52	-5.02	-2.34	5.90	84.06
	PBE15	78.54	-4.61	-2.34	5.90	77.49
Li_c	PBE20	71.49	-4.20	-2.34	5.90	70.86
	PBE25	64.69	-3.80	-2.34	5.90	64.45
	PBE30	57.99	-3.40	-2.34	5.90	58.15
	PBE35	52.39	-3.08	-2.34	5.90	52.88
	PBE40	46.85	-2.75	-2.34	5.90	47.66

[a] Equations 4.1-4.2 in Chapter 4 have been used for computing the total shielding tensor. Referenced against solid lithium lactate (cf. Computational Details in Chapter 4).
[b] HFC computations were done for a 2 × 2 × 1 super-cell using IGLO-II/8s7p4d basis sets (see Computational Details in Chapter 4).
[c] g-Tensor (PBC, Eq. 4.13 in Chapter 4) computations were done for a unit cell at PBE/def2-TZVP/IGLO-II level (see Computational Details in Chapter 4).
[d] Calculations of orbital shielding tensor were done for a unit cell at PBE/Ahlrich-VTZ/IGLO-II level (see Computational Details in Chapter 4).

Table B.6.: Computed[a] ^{7}Li chemical shifts for three distinct lithium sites Li_a, Li_b and Li_c of $Li_3V_2(PO_4)_3$ using the optimized structure, depending on the functional used for the hyperfine calculations.[b] g-Tensor[c] (cluster model) and orbital shielding[d] obtained at the PBE level.

Atom	functional	$\delta_{g_e A^{FC}}$ (ppm)	$\delta_{\Delta g A^{FC}}$ (ppm)	$\delta_{\Delta \tilde{g} A^{dip}}$ (ppm)	δ_{orb} (ppm)	δ_{total} (ppm)
	PBE	129.51	-8.28	-1.15	-6.77	113.32
	PBE5	126.73	-8.10	-1.14	-6.77	110.73
	PBE10	120.62	-7.71	-1.14	-6.77	105.00
	PBE15	114.57	-7.32	-1.14	-6.77	99.35
Li_a	PBE20	108.73	-6.95	-1.14	-6.77	93.88
	PBE25	103.22	-6.60	-1.14	-6.77	88.72
	PBE30	97.79	-6.25	-1.14	-6.77	83.63
	PBE35	93.20	-5.96	-1.14	-6.77	79.33
	PBE40	88.43	-5.65	-1.14	-6.77	74.88
	PBE	54.03	-3.45	1.97	-0.92	51.62
	PBE5	31.26	-2.00	1.95	-0.92	30.29
	PBE10	22.11	-1.41	1.94	-0.92	21.71
	PBE15	15.26	-0.98	1.94	-0.92	15.30
Li_b	PBE20	9.36	-0.60	1.93	-0.92	9.77
	PBE25	4.12	-0.26	1.93	-0.92	4.86
	PBE30	-1.02	0.07	1.93	-0.92	0.05
	PBE35	-5.06	0.32	1.93	-0.92	-3.73
	PBE40	-8.88	0.57	1.93	-0.92	-7.31
	PBE	85.73	-5.48	-2.28	5.90	83.87
	PBE5	91.58	-5.85	-2.29	5.90	89.34
	PBE10	85.52	-5.47	-2.29	5.90	83.67
	PBE15	78.54	-5.02	-2.29	5.90	77.14
Li_c	PBE20	71.49	-4.57	-2.29	5.90	70.54
	PBE25	64.69	-4.13	-2.29	5.90	64.17
	PBE30	57.99	-3.71	-2.29	5.90	57.90
	PBE35	52.39	-3.35	-2.29	5.90	52.66
	PBE40	46.85	-2.99	-2.29	5.90	47.47

[a] Equations 4.1-4.2 in Chapter 4 have been used for computing the total shielding tensor. Referenced against solid lithium lactate (cf. Computational Details in Chapter 4).
[b] HFC computations were done for a 2 × 2 × 1 super-cell using IGLO-II/8s7p4d basis sets (see Computational Details in Chapter 4).
[c] g-Tensor (PBC, Eq. 4.13 in Chapter 4) computations were done for a unit cell at PBE/def2-TZVP/IGLO-II level (see Computational Details in Chapter 4).
[d] Calculations of orbital shielding tensor were done for a unit cell at PBE/Ahlrich-VTZ/IGLO-II level (see Computational Details in Chapter 4).

Table B.7.: Computed ^{7}Li chemical shift anisotropy for three distinct lithium sites Li_a, Li_b and Li_c of $Li_3V_2(PO_4)_3$ computed using the optimized structure, varying the EXX admixture for the HFC[a] tensor computations. g-Tensor[b] (cluster model) and orbital shielding[c] obtained at the PBE level.

Atom	**Functional**	**Isotropic shift[d] (ppm)**	**Anisotropic shift tensor[d]**			**Anisotropy[e] (ppm)**	**Asymmetry[f]**
			δ_{11} (ppm)	δ_{22} (ppm)	δ_{33} (ppm)		
	PBE	114.24	-278.19	17.14	261.05	-417.29	0.88
	PBE5	111.63	-278.31	16.10	262.21	-417.47	0.88
	PBE10	105.88	-278.85	16.48	262.37	-418.27	0.88
	PBE15	100.20	-279.21	16.89	262.32	-418.81	0.88
Li_a	PBE20	94.70	-279.49	17.28	262.22	-419.24	0.88
	PBE25	89.52	-279.74	17.63	262.10	-419.60	0.87
	PBE30	84.41	-279.96	17.98	261.98	-419.94	0.87
	PBE35	80.09	-280.16	18.28	261.88	-420.24	0.87
	PBE40	75.61	-280.33	18.53	261.80	-420.50	0.87
	PBE	52.50	-264.46	-37.26	301.71	452.57	0.75
	PBE5	31.05	-261.39	-37.13	298.52	447.78	0.75
	PBE10	22.43	-260.37	-37.64	298.01	447.01	0.75
	PBE15	15.98	-259.73	-38.07	297.80	446.70	0.74
Li_b	PBE20	10.42	-259.24	-38.46	297.70	446.55	0.74
	PBE25	5.49	-258.83	-38.82	297.65	446.47	0.74
	PBE30	0.66	-258.53	-39.23	297.75	446.63	0.74
	PBE35	-3.15	-258.25	-39.56	297.81	446.71	0.73
	PBE40	-6.74	-257.98	-39.84	297.82	446.73	0.73
	PBE	84.27	-249.97	-192.87	442.85	664.27	0.13
	PBE5	89.77	-250.04	-193.85	443.89	665.83	0.13
	PBE10	84.06	-250.37	-194.11	444.48	666.72	0.13
	PBE15	77.49	-250.61	-194.33	444.94	667.41	0.13
Li_c	PBE20	70.86	-250.79	-194.48	445.28	667.91	0.13
	PBE25	64.45	-250.92	-194.58	445.50	668.25	0.13
	PBE30	58.15	-251.03	-194.62	445.65	668.47	0.13
	PBE35	52.88	-251.12	-194.61	445.72	668.58	0.13
	PBE40	47.66	-251.18	-194.60	445.78	668.67	0.13

[a] HFC computations were done for a 2 × 2 × 1 super-cell using IGLO-II/8s7p4d basis sets (see Computational Details in Chapter 4).
[b] g-Tensor (PBC, Eq. 4.13 in Chapter 4) computations were done for a unit cell at PBE/def2-TZVP/IGLO-II level (see Computational Details in Chapter 4).
[c] Calculations of orbital shielding tensor were done for a unit cell at PBE/Ahlrich-VTZ/IGLO-II level (see Computational Details in Chapter 4).
[d] Equations 4.1-4.2 in Chapter 4 have been used for computing the total shielding tensor. Referenced against solid lithium lactate (cf. Computational Details in Chapter 4).
[e] Anisotropy (Δ) = δ_{zz} - $\frac{1}{2}(\delta_{xx} + \delta_{yy})$; the components are ordered as $\mid \delta_{zz} - \delta_{iso} \mid \geq \mid \delta_{yy} - \delta_{iso} \mid \geq \mid \delta_{xx} - \delta_{iso} \mid$, $\delta_{iso} = \frac{1}{3}(\delta_{11} + \delta_{22} + \delta_{33})$ and $\delta_{11} \leq \delta_{22} \leq \delta_{33}$.
[f] Asymmetry (η) = $\frac{\delta_{xx} - \delta_{yy}}{\delta_{zz} - \delta_{iso}}$.

Table B.8.: Computed ^{7}Li chemical shift anisotropy for three distinct lithium sites Li_a, Li_b and Li_c of $Li_3V_2(PO_4)_3$ computed using the XRD structure, varying the EXX admixture for the HFC[a] tensor computations. g-Tensor[b] (PBC, Eq. 4.13 in Chapter 4) and orbital shielding[c] obtained at the PBE level.

Atom	**Functional**	**Isotropic shift[d] (ppm)**	**Anisotropic shift tensor[d]**			**Anisotropy[e] (ppm)**	**Asymmetry[f]**
			δ_{11} (ppm)	δ_{22} (ppm)	δ_{33} (ppm)		
Li_a	PBE	134.39	-279.88	24.15	255.72	-419.81	0.83
	PBE5	127.77	-278.07	20.82	257.25	-417.11	0.85
	PBE10	119.48	-278.62	20.73	257.88	-417.93	0.85
	PBE15	112.67	-279.00	20.99	258.01	-418.50	0.85
	PBE20	106.95	-279.33	21.38	257.94	-418.99	0.85
	PBE25	101.17	-279.62	21.68	257.94	-419.43	0.84
	PBE30	95.90	-279.86	21.96	257.90	-419.80	0.84
	PBE35	90.93	-280.11	22.27	257.84	-420.16	0.84
	PBE40	86.68	-280.32	22.56	257.75	-420.47	0.84
Li_b	PBE	60.49	-263.65	-15.82	279.47	419.20	0.89
	PBE5	33.32	-260.47	-13.84	274.31	411.46	0.90
	PBE10	25.42	-259.62	-13.84	273.47	410.20	0.90
	PBE15	19.33	-259.10	-14.08	273.19	409.78	0.90
	PBE20	13.60	-258.76	-14.49	273.26	409.89	0.89
	PBE25	8.73	-258.47	-14.74	273.21	409.82	0.89
	PBE30	4.44	-258.22	-15.00	273.22	409.83	0.89
	PBE35	0.10	-258.05	-15.29	273.34	410.01	0.89
	PBE40	-3.71	-257.89	-15.61	273.50	410.25	0.89
Li_c	PBE	47.47	-257.33	-180.11	437.44	656.16	0.18
	PBE5	61.80	-257.10	-181.95	439.05	658.57	0.17
	PBE10	58.75	-257.58	-182.28	439.86	659.79	0.17
	PBE15	53.23	-257.86	-182.47	440.32	660.49	0.17
	PBE20	47.03	-258.05	-182.55	440.60	660.90	0.17
	PBE25	41.38	-258.22	-182.64	440.86	661.30	0.17
	PBE30	36.03	-258.35	-182.68	441.03	661.54	0.17
	PBE35	30.94	-258.47	-182.66	441.14	661.71	0.17
	PBE40	26.10	-258.54	-182.62	441.16	661.75	0.17

[a] HFC computations were done for a 2 × 2 × 1 super-cell using IGLO-II/8s7p4d basis sets (see Computational Details in Chapter 4).

[b] g-Tensor (PBC, Eq. 4.13 in Chapter 4) computations were done for a unit cell at PBE/def2-TZVP/IGLO-II level (see Computational Details in Chapter 4).

[c] Calculations of orbital shielding tensor were done for a unit cell at PBE/Ahlrich-VTZ/IGLO-II level (see Computational Details in Chapter 4).

[d] Equations 4.1-4.2 in Chapter 4 have been used for computing the total shielding tensor. Referenced against solid lithium lactate (cf. Computational Details in Chapter 4).

[e] Anisotropy (Δ) = δ_{zz} - $\frac{1}{2}(\delta_{xx} + \delta_{yy})$; the components are ordered as $\mid \delta_{zz} - \delta_{iso} \mid \geq \mid \delta_{yy} - \delta_{iso} \mid \geq \mid \delta_{xx} - \delta_{iso} \mid$, $\delta_{iso} = \frac{1}{3}(\delta_{11} + \delta_{22} + \delta_{33})$ and $\delta_{11} \leq \delta_{22} \leq \delta_{33}$.

[f] Asymmetry (η) = $\frac{\delta_{xx} - \delta_{yy}}{\delta_{zz} - \delta_{iso}}$.

Table B.9.: Computed ^{7}Li chemical shift anisotropy for three distinct lithium sites Li_a, Li_b and Li_c of $Li_3V_2(PO_4)_3$ computed using the optimized structure, varying the EXX admixture for the HFC[a] tensor computations. g-Tensor[b] (PBC, Eq. 4.13 in Chapter 4) and orbital shielding[c] obtained at the PBE level.

Atom	**Functional**	**Isotropic shift[d] (ppm)**	**Anisotropic shift tensor[d]**			**Anisotropy[e] (ppm)**	**Asymmetry[f]**
			δ_{11} (ppm)	δ_{22} (ppm)	δ_{33} (ppm)		
	PBE	113.32	-277.31	15.48	261.84	-415.97	0.89
	PBE5	110.73	-277.45	14.48	262.97	-416.18	0.90
	PBE10	105.00	-278.02	14.91	263.11	-417.03	0.89
	PBE15	99.35	-278.41	15.38	263.04	-417.62	0.89
Li_a	PBE20	93.88	-278.73	15.82	262.91	-418.10	0.89
	PBE25	88.72	-279.00	16.23	262.77	-418.50	0.88
	PBE30	83.63	-279.26	16.63	262.62	-418.88	0.88
	PBE35	79.33	-279.47	16.97	262.51	-419.21	0.88
	PBE40	74.88	-279.67	17.26	262.41	-419.51	0.88
	PBE	51.62	-262.43	-36.38	298.80	448.20	0.76
	PBE5	30.29	-259.37	-36.37	295.74	443.60	0.75
	PBE10	21.71	-258.36	-36.92	295.27	442.91	0.75
	PBE15	15.30	-257.72	-37.37	295.09	442.64	0.75
Li_b	PBE20	9.77	-257.24	-37.79	295.02	442.53	0.74
	PBE25	4.86	-256.82	-38.17	295.00	442.49	0.74
	PBE30	0.05	-256.52	-38.60	295.12	442.68	0.74
	PBE35	-3.73	-256.24	-38.96	295.20	442.79	0.74
	PBE40	-7.31	-255.97	-39.25	295.22	442.84	0.73
	PBE	83.87	-249.50	-191.28	440.79	661.18	0.13
	PBE5	89.34	-249.54	-192.28	441.83	662.74	0.13
	PBE10	83.67	-249.91	-192.51	442.42	663.62	0.13
	PBE15	77.14	-250.18	-192.69	442.87	664.30	0.13
Li_c	PBE20	70.54	-250.40	-192.80	443.19	664.79	0.13
	PBE25	64.17	-250.56	-192.85	443.41	665.12	0.13
	PBE30	57.90	-250.70	-192.85	443.55	665.33	0.13
	PBE35	52.66	-250.81	-192.81	443.62	665.43	0.13
	PBE40	47.47	-250.91	-192.76	443.67	665.50	0.13

[a] HFC computations were done for a 2 × 2 × 1 super-cell using IGLO-II/8s7p4d basis sets (see Computational Details in Chapter 4).
[b] g-Tensor (PBC, Eq. 4.13 in Chapter 4) computations were done for a unit cell at PBE/def2-TZVP/IGLO-II level (see Computational Details in Chapter 4).
[c] Calculations of orbital shielding tensor were done for a unit cell at PBE/Ahlrich-VTZ/IGLO-II level (see Computational Details in Chapter 4).
[d] Equations 4.1-4.2 in Chapter 4 have been used for computing the total shielding tensor. Referenced against solid lithium lactate (cf. Computational Details in Chapter 4).
[e] Anisotropy (Δ) = δ_{zz} - $\frac{1}{2}(\delta_{xx} + \delta_{yy})$; the components are ordered as $\mid \delta_{zz} - \delta_{iso} \mid \geq \mid \delta_{yy} - \delta_{iso} \mid \geq \mid \delta_{xx} - \delta_{iso} \mid$, $\delta_{iso} = \frac{1}{3}(\delta_{11} + \delta_{22} + \delta_{33})$ and $\delta_{11} \leq \delta_{22} \leq \delta_{33}$.
[f] Asymmetry (η) = $\frac{\delta_{xx} - \delta_{yy}}{\delta_{zz} - \delta_{iso}}$.

Appendix C.

Additional figures and tables for $LiMPO_4$ (Mn, Fe, Co, Ni) and MPO_4 (Fe, Co) solids*

* Appendix C *(pre-print)* with all tables and graphics therein are reproduced in part with permission from A. Mondal and M. Kaupp, Quantum-chemical approach to NMR chemical shifts in paramagnetic solids applied to $LiFePO_4$ and $LiCoPO_4$, *J. Phys. Chem. Lett.*, **2018**, 9, 1480–1484. (https://doi.org/10.1021/acs.jpclett.8b00407) and A. Mondal and M. Kaupp, Computation of NMR shifts for paramagnetic solids including zero-field-splitting and beyond-DFT approaches. Application to $LiMPO_4$ (M = Mn, Fe, Co, Ni) and MPO_4 (M = Fe, Co), *J. Phys. Chem. C*, **2019**, 123, 8387–8405. (https://doi.org/10.1021/acs.jpcc.8b09645) Copyright 2018 American Chemical Society.

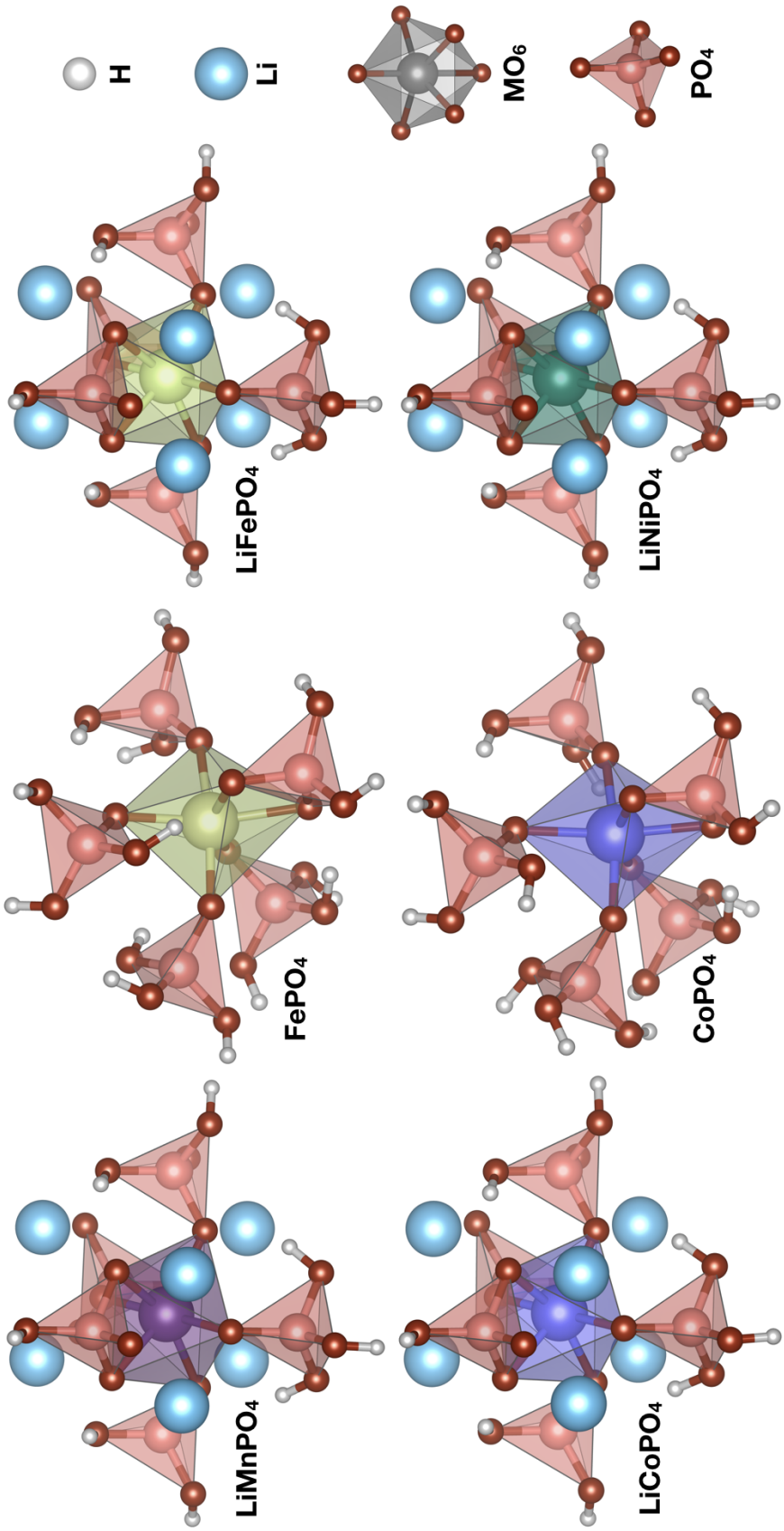

Figure C.1.: Molecular models of $LiMPO_4$ (M=Mn, Fe, Co, Ni) and MPO_4 (Fe, Co) solids extracted from XRD structures, where the terminal oxygens have been saturated with the hydrogen atoms. $LiMPO_4$ has six lithium atoms where as MPO_4 none.

Table C.1.: Multiplicity, term symbol, orbital degeneracy, number of microstates and energy levels computed from L and S quantum numbers for various electronic configurations of d orbitals.

$\mathbf{d}^n$	**multi**	**term**	**L**	**S**	**2L+1**	**2S+1**	**quantum states**			**orbital degeneracy**		
d^5	sextet	^{6}S	0	5/2	1	6	6	6	252	1	1	100
	quartet	^{4}G	4	3/2	9	4	36	96		9	24	
		^{4}F	3	3/2	7	4	28			7		
		^{4}D	2	3/2	5	4	20			5		
		^{4}P	1	3/2	3	4	12			3		
	doublet	^{2}I	6	1/2	13	2	26	150		13	75	
		^{2}H	5	1/2	11	2	22			11		
		^{2}G	4	1/2	9	2	18			9		
		^{2}G	4	1/2	9	2	18			9		
		^{2}F	3	1/2	7	2	14			7		
		^{2}F	3	1/2	7	2	14			7		
		^{2}D	2	1/2	5	2	10			5		
		^{2}D	2	1/2	5	2	10			5		
		^{2}D	2	1/2	5	2	10			5		
		^{2}P	1	1/2	3	2	6			3		
		^{2}S	0	1/2	1	2	2			1		
d^4,d^6	quintet	^{5}D	2	2	5	5	25	25	210	5	5	100
	triplet	^{3}H	5	1	11	3	33	135		11	45	
		^{3}G	4	1	9	3	27			9		
		^{3}F	3	1	7	3	21			7		
		^{3}F	3	1	7	3	21			7		
		^{3}D	2	1	5	3	15			5		
		^{3}P	1	1	3	3	9			3		
		^{3}P	1	1	3	3	9			3		
	singlet	^{1}I	6	0	13	1	13	50		13	50	
		^{1}G	4	0	9	1	9			9		
		^{1}G	4	0	9	1	9			9		
		^{1}F	3	0	7	1	7			7		
		^{1}D	2	0	5	1	5			5		
		^{1}D	2	0	5	1	5			5		
		^{1}S	0	0	1	1	1			1		
		^{1}S	0	0	1	1	1			1		
d^3,d^7	quartet	^{4}F	3	3/2	7	4	28	40	120	7	10	50
		^{4}P	3	3/2	3	4	12			3		
	doublet	^{2}H	5	1/2	11	2	22	80		11	40	
		^{2}G	4	1/2	9	2	18			9		
		^{2}F	3	1/2	7	2	14			7		
		^{2}D	2	1/2	5	2	10			5		
		^{2}D	2	1/2	5	2	10			5		
		^{2}P	1	1/2	3	2	6			3		
d^2, d^8	triplet	^{3}F	3	1	7	3	21	30	45	7	10	25
		^{3}P	1	1	3	3	9			3		
	singlet	^{1}G	4	0	9	1	9	15		9	15	
		^{1}D	2	0	5	1	5			5		
		^{1}S	0	0	1	1	1			1		
d^1,d^9	doublet	^{2}D	2	1/2	5	2	10	10	10	5	5	5
d^0,d^{10}	singlet	^{1}S	0	0	1	1	1	1	1	1	1	1

Table C.2.: Comparison of optimized[a] and XRD unit-cell parameters and volume for $LiMPO_4$ (M=Mn, Fe, Co, Ni) and MPO_4 (M=Fe, Co).

material	**structure**	**a (Å)**	**b (Å)**	**c (Å)**	**vloume (Å^3)**
$LiMnPO_4$	XRD[297]	10.460	6.100	4.744	302.696
	OPT	10.504	6.140	4.755	306.672
	% diff	0.42	0.66	0.23	1.31
$LiFePO_4$	XRD[298]	10.336	6.006	4.693	291.332
	OPT	10.380	6.037	4.710	295.148
	% diff	0.43	0.52	0.36	1.31
$LiCoPO_4$	XRD[299]	10.200	5.920	4.690	283.201
	OPT	10.265	5.945	4.714	287.674
	% diff	0.75	0.42	0.51	1.58
$LiNiPO_4$	XRD[300]	10.032	5.855	4.681	274.950
	OPT	10.108	5.888	4.687	278.951
	% diff	0.75	0.56	0.13	1.46
$FePO_4$	XRD[301]	9.823	5.786	4.785	271.960
	OPT	9.923	5.941	4.886	288.042
	% diff	1.02	2.68	2.11	5.91
$CoPO_4$	XRD[295]	9.581	5.789	4.769	264.510
	OPT	9.652	5.939	4.889	280.253
	% diff	0.74	2.59	2.52	5.95

[a] Cell parameter optimizations at GPW/DZVP-MOLOPT-SR-GTH level for a 2 × 2 × 4 super-cell (orthorhombic cell *pnma* space group).

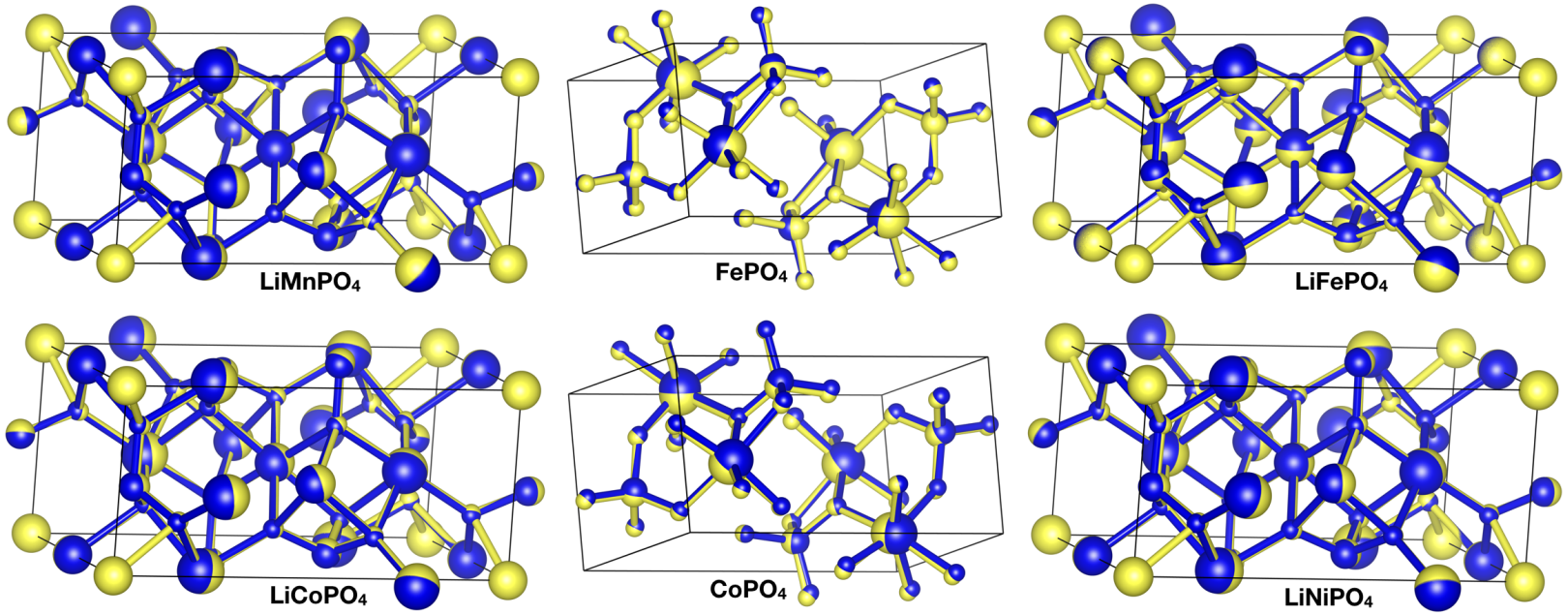

Figure C.2.: Comparison of XRD (in yellow) and optimized (in blue) structures of $LiMPO_4$ (M=Mn, Fe, Co, Ni) and MPO_4 (M=Fe, Co) (See Computational Details in Chapter 5).

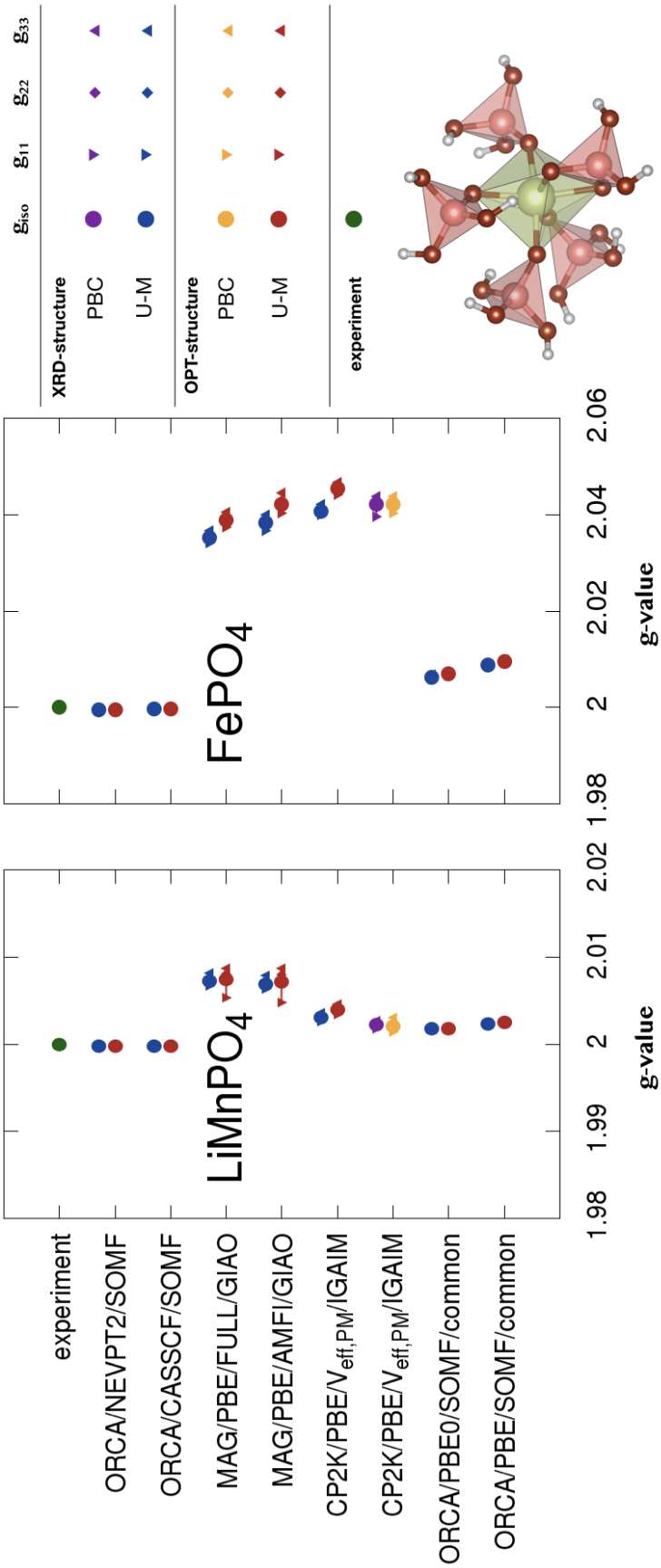

Figure C.3.: Comparison of computed g-tensors for cluster models (C-M), unit-cell g-tensors obtained from cluster models (U-M) and PBD unit-cell g-tensors for $LiMnPO_4$ and $FePO_4$ at various computation levels.

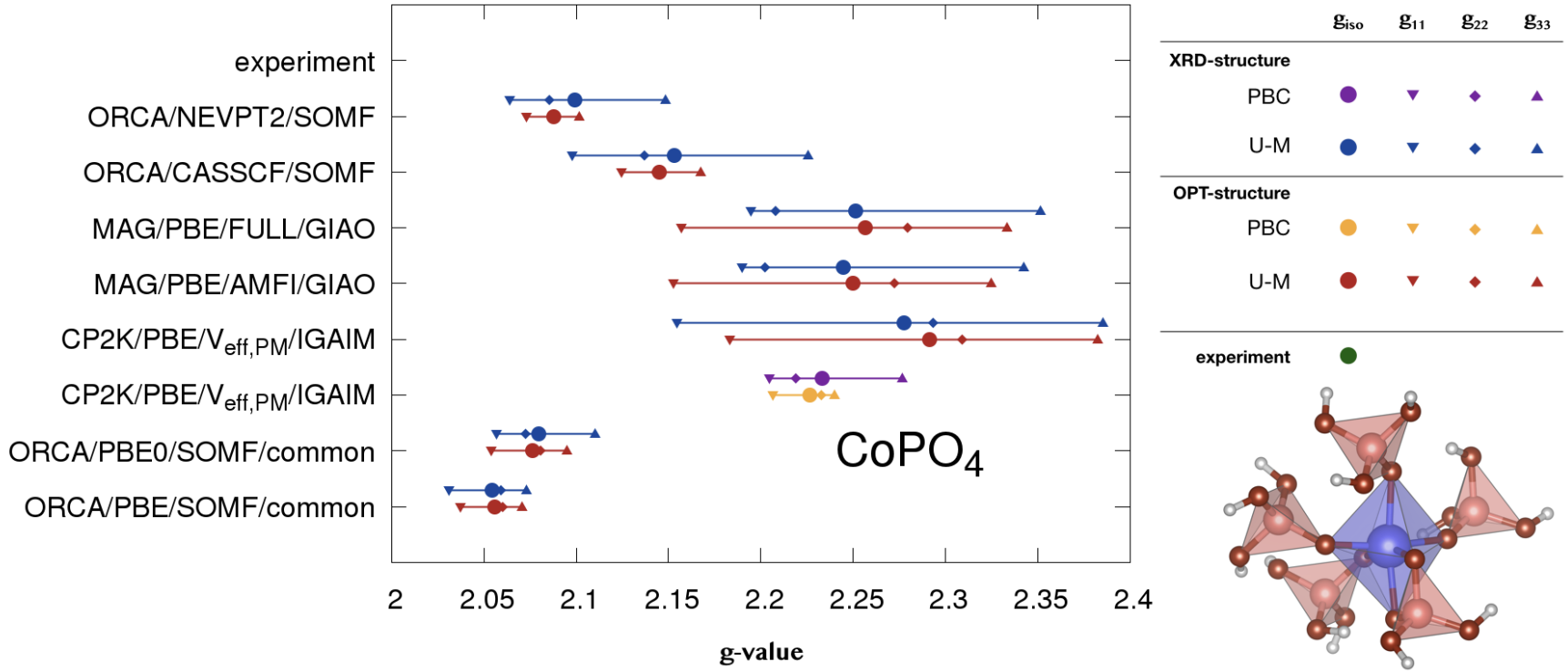

Figure C.4.: Comparison of computed g-tensors for cluster models (C-M), unit-cell g-tensors obtained from cluster models (U-M) and PBD unit-cell g-tensors for $CoPO_4$ at various computation levels.

Table C.3.: Comparison of computed[a] unit-cell g-tensors obtained from cluster models at various levels and PBC unit-cell g-tensors for $LiFePO_4$

Method	Cluster Model				Unitcell Model			
	$\mathbf{g}_{11}$	$\mathbf{g}_{22}$	$\mathbf{g}_{33}$	$\mathbf{g}_{iso}$	$\mathbf{g}_{11}$	$\mathbf{g}_{22}$	$\mathbf{g}_{33}$	$\mathbf{g}_{iso}$
XRD structure								
ORCA/NEVPT2	2.000	2.128	2.175	2.101	2.001	2.127	2.175	2.101
ORCA/CASSCF	1.999	2.148	2.210	2.119	2.000	2.147	2.210	2.119
ORCA/PBE0/SOMF/common	2.008	2.049	2.058	2.038	2.009	2.049	2.058	2.038
MAG/PBE/FULL/GIAO	2.091	2.161	2.197	2.150	2.098	2.153	2.197	2.150
MAG/PBE/AMFI/GIAO	2.102	2.180	2.220	2.167	2.111	2.171	2.220	2.167
MAG/PBE/FULL/common	2.019	2.030	2.037	2.029	2.021	2.028	2.037	2.029
MAG/PBE/AMFI/common	2.021	2.033	2.041	2.031	2.023	2.030	2.041	2.031
ORCA/PBE/SOMF/common	2.023	2.040	2.048	2.037	2.023	2.040	2.048	2.037
ORCA/PBE/AMFI/common	2.023	2.040	2.048	2.037	2.023	2.040	2.048	2.037
CP2K/PBE/Veff,PM/IGAIM	2.100	2.182	2.217	2.166	2.100	2.182	2.217	2.166
CP2K/PBE/Veff,PM/IGAIM				PBC[b]	2.088	2.181	2.220	2.163
OPT structure								
ORCA/NEVPT2	2.001	2.124	2.177	2.101	2.002	2.123	2.177	2.101
ORCA/CASSCF	2.000	2.144	2.214	2.119	2.002	2.142	2.214	2.119
ORCA/PBE0/SOMF/common	2.008	2.049	2.058	2.038	2.009	2.049	2.058	2.038
MAG/PBE/FULL/GIAO	2.093	2.159	2.197	2.150	2.101	2.152	2.197	2.150
MAG/PBE/AMFI/GIAO	2.105	2.178	2.220	2.167	2.114	2.169	2.220	2.167
MAG/PBE/FULL/common	2.020	2.029	2.038	2.029	2.022	2.027	2.038	2.029
MAG/PBE/AMFI/common	2.021	2.032	2.041	2.031	2.024	2.029	2.041	2.031
ORCA/PBE/SOMF/common	2.024	2.040	2.048	2.037	2.024	2.040	2.048	2.037
ORCA/PBE/AMFI/common	2.024	2.040	2.048	2.037	2.024	2.040	2.048	2.037
CP2K/PBE/Veff,PM/IGAIM	2.102	2.181	2.219	2.167	2.102	2.181	2.219	2.167
CP2K/PBE/Veff,PM/IGAIM				PBC[b]	2.088	2.173	2.220	2.160

[a] For the PBC calculation unit-cell g-tensor obtained after normalization[148] and for the cluster models g-tensor for unit-cell obtained by replacing the computed g-tensors into the solid-state structures after averaging.

[b] PBC computations were carried on $2 \times 2 \times 2$ super cell at PBE/def2-TZVP/IGLO-II level and cluster model calculations with the same basis sets at the level specified in the table (see Computational Details in Chapter 5).

Table C.4.: Comparison of computed[a] unit-cell g-tensors obtained from cluster models at various levels and PBC unit-cell g-tensors for $LiCoPO_4$

Method	Cluster Model				Unitcell Model			
	$\mathbf{g}_{11}$	$\mathbf{g}_{22}$	$\mathbf{g}_{33}$	$\mathbf{g}_{iso}$	$\mathbf{g}_{11}$	$\mathbf{g}_{22}$	$\mathbf{g}_{33}$	$\mathbf{g}_{iso}$
XRD structure								
ORCA/NEVPT2	1.971	2.497	2.719	2.396	2.024	2.444	2.719	2.396
ORCA/CASSCF	1.958	2.531	2.840	2.443	2.017	2.473	2.840	2.443
ORCA/PBE0/SOMF/common	2.095	2.130	2.135	2.120	2.096	2.129	2.135	2.120
MAG/PBE/FULL/GIAO	2.213	2.303	2.366	2.294	2.262	2.270	2.349	2.294
MAG/PBE/AMFI/GIAO	2.209	2.296	2.357	2.287	2.257	2.265	2.340	2.287
MAG/PBE/FULL/common	2.063	2.081	2.082	2.075	2.071	2.075	2.079	2.075
MAG/PBE/AMFI/common	2.061	2.078	2.080	2.073	2.070	2.073	2.076	2.073
ORCA/PBE/SOMF/common	2.069	2.092	2.104	2.088	2.080	2.083	2.102	2.088
ORCA/PBE/AMFI/common	2.069	2.092	2.104	2.088	2.080	2.083	2.102	2.088
CP2K/PBE/Veff,PM/IGAIM	2.248	2.352	2.414	2.338	2.291	2.315	2.407	2.338
CP2K/PBE/Veff,PM/IGAIM				PBC[b]	2.149	2.232	2.271	2.217
OPT structure								
ORCA/NEVPT2	1.965	2.497	2.729	2.397	2.030	2.433	2.728	2.397
ORCA/CASSCF	1.947	2.540	2.858	2.448	2.022	2.466	2.857	2.448
ORCA/PBE0/SOMF/common	2.095	2.129	2.137	2.120	2.096	2.129	2.136	2.120
MAG/PBE/FULL/GIAO	2.212	2.305	2.359	2.292	2.254	2.278	2.344	2.292
MAG/PBE/AMFI/GIAO	2.209	2.298	2.350	2.286	2.249	2.272	2.336	2.286
MAG/PBE/FULL/common	2.062	2.079	2.083	2.075	2.068	2.077	2.079	2.075
MAG/PBE/AMFI/common	2.060	2.077	2.081	2.073	2.067	2.075	2.077	2.073
ORCA/PBE/SOMF/common	2.069	2.093	2.103	2.088	2.078	2.085	2.101	2.088
ORCA/PBE/AMFI/common	2.069	2.093	2.103	2.088	2.078	2.085	2.101	2.088
CP2K/PBE/Veff,PM/IGAIM	2.259	2.342	2.414	2.338	2.283	2.323	2.408	2.338
CP2K/PBE/Veff,PM/IGAIM				PBC[b]	2.154	2.252	2.311	2.239

[a] For the PBC calculation unit-cell g-tensor obtained after normalization[148] and for the cluster models g-tensor for unit-cell obtained by replacing the computed g-tensors into the solid-state structures after averaging.

[b] PBC computations were carried on $2 \times 2 \times 2$ super cell at PBE/def2-TZVP/IGLO-II level and cluser model calculations with the same basis sets at the level specified in the table (see Computational Details in Chapter 5).

Table C.5.: Comparison of computed[a] unit-cell g-tensors obtained from cluster models at various levels and PBC unit-cell g-tensors for $LiNiPO_4$

Method	Cluster Model				Unitcell Model			
	$\mathbf{g}_{11}$	$\mathbf{g}_{22}$	$\mathbf{g}_{33}$	$\mathbf{g}_{iso}$	$\mathbf{g}_{11}$	$\mathbf{g}_{22}$	$\mathbf{g}_{33}$	$\mathbf{g}_{iso}$
XRD structure								
ORCA/NEVPT2	2.221	2.274	2.340	2.278	2.221	2.283	2.330	2.278
ORCA/CASSCF	2.307	2.388	2.476	2.390	2.307	2.398	2.465	2.390
ORCA/PBE0/SOMF/common	2.131	2.146	2.163	2.147	2.131	2.150	2.159	2.147
MAG/PBE/FULL/GIAO	2.205	2.207	2.258	2.223	2.205	2.211	2.254	2.223
MAG/PBE/AMFI/GIAO	2.204	2.207	2.257	2.223	2.204	2.210	2.253	2.223
MAG/PBE/FULL/common	2.092	2.094	2.112	2.099	2.092	2.094	2.111	2.099
MAG/PBE/AMFI/common	2.091	2.094	2.111	2.098	2.091	2.094	2.111	2.098
ORCA/PBE/SOMF/common	2.097	2.098	2.120	2.105	2.097	2.098	2.120	2.105
ORCA/PBE/AMFI/common	2.097	2.098	2.120	2.105	2.097	2.098	2.120	2.105
CP2K/PBE/Veff,PM/IGAIM	2.246	2.248	2.311	2.268	2.246	2.248	2.311	2.268
CP2K/PBE/Veff,PM/IGAIM				PBC[b]	2.196	2.205	2.236	2.212
OPT structure								
ORCA/NEVPT2	2.230	2.272	2.338	2.280	2.230	2.277	2.334	2.280
ORCA/CASSCF	2.321	2.387	2.479	2.395	2.321	2.392	2.473	2.395
ORCA/PBE0/SOMF/common	2.134	2.146	2.162	2.148	2.134	2.149	2.160	2.148
MAG/PBE/FULL/GIAO	2.207	2.208	2.275	2.230	2.208	2.211	2.271	2.230
MAG/PBE/AMFI/GIAO	2.206	2.207	2.275	2.229	2.207	2.211	2.270	2.229
MAG/PBE/FULL/common	2.091	2.093	2.114	2.100	2.092	2.093	2.114	2.100
MAG/PBE/AMFI/common	2.091	2.092	2.113	2.099	2.091	2.092	2.113	2.099
ORCA/PBE/SOMF/common	2.098	2.098	2.126	2.107	2.098	2.098	2.126	2.107
ORCA/PBE/AMFI/common	2.098	2.098	2.126	2.107	2.098	2.098	2.126	2.107
CP2K/PBE/Veff,PM/IGAIM	2.247	2.250	2.333	2.277	2.247	2.250	2.333	2.277
CP2K/PBE/Veff,PM/IGAIM				PBC[b]	2.202	2.202	2.272	2.225

[a] For the PBC calculation unit-cell g-tensor obtained after normalization[148] and for the cluster models g-tensor for unit-cell obtained by replacing the computed g-tensors into the solid-state structures after averaging.

[b] PBC computations were carried on $2 \times 2 \times 2$ super cell at PBE/def2-TZVP/IGLO-II level and cluster model calculations with the same basis sets at the level specified in the table (see Computational Details in Chapter 5).

Table C.6.: Comparison of computed[a] unit-cell g-tensors obtained from cluster models at various levels and PBC unit-cell g-tensors for $LiMnPO_4$

Method	Cluster Model				Unitcell Model			
	$\mathbf{g}_{11}$	$\mathbf{g}_{22}$	$\mathbf{g}_{33}$	$\mathbf{g}_{iso}$	$\mathbf{g}_{11}$	$\mathbf{g}_{22}$	$\mathbf{g}_{33}$	$\mathbf{g}_{iso}$
XRD structure								
ORCA/NEVPT2	2.000	2.000	2.000	2.000	2.000	2.000	2.000	2.000
ORCA/CASSCF	2.000	2.000	2.000	2.000	2.000	2.000	2.000	2.000
ORCA/PBE0/SOMF/common	2.002	2.002	2.002	2.002	2.002	2.002	2.002	2.002
MAG/PBE/FULL/GIAO	2.006	2.008	2.008	2.007	2.007	2.007	2.008	2.007
MAG/PBE/AMFI/GIAO	2.005	2.007	2.008	2.007	2.006	2.007	2.008	2.007
MAG/PBE/FULL/common	2.004	2.004	2.004	2.004	2.004	2.004	2.004	2.004
MAG/PBE/AMFI/common	2.003	2.003	2.003	2.003	2.003	2.003	2.003	2.003
ORCA/PBE/SOMF/common	2.002	2.002	2.002	2.002	2.002	2.002	2.002	2.002
ORCA/PBE/AMFI/common	2.002	2.002	2.002	2.002	2.002	2.002	2.002	2.002
CP2K/PBE/Veff,PM/IGAIM	2.003	2.003	2.004	2.003	2.003	2.003	2.004	2.003
CP2K/PBE/Veff,PM/IGAIM				PBC[b]	2.002	2.002	2.003	2.002
OPT structure								
ORCA/NEVPT2	2.000	2.000	2.000	2.000	2.000	2.000	2.000	2.000
ORCA/CASSCF	2.000	2.000	2.000	2.000	2.000	2.000	2.000	2.000
ORCA/PBE0/SOMF/common	2.002	2.002	2.002	2.002	2.002	2.002	2.002	2.002
MAG/PBE/FULL/GIAO	2.005	2.008	2.009	2.007	2.005	2.008	2.009	2.007
MAG/PBE/AMFI/GIAO	2.005	2.008	2.009	2.007	2.005	2.008	2.009	2.007
MAG/PBE/FULL/common	2.004	2.004	2.004	2.004	2.004	2.004	2.004	2.004
MAG/PBE/AMFI/common	2.003	2.003	2.003	2.003	2.003	2.003	2.003	2.003
ORCA/PBE/SOMF/common	2.002	2.003	2.003	2.003	2.002	2.003	2.003	2.003
ORCA/PBE/AMFI/common	2.002	2.003	2.003	2.003	2.002	2.003	2.003	2.003
CP2K/PBE/Veff,PM/IGAIM	2.003	2.004	2.005	2.004	2.003	2.004	2.005	2.004
CP2K/PBE/Veff,PM/IGAIM				PBC[b]	2.001	2.002	2.003	2.002

[a] For the PBC calculation unit-cell g-tensor obtained after normalization[148] and for the cluster models g-tensor for unit-cell obtained by replacing the computed g-tensors into the solid-state structures after averaging.

[b] PBC computations were carried on $2 \times 2 \times 2$ super cell at PBE/def2-TZVP/IGLO-II level and cluster model calculations with the same basis sets at the level specified in the table (see Computational Details in Chapter 5).

Table C.7.: Comparison of computed[a] unit-cell g-tensors obtained from cluster models at various levels and PBC unit-cell g-tensors for $FePO_4$

Method	Cluster Model				Unitcell Model			
	$\mathbf{g}_{11}$	$\mathbf{g}_{22}$	$\mathbf{g}_{33}$	$\mathbf{g}_{iso}$	$\mathbf{g}_{11}$	$\mathbf{g}_{22}$	$\mathbf{g}_{33}$	$\mathbf{g}_{iso}$
XRD structure								
ORCA/NEVPT2	1.999	1.999	1.999	1.999	1.999	1.999	1.999	1.999
ORCA/CASSCF	2.000	2.000	2.000	2.000	2.000	2.000	2.000	2.000
ORCA/PBE0/SOMF/common	2.006	2.006	2.007	2.006	2.006	2.006	2.007	2.006
MAG/PBE/FULL/GIAO	2.034	2.036	2.037	2.035	2.034	2.035	2.037	2.035
MAG/PBE/AMFI/GIAO	2.036	2.039	2.040	2.038	2.037	2.038	2.040	2.038
MAG/PBE/FULL/common	2.009	2.009	2.010	2.009	2.009	2.009	2.010	2.009
MAG/PBE/AMFI/common	2.009	2.009	2.010	2.009	2.009	2.009	2.010	2.009
ORCA/PBE/SOMF/common	2.009	2.009	2.009	2.009	2.009	2.009	2.009	2.009
ORCA/PBE/AMFI/common	2.009	2.009	2.009	2.009	2.009	2.009	2.009	2.009
CP2K/PBE/Veff,PM/IGAIM	2.039	2.041	2.042	2.041	2.040	2.040	2.042	2.041
CP2K/PBE/Veff,PM/IGAIM				PBC[b]	2.040	2.043	2.044	2.042
OPT structure								
ORCA/NEVPT2	1.999	2.000	2.000	2.000	2.000	2.000	2.000	2.000
ORCA/CASSCF	2.000	2.000	2.000	2.000	2.000	2.000	2.000	2.000
ORCA/PBE0/SOMF/common	2.007	2.007	2.007	2.007	2.007	2.007	2.007	2.007
MAG/PBE/FULL/GIAO	2.037	2.039	2.041	2.039	2.038	2.038	2.041	2.039
MAG/PBE/AMFI/GIAO	2.040	2.042	2.045	2.042	2.040	2.042	2.045	2.042
MAG/PBE/FULL/common	2.010	2.010	2.010	2.010	2.010	2.010	2.010	2.010
MAG/PBE/AMFI/common	2.010	2.010	2.010	2.010	2.010	2.010	2.010	2.010
ORCA/PBE/SOMF/common	2.009	2.010	2.010	2.010	2.009	2.010	2.010	2.010
ORCA/PBE/AMFI/common	2.009	2.010	2.010	2.010	2.009	2.010	2.010	2.010
CP2K/PBE/Veff,PM/IGAIM	2.044	2.046	2.046	2.046	2.044	2.046	2.047	2.046
CP2K/PBE/Veff,PM/IGAIM				PBC[b]	2.040	2.042	2.044	2.042

[a] For the PBC calculation unit-cell g-tensor obtained after normalization[148] and for the cluster models g-tensor for unit-cell obtained by replacing the computed g-tensors into the solid-state structures after averaging.

[b] PBC computations were carried on 2 × 2 × 2 super cell at PBE/def2-TZVP/IGLO-II level and cluster model calculations with the same basis sets at the level specified in the table (see Computational Details in Chapter 5).

Table C.8.: Comparison of computed[a] unit-cell g-tensors obtained from cluster models at various levels and PBC unit-cell g-tensors for $CoPO_4$

Method	Cluster Model				Unitcell Model			
	$\mathbf{g}_{11}$	$\mathbf{g}_{22}$	$\mathbf{g}_{33}$	$\mathbf{g}_{iso}$	$\mathbf{g}_{11}$	$\mathbf{g}_{22}$	$\mathbf{g}_{33}$	$\mathbf{g}_{iso}$
XRD structure								
ORCA/NEVPT2	2.062	2.087	2.149	2.099	2.064	2.085	2.148	2.099
ORCA/CASSCF	2.097	2.137	2.226	2.153	2.098	2.137	2.225	2.153
ORCA/PBE0/SOMF/common	2.044	2.085	2.110	2.080	2.057	2.073	2.110	2.080
MAG/PBE/FULL/GIAO	2.124	2.278	2.353	2.251	2.194	2.208	2.352	2.251
MAG/PBE/AMFI/GIAO	2.121	2.270	2.343	2.245	2.190	2.202	2.342	2.245
MAG/PBE/FULL/common	2.029	2.048	2.053	2.043	2.034	2.043	2.052	2.043
MAG/PBE/AMFI/common	2.028	2.046	2.051	2.042	2.033	2.041	2.050	2.042
ORCA/PBE/SOMF/common	2.029	2.061	2.073	2.055	2.031	2.059	2.073	2.055
ORCA/PBE/AMFI/common	2.030	2.061	2.074	2.055	2.032	2.059	2.073	2.055
CP2K/PBE/Veff,PM/IGAIM	2.139	2.308	2.387	2.278	2.155	2.293	2.385	2.278
CP2K/PBE/Veff,PM/IGAIM				PBC[b]	2.142	2.205	2.238	2.195
OPT structure								
ORCA/NEVPT2	2.073	2.089	2.102	2.088	2.073	2.089	2.102	2.088
ORCA/CASSCF	2.119	2.148	2.169	2.145	2.125	2.143	2.167	2.145
ORCA/PBE0/SOMF/common	2.048	2.086	2.095	2.076	2.054	2.081	2.095	2.076
MAG/PBE/FULL/GIAO	2.155	2.280	2.334	2.257	2.157	2.280	2.334	2.257
MAG/PBE/AMFI/GIAO	2.151	2.273	2.326	2.250	2.152	2.272	2.325	2.250
MAG/PBE/FULL/common	2.036	2.046	2.052	2.045	2.037	2.045	2.052	2.045
MAG/PBE/AMFI/common	2.034	2.044	2.050	2.043	2.035	2.043	2.050	2.043
ORCA/PBE/SOMF/common	2.036	2.061	2.071	2.056	2.037	2.060	2.071	2.056
ORCA/PBE/AMFI/common	2.036	2.061	2.071	2.056	2.037	2.060	2.071	2.056
CP2K/PBE/Veff,PM/IGAIM	2.170	2.321	2.383	2.291	2.183	2.309	2.382	2.291
CP2K/PBE/Veff,PM/IGAIM				PBC[b]	2.179	2.220	2.225	2.208

[a] For the PBC calculation unit-cell g-tensor obtained after normalization[148] and for the cluster models g-tensor for unit-cell obtained by replacing the computed g-tensors into the solid-state structures after averaging.

[b] PBC computations were carried on $2 \times 2 \times 2$ super cell at PBE/def2-TZVP/IGLO-II level and cluster model calculations with the same basis sets at the level specified in the table (see Computational Details in Chapter 5).

Table C.9.: Comparison of computed[a] unit-cell ZFS obtained from cluster models at various levels for $LiMnPO_4$

Method	**Cluster Model**					**Unitcell Model**				
	$\mathbf{D_{11}}$ (cm^{-1})	$\mathbf{D_{22}}$ (cm^{-1})	$\mathbf{D_{33}}$ (cm^{-1})	**D** (cm^{-1})	**E/D**	$\mathbf{D_{11}}$ (cm^{-1})	$\mathbf{D_{22}}$ (cm^{-1})	$\mathbf{D_{33}}$ (cm^{-1})	**D** (cm^{-1})	**E/D**
XRD structure										
NEVPT2/EFFECTIVE	-0.001	-0.023	0.023	0.035	0.315	-0.001	-0.023	0.023	0.035	0.315
NEVPT2/2NDORDER	0.002	0.021	-0.023	-0.035	0.277	0.002	0.021	-0.023	-0.035	0.277
CASSCF/EFFECTIVE	-0.005	-0.017	0.022	0.033	0.175	-0.005	-0.017	0.022	0.033	0.175
CASSCF/2NDORDER	-0.004	-0.017	0.021	0.031	0.215	-0.004	-0.017	0.021	0.031	0.215
PBE0/SOMF/common	0.004	0.052	-0.057	-0.085	0.283	0.004	0.052	-0.057	-0.085	0.283
PBE/SOMF/common	0.011	0.023	-0.034	-0.051	0.112	0.011	0.023	-0.034	-0.051	0.112
PBE/AMFI/common	0.011	0.023	-0.034	-0.051	0.112	0.011	0.023	-0.034	-0.051	0.112
OPT structure										
NEVPT2/EFFECTIVE	0.008	0.025	-0.034	-0.051	0.169	0.008	0.025	-0.034	-0.051	0.169
NEVPT2/2NDORDER	0.010	0.023	-0.033	-0.050	0.126	0.010	0.023	-0.033	-0.050	0.126
CASSCF/EFFECTIVE	-0.002	-0.021	0.023	0.035	0.276	-0.002	-0.021	0.023	0.035	0.276
CASSCF/2NDORDER	-0.001	-0.021	0.021	0.032	0.311	-0.001	-0.021	0.021	0.032	0.311
PBE0/SOMF/common	0.016	0.036	-0.052	-0.078	0.127	0.016	0.036	-0.052	-0.078	0.127
PBE/SOMF/common	0.026	0.048	-0.074	-0.111	0.100	0.026	0.048	-0.074	-0.111	0.100
PBE/AMFI/common	-0.049	-0.071	0.120	0.181	0.061	-0.049	-0.071	0.120	0.181	0.061

[a] The cluster models ZFS for unit.cell obtained by replacing the computed ZFS into the solid-state structures after averaging. ZFS have been computed at PBE/def2-TZVP/IGLO-II level (see Computational Details in Chapter 5).

Table C.10.: Comparison of computed[a] unit-cell ZFS obtained from cluster models at various levels for $FePO_4$

Method	**Cluster Model**					**Unitcell Model**				
	$\mathbf{D_{11}}$ (cm^{-1})	$\mathbf{D_{22}}$ (cm^{-1})	$\mathbf{D_{33}}$ (cm^{-1})	**D** (cm^{-1})	**E/D**	$\mathbf{D_{11}}$ (cm^{-1})	$\mathbf{D_{22}}$ (cm^{-1})	$\mathbf{D_{33}}$ (cm^{-1})	**D** (cm^{-1})	**E/D**
XRD structure										
NEVPT2/EFFECTIVE	0.076	0.179	-0.254	-0.381	0.135	0.076	0.179	-0.254	-0.381	0.135
NEVPT2/2NDORDER	0.080	0.165	-0.245	-0.368	0.116	0.080	0.165	-0.245	-0.368	0.116
CASSCF/EFFECTIVE	0.030	0.093	-0.123	-0.184	0.171	0.030	0.093	-0.123	-0.184	0.171
CASSCF/2NDORDER	0.032	0.086	-0.119	-0.178	0.151	0.032	0.086	-0.119	-0.178	0.151
PBE0/SOMF/common	0.083	0.220	-0.304	-0.455	0.150	0.083	0.220	-0.304	-0.455	0.150
PBE/SOMF/common	0.128	0.186	-0.314	-0.472	0.062	0.128	0.186	-0.314	-0.472	0.062
PBE/AMFI/common	0.128	0.186	-0.314	-0.472	0.062	0.128	0.186	-0.314	-0.472	0.062
OPT structure										
NEVPT2/EFFECTIVE	0.040	0.118	-0.159	-0.238	0.164	0.040	0.118	-0.159	-0.238	0.164
NEVPT2/2NDORDER	0.040	0.108	-0.148	-0.221	0.153	0.040	0.108	-0.148	-0.221	0.153
CASSCF/EFFECTIVE	0.014	0.066	-0.080	-0.120	0.215	0.014	0.066	-0.080	-0.120	0.215
CASSCF/2NDORDER	0.014	0.061	-0.075	-0.112	0.212	0.014	0.061	-0.075	-0.112	0.212
PBE0/SOMF/common	0.058	0.125	-0.183	-0.274	0.121	0.058	0.125	-0.183	-0.274	0.121
PBE/SOMF/common	0.046	0.107	-0.153	-0.229	0.134	0.046	0.107	-0.153	-0.229	0.134
PBE/AMFI/common	0.046	0.107	-0.153	-0.229	0.134	0.046	0.107	-0.153	-0.229	0.134

[a] The cluster models ZFS for unit.cell obtained by replacing the computed ZFS into the solid-state structures after averaging. ZFS have been computed at PBE/def2-TZVP/IGLO-II level (see Computational Details in Chapter 5).

Table C.11.: Comparison of computed[a] unit-cell ZFS obtained from cluster models at various levels for $LiFePO_4$

Method	Cluster Model					Unitcell Model				
	$\mathbf{D_{11}}$ (cm^{-1})	$\mathbf{D_{22}}$ (cm^{-1})	$\mathbf{D_{33}}$ (cm^{-1})	**D** (cm^{-1})	**E/D**	$\mathbf{D_{11}}$ (cm^{-1})	$\mathbf{D_{22}}$ (cm^{-1})	$\mathbf{D_{33}}$ (cm^{-1})	**D** (cm^{-1})	**E/D**
XRD structure										
NEVPT2/EFFECTIVE	-1.532	-5.093	6.626	9.938	0.179	-1.532	-5.093	6.626	9.938	0.179
NEVPT2/2NDORDER	-1.589	-5.521	7.110	10.666	0.184	-1.589	-5.521	7.110	10.666	0.184
CASSCF/EFFECTIVE	-1.578	-5.780	7.359	11.038	0.190	-1.578	-5.780	7.359	11.038	0.190
CASSCF/2NDORDER	-1.616	-6.329	7.945	11.918	0.198	-1.616	-6.329	7.945	11.918	0.198
PBE0/SOMF/common	-0.808	-2.143	2.950	4.425	0.151	-0.808	-2.143	2.950	4.425	0.151
PBE/SOMF/common	-0.457	-1.388	1.844	2.767	0.168	-0.457	-1.388	1.844	2.767	0.168
PBE/AMFI/common	-0.460	-1.386	1.845	2.768	0.167	-0.460	-1.386	1.845	2.768	0.167
OPT structure										
NEVPT2/EFFECTIVE	-1.282	-5.240	6.521	9.782	0.202	-1.282	-5.240	6.521	9.782	0.202
NEVPT2/2NDORDER	-1.316	-5.683	6.999	10.498	0.208	-1.316	-5.683	6.999	10.498	0.208
CASSCF/EFFECTIVE	-1.290	-5.973	7.263	10.894	0.215	-1.290	-5.973	7.263	10.894	0.215
CASSCF/2NDORDER	-1.299	-6.543	7.843	11.764	0.223	-1.299	-6.543	7.843	11.764	0.223
PBE0/SOMF/common	-0.779	-2.183	2.962	4.443	0.158	-0.779	-2.183	2.962	4.443	0.158
PBE/SOMF/common	-0.380	-1.425	1.805	2.707	0.193	-0.380	-1.425	1.805	2.707	0.193
PBE/AMFI/common	-0.380	-1.425	1.805	2.707	0.193	-0.380	-1.425	1.805	2.707	0.193

[a] The cluster models ZFS for unit.cell obtained by replacing the computed ZFS into the solid-state structures after averaging. ZFS have been computed at PBE/def2-TZVP/IGLO-II level (see Computational Details in Chapter 5).

Table C.12.: Comparison of computed[a] unit-cell ZFS obtained from cluster models at various levels for $LiCoPO_4$

Method	Cluster Model					Unitcell Model				
	$\mathbf{D_{11}}$ (cm^{-1})	$\mathbf{D_{22}}$ (cm^{-1})	$\mathbf{D_{33}}$ (cm^{-1})	**D** (cm^{-1})	**E/D**	$\mathbf{D_{11}}$ (cm^{-1})	$\mathbf{D_{22}}$ (cm^{-1})	$\mathbf{D_{33}}$ (cm^{-1})	**D** (cm^{-1})	**E/D**
XRD structure										
NEVPT2/EFFECTIVE	-13.662	-34.199	47.862	71.793	0.143	-13.662	-34.199	47.862	71.793	0.143
NEVPT2/2NDORDER	-12.209	-39.584	51.793	77.690	0.176	-12.209	-39.584	51.793	77.690	0.176
CASSCF/EFFECTIVE	-14.974	-42.292	57.266	85.898	0.159	-14.974	-42.292	57.266	85.898	0.159
CASSCF/2NDORDER	-10.761	-56.379	67.140	100.710	0.226	-10.761	-56.379	67.140	100.710	0.226
PBE/SOMF/common	0.386	-1.834	1.448	2.172	0.511	0.386	-1.834	1.448	2.172	0.511
PBE/AMFI/common	0.387	-1.844	1.457	2.185	0.511	0.387	-1.844	1.457	2.185	0.511
OPT structure										
NEVPT2/EFFECTIVE	-12.961	-34.329	47.290	70.935	0.151	-12.961	-34.329	47.290	70.935	0.151
NEVPT2/2NDORDER	-11.967	-40.062	52.029	78.044	0.180	-11.967	-40.062	52.029	78.044	0.180
CASSCF/EFFECTIVE	-13.966	-42.634	56.600	84.899	0.169	-13.966	-42.634	56.600	84.899	0.169
CASSCF/2NDORDER	-10.430	-57.186	67.616	101.424	0.230	-10.430	-57.186	67.616	101.424	0.230
PBE/SOMF/common	0.414	-2.086	1.673	2.509	0.498	0.414	-2.086	1.673	2.509	0.498
PBE/AMFI/common	0.412	-2.068	1.655	2.483	0.499	0.412	-2.068	1.655	2.483	0.499

[a] The cluster models ZFS for unit.cell obtained by replacing the computed ZFS into the solid-state structures after averaging. ZFS have been computed at PBE/def2-TZVP/IGLO-II level (see Computational Details in Chapter 5).

Table C.13.: Comparison of computed[a] unit-cell ZFS obtained from cluster models at various levels for $LiNiPO_4$

Method	**Cluster Model**					**Unitcell Model**				
	$\mathbf{D_{11}}$ (cm^{-1})	$\mathbf{D_{22}}$ (cm^{-1})	$\mathbf{D_{33}}$ (cm^{-1})	**D** (cm^{-1})	**E/D**	$\mathbf{D_{11}}$ (cm^{-1})	$\mathbf{D_{22}}$ (cm^{-1})	$\mathbf{D_{33}}$ (cm^{-1})	**D** (cm^{-1})	**E/D**
XRD structure										
NEVPT2/EFFECTIVE	0.814	8.188	-9.002	-13.502	0.273	0.814	8.188	-9.002	-13.502	0.273
NEVPT2/2NDORDER	0.672	9.249	-9.921	-14.881	0.288	0.672	9.249	-9.921	-14.881	0.288
CASSCF/EFFECTIVE	0.811	12.064	-12.874	-19.311	0.291	0.811	12.064	-12.874	-19.311	0.291
CASSCF/2NDORDER	0.455	14.598	-15.053	-22.579	0.313	0.455	14.598	-15.053	-22.579	0.313
PBE0/SOMF/common	6.741	20.014	-26.755	-40.132	0.165	6.741	20.014	-26.755	-40.132	0.165
PBE/SOMF/common	0.696	1.543	-2.239	-3.359	0.126	0.696	1.543	-2.239	-3.359	0.126
PBE/AMFI/common	0.696	1.543	-2.239	-3.359	0.126	0.696	1.543	-2.239	-3.359	0.126
OPT structure										
NEVPT2/EFFECTIVE	1.457	7.264	-8.721	-13.082	0.222	1.457	7.264	-8.721	-13.082	0.222
NEVPT2/2NDORDER	1.414	8.151	-9.565	-14.347	0.235	1.414	8.151	-9.565	-14.347	0.235
CASSCF/EFFECTIVE	1.776	10.888	-12.664	-18.996	0.240	1.776	10.888	-12.664	-18.996	0.240
CASSCF/2NDORDER	1.657	13.058	-14.715	-22.072	0.258	1.657	13.058	-14.715	-22.072	0.258
PBE0/SOMF/common	5.679	7.220	-12.899	-19.349	0.040	5.679	7.220	-12.899	-19.349	0.040
PBE/SOMF/common	1.011	1.702	-2.714	-4.070	0.085	1.011	1.702	-2.714	-4.070	0.085
PBE/AMFI/common	1.011	1.702	-2.714	-4.070	0.085	1.011	1.702	-2.714	-4.070	0.085

[a] The cluster models ZFS for unit.cell obtained by replacing the computed ZFS into the solid-state structures after averaging. ZFS have been computed at PBE/def2-TZVP/IGLO-II level (see Computational Details in Chapter 5).

Table C.14.: Comparison of computed[a] unit-cell ZFS obtained from cluster models at various levels for $CoPO_4$

Method	Cluster Model					Unitcell Model				
	$\mathbf{D_{11}}$ (cm^{-1})	$\mathbf{D_{22}}$ (cm^{-1})	$\mathbf{D_{33}}$ (cm^{-1})	**D** (cm^{-1})	**E/D**	$\mathbf{D_{11}}$ (cm^{-1})	$\mathbf{D_{22}}$ (cm^{-1})	$\mathbf{D_{33}}$ (cm^{-1})	**D** (cm^{-1})	**E/D**
XRD structure										
NEVPT2/EFFECTIVE	-0.344	-5.744	6.088	9.133	0.296	-0.344	-5.744	6.088	9.133	0.296
NEVPT2/2NDORDER	-0.337	-6.724	7.061	10.592	0.301	-0.337	-6.724	7.061	10.592	0.301
CASSCF/EFFECTIVE	-0.648	-3.927	4.575	6.863	0.239	-0.648	-3.927	4.575	6.863	0.239
CASSCF/2NDORDER	-2.604	-3.891	6.495	9.742	0.066	-2.604	-3.891	6.495	9.742	0.066
PBE/SOMF/common	-0.803	-3.067	3.870	5.804	0.195	-0.803	-3.067	3.870	5.804	0.195
PBE/AMFI/common	-0.761	-3.060	3.821	5.732	0.201	-0.761	-3.060	3.821	5.732	0.201
OPT structure										
NEVPT2/EFFECTIVE	1.408	4.174	-5.582	-8.373	0.165	1.408	4.174	-5.582	-8.373	0.165
NEVPT2/2NDORDER	1.737	4.726	-6.463	-9.695	0.154	1.737	4.726	-6.463	-9.695	0.154
CASSCF/EFFECTIVE	-0.515	-2.511	3.027	4.540	0.220	-0.515	-2.511	3.027	4.540	0.220
CASSCF/2NDORDER	0.271	4.328	-4.599	-6.899	0.294	0.271	4.328	-4.599	-6.899	0.294
PBE/SOMF/common	-0.280	-2.470	2.751	4.126	0.265	-0.280	-2.470	2.751	4.126	0.265
PBE/AMFI/common	-0.280	-2.470	2.751	4.126	0.265	-0.280	-2.470	2.751	4.126	0.265

[a] The cluster models ZFS for unit.cell obtained by replacing the computed ZFS into the solid-state structures after averaging. ZFS have been computed at PBE/def2-TZVP/IGLO-II level (see Computational Details in Chapter 5).

Table C.15.: Comparison of P-O, Li-O bond distance, O-P-O, O-Li-O bond length extracted from the XRD structures of the phosphate materials

bond	**material**	$\mathbf{d}_1$	$\mathbf{d}_2$	$\mathbf{d}_3$	$\mathbf{a}_1$	$\mathbf{a}_2$	$\mathbf{a}_3$
P-O	$LiMnPO_4$	1.53	1.54	1.55	104.63	106.85	112.59
	$LiFePO_4$	1.53	1.54	1.55	103.55	106.48	113.28
	$LiCoPO_4$	1.51	1.53	1.56	102.68	106.38	113.62
	$LiNiPO_4$	1.52	1.54	1.55	102.71	106.12	113.84
	$FePO_4$	1.48	1.52	1.58	103.52	109.63	114.86
	$CoPO_4$	1.53	1.54	1.54	103.36	110.68	112.98
Li-O	$LiMnPO_4$	2.09	2.17	2.19	91.29	95.91	109.42
	$LiFePO_4$	2.09	2.17	2.19	91.83	96.34	109.34
	$LiCoPO_4$	2.08	2.16	2.17	90.62	95.82	108.73
	$LiNiPO_4$	2.08	2.13	2.14	90.40	95.81	108.14

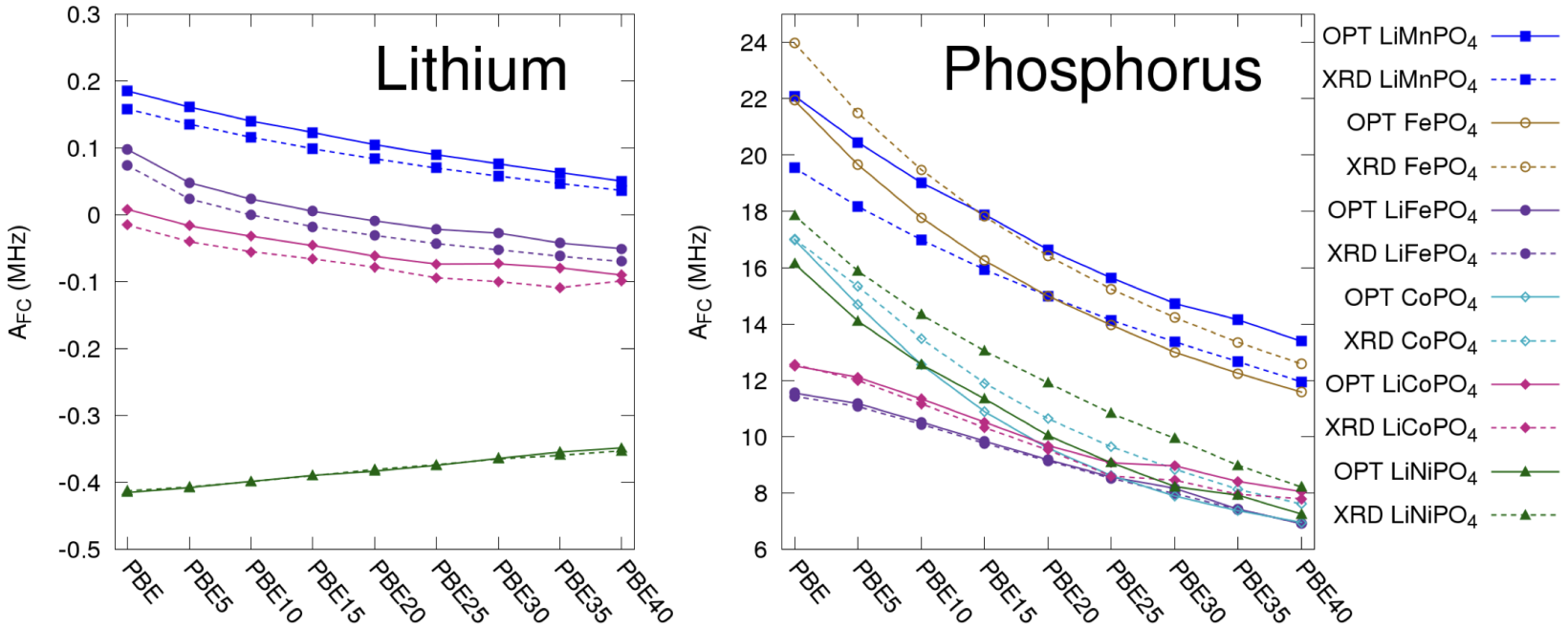

Figure C.5.: Comparison of lithium (left) and phosphorus (right) HFCs computed for both XRD and optimized (OPT) structures. Variations with EXX admixture to PBE-based functionals for the HFC tensors are shown. (see Tables from S16 till S20 in Supporting Information for numerical values).

Table C.16.: Comparison of computed[a] HFC tensors using both PBE and PBE-based global hybrids with varying EXX admixture between 5% (PBE5) and 40% (PBE40) for lithium and phosphorus sites of $LiMnPO_4$ for the XRD and optimized structures

Atom	**Functional**	**XRD**						**OPT**					
		$\mathbf{A_{FC}}$	$\mathbf{A_{dip}}$ (MHz)			$\boldsymbol{\Delta}$[b]	$\boldsymbol{\eta}$[c]	$\mathbf{A_{FC}}$	$\mathbf{A_{dip}}$ (MHz)			$\boldsymbol{\Delta}$[b]	$\boldsymbol{\eta}$[c]
		(MHz)	A_{11}	A_{22}	A_{33}	(MHz)		(MHz)	A_{11}	A_{22}	A_{33}	(MHz)	
Li	PBE	0.16	-1.31	-0.85	2.16	3.25	0.21	0.19	-1.29	-0.87	2.16	3.23	0.20
	PBE5	0.14	-1.32	-0.86	2.18	3.26	0.21	0.16	-1.29	-0.87	2.17	3.25	0.19
	PBE10	0.12	-1.32	-0.87	2.19	3.28	0.21	0.14	-1.30	-0.88	2.18	3.27	0.19
	PBE15	0.10	-1.32	-0.87	2.20	3.29	0.21	0.12	-1.30	-0.89	2.19	3.28	0.19
	PBE20	0.08	-1.33	-0.88	2.20	3.31	0.20	0.10	-1.30	-0.89	2.19	3.29	0.19
	PBE25	0.07	-1.33	-0.88	2.21	3.32	0.20	0.09	-1.31	-0.89	2.20	3.30	0.19
	PBE30	0.06	-1.33	-0.88	2.22	3.33	0.20	0.08	-1.31	-0.90	2.21	3.31	0.19
	PBE35	0.05	-1.33	-0.89	2.22	3.33	0.20	0.06	-1.31	-0.90	2.21	3.32	0.19
	PBE40	0.04	-1.34	-0.89	2.23	3.34	0.20	0.05	-1.31	-0.90	2.22	3.33	0.19
P	PBE	19.54	-0.59	-0.45	1.05	1.57	0.13	22.10	-0.59	-0.40	0.99	1.49	0.19
	PBE5	18.18	-0.61	-0.46	1.07	1.60	0.13	20.45	-0.61	-0.41	1.02	1.53	0.20
	PBE10	16.99	-0.62	-0.47	1.09	1.63	0.13	19.02	-0.62	-0.42	1.04	1.56	0.20
	PBE15	15.93	-0.63	-0.48	1.11	1.66	0.13	17.89	-0.63	-0.42	1.06	1.59	0.20
	PBE20	15.00	-0.64	-0.48	1.12	1.68	0.14	16.64	-0.65	-0.43	1.07	1.61	0.20
	PBE25	14.14	-0.65	-0.49	1.13	1.70	0.14	15.64	-0.66	-0.43	1.09	1.63	0.21
	PBE30	13.37	-0.65	-0.49	1.15	1.72	0.14	14.73	-0.67	-0.43	1.10	1.65	0.21
	PBE35	12.66	-0.66	-0.49	1.16	1.74	0.15	14.15	-0.67	-0.43	1.11	1.66	0.22
	PBE40	11.95	-0.67	-0.50	1.17	1.75	0.15	13.39	-0.68	-0.44	1.12	1.68	0.22

[a] All computations were done for a 2 × 2 × 2 super-cell using IGLO-II/8s7p4d basis sets (see Computational Details in Chapter 5).

[b] Anisotropy (Δ) = A_{zz} - $\frac{1}{2}(A_{xx} + A_{yy})$; the components are ordered as $\mid A_{zz} - A_{iso} \mid \geq \mid A_{yy} - A_{iso} \mid \geq \mid A_{xx} - A_{iso} \mid$ and $A_{iso} = \frac{1}{3}(A_{xx} + A_{yy} + A_{zz})$.

[c] Asymmetry (η) = $\frac{A_{xx} - A_{yy}}{A_{zz} - A_{iso}}$.

Table C.17.: Comparison of computed[a] HFC tensors using both PBE and PBE-based global hybrids with varying EXX admixture between 5% (PBE5) and 40% (PBE40) for lithium and phosphorus sites of $LiFePO_4$ for the XRD and optimized structures

Atom	Functional	XRD						OPT					
		$\mathbf{A_{FC}}$	$\mathbf{A_{dip}}$ (MHz)			$\mathbf{\Delta}^{b}$	$\boldsymbol{\eta}^{c}$	$\mathbf{A_{FC}}$	$\mathbf{A_{dip}}$ (MHz)			$\mathbf{\Delta}^{b}$	$\boldsymbol{\eta}^{c}$
		(MHz)	A_{11}	A_{22}	A_{33}	(MHz)		(MHz)	A_{11}	A_{22}	A_{33}	(MHz)	
Li	PBE	0.07	-1.41	-0.82	2.22	3.33	0.27	0.10	-1.38	-0.83	2.21	3.31	0.25
	PBE5	0.02	-1.41	-0.83	2.24	3.36	0.26	0.05	-1.39	-0.84	2.23	3.34	0.25
	PBE10	0.00	-1.42	-0.84	2.26	3.39	0.25	0.02	-1.39	-0.85	2.24	3.36	0.24
	PBE15	-0.02	-1.42	-0.85	2.27	3.41	0.25	0.01	-1.40	-0.86	2.26	3.38	0.24
	PBE20	-0.03	-1.42	-0.86	2.28	3.42	0.25	-0.01	-1.40	-0.87	2.27	3.40	0.23
	PBE25	-0.04	-1.43	-0.87	2.29	3.44	0.24	-0.02	-1.40	-0.88	2.28	3.42	0.23
	PBE30	-0.05	-1.43	-0.87	2.30	3.45	0.24	-0.03	-1.40	-0.88	2.29	3.43	0.23
	PBE35	-0.06	-1.43	-0.88	2.31	3.46	0.24	-0.04	-1.41	-0.89	2.29	3.44	0.23
	PBE40	-0.07	-1.43	-0.88	2.31	3.47	0.24	-0.05	-1.41	-0.89	2.30	3.45	0.22
P	PBE	11.44	-0.30	-0.25	0.55	0.82	0.08	11.55	-0.30	-0.26	0.56	0.84	0.08
	PBE5	11.07	-0.35	-0.20	0.55	0.82	0.26	11.18	-0.35	-0.21	0.56	0.84	0.25
	PBE10	10.44	-0.38	-0.20	0.59	0.88	0.31	10.52	-0.39	-0.21	0.59	0.89	0.30
	PBE15	9.77	-0.41	-0.21	0.62	0.94	0.32	9.84	-0.41	-0.22	0.63	0.95	0.30
	PBE20	9.14	-0.43	-0.23	0.66	0.99	0.32	9.18	-0.43	-0.23	0.67	1.00	0.30
	PBE25	8.52	-0.45	-0.24	0.69	1.04	0.32	8.57	-0.45	-0.24	0.70	1.05	0.30
	PBE30	7.98	-0.47	-0.25	0.72	1.08	0.31	8.17	-0.46	-0.26	0.72	1.09	0.28
	PBE35	7.42	-0.49	-0.26	0.74	1.12	0.31	7.43	-0.48	-0.27	0.75	1.12	0.29
	PBE40	6.92	-0.50	-0.27	0.77	1.15	0.30	6.91	-0.50	-0.27	0.77	1.16	0.29

[a] All computations were done for a 2 × 2 × 2 super-cell using IGLO-II/8s7p4d basis sets (see Computational Details in Chapter 5).

[b] Anisotropy $(\Delta) = A_{zz}$ - $\frac{1}{2}(A_{xx} + A_{yy})$; the components are ordered as $\mid A_{zz} - A_{iso} \mid \geq \mid A_{yy} - A_{iso} \mid \geq \mid A_{xx} - A_{iso} \mid$ and $A_{iso} = \frac{1}{3}(A_{xx} + A_{yy} + A_{zz})$.

[c] Asymmetry $(\eta) = \frac{A_{xx} - A_{yy}}{A_{zz} - A_{iso}}$.

Table C.18.: Comparison of computed[a] HFC tensors using both PBE and PBE-based global hybrids with varying EXX admixture between 5% (PBE5) and 40% (PBE40) for lithium and phosphorus sites of $LiCoPO_4$ for the XRD and optimized structures

Atom	**Functional**	**XRD**						**OPT**					
		$\mathbf{A_{FC}}$	$\mathbf{A_{dip}}$ (MHz)			$\boldsymbol{\Delta}$[b]	$\boldsymbol{\eta}$[c]	$\mathbf{A_{FC}}$	$\mathbf{A_{dip}}$ (MHz)			$\boldsymbol{\Delta}$[b]	$\boldsymbol{\eta}$[c]
		(MHz)	A_{11}	A_{22}	A_{33}	(MHz)		(MHz)	A_{11}	A_{22}	A_{33}	(MHz)	
Li	PBE	-0.02	-1.37	-0.94	2.32	3.47	0.19	0.01	-1.37	-0.92	2.29	3.44	0.20
	PBE5	-0.04	-1.38	-0.96	2.34	3.51	0.18	-0.02	-1.37	-0.94	2.32	3.47	0.19
	PBE10	-0.06	-1.38	-0.98	2.36	3.55	0.17	-0.03	-1.38	-0.96	2.34	3.51	0.18
	PBE15	-0.07	-1.39	-1.00	2.38	3.58	0.16	-0.05	-1.38	-0.97	2.36	3.54	0.17
	PBE20	-0.08	-1.39	-1.01	2.40	3.60	0.16	-0.06	-1.39	-0.99	2.37	3.56	0.17
	PBE25	-0.09	-1.39	-1.02	2.42	3.62	0.15	-0.07	-1.39	-1.00	2.39	3.58	0.17
	PBE30	-0.10	-1.40	-1.03	2.43	3.64	0.15	-0.07	-1.40	-1.01	2.40	3.60	0.16
	PBE35	-0.11	-1.40	-1.04	2.44	3.65	0.15	-0.08	-1.40	-1.01	2.41	3.62	0.16
	PBE40	-0.10	-1.40	-1.05	2.45	3.67	0.14	-0.09	-1.40	-1.02	2.42	3.63	0.16
P	PBE	12.57	-0.92	0.42	0.50	-1.37	0.08	12.52	-0.92	0.43	0.49	-1.39	0.07
	PBE5	12.00	-0.91	0.43	0.48	-1.37	0.06	12.11	-0.94	0.45	0.49	-1.40	0.05
	PBE10	11.17	-0.91	0.38	0.54	-1.37	0.18	11.34	-0.95	0.40	0.55	-1.42	0.16
	PBE15	10.32	-0.93	0.34	0.59	-1.39	0.27	10.52	-0.96	0.35	0.60	-1.44	0.26
	PBE20	9.53	-0.95	0.30	0.65	-1.42	0.37	9.69	-0.96	0.31	0.65	-1.45	0.35
	PBE25	8.61	-0.96	0.27	0.69	-1.43	0.44	9.07	-0.97	0.27	0.69	-1.45	0.44
	PBE30	8.45	-0.96	0.23	0.73	-1.43	0.53	8.96	-0.95	0.22	0.73	-1.43	0.53
	PBE35	7.96	-0.97	0.20	0.77	-1.45	0.59	8.41	-0.98	0.22	0.76	-1.47	0.55
	PBE40	7.79	-0.95	0.16	0.79	-1.42	0.67	8.05	-0.94	0.15	0.79	-1.41	0.69

[a] All computations were done for a 2 × 2 × 2 super-cell using IGLO-II/8s7p4d basis sets (see Computational Details in Chapter 5).

[b] Anisotropy (Δ) = A_{zz} - $\frac{1}{2}(A_{xx} + A_{yy})$; the components are ordered as $\mid A_{zz} - A_{iso} \mid \geq \mid A_{yy} - A_{iso} \mid \geq \mid A_{xx} - A_{iso} \mid$ and $A_{iso} = \frac{1}{3}(A_{xx} + A_{yy} + A_{zz})$.

[c] Asymmetry (η) = $\frac{A_{xx} - A_{yy}}{A_{zz} - A_{iso}}$.

Table C.19.: Comparison of computed[a] HFC tensors using both PBE and PBE-based global hybrids with varying EXX admixture between 5% (PBE5) and 40% (PBE40) for lithium and phosphorus sites of $LiNiPO_4$ for the XRD and optimized structures

Atom	Functional	XRD						OPT					
		$\mathbf{A_{FC}}$	$\mathbf{A_{dip}}$ (MHz)			$\mathbf{\Delta}^b$	$\boldsymbol{\eta}^c$	$\mathbf{A_{FC}}$	$\mathbf{A_{dip}}$ (MHz)			$\mathbf{\Delta}^b$	$\boldsymbol{\eta}^c$
		(MHz)	A_{11}	A_{22}	A_{33}	(MHz)		(MHz)	A_{11}	A_{22}	A_{33}	(MHz)	
Li	PBE	-0.41	-1.35	-1.08	2.42	3.63	0.11	-0.41	-1.31	-1.11	2.42	3.63	0.08
	PBE5	-0.41	-1.36	-1.11	2.48	3.72	0.10	-0.41	-1.32	-1.15	2.48	3.72	0.07
	PBE10	-0.40	-1.38	-1.15	2.53	3.79	0.09	-0.40	-1.34	-1.19	2.53	3.79	0.06
	PBE15	-0.39	-1.39	-1.18	2.57	3.86	0.08	-0.39	-1.35	-1.22	2.57	3.86	0.05
	PBE20	-0.38	-1.40	-1.21	2.61	3.91	0.08	-0.38	-1.37	-1.24	2.61	3.91	0.05
	PBE25	-0.37	-1.41	-1.23	2.64	3.96	0.07	-0.37	-1.38	-1.27	2.64	3.96	0.04
	PBE30	-0.36	-1.42	-1.25	2.67	4.00	0.06	-0.36	-1.38	-1.29	2.67	4.01	0.04
	PBE35	-0.36	-1.42	-1.27	2.69	4.03	0.06	-0.35	-1.39	-1.30	2.69	4.04	0.03
	PBE40	-0.35	-1.43	-1.28	2.71	4.07	0.06	-0.35	-1.40	-1.32	2.72	4.07	0.03
P	PBE	17.85	-1.18	-0.90	2.08	3.12	0.14	16.14	-1.13	-0.86	1.99	2.98	0.13
	PBE5	15.88	-1.28	-0.66	1.95	2.92	0.32	14.11	-1.22	-0.62	1.84	2.76	0.32
	PBE10	14.33	-1.35	-0.47	1.82	2.73	0.48	12.56	-1.28	-0.43	1.71	2.57	0.50
	PBE15	13.05	-1.41	-0.30	1.71	2.56	0.65	11.34	-1.33	-0.26	1.59	2.39	0.67
	PBE20	11.91	-1.45	-0.16	1.60	2.41	0.80	10.04	-1.37	-0.12	1.49	2.24	0.84
	PBE25	10.82	-1.48	-0.03	1.51	2.27	0.96	9.07	-1.40	0.01	1.39	-2.10	0.99
	PBE30	9.94	-1.50	0.08	1.42	-2.25	0.90	8.23	-1.42	0.12	1.31	-2.13	0.84
	PBE35	8.98	-1.52	0.18	1.35	-2.28	0.77	7.92	-1.42	0.21	1.21	-2.13	0.70
	PBE40	8.21	-1.53	0.26	1.27	-2.30	0.66	7.25	-1.43	0.30	1.14	-2.15	0.59

[a] All computations were done for a 2 × 2 × 2 super-cell using IGLO-II/8s7p4d basis sets (see Computational Details in Chapter 5).

[b] Anisotropy $(\Delta) = A_{zz}$ - $\frac{1}{2}(A_{xx} + A_{yy})$; the components are ordered as $\mid A_{zz} - A_{iso} \mid \geq \mid A_{yy} - A_{iso} \mid \geq \mid A_{xx} - A_{iso} \mid$ and $A_{iso} = \frac{1}{3}(A_{xx} + A_{yy} + A_{zz})$.

[c] Asymmetry $(\eta) = \frac{A_{xx} - A_{yy}}{A_{zz} - A_{iso}}$.

Table C.20.: Comparison of computed[a] HFC tensors using both PBE and PBE-based global hybrids with varying EXX admixture between 5% (PBE5) and 40% (PBE40) for lithium and phosphorus sites of $FePO_4$ and $CoPO_4$for the XRD and optimized structures

Material	**Functional**	**XRD**						**OPT**					
		$\mathbf{A_{FC}}$	$\mathbf{A_{dip}}$ (MHz)			$\boldsymbol{\Delta}$[b]	$\boldsymbol{\eta}$[c]	$\mathbf{A_{FC}}$	$\mathbf{A_{dip}}$ (MHz)			$\boldsymbol{\Delta}$[b]	$\boldsymbol{\eta}$[c]
		(MHz)	A_{11}	A_{22}	A_{33}	(MHz)		(MHz)	A_{11}	A_{22}	A_{33}	(MHz)	
$FePO_4$	PBE	23.97	-1.74	0.61	1.13	-2.61	0.30	21.94	-1.91	0.39	1.52	-2.86	0.59
	PBE5	21.50	-1.71	0.62	1.09	-2.57	0.27	19.66	-1.90	0.44	1.46	-2.85	0.54
	PBE10	19.48	-1.68	0.63	1.05	-2.53	0.25	17.78	-1.89	0.48	1.41	-2.84	0.49
	PBE15	17.81	-1.66	0.64	1.02	-2.48	0.23	16.25	-1.89	0.52	1.37	-2.83	0.45
	PBE20	16.42	-1.63	0.65	0.98	-2.44	0.21	14.99	-1.88	0.55	1.32	-2.81	0.41
	PBE25	15.24	-1.60	0.65	0.95	-2.41	0.19	13.96	-1.87	0.58	1.28	-2.80	0.38
	PBE30	14.23	-1.58	0.66	0.92	-2.37	0.17	13.00	-1.86	0.61	1.24	-2.78	0.34
	PBE35	13.35	-1.56	0.66	0.89	-2.33	0.15	12.25	-1.84	0.64	1.21	-2.76	0.31
	PBE40	12.58	-1.53	0.67	0.86	-2.30	0.12	11.58	-1.83	0.66	1.17	-2.75	0.28
$CoPO_4$	PBE	17.01	-2.61	-0.36	2.97	4.45	0.76	16.99	-2.78	-0.13	2.90	4.36	0.91
	PBE5	15.34	-2.55	-0.30	2.85	4.27	0.79	14.68	-2.73	-0.05	2.79	4.18	0.96
	PBE10	13.48	-2.55	-0.20	2.75	4.12	0.85	12.56	-2.75	0.04	2.70	-4.12	0.97
	PBE15	11.90	-2.55	-0.11	2.66	3.99	0.92	10.89	-2.76	0.13	2.63	-4.13	0.91
	PBE20	10.64	-2.55	-0.03	2.57	3.86	0.98	9.59	-2.76	0.20	2.56	-4.14	0.85
	PBE25	9.64	-2.55	0.05	2.50	-3.82	0.96	8.62	-2.77	0.28	2.49	-4.16	0.80
	PBE30	8.85	-2.55	0.12	2.42	-3.82	0.90	7.89	-2.78	0.34	2.44	-4.17	0.75
	PBE35	8.13	-2.54	0.18	2.36	-3.81	0.86	7.37	-2.78	0.40	2.38	-4.17	0.71
	PBE40	7.61	-2.54	0.24	2.29	-3.81	0.81	6.96	-2.78	0.46	2.33	-4.18	0.67

[a] All computations were done for a 2 × 2 × 2 super-cell using IGLO-II/8s7p4d basis sets (see Computational Details in Chapter 5).

[b] Anisotropy (Δ) = A_{zz} - $\frac{1}{2}(A_{xx} + A_{yy})$; the components are ordered as $\mid A_{zz} - A_{iso} \mid \geq \mid A_{yy} - A_{iso} \mid \geq \mid A_{xx} - A_{iso} \mid$ and $A_{iso} = \frac{1}{3}(A_{xx} + A_{yy} + A_{zz})$.

[c] Asymmetry (η) = $\frac{A_{xx} - A_{yy}}{A_{zz} - A_{iso}}$.

Table C.21.: Orbital shift tensors[a] for lithium and phosphorus sites in $LiMPO_4$ (M=Mn, Fe, Co, Ni) and MPO_4 M=(Fe, Co) using both XRD and optimized structures

Atom	**Material**	**XRD**						**OPT**					
		$\boldsymbol{\delta}_{\mathbf{orb}}$ (ppm)				$\boldsymbol{\Delta}$[b] (ppm)	$\boldsymbol{\eta}$[c]	$\boldsymbol{\delta}_{\mathbf{orb}}$ (ppm)				$\boldsymbol{\Delta}$[b] (ppm)	$\boldsymbol{\eta}$[c]
		$\delta_{\mathrm{orb,iso}}$	δ_{11}	δ_{22}	δ_{33}			$\delta_{\mathrm{orb,iso}}$	δ_{11}	δ_{22}	δ_{33}		
Li	LiMnPO4	3.70	-2.51	0.17	13.43	14.60	0.28	4.70	-1.58	0.80	14.86	15.25	0.23
Li	LiFePO4	5.56	-0.35	4.50	12.55	10.48	0.69	7.29	1.12	7.97	12.79	-9.26	0.78
Li	LiCoPO4	8.79	1.00	5.26	20.11	16.98	0.38	10.39	2.63	9.11	19.43	13.57	0.72
Li	LiNiPO4	14.22	7.27	16.57	18.81	-10.42	0.32	17.11	11.11	19.85	20.36	-9.00	0.09
P	LiMnPO4	9.86	-23.66	19.67	33.58	-50.28	0.41	-20.26	-38.04	-26.61	3.86	36.18	0.47
P	LiFePO4	9.99	-18.96	13.95	35.00	-43.44	0.73	-5.48	-42.81	11.01	15.37	-56.00	0.12
P	LiCoPO4	3.54	-33.03	15.87	27.77	-54.85	0.33	-22.14	-62.90	-4.55	1.04	-61.15	0.14
P	LiNiPO4	13.94	-13.25	21.23	33.84	-40.79	0.46	3.28	-21.77	1.34	30.28	40.79	0.86
P	FePO4	-44.62	-61.33	-44.05	-28.49	-25.05	0.93	-60.30	-80.20	-58.11	-42.59	-29.86	0.78
P	CoPO4	9.98	-8.33	11.18	27.10	-27.47	0.87	-10.65	-28.74	-12.45	9.23	29.83	0.82

[a] Computations on $2 \times 2 \times 2$ cells at PBE/Ahlrichs-VTZ/IGLO-II level (see Computational Details in Chapter 5).

[b] Anisotropy $(\Delta) = \delta_{zz}$ - $\frac{1}{2}(\delta_{xx} + \delta_{yy})$; the components are ordered as $\mid \delta_{zz} - \delta_{iso} \mid \geq \mid \delta_{yy} - \delta_{iso} \mid \geq \mid \delta_{xx} - \delta_{iso} \mid$, $\delta_{iso} = \frac{1}{3}(\delta_{11} + \delta_{22} + \delta_{33})$ and $\delta_{11} \leq \delta_{22} \leq \delta_{33}$.

[c] Asymmetry $(\eta) = \frac{\delta_{xx} - \delta_{yy}}{\delta_{zz} - \delta_{iso}}$.

Table C.22.: pNMR shifts for $LiFePO_4$ for the optimized structure depending on the EXX admixture used for the HFC calculations[a]

$LiFePO_4$		**Isotropic chemical shift (ppm)**									
	atom	**terms**	**PBE**	**PBE5**	**PBE10**	**PBE15**	**PBE20**	**PBE25**	**PBE30**	**PBE35**	**PBE40**
OPT	^{7}Li	$\boldsymbol{\delta_{orb}}$	5.56	5.56	5.56	5.56	5.56	5.56	5.56	5.56	5.56
		$\boldsymbol{\delta_{(g_e\langle SS\rangle A_{FC})}}$	39.53	19.54	9.53	2.23	-3.68	-8.69	-10.97	-16.98	-20.44
		$\boldsymbol{\delta_{(\Delta g_{iso}\langle SS\rangle A_{FC})}}$	1.95	0.96	0.47	0.11	-0.18	-0.43	-0.54	-0.84	-1.01
		$\boldsymbol{\delta_{(\Delta \tilde{g}_e\langle SS\rangle A_{dip})}}$	1.07	1.16	1.22	1.28	1.33	1.37	1.41	1.44	1.47
		$\boldsymbol{\delta_{(g_e\langle SS\rangle A_{dip})}}$	0.65	0.76	0.84	0.90	0.96	1.01	1.06	1.09	1.13
		$\boldsymbol{\delta_{(\Delta g_{iso}\langle SS\rangle A_{dip})}}$	0.03	0.04	0.04	0.04	0.05	0.05	0.05	0.05	0.06
		$\boldsymbol{\delta_{(\Delta \tilde{g}_e\langle SS\rangle A_{FC})}}$	0.07	0.03	0.02	0.00	-0.01	-0.01	-0.02	-0.03	-0.03
		$\boldsymbol{\delta_{total}}$	48.86	28.04	17.68	10.14	4.03	-1.14	-3.45	-9.69	-13.27
	^{31}P	$\boldsymbol{\delta_{orb}}$	9.99	9.99	9.99	9.99	9.99	9.99	9.99	9.99	9.99
		$\boldsymbol{\delta_{(g_e\langle SS\rangle A_{FC})}}$	4477.85	4332.50	4078.38	3815.02	3560.14	3321.31	3165.96	2879.68	2678.62
		$\boldsymbol{\delta_{(\Delta g_{iso}\langle SS\rangle A_{FC})}}$	220.48	213.32	200.81	187.84	175.29	163.53	155.88	141.79	131.89
		$\boldsymbol{\delta_{(\Delta \tilde{g}_e\langle SS\rangle A_{dip})}}$	0.78	0.26	0.13	0.10	0.12	0.14	0.23	0.18	0.20
		$\boldsymbol{\delta_{(g_e\langle SS\rangle A_{dip})}}$	0.82	0.15	-0.02	-0.06	-0.06	-0.04	0.07	0.00	0.02
		$\boldsymbol{\delta_{(\Delta g_{iso}\langle SS\rangle A_{dip})}}$	0.04	0.01	-0.00	-0.00	-0.00	-0.00	0.00	0.00	0.00
		$\boldsymbol{\delta_{(\Delta \tilde{g}_e\langle SS\rangle A_{FC})}}$	7.43	7.18	6.76	6.33	5.90	5.51	5.25	4.78	4.44
		$\boldsymbol{\delta_{total}}$	4717.38	4563.42	4296.05	4019.22	3751.38	3500.45	3337.39	3036.42	2825.16

[a] Equation 5.3 in Chapter 5 has been used for computing the total shielding tensor. Shieldings converted to shifts for Li and P relative to aq. lithium chloride (LiCl) and 85% aq. phosphoric acid (H_3PO_4). HFC computations were done for a $2 \times 2 \times 2$ super-cell using IGLO-II/8s7p4d basis sets. g-Tensor and ZFS computations were done NEVPT2/def2-TZVP/IGLO-II level. Calculations of orbital shielding tensor were done for a unit cell at PBE/Ahlrich-VTZ/IGLO-II level (see Computational Details in Chapter 5).

Table C.23.: pNMR shifts for $LiFePO_4$ for the XRD structure depending on the EXX admixture used for the HFC calculations[a]

$LiFePO_4$		**Isotropic chemical shift (ppm)**								
	atom	**terms**	**PBE**	**PBE5**	**PBE10**	**PBE15**	**PBE20**	**PBE25**	**PBE30**	**PBE35**	**PBE40**
XRD	^{7}Li	$\boldsymbol{\delta_{orb}}$	7.29	7.29	7.29	7.29	7.29	7.29	7.29	7.29	7.29
		$\boldsymbol{\delta_{(g_e\langle SS\rangle A_{FC})}}$	29.78	9.71	0.01	-7.06	-12.49	-17.28	-21.13	-24.97	-28.11
		$\boldsymbol{\delta_{(\Delta g_{iso}\langle SS\rangle A_{FC})}}$	1.46	0.48	0.00	-0.35	-0.61	-0.85	-1.04	-1.23	-1.38
		$\boldsymbol{\delta_{(\Delta \tilde{g}_e\langle SS\rangle A_{dip})}}$	1.78	1.88	1.95	2.02	2.07	2.12	2.16	2.20	2.23
		$\boldsymbol{\delta_{(g_e\langle SS\rangle A_{dip})}}$	1.53	1.65	1.74	1.82	1.88	1.94	1.99	2.03	2.07
		$\boldsymbol{\delta_{(\Delta g_{iso}\langle SS\rangle A_{dip})}}$	0.08	0.08	0.09	0.09	0.09	0.10	0.10	0.10	0.10
		$\boldsymbol{\delta_{(\Delta \tilde{g}_e\langle SS\rangle A_{FC})}}$	0.05	0.02	0.00	-0.01	-0.02	-0.03	-0.04	-0.04	-0.05
		$\boldsymbol{\delta_{total}}$	41.98	21.10	11.08	3.80	-1.78	-6.71	-10.66	-14.61	-17.84
	^{31}P	$\boldsymbol{\delta_{orb}}$	-5.48	-5.48	-5.48	-5.48	-5.48	-5.48	-5.48	-5.48	-5.48
		$\boldsymbol{\delta_{(g_e\langle SS\rangle A_{FC})}}$	4434.07	4291.27	4047.78	3785.48	3543.27	3302.56	3093.49	2874.66	2683.11
		$\boldsymbol{\delta_{(\Delta g_{iso}\langle SS\rangle A_{FC})}}$	218.05	211.03	199.05	186.15	174.24	162.41	152.13	141.36	131.94
		$\boldsymbol{\delta_{(\Delta \tilde{g}_e\langle SS\rangle A_{dip})}}$	0.97	0.45	0.32	0.30	0.32	0.34	0.38	0.41	0.43
		$\boldsymbol{\delta_{(g_e\langle SS\rangle A_{dip})}}$	1.06	0.39	0.21	0.18	0.20	0.21	0.26	0.28	0.31
		$\boldsymbol{\delta_{(\Delta g_{iso}\langle SS\rangle A_{dip})}}$	0.05	0.02	0.01	0.01	0.01	0.01	0.01	0.01	0.02
		$\boldsymbol{\delta_{(\Delta \tilde{g}_e\langle SS\rangle A_{FC})}}$	7.39	7.15	6.75	6.31	5.90	5.50	5.15	4.79	4.47
		$\boldsymbol{\delta_{total}}$	4656.12	4504.84	4248.64	3972.95	3718.46	3465.55	3245.95	3016.03	2814.80

[a] Equation 5.3 in Chapter 5 has been used for computing the total shielding tensor. Shieldings converted to shifts for Li and P relative to aq. lithium chloride (LiCl) and 85% aq. phosphoric acid (H_3PO_4). HFC computations were done for a $2 \times 2 \times 2$ super-cell using IGLO-II/8s7p4d basis sets. g-Tensor and ZFS computations were done NEVPT2/def2-TZVP/IGLO-II level. Calculations of orbital shielding tensor were done for a unit cell at PBE/Ahlrich-VTZ/IGLO-II level (see Computational Details in Chapter 5).

Table C.24.: Comparison of experimental and computed[a] effective g-tensor for the lowest Kramers doublet of $LiCoPO_4$.

material	**structure**	$\mathbf{g_{11}}$	$\mathbf{g_{22}}$	$\mathbf{g_{33}}$
$LiCoPO_4$	XRD	6.5623	3.8217	1.8377
	OPT	6.4907	3.8811	1.8550
	exp[304]	6.16	4.14	2.53

[a] Computed effective g-values for the lowest Kramers doublet, extracted from the g- and D-tensors (EPR spin Hamiltonian parameters) computed at NEVPT2 level.

Table C.25.: pNMR shifts for $LiCoPO_4$ for the optimized structure depending on the EXX admixture used for the HFC calculations[a]

$LiCoPO_4$		**Isotropic chemical shift (ppm)**								
	atom	**terms**	**PBE**	**PBE5**	**PBE10**	**PBE15**	**PBE20**	**PBE25**	**PBE30**	**PBE35**	**PBE40**
OPT	^{7}Li	$\boldsymbol{\delta_{orb}}$	8.79	8.79	8.79	8.79	8.79	8.79	8.79	8.79	8.79
		$\boldsymbol{\delta_{(g_e\langle SS\rangle A_{FC})}}$	2.14	-4.18	-8.13	-11.66	-15.72	-18.69	-18.63	-20.20	-22.84
		$\boldsymbol{\delta_{(\Delta g_{iso}\langle SS\rangle A_{FC})}}$	0.42	-0.82	-1.60	-2.30	-3.10	-3.69	-3.67	-3.98	-4.50
		$\boldsymbol{\delta_{(\Delta \tilde{g}_e\langle SS\rangle A_{dip})}}$	-52.44	-52.79	-53.16	-53.49	-53.79	-54.05	-54.28	-54.48	-54.64
		$\boldsymbol{\delta_{(g_e\langle SS\rangle A_{dip})}}$	-63.47	-63.95	-64.42	-64.87	-65.25	-65.59	-65.88	-66.15	-66.34
		$\boldsymbol{\delta_{(\Delta g_{iso}\langle SS\rangle A_{dip})}}$	-12.51	-12.61	-12.70	-12.79	-12.87	-12.93	-12.99	-13.04	-13.08
		$\boldsymbol{\delta_{(\Delta \tilde{g}_e\langle SS\rangle A_{FC})}}$	0.05	-0.10	-0.19	-0.27	-0.36	-0.43	-0.43	-0.46	-0.52
		$\boldsymbol{\delta_{total}}$	-117.03	-125.67	-131.42	-136.58	-142.31	-146.59	-147.09	-149.53	-153.14
	^{31}P	$\boldsymbol{\delta_{orb}}$	3.54	3.54	3.54	3.54	3.54	3.54	3.54	3.54	3.54
		$\boldsymbol{\delta_{(g_e\langle SS\rangle A_{FC})}}$	3054.24	2954.40	2767.71	2565.81	2363.28	2213.14	2187.26	1905.37	1964.79
		$\boldsymbol{\delta_{(\Delta g_{iso}\langle SS\rangle A_{FC})}}$	602.22	582.53	545.72	505.91	465.98	436.38	431.27	375.69	387.41
		$\boldsymbol{\delta_{(\Delta \tilde{g}_e\langle SS\rangle A_{dip})}}$	-19.04	-20.00	-21.01	-21.88	-22.57	-23.16	-23.42	-24.30	-24.08
		$\boldsymbol{\delta_{(g_e\langle SS\rangle A_{dip})}}$	-20.15	-21.41	-22.74	-23.89	-24.82	-25.64	-26.11	-27.13	-27.13
		$\boldsymbol{\delta_{(\Delta g_{iso}\langle SS\rangle A_{dip})}}$	-3.97	-4.22	-4.48	-4.71	-4.89	-5.06	-5.15	-5.35	-5.35
		$\boldsymbol{\delta_{(\Delta \tilde{g}_e\langle SS\rangle A_{FC})}}$	70.00	67.72	63.44	58.81	54.17	50.73	50.13	43.67	45.03
		$\boldsymbol{\delta_{total}}$	3686.85	3562.55	3332.17	3083.57	2834.69	2649.92	2617.53	2271.48	2344.20

[a] Equation 5.3 in Chapter 5 has been used for computing the total shielding tensor. Shieldings converted to shifts for Li and P relative to aq. lithium chloride (LiCl) and 85% aq. phosphoric acid (H_3PO_4). HFC computations were done for a $2 \times 2 \times 2$ super-cell using IGLO-II/8s7p4d basis sets. g-Tensor and ZFS computations were done NEVPT2/def2-TZVP/IGLO-II level. Calculations of orbital shielding tensor were done for a unit cell at PBE/Ahlrich-VTZ/IGLO-II level (see Computational Details in Chapter 5).

Table C.26.: pNMR shifts for $LiCoPO_4$ for the XRD structure depending on the EXX admixture used for the HFC calculations[a]

$LiCoPO_4$		**Isotropic chemical shift (ppm)**								
	atom	**terms**	**PBE**	**PBE5**	**PBE10**	**PBE15**	**PBE20**	**PBE25**	**PBE30**	**PBE35**	**PBE40**
XRD	^{7}Li	$\boldsymbol{\delta_{orb}}$	10.39	10.39	10.39	10.39	10.39	10.39	10.39	10.39	10.39
		$\boldsymbol{\delta_{(g_e\langle SS\rangle A_{FC})}}$	-3.87	-10.13	-14.02	-16.71	-19.86	-23.90	-25.41	-27.60	-25.14
		$\boldsymbol{\delta_{(\Delta g_{iso}\langle SS\rangle A_{FC})}}$	-0.76	-1.99	-2.75	-3.28	-3.90	-4.70	-4.99	-5.42	-4.94
		$\boldsymbol{\delta_{(\Delta \tilde{g}_e\langle SS\rangle A_{dip})}}$	-52.85	-53.28	-53.65	-54.00	-54.31	-54.56	-54.74	-54.93	-55.16
		$\boldsymbol{\delta_{(g_e\langle SS\rangle A_{dip})}}$	-65.86	-66.44	-66.95	-67.42	-67.84	-68.17	-68.43	-68.67	-68.99
		$\boldsymbol{\delta_{(\Delta g_{iso}\langle SS\rangle A_{dip})}}$	-12.94	-13.05	-13.16	-13.25	-13.33	-13.40	-13.45	-13.49	-13.55
		$\boldsymbol{\delta_{(\Delta \tilde{g}_e\langle SS\rangle A_{FC})}}$	-0.09	-0.24	-0.33	-0.39	-0.46	-0.56	-0.59	-0.65	-0.59
		$\boldsymbol{\delta_{total}}$	-125.98	-134.74	-140.47	-144.66	-149.31	-154.89	-157.22	-160.37	-157.98
	^{31}P	$\boldsymbol{\delta_{orb}}$	-22.14	-22.14	-22.14	-22.14	-22.14	-22.14	-22.14	-22.14	-22.14
		$\boldsymbol{\delta_{(g_e\langle SS\rangle A_{FC})}}$	3065.71	2925.91	2723.51	2516.67	2323.05	2098.41	2061.48	1940.22	1900.61
		$\boldsymbol{\delta_{(\Delta g_{iso}\langle SS\rangle A_{FC})}}$	602.36	574.89	535.13	494.48	456.44	412.30	405.05	381.22	373.44
		$\boldsymbol{\delta_{(\Delta \tilde{g}_e\langle SS\rangle A_{dip})}}$	-18.19	-19.06	-19.75	-20.77	-21.82	-22.43	-23.05	-23.72	-23.81
		$\boldsymbol{\delta_{(g_e\langle SS\rangle A_{dip})}}$	-19.66	-20.93	-21.93	-23.28	-24.66	-25.48	-26.36	-27.27	-27.52
		$\boldsymbol{\delta_{(\Delta g_{iso}\langle SS\rangle A_{dip})}}$	-3.86	-4.11	-4.31	-4.57	-4.84	-5.01	-5.18	-5.36	-5.41
		$\boldsymbol{\delta_{(\Delta \tilde{g}_e\langle SS\rangle A_{FC})}}$	71.67	68.40	63.67	58.83	54.31	49.06	48.19	45.36	44.43
		$\boldsymbol{\delta_{total}}$	3675.88	3502.97	3254.17	2999.22	2760.34	2484.71	2437.99	2288.32	2239.61

[a] Equation 5.3 in Chapter 5 has been used for computing the total shielding tensor. Shieldings converted to shifts for Li and P relative to aq. lithium chloride (LiCl) and 85% aq. phosphoric acid (H_3PO_4). HFC computations were done for a $2 \times 2 \times 2$ super-cell using IGLO-II/8s7p4d basis sets. g-Tensor and ZFS computations were done NEVPT2/def2-TZVP/IGLO-II level. Calculations of orbital shielding tensor were done for a unit cell at PBE/Ahlrich-VTZ/IGLO-II level (see Computational Details in Chapter 5).

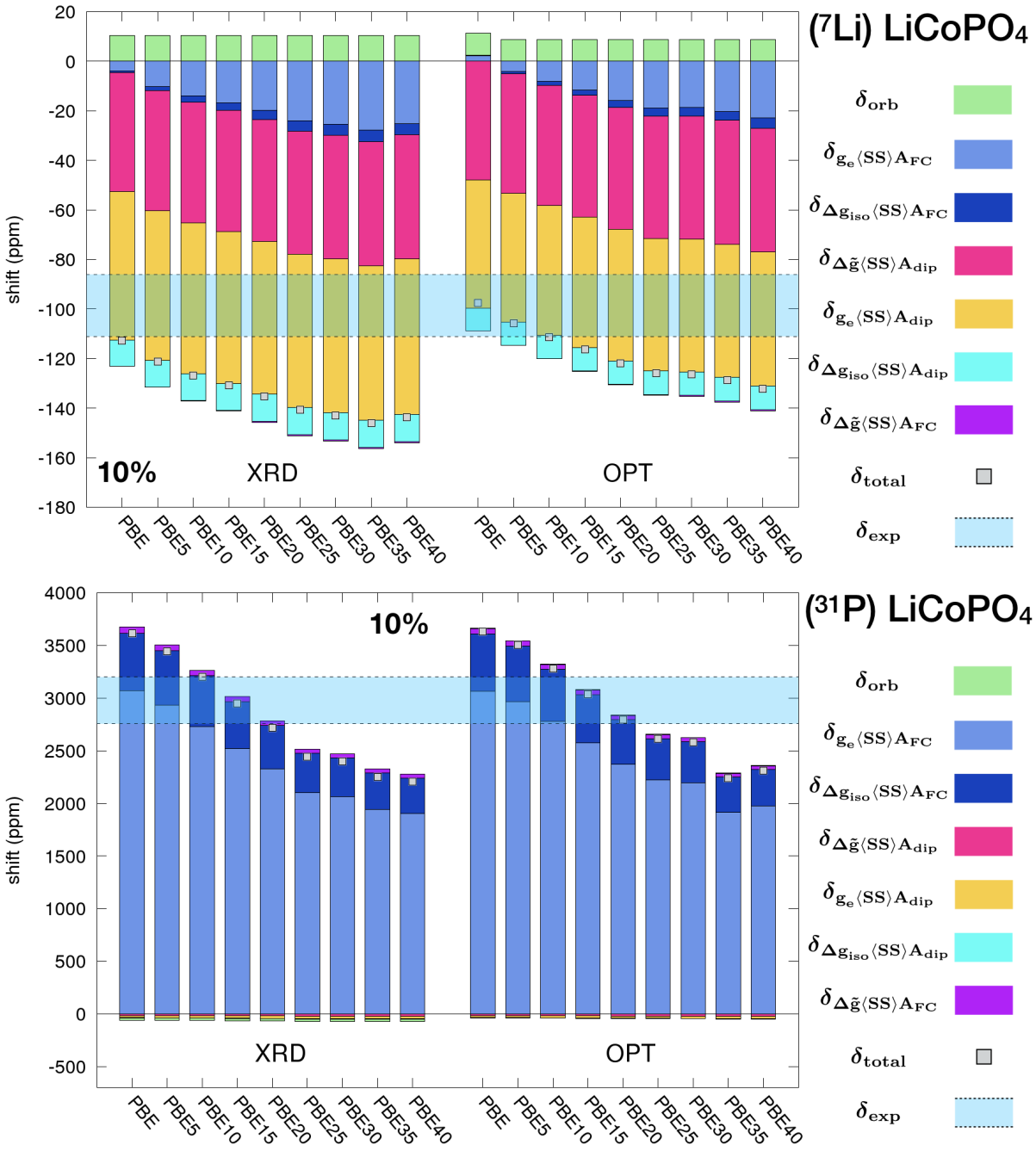

Figure C.6.: Comparison of ^{7}Li and ^{31}P chemical shifts of for $LiCoPO_4$ computed for both XRD and optimized (OPT) structures. Variations with EXX admixture to PBE-based functionals for the HFC tensors are shown. NEVPT2 g-shift- and D-tensors scaled by 10%. Orbital shielding obtained at PBE level. Shieldings converted to shifts for Li and P relative to aq. lithium chloride (LiCl) and 85 % aq. phosphoric acid (H_3PO_4) respectively. Experimental range shown according to refs. 40,41,61,296.

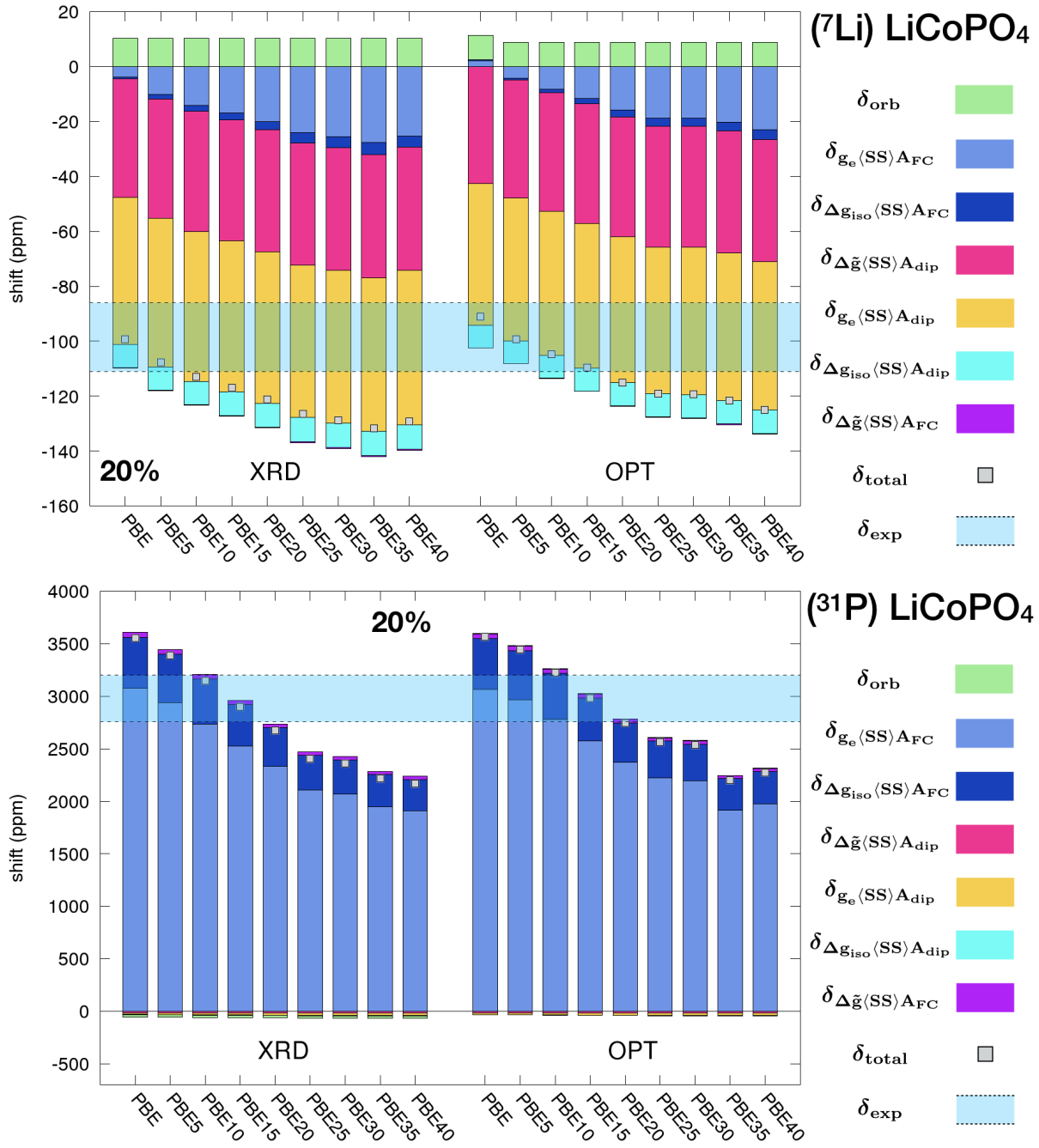

Figure C.7.: Comparison of ^{7}Li and ^{31}P chemical shifts of for $LiCoPO_4$ computed for both XRD and optimized (OPT) structures. Variations with EXX admixture to PBE-based functionals for the HFC tensors are shown. NEVPT2 g-shift- and D-tensors scaled by 20%. Orbital shielding obtained at PBE level. Shieldings converted to shifts for Li and P relative to aq. lithium chloride (LiCl) and 85 % aq. phosphoric acid (H_3PO_4) respectively. Experimental range shown according to refs. 40,41,61,296.

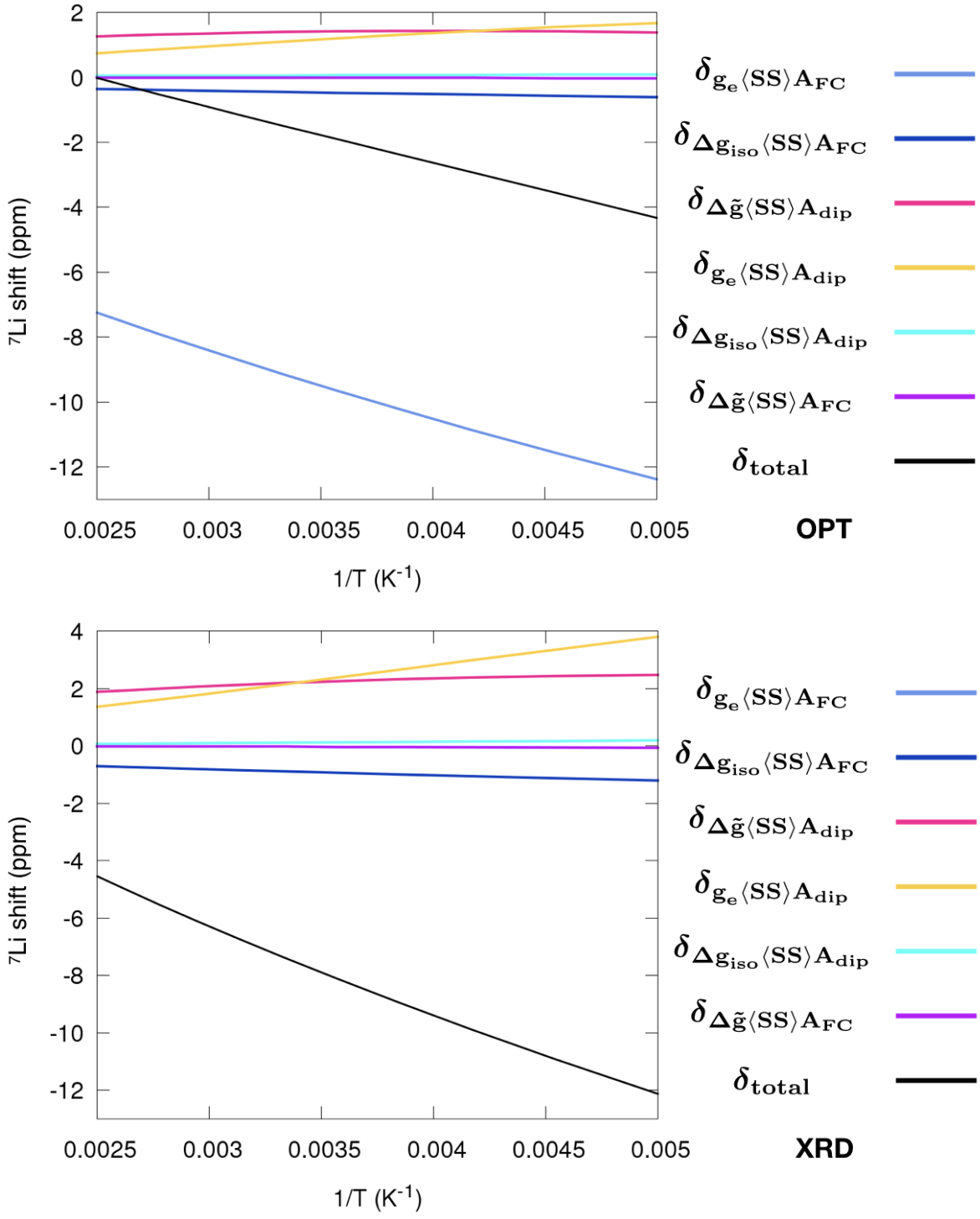

Figure C.8.: Inverse temperature dependence of various contributions to ^{7}Li pNMR shifts for $LiFePO_4$ computed at the XRD structure. HFC tensor obtained at PBE0 level (25 % EXX), g-Tensor and D-tensor at NEVPT2 level. Shieldings converted to shifts relative to aq. lithium chloride (LiCl).

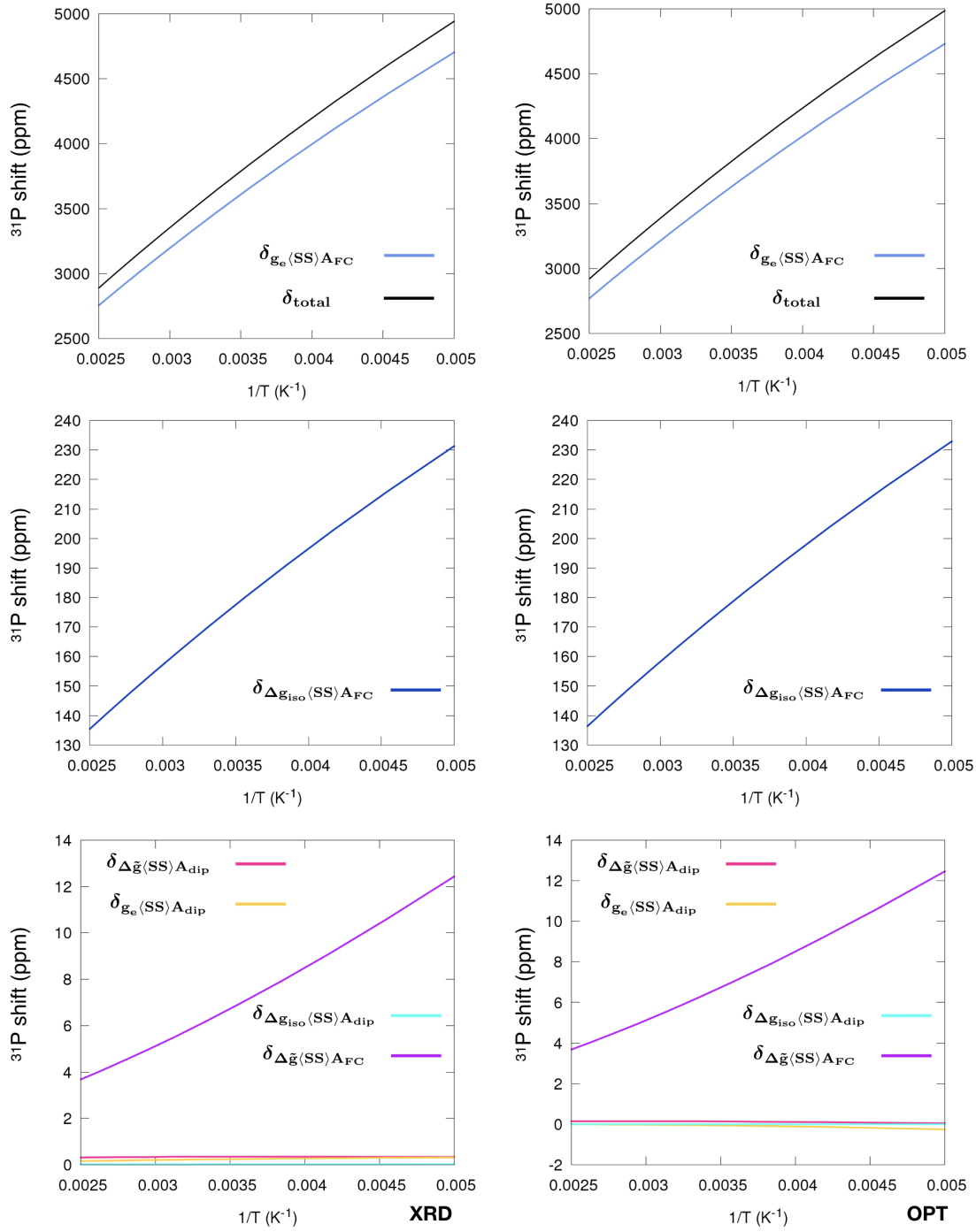

Figure C.9.: Inverse temperature dependence of various contributions to ^{31}P pNMR shifts for $LiFePO_4$ computed at both XRD and optimized (OPT) structures. HFC tensor obtained at PBE0 level (25 % EXX), g-Tensor and D-tensor at NEVPT2 level. Shieldings converted to shifts relative to 85 % aq. phosphoric acid (H_3PO_4).

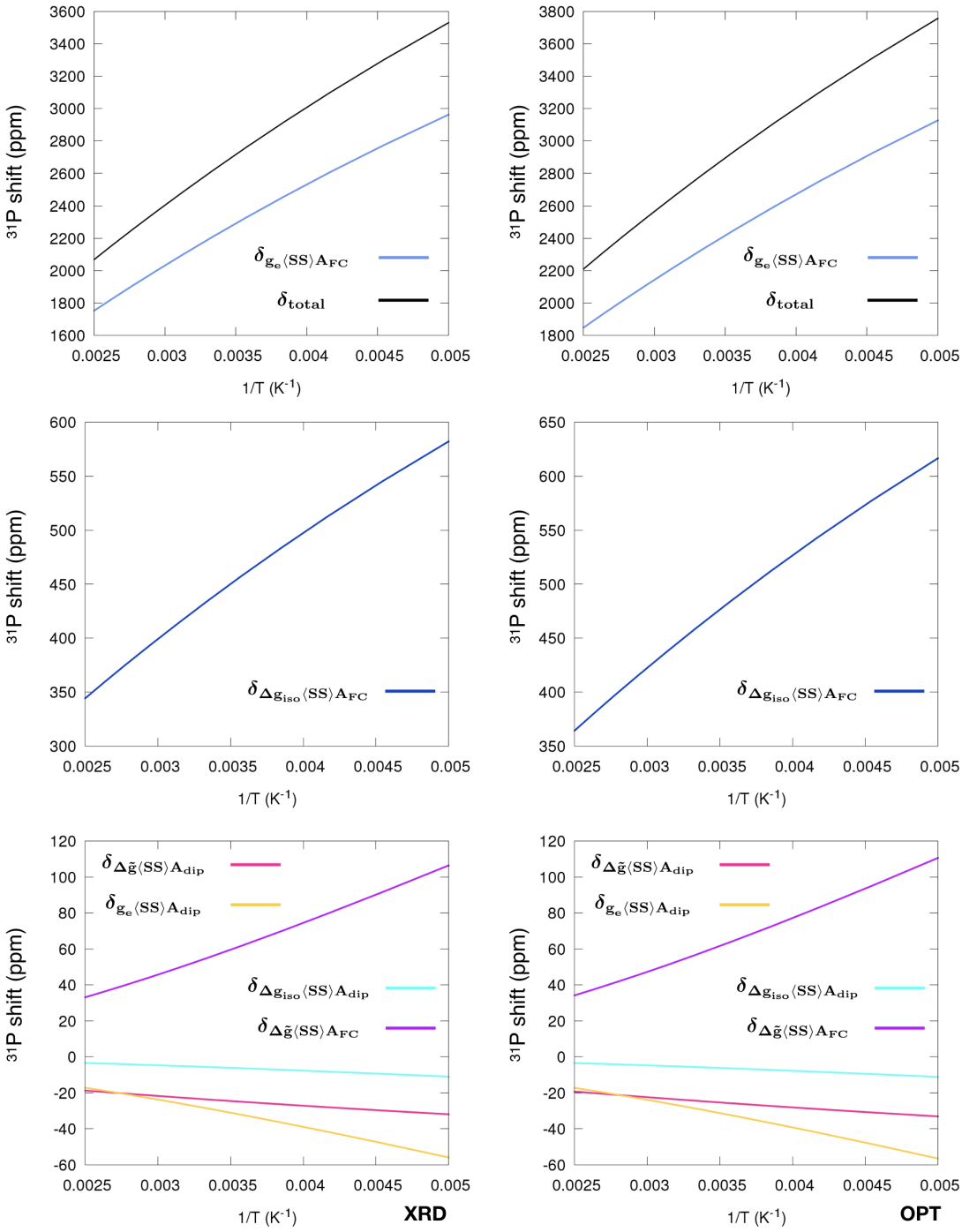

Figure C.10.: Inverse temperature dependence of various contributions to ^{31}P pNMR shifts for $LiCoPO_4$ computed at both XRD and optimized (OPT) structures. HFC tensor obtained at PBE0 level (25 % EXX), g-Tensor and D-tensor at NEVPT2 level. Shieldings converted to shifts relative to 85 % aq. phosphoric acid (H_3PO_4).

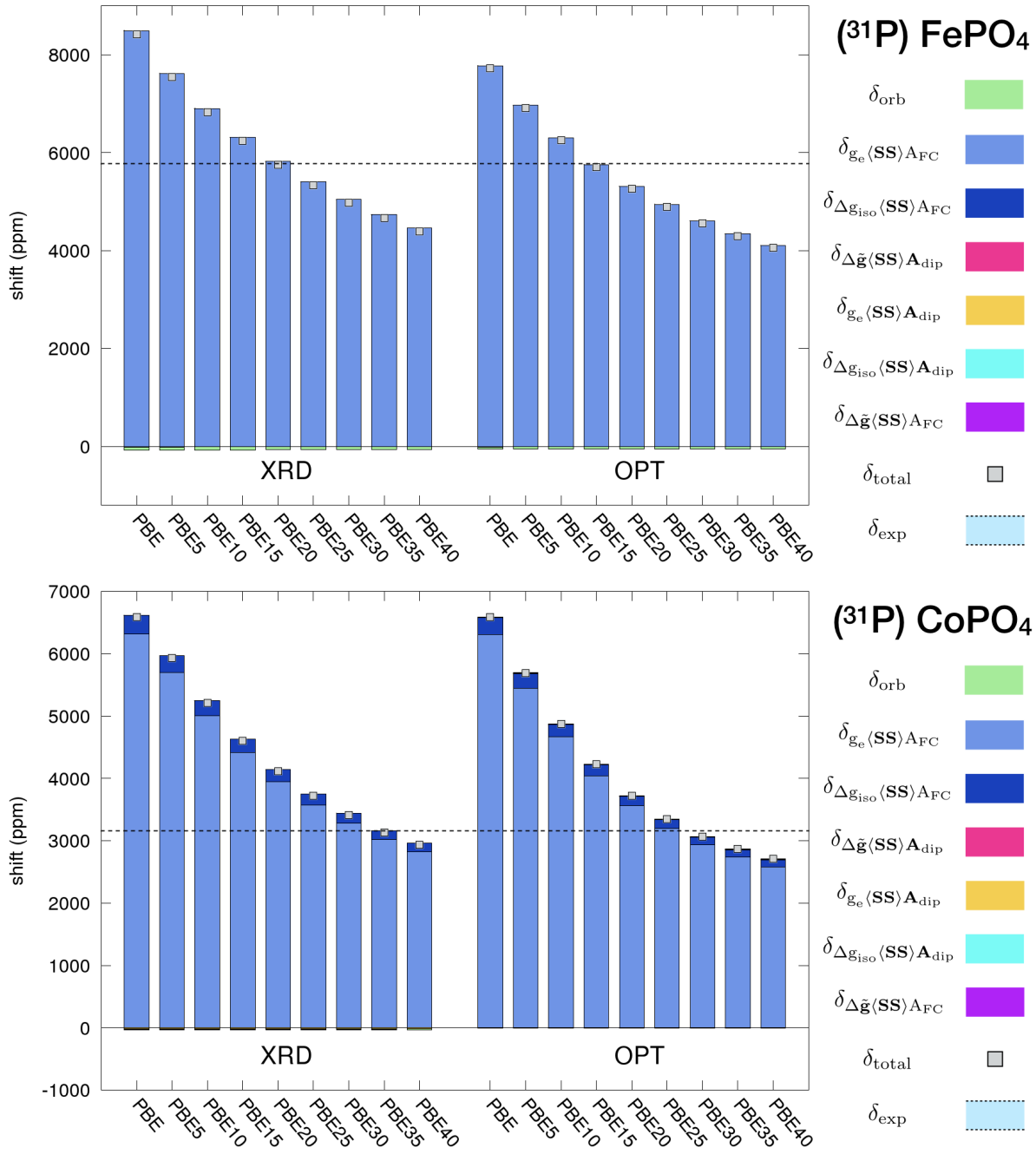

Figure C.11.: Comparison of ^{31}P chemical shifts of for $FePO_4$ and $CoPO_4$ computed for both XRD and optimized (OPT) structures. Variations with EXX admixture to PBE-based functionals for the HFC tensors are shown. g-Tensor and D-tensor obtained at NEVPT2 level. Orbital shielding obtained at PBE level. Shieldings converted to shifts for P relative to 85 % aq. phosphoric acid (H_3PO_4). Experimental shifts are from ref. 58 (see Tables C.31, C.32 for numerical values).

Table C.27.: pNMR shifts for $LiMnPO_4$ for the XRD structure depending on the EXX admixture used for the HFC calculations[a]

$LiMnPO_4$		**Isotropic chemical shift (ppm)**								
	atom	**terms**	**PBE**	**PBE5**	**PBE10**	**PBE15**	**PBE20**	**PBE25**	**PBE30**	**PBE35**	**PBE40**
XRD	^{7}Li	$\boldsymbol{\delta_{orb}}$	4.70	4.70	4.70	4.70	4.70	4.70	4.70	4.70	4.70
		$\boldsymbol{\delta_{(g_e\langle SS\rangle A_{FC})}}$	97.41	83.50	71.53	60.87	51.63	43.17	35.66	28.93	22.41
		$\boldsymbol{\delta_{(\Delta g_{iso}\langle SS\rangle A_{FC})}}$	-0.12	-0.11	-0.09	-0.08	-0.07	-0.06	-0.05	-0.04	-0.03
		$\boldsymbol{\delta_{(\Delta \tilde{g}_e\langle SS\rangle A_{dip})}}$	-0.00	-0.00	-0.00	-0.00	-0.00	-0.00	-0.00	-0.00	-0.00
		$\boldsymbol{\delta_{(g_e\langle SS\rangle A_{dip})}}$	0.14	0.14	0.15	0.15	0.15	0.15	0.15	0.15	0.15
		$\boldsymbol{\delta_{(\Delta g_{iso}\langle SS\rangle A_{dip})}}$	-0.00	-0.00	-0.00	-0.00	-0.00	-0.00	-0.00	-0.00	-0.00
		$\boldsymbol{\delta_{(\Delta \tilde{g}_e\langle SS\rangle A_{FC})}}$	-0.00	-0.00	-0.00	-0.00	-0.00	-0.00	-0.00	-0.00	-0.00
		$\boldsymbol{\delta_{total}}$	102.13	88.23	76.28	65.64	56.40	47.96	40.46	33.74	27.23
	^{31}P	$\boldsymbol{\delta_{orb}}$	-20.26	-20.26	-20.26	-20.26	-20.26	-20.26	-20.26	-20.26	-20.26
		$\boldsymbol{\delta_{(g_e\langle SS\rangle A_{FC})}}$	11540.80	10736.27	10036.07	9412.01	8858.41	8350.65	7894.81	7478.99	7057.87
		$\boldsymbol{\delta_{(\Delta g_{iso}\langle SS\rangle A_{FC})}}$	-14.74	-13.72	-12.82	-12.02	-11.32	-10.67	-10.09	-9.55	-9.02
		$\boldsymbol{\delta_{(\Delta \tilde{g}_e\langle SS\rangle A_{dip})}}$	-0.00	-0.00	-0.00	-0.00	-0.00	-0.00	-0.00	-0.00	-0.00
		$\boldsymbol{\delta_{(g_e\langle SS\rangle A_{dip})}}$	0.06	0.07	0.07	0.07	0.07	0.07	0.07	0.07	0.07
		$\boldsymbol{\delta_{(\Delta g_{iso}\langle SS\rangle A_{dip})}}$	-0.00	-0.00	-0.00	-0.00	-0.00	-0.00	-0.00	-0.00	-0.00
		$\boldsymbol{\delta_{(\Delta \tilde{g}_e\langle SS\rangle A_{FC})}}$	-0.00	-0.00	-0.00	-0.00	-0.00	-0.00	-0.00	-0.00	-0.00
		$\boldsymbol{\delta_{total}}$	11505.86	10702.36	10003.06	9379.80	8826.90	8319.79	7864.53	7449.25	7028.67

[a] Equation 1-4 have been used for computing the total shielding tensor. Shieldings converted to shifts for Li and P relative to aq. lithium chloride (LiCl) and 85% aq. phosphoric acid (H_3PO_4). HFC computations were done for a 2 × 2 × 2 super-cell using IGLO-II/8s7p4d basis sets. g-Tensor and ZFS computations were done NEVPT2/def2-TZVP/IGLO-II level. Calculations of orbital shielding tensor were done for a unit cell at PBE/Ahlrich-VTZ/IGLO-II level (see Computational Details).

Table C.28.: pNMR shifts for $LiMnPO_4$ for the optimized structure depending on the EXX admixture used for the HFC calculations[a]

$LiMnPO_4$		**Isotropic chemical shift (ppm)**									
	atom	**terms**	**PBE**	**PBE5**	**PBE10**	**PBE15**	**PBE20**	**PBE25**	**PBE30**	**PBE35**	**PBE40**
OPT	^{7}Li	$\boldsymbol{\delta_{orb}}$	3.70	3.70	3.70	3.70	3.70	3.70	3.70	3.70	3.70
		$\boldsymbol{\delta_{(g_e\langle SS\rangle A_{FC})}}$	114.11	99.39	86.38	75.88	64.61	55.34	47.02	38.83	31.16
		$\boldsymbol{\delta_{(\Delta g_{iso}\langle SS\rangle A_{FC})}}$	-0.15	-0.13	-0.11	-0.10	-0.08	-0.07	-0.06	-0.05	-0.04
		$\boldsymbol{\delta_{(\Delta \tilde{g}_e\langle SS\rangle A_{dip})}}$	-0.00	-0.00	-0.00	-0.00	-0.00	-0.00	-0.00	-0.00	-0.00
		$\boldsymbol{\delta_{(g_e\langle SS\rangle A_{dip})}}$	0.19	0.19	0.19	0.19	0.20	0.20	0.20	0.20	0.20
		$\boldsymbol{\delta_{(\Delta g_{iso}\langle SS\rangle A_{dip})}}$	-0.00	-0.00	-0.00	-0.00	-0.00	-0.00	-0.00	-0.00	-0.00
		$\boldsymbol{\delta_{(\Delta \tilde{g}_e\langle SS\rangle A_{FC})}}$	-0.00	-0.00	-0.00	-0.00	-0.00	-0.00	-0.00	-0.00	-0.00
		$\boldsymbol{\delta_{total}}$	117.86	103.15	90.16	79.67	68.42	59.17	50.85	42.67	35.01
	^{31}P	$\boldsymbol{\delta_{orb}}$	9.86	9.86	9.86	9.86	9.86	9.86	9.86	9.86	9.86
		$\boldsymbol{\delta_{(g_e\langle SS\rangle A_{FC})}}$	13052.72	12081.32	11234.79	10564.89	9829.54	9237.00	8700.83	8358.07	7907.29
		$\boldsymbol{\delta_{(\Delta g_{iso}\langle SS\rangle A_{FC})}}$	-16.67	-15.43	-14.35	-13.50	-12.56	-11.80	-11.12	-10.68	-10.10
		$\boldsymbol{\delta_{(\Delta \tilde{g}_e\langle SS\rangle A_{dip})}}$	-0.00	-0.00	-0.00	-0.00	-0.00	-0.00	-0.00	-0.00	-0.00
		$\boldsymbol{\delta_{(g_e\langle SS\rangle A_{dip})}}$	0.08	0.09	0.09	0.09	0.09	0.09	0.09	0.09	0.10
		$\boldsymbol{\delta_{(\Delta g_{iso}\langle SS\rangle A_{dip})}}$	-0.00	-0.00	-0.00	-0.00	-0.00	-0.00	-0.00	-0.00	-0.00
		$\boldsymbol{\delta_{(\Delta \tilde{g}_e\langle SS\rangle A_{FC})}}$	-0.00	-0.00	-0.00	-0.00	-0.00	-0.00	-0.00	-0.00	-0.00
		$\boldsymbol{\delta_{total}}$	13045.99	12075.84	11230.39	10561.34	9826.94	9235.15	8699.67	8357.35	7907.15

[a] Equation 5.3 in Chapter 5 has been used for computing the total shielding tensor. Shieldings converted to shifts for Li and P relative to aq. lithium chloride (LiCl) and 85% aq. phosphoric acid (H_3PO_4). HFC computations were done for a $2 \times 2 \times 2$ super-cell using IGLO-II/8s7p4d basis sets. g-Tensor and ZFS computations were done NEVPT2/def2-TZVP/IGLO-II level. Calculations of orbital shielding tensor were done for a unit cell at PBE/Ahlrich-VTZ/IGLO-II level (see Computational Details in Chapter 5).

Table C.29.: pNMR shifts for $LiNiPO_4$ for the XRD structure depending on the EXX admixture used for the HFC calculations[a]

$LiNiPO_4$		**Isotropic chemical shift (ppm)**									
	atom	**terms**	**PBE**	**PBE5**	**PBE10**	**PBE15**	**PBE20**	**PBE25**	**PBE30**	**PBE35**	**PBE40**
XRD	^{7}Li	$\boldsymbol{\delta_{orb}}$	17.11	17.11	17.11	17.11	17.11	17.11	17.11	17.11	17.11
		$\boldsymbol{\delta_{(g_e\langle SS\rangle A_{FC})}}$	-56.70	-55.93	-54.83	-53.57	-52.35	-51.34	-50.15	-49.43	-48.51
		$\boldsymbol{\delta_{(\Delta g_{iso}\langle SS\rangle A_{FC})}}$	-7.81	-7.70	-7.55	-7.38	-7.21	-7.07	-6.91	-6.81	-6.68
		$\boldsymbol{\delta_{(\Delta \tilde{g}_e\langle SS\rangle A_{dip})}}$	0.69	0.67	0.65	0.64	0.62	0.61	0.60	0.59	0.58
		$\boldsymbol{\delta_{(g_e\langle SS\rangle A_{dip})}}$	0.29	0.28	0.26	0.25	0.23	0.22	0.21	0.20	0.20
		$\boldsymbol{\delta_{(\Delta g_{iso}\langle SS\rangle A_{dip})}}$	0.04	0.04	0.04	0.03	0.03	0.03	0.03	0.03	0.03
		$\boldsymbol{\delta_{(\Delta \tilde{g}_e\langle SS\rangle A_{FC})}}$	-0.02	-0.02	-0.02	-0.02	-0.02	-0.02	-0.02	-0.02	-0.02
		$\boldsymbol{\delta_{total}}$	-46.39	-45.56	-44.35	-42.94	-41.58	-40.46	-39.13	-38.32	-37.30
	^{31}P	$\boldsymbol{\delta_{orb}}$	3.28	3.28	3.28	3.28	3.28	3.28	3.28	3.28	3.28
		$\boldsymbol{\delta_{(g_e\langle SS\rangle A_{FC})}}$	2354.36	2094.87	1890.42	1720.76	1570.85	1427.51	1310.83	1184.87	1082.96
		$\boldsymbol{\delta_{(\Delta g_{iso}\langle SS\rangle A_{FC})}}$	324.17	288.44	260.29	236.93	216.29	196.55	180.49	163.14	149.11
		$\boldsymbol{\delta_{(\Delta \tilde{g}_e\langle SS\rangle A_{dip})}}$	3.79	3.79	3.75	3.70	3.65	3.59	3.53	3.47	3.41
		$\boldsymbol{\delta_{(g_e\langle SS\rangle A_{dip})}}$	2.59	2.57	2.53	2.49	2.44	2.39	2.34	2.30	2.25
		$\boldsymbol{\delta_{(\Delta g_{iso}\langle SS\rangle A_{dip})}}$	0.36	0.35	0.35	0.34	0.34	0.33	0.32	0.32	0.31
		$\boldsymbol{\delta_{(\Delta \tilde{g}_e\langle SS\rangle A_{FC})}}$	0.78	0.70	0.63	0.57	0.52	0.47	0.44	0.39	0.36
		$\boldsymbol{\delta_{total}}$	2689.33	2394.00	2161.25	1968.07	1797.36	1634.13	1501.22	1357.78	1241.68

[a] Equation 1-4 have been used for computing the total shielding tensor. Shieldings converted to shifts for Li and P relative to aq. lithium chloride (LiCl) and 85% aq. phosphoric acid (H_3PO_4). HFC computations were done for a 2 × 2 × 2 super-cell using IGLO-II/8s7p4d basis sets. g-Tensor and ZFS computations were done NEVPT2/def2-TZVP/IGLO-II level. Calculations of orbital shielding tensor were done for a unit cell at PBE/Ahlrich-VTZ/IGLO-II level (see Computational Details).

Table C.30.: pNMR shifts for $LiNiPO_4$ for the optimized structure depending on the EXX admixture used for the HFC calculations[a]

$LiNiPO_4$		**Isotropic chemical shift (ppm)**									
	atom	**terms**	**PBE**	**PBE5**	**PBE10**	**PBE15**	**PBE20**	**PBE25**	**PBE30**	**PBE35**	**PBE40**
OPT	^{7}Li	$\boldsymbol{\delta_{orb}}$	14.22	14.22	14.22	14.22	14.22	14.22	14.22	14.22	14.22
		$\boldsymbol{\delta_{(g_e\langle SS\rangle A_{FC})}}$	-57.05	-56.05	-54.79	-53.51	-52.68	-51.50	-50.03	-47.95	-46.78
		$\boldsymbol{\delta_{(\Delta g_{iso}\langle SS\rangle A_{FC})}}$	-7.92	-7.78	-7.60	-7.43	-7.31	-7.15	-6.94	-6.65	-6.49
		$\boldsymbol{\delta_{(\Delta \tilde{g}_e\langle SS\rangle A_{dip})}}$	-0.10	-0.14	-0.17	-0.19	-0.22	-0.24	-0.26	-0.27	-0.28
		$\boldsymbol{\delta_{(g_e\langle SS\rangle A_{dip})}}$	-0.22	-0.24	-0.26	-0.29	-0.30	-0.32	-0.33	-0.34	-0.36
		$\boldsymbol{\delta_{(\Delta g_{iso}\langle SS\rangle A_{dip})}}$	-0.03	-0.03	-0.04	-0.04	-0.04	-0.04	-0.05	-0.05	-0.05
		$\boldsymbol{\delta_{(\Delta \tilde{g}_e\langle SS\rangle A_{FC})}}$	-0.02	-0.02	-0.02	-0.02	-0.02	-0.02	-0.02	-0.01	-0.01
		$\boldsymbol{\delta_{total}}$	-51.12	-50.04	-48.66	-47.26	-46.35	-45.04	-43.41	-41.07	-39.76
	^{31}P	$\boldsymbol{\delta_{orb}}$	13.94	13.94	13.94	13.94	13.94	13.94	13.94	13.94	13.94
		$\boldsymbol{\delta_{(g_e\langle SS\rangle A_{FC})}}$	2129.13	1860.68	1657.28	1496.34	1324.41	1196.67	1085.58	1044.75	956.68
		$\boldsymbol{\delta_{(\Delta g_{iso}\langle SS\rangle A_{FC})}}$	295.43	258.18	229.96	207.63	183.77	166.05	150.63	144.97	132.75
		$\boldsymbol{\delta_{(\Delta \tilde{g}_e\langle SS\rangle A_{dip})}}$	3.68	3.59	3.49	3.38	3.30	3.20	3.11	2.99	2.90
		$\boldsymbol{\delta_{(g_e\langle SS\rangle A_{dip})}}$	2.52	2.44	2.36	2.28	2.21	2.14	2.08	1.99	1.92
		$\boldsymbol{\delta_{(\Delta g_{iso}\langle SS\rangle A_{dip})}}$	0.35	0.34	0.33	0.32	0.31	0.30	0.29	0.28	0.27
		$\boldsymbol{\delta_{(\Delta \tilde{g}_e\langle SS\rangle A_{FC})}}$	0.65	0.57	0.50	0.46	0.40	0.36	0.33	0.32	0.29
		$\boldsymbol{\delta_{total}}$	2445.70	2139.74	1907.86	1724.34	1528.35	1382.66	1255.96	1209.23	1108.75

[a] Equation 1-4 have been used for computing the total shielding tensor. Shieldings converted to shifts for Li and P relative to aq. lithium chloride (LiCl) and 85% aq. phosphoric acid (H_3PO_4). HFC computations were done for a 2 × 2 × 2 super-cell using IGLO-II/8s7p4d basis sets. g-Tensor and ZFS computations were done NEVPT2/def2-TZVP/IGLO-II level. Calculations of orbital shielding tensor were done for a unit cell at PBE/Ahlrich-VTZ/IGLO-II level (see Computational Details).

Table C.31.: pNMR shifts for $FePO_4$ for the XRD and optimized structure depending on the EXX admixture used for the HFC calculations[a]

$FePO_4$		**Isotropic chemical shift (ppm)**								
		terms	**PBE**	**PBE5**	**PBE10**	**PBE15**	**PBE20**	**PBE25**	**PBE30**	**PBE35**	**PBE40**
^{31}P	XRD	$\boldsymbol{\delta_{orb}}$	-60.30	-60.30	-60.30	-60.30	-60.30	-60.30	-60.30	-60.30	-60.30
		$\boldsymbol{\delta_{(g_e\langle SS\rangle A_{FC})}}$	8494.20	7619.62	6904.52	6313.56	5820.31	5402.77	5043.81	4732.72	4459.22
		$\boldsymbol{\delta_{(\Delta g_{iso}\langle SS\rangle A_{FC})}}$	-12.22	-10.96	-9.94	-9.09	-8.38	-7.77	-7.26	-6.81	-6.42
		$\boldsymbol{\delta_{(\Delta \tilde{g}_e\langle SS\rangle A_{dip})}}$	-0.00	-0.00	-0.00	-0.00	-0.00	-0.00	-0.00	-0.00	-0.00
		$\boldsymbol{\delta_{(g_e\langle SS\rangle A_{dip})}}$	0.18	0.18	0.18	0.18	0.18	0.18	0.18	0.18	0.18
		$\boldsymbol{\delta_{(\Delta g_{iso}\langle SS\rangle A_{dip})}}$	-0.00	-0.00	-0.00	-0.00	-0.00	-0.00	-0.00	-0.00	-0.00
		$\boldsymbol{\delta_{(\Delta \tilde{g}_e\langle SS\rangle A_{FC})}}$	-0.00	-0.00	-0.00	-0.00	-0.00	-0.00	-0.00	-0.00	-0.00
		$\boldsymbol{\delta_{total}}$	8421.86	7548.54	6834.46	6244.36	5751.81	5334.87	4976.43	4665.78	4392.68
	OPT	$\boldsymbol{\delta_{orb}}$	-44.62	-44.62	-44.62	-44.62	-44.62	-44.62	-44.62	-44.62	-44.62
		$\boldsymbol{\delta_{(g_e\langle SS\rangle A_{FC})}}$	7776.86	6967.17	6302.61	5759.07	5312.86	4946.75	4608.77	4340.80	4105.57
		$\boldsymbol{\delta_{(\Delta g_{iso}\langle SS\rangle A_{FC})}}$	-10.93	-9.79	-8.86	-8.09	-7.47	-6.95	-6.48	-6.10	-5.77
		$\boldsymbol{\delta_{(\Delta \tilde{g}_e\langle SS\rangle A_{dip})}}$	0.00	0.00	0.00	0.00	0.00	0.00	0.00	0.00	0.00
		$\boldsymbol{\delta_{(g_e\langle SS\rangle A_{dip})}}$	0.07	0.07	0.08	0.08	0.09	0.09	0.09	0.09	0.10
		$\boldsymbol{\delta_{(\Delta g_{iso}\langle SS\rangle A_{dip})}}$	-0.00	-0.00	-0.00	-0.00	-0.00	-0.00	-0.00	-0.00	-0.00
		$\boldsymbol{\delta_{(\Delta \tilde{g}_e\langle SS\rangle A_{FC})}}$	-0.00	-0.00	-0.00	-0.00	-0.00	-0.00	-0.00	-0.00	-0.00
		$\boldsymbol{\delta_{total}}$	7721.37	6912.84	6249.21	5706.43	5260.85	4895.26	4557.77	4290.18	4055.28

[a] Equation 5.3 in Chapter 5 has been used for computing the total shielding tensor. Shieldings converted to shifts for P relative to 85% aq. phosphoric acid (H_3PO_4). HFC computations were done for a $2 \times 2 \times 2$ super-cell using IGLO-II/8s7p4d basis sets. g-Tensor and ZFS computations were done NEVPT2/def2-TZVP/IGLO-II level. Calculations of orbital shielding tensor were done for a unit cell at PBE/Ahlrich-VTZ/IGLO-II level (see Computational Details in Chapter 5).

Table C.32.: pNMR shifts for $CoPO_4$ for XRD and optimized structure depending on the EXX admixture used for the HFC calculations[a]

$CoPO_4$		Isotropic chemical shift (ppm)								
		terms	**PBE**	**PBE5**	**PBE10**	**PBE15**	**PBE20**	**PBE25**	**PBE30**	**PBE35**	**PBE40**
^{31}P	XRD	$\boldsymbol{\delta_{orb}}$	-10.65	-10.65	-10.65	-10.65	-10.65	-10.65	-10.65	-10.65	-10.65
		$\boldsymbol{\delta_{(g_e\langle SS\rangle A_{FC})}}$	6313.19	5694.06	5003.72	4417.24	3951.36	3576.88	3285.91	3017.53	2825.25
		$\boldsymbol{\delta_{(\Delta g_{iso}\langle SS\rangle A_{FC})}}$	305.37	275.42	242.03	213.66	191.13	173.02	158.94	145.96	136.66
		$\boldsymbol{\delta_{(\Delta \tilde{g}_e\langle SS\rangle A_{dip})}}$	-13.96	-13.58	-13.46	-13.35	-13.24	-13.14	-13.05	-12.95	-12.86
		$\boldsymbol{\delta_{(g_e\langle SS\rangle A_{dip})}}$	-12.40	-11.77	-11.13	-10.53	-9.99	-9.48	-9.02	-8.60	-8.19
		$\boldsymbol{\delta_{(\Delta g_{iso}\langle SS\rangle A_{dip})}}$	-0.60	-0.57	-0.54	-0.51	-0.48	-0.46	-0.44	-0.42	-0.40
		$\boldsymbol{\delta_{(\Delta \tilde{g}_e\langle SS\rangle A_{FC})}}$	0.84	0.76	0.67	0.59	0.53	0.48	0.44	0.40	0.38
		$\boldsymbol{\delta_{total}}$	6581.79	5933.67	5210.64	4596.45	4108.66	3716.63	3412.13	3131.27	2930.19
	OPT	$\boldsymbol{\delta_{orb}}$	9.98	9.98	9.98	9.98	9.98	9.98	9.98	9.98	9.98
		$\boldsymbol{\delta_{(g_e\langle SS\rangle A_{FC})}}$	6306.22	5449.19	4664.21	4042.57	3558.77	3201.18	2930.87	2737.97	2583.72
		$\boldsymbol{\delta_{(\Delta g_{iso}\langle SS\rangle A_{FC})}}$	269.36	232.76	199.23	172.67	152.01	136.74	125.19	116.95	110.36
		$\boldsymbol{\delta_{(\Delta \tilde{g}_e\langle SS\rangle A_{dip})}}$	-1.93	-1.98	-2.09	-2.18	-2.27	-2.35	-2.42	-2.49	-2.54
		$\boldsymbol{\delta_{(g_e\langle SS\rangle A_{dip})}}$	4.81	4.83	4.98	5.12	5.23	5.34	5.44	5.52	5.60
		$\boldsymbol{\delta_{(\Delta g_{iso}\langle SS\rangle A_{dip})}}$	0.21	0.21	0.21	0.22	0.22	0.23	0.23	0.24	0.24
		$\boldsymbol{\delta_{(\Delta \tilde{g}_e\langle SS\rangle A_{FC})}}$	-0.38	-0.33	-0.28	-0.24	-0.21	-0.19	-0.18	-0.16	-0.15
		$\boldsymbol{\delta_{total}}$	6588.28	5694.67	4876.25	4228.13	3723.74	3350.93	3069.12	2868.02	2707.20

[a] Equation 5.3 in Chapter 5 has been used for computing the total shielding tensor. Shieldings converted to shifts for P relative to 85% aq. phosphoric acid (H_3PO_4). HFC computations were done for a $2 \times 2 \times 2$ super-cell using IGLO-II/8s7p4d basis sets. g-Tensor and ZFS computations were done NEVPT2/def2-TZVP/IGLO-II level. Calculations of orbital shielding tensor were done for a unit cell at PBE/Ahlrich-VTZ/IGLO-II level (see Computational Details in Chapter 5).

Table C.33.: Chemical shift anisotropy for $LiMnPO_4$ computed[a] for both XRD and optimized structures depending on the EXX admixture used for the HFC calculations

Atom	Functional	XRD δ_{iso} (ppm)	XRD δ (ppm) δ_{11}	XRD δ_{22}	XRD δ_{33}	XRD Δ[b] (ppm)	XRD η[c]	OPT δ_{FC} (ppm)	OPT δ (ppm) δ_{11}	OPT δ_{22}	OPT δ_{33}	OPT Δ[b] (ppm)	OPT η[c]
^{7}Li	PBE	102.13	-693.43	-426.71	1426.52	1986.60	0.20	117.86	-664.80	-419.24	1437.60	1979.62	0.19
	PBE5	88.23	-710.60	-445.06	1420.34	1998.17	0.20	103.15	-682.66	-438.13	1430.26	1990.65	0.18
	PBE10	76.28	-725.32	-460.83	1414.98	2008.06	0.20	90.16	-698.34	-454.73	1423.54	2000.08	0.18
	PBE15	65.64	-738.34	-474.77	1410.02	2016.57	0.20	79.67	-711.15	-468.31	1418.48	2008.21	0.18
	PBE20	56.40	-749.63	-486.87	1405.70	2023.95	0.19	68.42	-724.38	-482.28	1411.91	2015.24	0.18
	PBE25	47.96	-759.86	-497.82	1401.55	2030.39	0.19	59.17	-735.37	-493.89	1406.76	2021.39	0.18
	PBE30	40.46	-768.93	-507.51	1397.81	2036.03	0.19	50.85	-745.20	-504.28	1402.04	2026.78	0.18
	PBE35	33.74	-777.03	-516.16	1394.41	2041.00	0.19	42.67	-754.74	-514.28	1397.05	2031.56	0.18
	PBE40	27.23	-784.77	-524.41	1390.87	2045.46	0.19	35.01	-763.60	-523.58	1392.21	2035.80	0.18
^{31}P	PBE	11505.86	11146.84	11220.74	12150.00	966.21	0.11	13045.99	12717.53	12773.79	13646.66	901.00	0.09
	PBE5	10702.36	10336.25	10411.11	11359.72	986.04	0.11	12075.84	11738.88	11798.28	12690.35	921.77	0.10
	PBE10	10003.06	9630.47	9706.79	10671.92	1003.28	0.11	11230.39	10885.55	10948.76	11856.86	939.70	0.10
	PBE15	9379.80	9001.16	9079.60	10058.63	1018.25	0.12	10561.34	10210.12	10275.62	11198.30	955.43	0.10
	PBE20	8826.90	8442.77	8523.45	9514.48	1031.37	0.12	9826.94	9468.21	9539.78	10472.83	968.84	0.11
	PBE25	8319.79	7930.41	8013.93	9015.03	1042.86	0.12	9235.15	8870.26	8946.22	9888.98	980.73	0.12
	PBE30	7864.53	7470.38	7556.67	8566.55	1053.02	0.12	8699.67	8329.03	8409.49	9360.48	991.22	0.12
	PBE35	7449.25	7050.66	7139.77	8157.32	1062.10	0.13	8357.35	7982.17	8065.92	9023.95	999.91	0.13
	PBE40	7028.67	6625.25	6718.70	7742.05	1070.07	0.13	7907.15	7526.72	7615.58	8579.15	1008.00	0.13

[a] Equation 5.3 in Chapter 5 has been used for computing the total shielding tensor. Shieldings converted to shifts for Li and P relative to aq. lithium chloride (LiCl) and 85% aq. phosphoric acid (H_3PO_4). HFC computations were done for a 2 × 2 × 2 super-cell using IGLO-II/8s7p4d basis sets. g-Tensor and ZFS computations were done NEVPT2/def2-TZVP/IGLO-II level. Calculations of orbital shielding tensor were done for a unit cell at PBE/Ahlrich-VTZ/IGLO-II level (see Computational Details in Chapter 5).

[b] Anisotropy (Δ) = δ_{zz} - $\frac{1}{2}(\delta_{xx}+\delta_{yy})$; the components are ordered as $\mid \delta_{zz}-\delta_{iso} \mid \geq \mid \delta_{yy}-\delta_{iso} \mid \geq \mid \delta_{xx}-\delta_{iso} \mid$, $\delta_{iso} = \frac{1}{3}(\delta_{11}+\delta_{22}+\delta_{33})$ and $\delta_{11} \leq \delta_{22} \leq \delta_{33}$.

[c] Asymmetry (η) = $\frac{\delta_{xx}-\delta_{yy}}{\delta_{zz}-\delta_{iso}}$.

Table C.34.: Chemical shift anisotropy for $LiFePO_4$ computed[a] for both XRD and optimized structures depending on the EXX admixture used for the HFC calculations

Atom	Functional	XRD δ_{iso} (ppm)	XRD δ (ppm) δ_{11}	XRD δ_{22}	XRD δ_{33}	XRD Δ[b] (ppm)	XRD η[c]	OPT δ_{FC} (ppm)	OPT δ (ppm) δ_{11}	OPT δ_{22}	OPT δ_{33}	OPT Δ[b] (ppm)	OPT η[c]
^{7}Li	PBE	41.98	-605.27	-280.33	1011.55	1454.35	0.34	48.86	-587.19	-277.19	1010.97	1443.15	0.32
	PBE5	21.10	-630.71	-304.46	998.48	1466.06	0.33	28.04	-612.69	-301.24	998.07	1455.03	0.32
	PBE10	11.08	-643.71	-317.81	994.77	1475.53	0.33	17.68	-626.22	-314.84	994.12	1464.65	0.32
	PBE15	3.80	-653.44	-328.04	992.89	1483.64	0.33	10.14	-636.39	-325.24	992.04	1472.86	0.32
	PBE20	-1.78	-661.12	-336.24	992.00	1490.68	0.33	4.03	-644.72	-333.82	990.65	1479.92	0.32
	PBE25	-6.71	-667.83	-343.38	991.08	1496.68	0.33	-1.14	-651.82	-341.14	989.55	1486.03	0.31
	PBE30	-10.66	-673.31	-349.30	990.65	1501.95	0.32	-3.45	-655.58	-345.52	990.75	1491.30	0.31
	PBE35	-14.61	-678.65	-354.94	989.75	1506.55	0.32	-9.69	-663.49	-353.16	987.59	1495.91	0.31
	PBE40	-17.84	-683.05	-359.64	989.16	1510.51	0.32	-13.27	-668.35	-358.16	986.70	1499.95	0.31
^{31}P	PBE	4656.12	4025.86	4932.18	5010.31	-945.39	0.12	4717.38	4096.05	5011.77	5044.32	-931.99	0.05
	PBE5	4504.84	3908.75	4747.66	4858.09	-894.13	0.19	4563.42	3976.41	4825.00	4888.85	-880.51	0.11
	PBE10	4248.64	3680.59	4453.78	4611.56	-852.08	0.28	4296.05	3737.49	4519.05	4631.60	-837.84	0.20
	PBE15	3972.95	3431.07	4142.69	4345.08	-812.81	0.37	4019.22	3486.21	4206.63	4364.82	-799.51	0.30
	PBE20	3718.46	3199.28	3857.06	4099.06	-778.78	0.47	3751.38	3242.11	3906.11	4105.92	-763.91	0.39
	PBE25	3465.55	2969.41	3574.07	3853.17	-744.20	0.56	3500.45	3013.13	3625.41	3862.81	-730.99	0.49
	PBE30	3245.95	2768.82	3329.00	3640.03	-715.70	0.65	3337.39	2861.01	3443.74	3707.43	-714.58	0.55
	PBE35	3016.03	2560.06	3073.04	3415.00	-683.96	0.75	3036.42	2590.40	3107.67	3411.21	-669.04	0.68
	PBE40	2814.80	2376.98	2849.05	3218.38	-656.73	0.84	2825.16	2398.23	2872.38	3204.88	-640.40	0.78

[a] Equation 5.3 in Chapter 5 has been used for computing the total shielding tensor. Shieldings converted to shifts for Li and P relative to aq. lithium chloride (LiCl) and 85% aq. phosphoric acid (H_3PO_4). HFC computations were done for a 2 × 2 × 2 super-cell using IGLO-II/8s7p4d basis sets. g-Tensor and ZFS computations were done NEVPT2/def2-TZVP/IGLO-II level. Calculations of orbital shielding tensor were done for a unit cell at PBE/Ahlrich-VTZ/IGLO-II level (see Computational Details in Chapter 5).

[b] Anisotropy (Δ) = δ_{zz} - $\frac{1}{2}(\delta_{xx}+\delta_{yy})$; the components are ordered as $\mid \delta_{zz}-\delta_{iso} \mid \geq \mid \delta_{yy}-\delta_{iso} \mid \geq \mid \delta_{xx}-\delta_{iso} \mid$, $\delta_{iso} = \frac{1}{3}(\delta_{11}+\delta_{22}+\delta_{33})$ and $\delta_{11} \leq \delta_{22} \leq \delta_{33}$.

[c] Asymmetry (η) = $\frac{\delta_{xx}-\delta_{yy}}{\delta_{zz}-\delta_{iso}}$.

Table C.35.: Chemical shift anisotropy for $LiCoPO_4$ computed[a] for both XRD and optimized structures depending on the EXX admixture used for the HFC calculations

Atom	Functional	XRD δ_{iso} (ppm)	XRD δ (ppm) δ_{11}	XRD δ_{22}	XRD δ_{33}	XRD Δ[b] (ppm)	XRD η[c]	OPT δ_{FC} (ppm)	OPT δ (ppm) δ_{11}	OPT δ_{22}	OPT δ_{33}	OPT Δ[b] (ppm)	OPT η[c]
^{7}Li	PBE	-125.98	-558.35	-303.47	483.88	914.79	0.42	-117.03	-554.40	-287.60	490.92	911.92	0.44
	PBE5	-134.74	-570.03	-318.27	484.07	928.22	0.41	-125.67	-565.67	-301.83	490.49	924.24	0.43
	PBE10	-140.47	-577.92	-328.94	485.44	938.87	0.40	-131.42	-573.85	-312.06	491.66	934.62	0.42
	PBE15	-144.66	-583.90	-337.46	487.37	948.05	0.39	-136.58	-581.41	-321.14	492.80	944.08	0.41
	PBE20	-149.31	-590.50	-345.88	488.43	956.62	0.38	-142.31	-589.70	-330.23	493.02	952.98	0.41
	PBE25	-154.89	-598.27	-354.46	488.08	964.44	0.38	-146.59	-596.06	-337.29	493.58	960.26	0.40
	PBE30	-157.22	-601.68	-359.03	489.04	969.40	0.38	-147.09	-597.38	-340.06	496.18	964.90	0.40
	PBE35	-160.37	-606.17	-364.32	489.37	974.62	0.37	-149.53	-601.14	-344.78	497.33	970.29	0.40
	PBE40	-157.98	-603.44	-364.51	494.01	977.98	0.37	-153.14	-606.37	-349.96	496.92	975.08	0.39
^{31}P	PBE	3675.88	2517.09	3947.21	4563.34	-1738.19	0.53	3686.85	2567.88	3912.87	4579.80	-1678.46	0.60
	PBE5	3502.97	2418.68	3750.29	4339.95	-1626.44	0.54	3562.55	2499.27	3774.26	4414.12	-1594.92	0.60
	PBE10	3254.17	2267.87	3479.24	4015.41	-1479.45	0.54	3332.17	2361.12	3527.95	4107.46	-1456.58	0.60
	PBE15	2999.22	2114.43	3207.38	3675.86	-1327.19	0.53	3083.57	2209.52	3263.48	3777.73	-1311.08	0.59
	PBE20	2760.34	1971.77	2951.80	3357.44	-1182.84	0.51	2834.69	2055.75	2999.15	3449.15	-1168.40	0.58
	PBE25	2484.71	1800.54	2659.87	2993.72	-1026.26	0.49	2649.92	1943.38	2800.13	3206.26	-1059.81	0.57
	PBE30	2437.99	1779.71	2600.03	2934.23	-987.42	0.51	2617.53	1929.42	2753.12	3170.04	-1032.16	0.61
	PBE35	2288.32	1691.00	2438.45	2735.50	-895.98	0.50	2271.48	1709.22	2402.10	2703.14	-843.40	0.54
	PBE40	2239.61	1664.15	2375.62	2679.07	-863.20	0.53	2344.20	1763.15	2453.07	2816.38	-871.58	0.63

[a] Equation 5.3 in Chapter 5 has been used for computing the total shielding tensor. Shieldings converted to shifts for Li and P relative to aq. lithium chloride (LiCl) and 85% aq. phosphoric acid (H_3PO_4). HFC computations were done for a 2 × 2 × 2 super-cell using IGLO-II/8s7p4d basis sets. g-Tensor and ZFS computations were done NEVPT2/def2-TZVP/IGLO-II level. Calculations of orbital shielding tensor were done for a unit cell at PBE/Ahlrich-VTZ/IGLO-II level (see Computational Details in Chapter 5).

[b] Anisotropy (Δ) = δ_{zz} - $\frac{1}{2}(\delta_{xx}+\delta_{yy})$; the components are ordered as $\mid \delta_{zz}-\delta_{iso} \mid \geq \mid \delta_{yy}-\delta_{iso} \mid \geq \mid \delta_{xx}-\delta_{iso} \mid$, $\delta_{iso} = \frac{1}{3}(\delta_{11}+\delta_{22}+\delta_{33})$ and $\delta_{11} \leq \delta_{22} \leq \delta_{33}$.

[c] Asymmetry (η) = $\frac{\delta_{xx}-\delta_{yy}}{\delta_{zz}-\delta_{iso}}$.

Table C.36.: Chemical shift anisotropy for $LiNiPO_4$ computed[a] for both XRD and optimized structures depending on the EXX admixture used for the HFC calculations

Atom	Functional	XRD δ_{iso} (ppm)	XRD δ (ppm) δ_{11}	XRD δ_{22}	XRD δ_{33}	XRD Δ[b] (ppm)	XRD η[c]	OPT δ_{FC} (ppm)	OPT δ (ppm) δ_{11}	OPT δ_{22}	OPT δ_{33}	OPT Δ[b] (ppm)	OPT η[c]
^{7}Li	PBE	-46.39	-243.59	-231.24	335.65	573.06	0.03	-51.12	-242.74	-242.08	331.46	573.88	0.00
	PBE5	-45.56	-245.25	-236.73	345.30	586.30	0.02	-50.04	-247.35	-244.39	341.61	587.48	0.01
	PBE10	-44.35	-246.22	-241.04	354.22	597.85	0.01	-48.66	-251.54	-245.37	350.92	599.37	0.02
	PBE15	-42.94	-246.69	-244.45	362.33	607.90	0.01	-47.26	-254.99	-246.00	359.21	609.70	0.02
	PBE20	-41.58	-247.30	-246.94	369.49	616.61	0.00	-46.35	-258.37	-246.79	366.11	618.70	0.03
	PBE25	-40.46	-249.84	-247.18	375.64	624.14	0.01	-45.04	-260.74	-246.95	372.57	626.41	0.03
	PBE30	-39.13	-251.66	-247.02	381.29	630.63	0.01	-43.41	-262.28	-246.57	378.63	633.05	0.04
	PBE35	-38.32	-253.61	-247.20	385.84	636.25	0.02	-41.07	-262.60	-245.33	384.73	638.69	0.04
	PBE40	-37.30	-254.95	-247.04	390.09	641.09	0.02	-39.76	-263.66	-244.94	389.32	643.62	0.04
^{31}P	PBE	2689.33	2395.07	2580.39	3092.53	604.80	0.46	2445.70	2190.55	2320.65	2825.88	570.28	0.34
	PBE5	2394.00	2098.01	2319.63	2764.35	555.53	0.60	2139.74	1883.40	2051.30	2484.52	517.17	0.49
	PBE10	2161.25	1865.21	2115.79	2502.74	512.24	0.73	1907.86	1651.38	1849.68	2222.52	471.99	0.63
	PBE15	1968.07	1672.87	1947.37	2283.98	473.86	0.87	1724.34	1468.23	1692.44	2012.35	432.02	0.78
	PBE20	1797.36	1503.78	1798.15	2090.16	-440.37	0.99	1528.35	1273.73	1518.54	1792.76	396.63	0.93
	PBE25	1634.13	1343.02	1653.64	1905.74	-436.67	0.87	1382.66	1129.62	1392.60	1625.77	-379.57	0.92
	PBE30	1501.22	1212.84	1537.17	1753.66	-432.58	0.75	1255.96	1004.82	1282.88	1480.17	-376.71	0.79
	PBE35	1357.78	1072.81	1408.09	1592.43	-427.45	0.65	1209.23	960.14	1250.74	1416.82	-373.63	0.67
	PBE40	1241.68	960.22	1304.72	1460.10	-422.18	0.55	1108.75	862.43	1163.45	1300.38	-369.48	0.56

[a] Equation 5.3 in Chapter 5 has been used for computing the total shielding tensor. Shieldings converted to shifts for Li and P relative to aq. lithium chloride (LiCl) and 85% aq. phosphoric acid (H_3PO_4). HFC computations were done for a 2 × 2 × 2 super-cell using IGLO-II/8s7p4d basis sets. g-Tensor and ZFS computations were done NEVPT2/def2-TZVP/IGLO-II level. Calculations of orbital shielding tensor were done for a unit cell at PBE/Ahlrich-VTZ/IGLO-II level (see Computational Details in Chapter 5).

[b] Anisotropy (Δ) = δ_{zz} - $\frac{1}{2}(\delta_{xx}+\delta_{yy})$; the components are ordered as $\mid \delta_{zz}-\delta_{iso} \mid \geq \mid \delta_{yy}-\delta_{iso} \mid \geq \mid \delta_{xx}-\delta_{iso} \mid$, $\delta_{iso} = \frac{1}{3}(\delta_{11}+\delta_{22}+\delta_{33})$ and $\delta_{11} \leq \delta_{22} \leq \delta_{33}$.

[c] Asymmetry (η) = $\frac{\delta_{xx}-\delta_{yy}}{\delta_{zz}-\delta_{iso}}$.

Table C.37.: Chemical shift anisotropy for $FePO_4$ and $CoPO_4$ computed[a] for both XRD and optimized structures depending on the EXX admixture used for the HFC calculations

Atom	Functional	XRD δ_{iso} (ppm)	XRD δ (ppm) δ_{11}	XRD δ_{22}	XRD δ_{33}	XRD Δ[b] (ppm)	XRD η[c]	OPT δ_{FC} (ppm)	OPT δ (ppm) δ_{11}	OPT δ_{22}	OPT δ_{33}	OPT Δ[b] (ppm)	OPT η[c]
$FePO_4$	PBE	8421.86	7817.34	8648.77	8799.46	-906.77	0.25	7721.37	7059.55	7847.98	8256.60	-992.74	0.62
	PBE5	7548.54	6955.03	7779.25	7911.33	-890.26	0.22	6912.84	6253.21	7056.18	7429.11	-989.44	0.57
	PBE10	6834.46	6251.56	7067.77	7184.07	-874.36	0.20	6249.21	5592.57	6407.04	6748.02	-984.96	0.52
	PBE15	6244.36	5671.67	6479.54	6581.86	-859.04	0.18	5706.43	5053.15	5877.07	6189.08	-979.93	0.48
	PBE20	5751.81	5188.87	5988.65	6077.92	-844.42	0.16	5260.85	4611.23	5443.06	5728.27	-974.44	0.44
	PBE25	5334.87	4781.24	5573.35	5650.02	-830.45	0.14	4895.26	4249.60	5088.08	5348.11	-968.50	0.40
	PBE30	4976.43	4431.69	5216.73	5280.87	-817.11	0.12	4557.77	3915.72	4760.43	4997.14	-963.06	0.37
	PBE35	4665.78	4129.58	4908.22	4959.54	-804.30	0.10	4290.18	3652.53	4501.87	4716.13	-956.47	0.34
	PBE40	4392.68	3864.72	4637.60	4675.73	-791.94	0.07	4055.28	3422.30	4275.37	4468.16	-949.46	0.30
$CoPO_4$	PBE	6581.79	5725.56	6580.70	7439.12	1285.99	1.00	6588.28	5455.57	6583.16	7726.09	1706.73	0.99
	PBE5	5933.67	5081.94	5945.38	6773.68	-1277.59	0.97	5694.67	4584.63	5714.31	6785.07	-1665.06	0.96
	PBE10	5210.64	4338.64	5247.90	6045.39	-1308.00	0.91	4876.25	3766.71	4929.57	5932.47	-1664.31	0.90
	PBE15	4596.45	3707.07	4658.78	5423.51	-1334.08	0.86	4228.13	3118.71	4312.10	5253.58	-1664.13	0.85
	PBE20	4108.66	3206.14	4193.96	4925.87	-1353.78	0.81	3723.74	2615.06	3834.64	4721.51	-1663.02	0.80
	PBE25	3716.63	2802.92	3825.05	4521.93	-1370.57	0.76	3350.93	2241.50	3487.92	4323.36	-1664.14	0.75
	PBE30	3412.13	2490.49	3542.50	4203.40	-1382.46	0.72	3069.12	1958.43	3230.21	4018.71	-1666.03	0.71
	PBE35	3131.27	2203.36	3280.34	3910.12	-1391.87	0.68	2868.02	1757.54	3051.68	3794.83	-1665.72	0.67
	PBE40	2930.19	1997.59	3099.44	3693.53	-1398.89	0.64	2707.20	1597.09	2911.54	3612.98	-1665.17	0.63

[a] Equation 5.3 in Chapter 5 has been used for computing the total shielding tensor. Shieldings converted to shifts for Li and P relative to aq. lithium chloride (LiCl) and 85% aq. phosphoric acid (H_3PO_4). HFC computations were done for a 2 × 2 × 2 super-cell using IGLO-II/8s7p4d basis sets. g-Tensor and ZFS computations were done NEVPT2/def2-TZVP/IGLO-II level. Calculations of orbital shielding tensor were done for a unit cell at PBE/Ahlrich-VTZ/IGLO-II level (see Computational Details in Chapter 5).

[b] Anisotropy (Δ) = δ_{zz} - $\frac{1}{2}(\delta_{xx}+\delta_{yy})$; the components are ordered as $\mid \delta_{zz}-\delta_{iso} \mid \geq \mid \delta_{yy}-\delta_{iso} \mid \geq \mid \delta_{xx}-\delta_{iso} \mid$, $\delta_{iso} = \frac{1}{3}(\delta_{11}+\delta_{22}+\delta_{33})$ and $\delta_{11} \leq \delta_{22} \leq \delta_{33}$.

[c] Asymmetry (η) = $\frac{\delta_{xx}-\delta_{yy}}{\delta_{zz}-\delta_{iso}}$.

Appendix D.

Additional figures for dinuclear iron complex

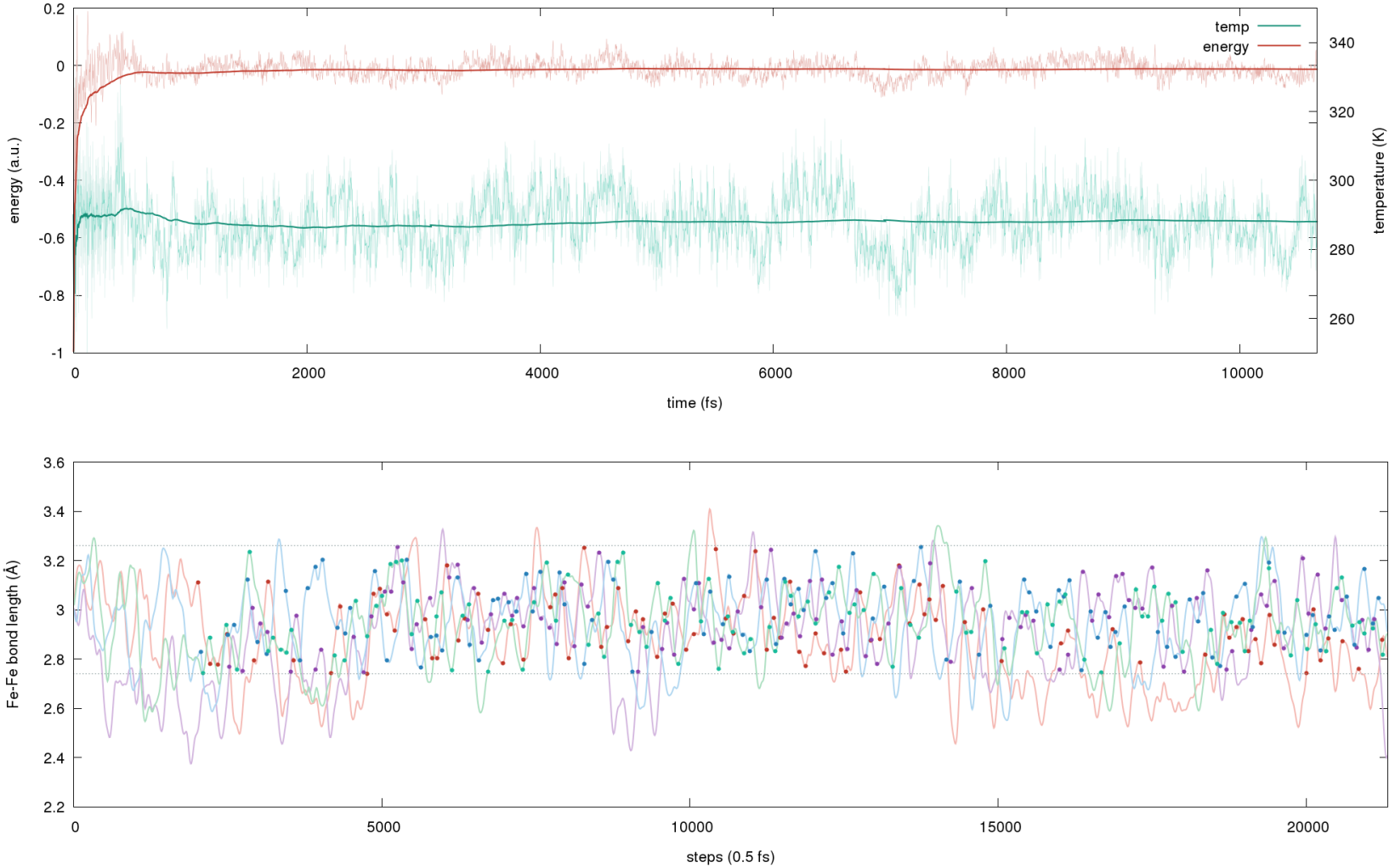

Figure D.1.: AIMD trajectory of crystalline solids of the dinuclear iron complex at 290 K. The simulation cell contains four dinuclear iron complexes having 712 atoms (see Computational Details). Top: the thin red and green curves represent the energy and temperature of the system at each step, respectively. The bold red and green curves represent the averaged energy and temperature with propagation steps from the beginning of the trajectory, respectively. Bottom: the Fe-Fe distance for all four dinuclear iron complexes in the simulation cell for each step of the AIMD trajectory. The dots represent the sampled snapshots of the dinuclear iron complexes for pNMR shift calculations.

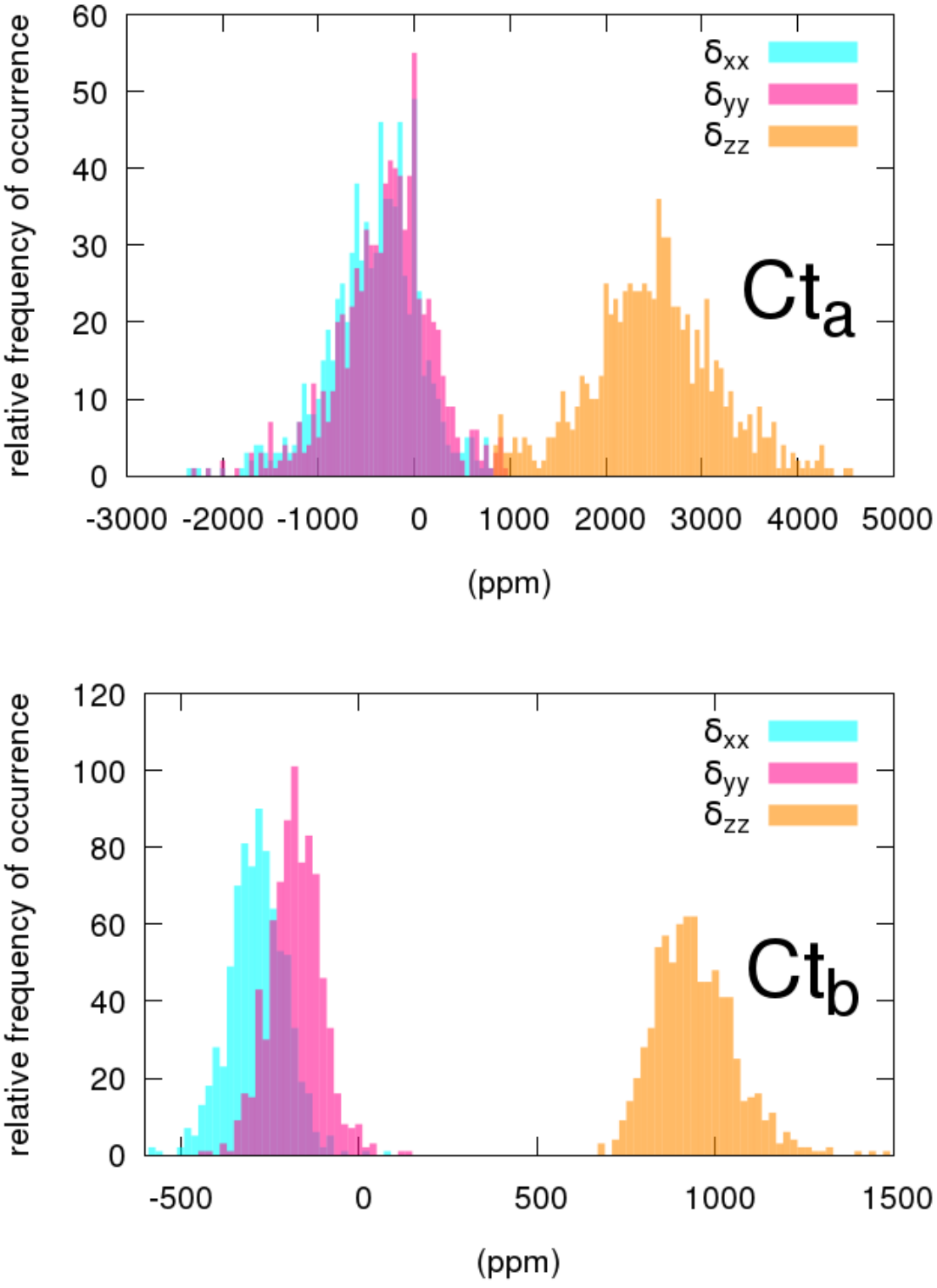

Figure D.2.: Histogram for the occurrence of the principal values of ^{13}C shift tensors for C_{t_a} (top) and C_{t_b} (bottom).

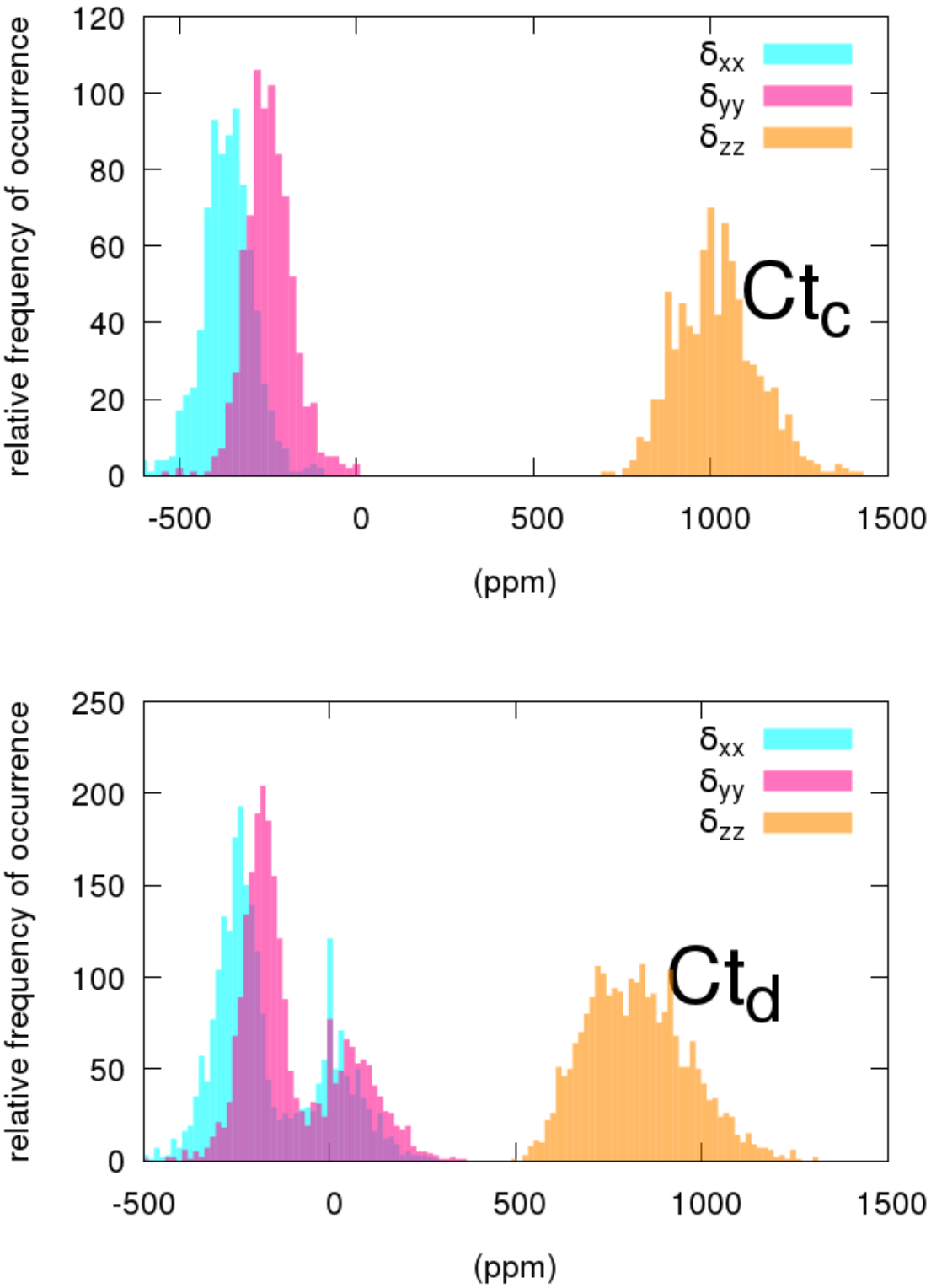

Figure D.3.: Histogram for the occurrence of the principal values of ^{13}C shift tensors for C_{t_c} (top) and C_{t_d} (bottom).

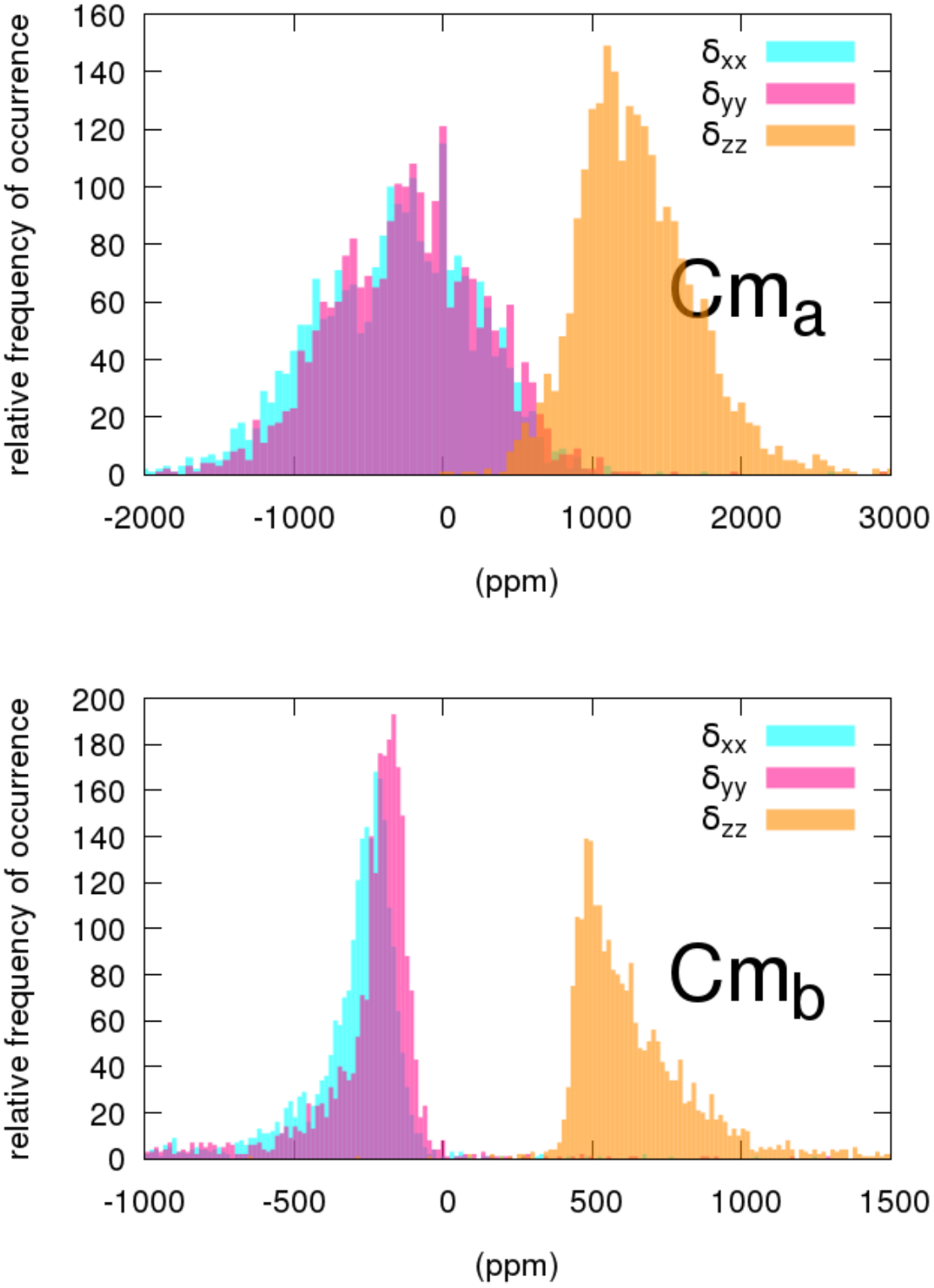

Figure D.4.: Histogram for the occurrence of the principal values of ^{13}C shift tensors for C_{m_a} (top) and C_{m_b} (bottom).

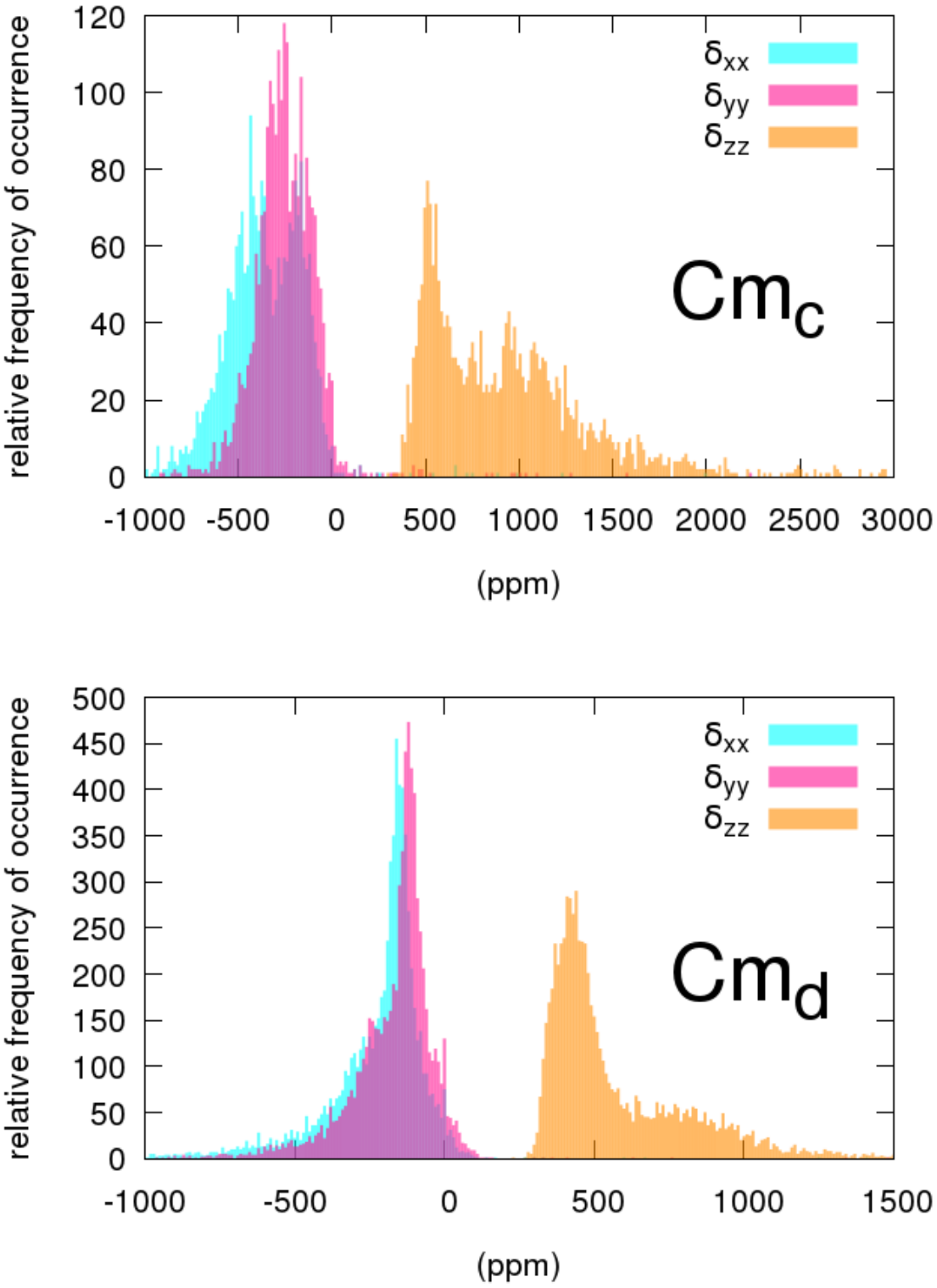

Figure D.5.: Histogram for the occurrence of the principal values of ^{13}C shift tensors for C_{m_c} (top) and C_{m_d} (bottom).

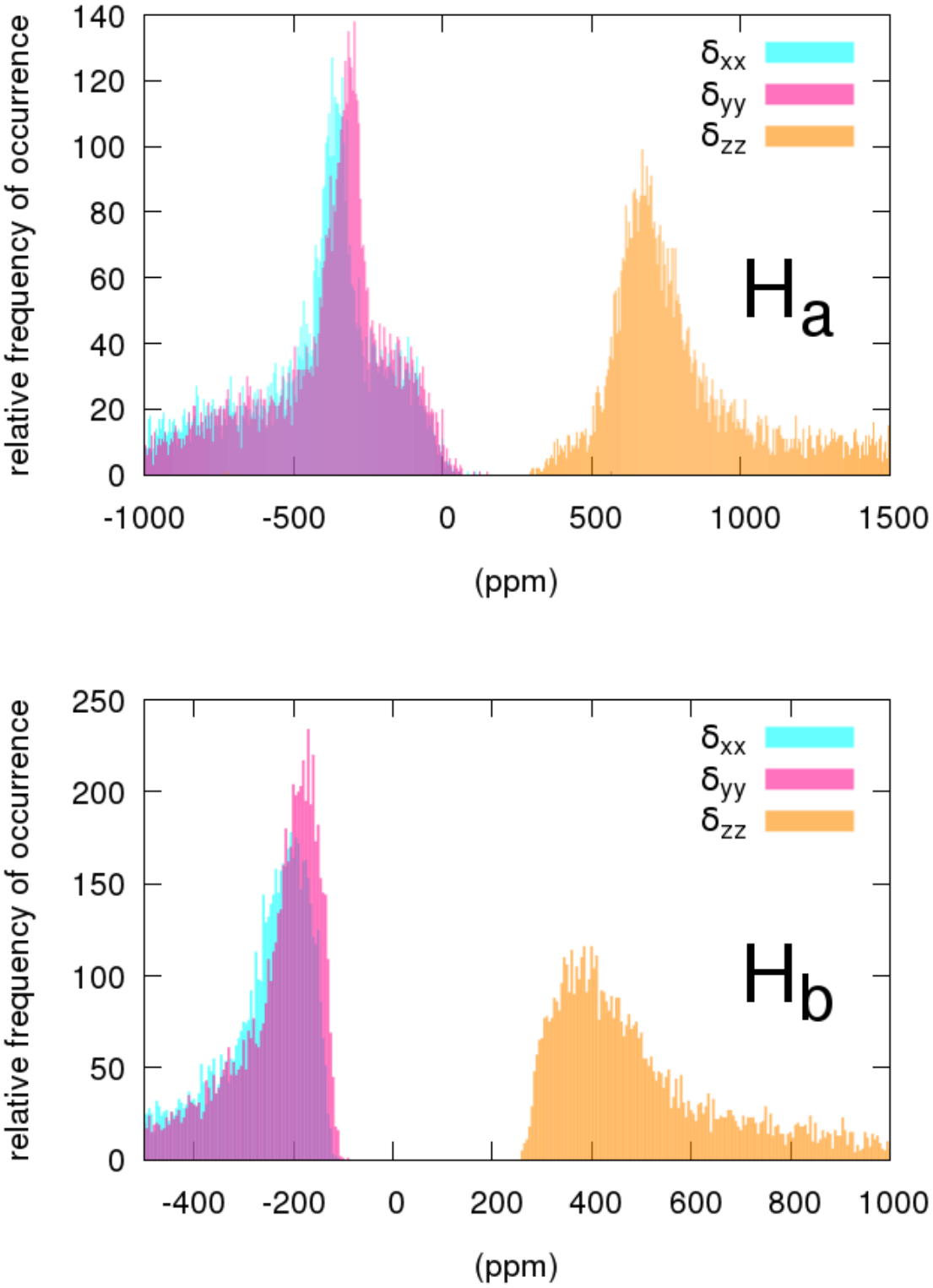

Figure D.6.: Histogram for the occurrence of the principal values of ^{1}H shift tensors for H_a (top) and H_b (bottom).

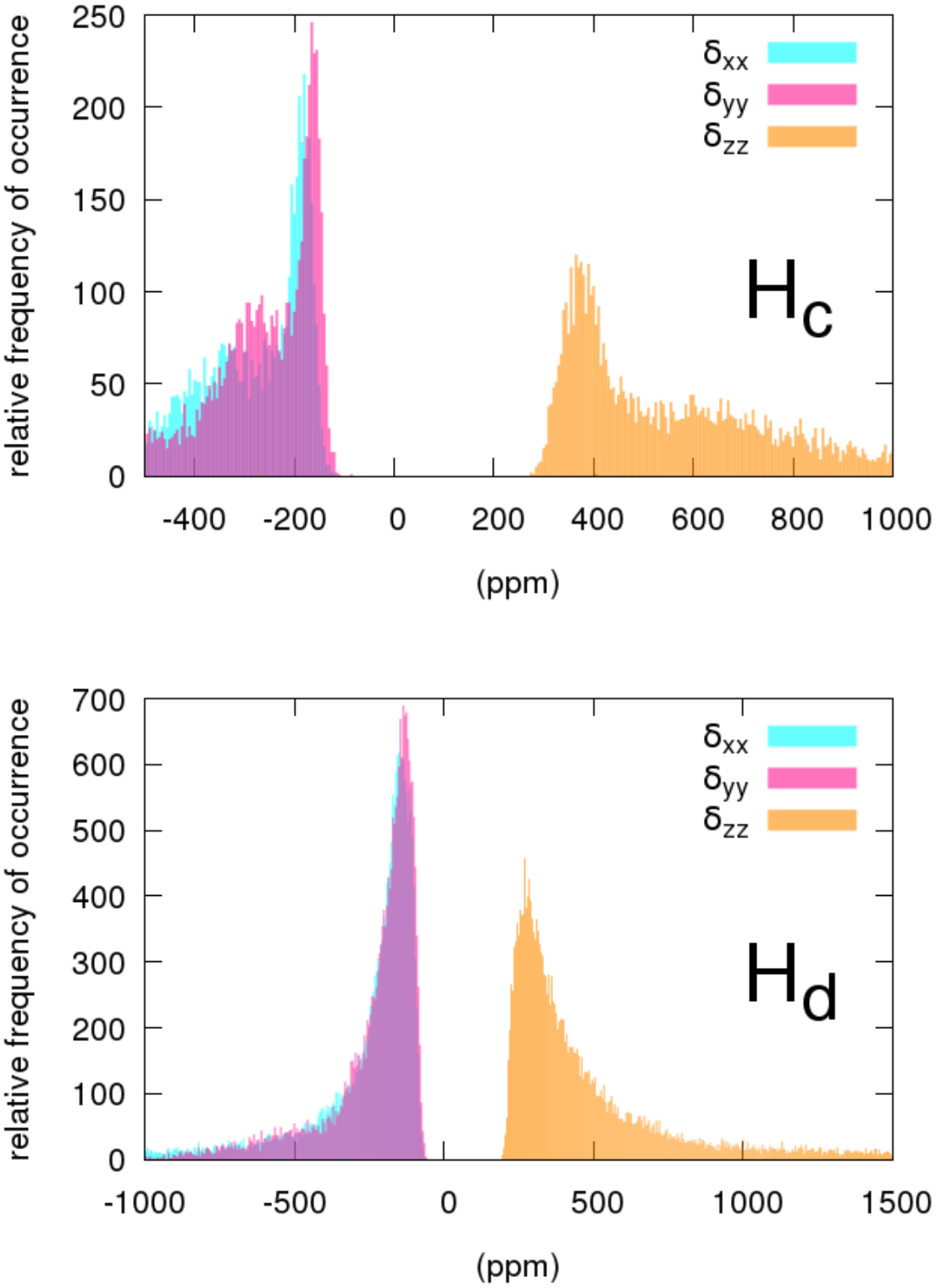

Figure D.7.: Histogram for the occurrence of the principal values of ^{1}H shift tensors for H_c (top) and H_d (bottom).

List of Figures

List of Tables

Bibliography

[1] Abragam, A. *The principles of nuclear magnetism.*; Clarendon Press, 1961.

[2] Levitt, M. H. *Spin dynamics: Basics of nuclear magnetic resonance*, 2nd ed.; Wiley, 2008.

[3] Bertini, I.; Luchinat, C.; Parigi, G.; Ravera, E. *NMR of paramagnetic molecules: Applications to metallobiomolecules and models*; Elsevier, 2016; Vol. 2.

[4] Slichter, C. P. *Principles of magnetic resonance*; Springer Science & Business Media, 2013; Vol. 1.

[5] Silverstein, R. M.; Webster, F. X.; Kiemle, D. J.; Bryce, D. L. *Spectrometric identification of organic compounds*; John wiley & sons, 2014.

[6] Kemp, W. *Organic Spectroscopy*; Springer, 1991; pp 101–241.

[7] Darbeau, R. W. *Appl. Spectrosc. Rev.* **2006**, *41*, 401–425.

[8] Balci, M. *Basic ^{1}H-and ^{13}C-NMR spectroscopy*; Elsevier, 2005.

[9] Jackman, L. M.; Sternhell, S. *Application of nuclear magnetic resonance spectroscopy in organic chemistry: International series in organic chemistry*; Elsevier, 2013.

[10] Apperley, D. C.; Harris, R. K.; Hodgkinson, P. *Solid-state NMR: Basic principles and practice*; Momentum Press, 2012.

[11] Baldus, M. *Angew. Chem. Int. Ed.* **2006**, *45*, 1186–1188.

[12] Blanc, F.; Coperet, C.; Lesage, A.; Emsley, L. *Chem. Soc. Rev.* **2008**, *37*, 518–526.

[13] Böckmann, A. *Angew. Chem. Int. Ed.* **2008**, *47*, 6110–6113.

[14] Bovey, F. A.; Mirau, P. A.; Gutowsky, H. *Nuclear magnetic resonance spectroscopy*; Elsevier, 1988.

[15] Pauli, W. *Naturwissenschaften* **1924**, *12*, 741–743.

[16] Gerlach, W.; Stern, O. *Z. Phys.* **1922**, *9*, 353–355.

[17] Frisch, R.; Stern, O. *Z. Phys.* **1933**, *85*, 4–16.

[18] Estermann, I.; Stern, O. *Z. Phys.* **1933**, *85*, 17–24.

[19] Estermann, I.; Stern, O. *Z. Phys.* **1933**, *86*, 132–134.

[20] Estermann, I.; Simpson, O. C.; Stern, O. *Phys. Rev.* **1937**, *52*, 535–545.

[21] Gorter, C. *Physica* **1936**, *3*, 995 – 998.

[22] Rabi, I. I.; Zacharias, J. R.; Millman, S.; Kusch, P. *Phys. Rev.* **1938**, *53*, 318–318.

[23] Rabi, I. I.; Millman, S.; Kusch, P.; Zacharias, J. R. *Phys. Rev.* **1939**, *55*, 526–535.

[24] Boesch, C. *J. Magn. Reson. Imaging* **2004**, *20*, 177–179.

[25] Ramsey, N. F. *Phys. perspect.* **1999**, *1*, 123–135.

[26] Sanders, J. K.; Hunter, B. K. *Modern NMR spectroscopy: a guide for chemists*; Oxford University Press, New York, NY, 1988.

[27] Schmidt-Rohr, K.; Spiess, H. W. *Multidimensional solid-state NMR and polymers*; Academic Press, 1994.

[28] Bonhomme, C.; Gervais, C.; Babonneau, F.; Coelho, C.; Pourpoint, F.; Azaïs, T.; Ashbrook, S. E.; Griffin, J. M.; Yates, J. R.; Mauri, F.; Pickard, C. J. *Chem. Rev.* **2012**, *112*, 5733–5779.

[29] Berliner, L. In *NMR of paramagnetic molecules*; Reuben, J., Ed.; Plenum Press, New York, 1993.

[30] Bertini, I.; Luchinat, C.; Parigi, G. *Solution NMR of paramagnetic molecules*; Elsevier, Amsterdam, 2001.

[31] Helm, L. *Prog. Nucl. Magn. Reson. Spectrosc.* **2006**, *49*, 45–64.

[32] Cole, K. E.; Paik, Y.; Reeder, R. J.; Schoonen, M.; Grey, C. P. *J. Phys. Chem. B* **2004**, *108*, 6938–6940.

[33] Grey, C. P.; Dupré, N. *Chem. Rev.* **2004**, *104*, 4493–4512.

[34] Nielsen, U. G.; Paik, Y.; Julmis, K.; Schoonen, M. A. A.; Reeder, R. J.; Grey, C. P. *J. Phys. Chem. B* **2005**, *109*, 18310–18315.

[35] Kowalewski, J.; Kruk, D.; Parigi, G. *Adv. Inorg. Chem.* **2005**, *57*, 41–104.

[36] Kim, J.; Nielsen, U. G.; Grey, C. P. *J. Am. Chem. Soc.* **2008**, *130*, 1285–1295.

[37] Kaupp, M.; Köhler, F. H. *Coord. Chem. Rev.* **2009**, *253*, 2376–2386.

[38] Lauffer, R. B. *Chem. Rev.* **1987**, *87*, 901–927.

[39] Sinharay, S.; Pagel, M. D. *Annu. Rev. Anal. Chem.* **2016**, *9*, 95–115.

[40] Tucker, M. C.; Doeff, M. M.; Richardson, T. J.; Fiñones, R.; Cairns, E. J.; ; Reimer, J. A. *J. Am. Chem. Soc.* **2002**, *124*, 3832–3833.

[41] Wilcke, L. S.; Lee, Y.-J.; Cairns, J. E.; Reimer, A. J. *Appl. Magn. Reson.* **2007**, *32*, 547–563.

[42] Tucker, M. C.; Doeff, M. M.; Richardson, T. J.; Fiñones, R.; Reimer, J. A.; Cairns, E. J. *Electrochem. Solid-State Lett.* **2002**, *5*, A95–A98.

[43] Cahill, S. L.; Chapman, P. R.; Kirby, W. C.; Goward, R. G. *Appl. Magn. Reson.* **2007**, *32*, 565–581.

[44] Kim, J.; Middlemiss, D. S.; Chernova, N. A.; Zhu, B. Y. X.; Masquelier, C.; Grey, C. P. *J. Am. Chem. Soc.* **2010**, *132*, 16825–16840.

[45] Mali, G.; Sirisopanaporn, C.; Masquelier, C.; Hanzel, D.; Dominko, R. *Chem. Mater.* **2011**, *23*, 2735–2744.

[46] Lee, J.; Seymour, I. D.; Pell, A. J.; Dutton, S. E.; Grey, C. P. *Phys. Chem. Chem. Phys.* **2017**, *19*, 613–625.

[47] Clément, R. J.; Xu, J.; Middlemiss, D. S.; Alvarado, J.; Ma, C.; Meng, Y. S.; Grey, C. P. *J. Mater. Chem. A* **2017**, *5*, 4129–4143.

[48] Seymour, I. D.; Middlemiss, D. S.; Halat, D. M.; Trease, N. M.; Pell, A. J.; Grey, C. P. *J. Am. Chem. Soc.* **2016**, *138*, 9405–9408.

[49] Trease, N. M. et al. *Chem. Mater.* **2016**, *28*, 8170–8180.

[50] Clément, R. J.; Middlemiss, D. S.; Seymour, I. D.; Ilott, A. J.; Grey, C. P. *Chem. Mater.* **2016**, *28*, 8228–8239.

[51] Keizers, P. H.; Ubbink, M. *Prog. Nucl. Magn. Reson. Spectrosc.* **2011**, *58*, 88 – 96.

[52] Capsoni, D.; Bini, M.; Massarotti, V.; Mustarelli, P.; Chiodelli, G.; Azzoni, C. B.; Mozzati, M. C.; Linati, L.; Ferrari, S. *Chem. Mater.* **2008**, *20*, 4291–4298.

[53] Villa, M.; Carduner, K. R.; Chiodelli, G. *J. Solid State Chem.* **1987**, *69*, 19 – 23.

[54] Clément, R. J.; Pell, A. J.; Middlemiss, D. S.; Strobridge, F. C.; Miller, J. K.; Whittingham, M. S.; Emsley, L.; Grey, C. P.; Pintacuda, G. *J. Am. Chem. Soc.* **2012**, *134*, 17178–17185.

[55] Kowalewski, J.; Maler, L. *Nuclear spin relaxation in liquids: theory, experiments, and applications*; CRC press, 2017.

[56] Bertini, I.; Luchinat, C.; Parigi, G. *Prog. Nucl. Magn. Reson. Spectrosc.* **2002**, *40*, 249–273.

[57] Pennanen, T. O.; Vaara, J. *Phys. Rev. Lett.* **2008**, *100*, 133002.

[58] Middlemiss, D. S.; Ilott, A. J.; Clément, R. J.; Strobridge, F. C.; Grey, C. P. *Chem. Mater.* **2013**, *25*, 1723–1734.

[59] Komorovský, S.; Repiský, M.; Ruud, K.; Malkina, O. L.; Malkin, V. G. *J. Phys. Chem. A* **2013**, *117*, 14209–14219.

[60] den Heuvel, W. V.; Soncini, A. *J. Chem. Phys.* **2013**, *138*, 054113.

[61] Strobridge, F. C.; Middlemiss, D. S.; Pell, A. J.; Leskes, M.; Clément, R. J.; Pourpoint, F.; Lu, Z.; Hanna, J. V.; Pintacuda, G.; Emsley, L.; Samoson, A.; Grey, C. P. *J. Mater. Chem. A* **2014**, *2*, 11948–11957.

[62] Ashbrook, S. E.; Sneddon, S. *J. Am. Chem. Soc.* **2014**, *136*, 15440–15456.

[63] Rouf, S. A.; Mareš, J.; Vaara, J. *J. Chem. Theory Comput.* **2015**, *11*, 1683–1691.

[64] Holmes, S. T.; Iuliucci, R. J.; Mueller, K. T.; Dybowski, C. *J. Chem. Theory Comput.* **2015**, *11*, 5229–5241.

[65] Benda, L.; Mareš, J.; Ravera, E.; Parigi, G.; Luchinat, C.; Kaupp, M.; Vaara, J. *Angew. Chem. Int. Ed.* **2016**, *55*, 14713–14717.

[66] Halat, D. M.; Dervişoğlu, R.; Kim, G.; Dunstan, M. T.; Blanc, F.; Middlemiss, D. S.; Grey, C. P. *J. Am. Chem. Soc.* **2016**, *138*, 11958–11969.

[67] Pecher, O.; Carretero-González, J.; Griffith, K. J.; Grey, C. P. *Chem. Mater.* **2017**, *29*, 213–242.

[68] Pigliapochi, R.; Pell, A. J.; Seymour, I. D.; Grey, C. P.; Ceresoli, D.; Kaupp, M. *Phys. Rev. B* **2017**, *95*, 054412.

[69] The CP2K developer group. CP2K is freely available from `http://www.cp2k.org/`, 2016.

[70] Neese, F. ORCA, An ab Initio, density functional and semiempirical program package, version 3.0.1. 2012.

[71] TURBOMOLE V7.0 2015, a development of University of Karlsruhe and Forschungszentrum Karlsruhe GmbH, 1989-2007, TURBOMOLE GmbH, since 2007; available from
`http://www.turbomole.com`.

[72] Dovesi, R.; Saunders, V. R.; Roetti, C.; Orlando, R.; Zicovich-Wilson, C. M.; Pascale, F.; Civalleri, B.; Doll, K.; Harrison, N. M.; Bush, I. J.; D'Arco, P.; Llunell, M. CRYSTAL09 User's Manual. University of Torino: Torino.

[73] Malkin, V. G.; Malkina, O. L.; Reviakine, R.; Arbuznikov, A. V.; Kaupp, M.; Schimmelpfennig, B.; Malkin, I.; Repiský, M.; Komorovský, S.; Hrobárik, P.; Malkin, E.; Helgaker, T.; Ruud, K. MAG-ReSpect, version 2.3, 2010.

[74] Frisch, M. J. et al. Gaussian09 Revision E.01. Gaussian Inc. Wallingford CT 2009.

[75] Blaha, P.; Schwarz, K.; Madsen, G. K. H.; Kvasnicka, D.; Luitz, J. WIEN2k, an augmented plane wave + local orbitals program for calculating crystal properties.

[76] Pickard, C. J.; Mauri, F. *Phys. Rev. Lett.* **2002**, *88*, 086403.

[77] Pickard, C. J.; Mauri, F. *Phys. Rev. B* **2001**, *63*, 245101.

[78] Hutter, J.; Iannuzzi, M.; Schiffmann, F.; VandeVondele, J. *WIREs Comput. Mol. Sci.* **2014**, *4*, 15–25.

[79] Sumowski, C. V.; Hanni, M.; Schweizer, S.; Ochsenfeld, C. *J. Chem. Theory Comput.* **2014**, *10*, 122–133.

[80] Flaig, D.; Maurer, M.; Hanni, M.; Braunger, K.; Kick, L.; Thubauville, M.; Ochsenfeld, C. *J. Chem. Theory Comput.* **2014**, *10*, 572–578.

[81] Greif, A. H.; Hrobárik, P.; Hrobáriková, V.; Arbuznikov, A. V.; Autschbach, J.; Kaupp, M. *Inorg. Chem.* **2015**, *54*, 7199–7208.

[82] Kussmann, J.; Ochsenfeld, C. *J. Chem. Phys.* **2007**, *127*, 054103.

[83] Hrobárik, P.; Hrobáriková, V.; Greif, A. H.; Kaupp, M. *Angew. Chem. Int. Ed.* **2012**, *51*, 10884–10888.

[84] Greif, A. H.; Hrobárik, P.; Kaupp, M. *Chem. Eur. J.* **2017**, *23*, 9790–9803.

[85] Greif, A. H.; Hrobárik, P.; Autschbach, J.; Kaupp, M. *Phys. Chem. Chem. Phys.* **2016**, *18*, 30462–30474.

[86] Ashbrook, S. E.; McKay, D. *Chem. Commun.* **2016**, *52*, 7186–7204.

[87] Bonnet, M.-L.; Iannuzzi, M.; Sebastiani, D.; Hutter, J. *J. Phys. Chem. C* **2012**, *116*, 18577–18583.

[88] Ramsey, N. F. *Phys. Rev.* **1950**, *78*, 695–699.

[89] Ramsey, N. F. *Phys. Rev.* **1952**, *86*, 243–246.

[90] Ramsey, N. F. *Phys. Rev.* **1953**, *91*, 303–307.

[91] Wolinski, K.; Hinton, J. F.; Pulay, P. *J. Am. Chem. Soc.* **1990**, *112*, 8251–8260.

[92] Helgaker, T.; Jørgensen, P. *J. Chem. Phys.* **1991**, *95*, 2595–2601.

[93] Helgaker, T.; Jaszuński, M.; Ruud, K. *Chem. Rev.* **1999**, *99*, 293–352.

[94] M. Kaupp, M. Bühl, and V. G. Malkin, (editors)*, Calculation of NMR and EPR parameters. Theory and applications*; Wiley-VCH, Weinheim, 2004.

[95] Vaara, J. *Phys. Chem. Chem. Phys.* **2007**, *9*, 5399–5418.

[96] Ochsenfeld, C.; Kussmann, J.; Koziol, F. *Angew. Chem. Int. Ed.* **2004**, *43*, 4485–4489.

[97] Auer, A. A.; Gauss, J. *J. Chem. Phys.* **2001**, *115*, 1619–1622.

[98] Aucar, G. A.; Saue, T.; Visscher, L.; Jensen, H. J. A. *J. Chem. Phys.* **1999**, *110*, 6208–6218.

[99] Visscher, L.; Enevoldsen, T.; Saue, T.; Jensen, H. J. A.; Oddershede, J. *J. Comput. Chem.* **1999**, *20*, 1262–1273.

[100] Enevoldsen, T.; Visscher, L.; Saue, T.; Jensen, H. J. A.; Oddershede, J. *J. Chem. Phys.* **2000**, *112*, 3493–3498.

[101] Cheng, L.; Xiao, Y.; Liu, W. *J. Chem. Phys.* **2009**, *131*, 244113.

[102] Komorovský, S.; Repiský, M.; Malkina, O. L.; Malkin, V. G. *J. Chem. Phys.* **2010**, *132*, 154101.

[103] Manninen, P.; Lantto, P.; Vaara, J.; Ruud, K. *J. Chem. Phys.* **2003**, *119*, 2623–2637.

[104] Manninen, P.; Ruud, K.; Lantto, P.; Vaara, J. *J. Chem. Phys.* **2005**, *122*, 114107.

[105] Melo, J. I.; de Azua, M. C. R.; Giribet, C. G.; Aucar, G. A.; Romero, R. H. *J. Chem. Phys.* **2003**, *118*, 471–486.

[106] Autschbach, J. In *High resolution NMR spectroscopy*; Contreras, R. H., Ed.; Science and technology of atomic, molecular, condensed matter & biological systems; Elsevier, 2013; Vol. 3; pp 69 – 117.

[107] Harriman, J. E. *Theoretical foundations of electron spin resonance*; Academic Press, New York, 1978.

[108] McConnell, H. M.; Chesnut, D. B. *J. Chem. Phys.* **1958**, *28*, 107–117.

[109] McConnell, H. M.; Robertson, R. E. *J. Chem. Phys.* **1958**, *29*, 1361–1365.

[110] Kurland, R. J.; McGarvey, B. R. *J. Magn. Reson.* **1970**, *2*, 286–301.

[111] McConnell, H. M. *J. Chem. Phys.* **1956**, *25*, 709–711.

[112] Morishima, L.; Endo, K.; Yonezawa, T. *Chem. Phys. Lett.* **1971**, *9*, 143 – 146.

[113] Lazzeretti, P.; Malagoli, M.; Zanasi, R. *Chem. Phys.* **1991**, *150*, 173 – 185.

[114] Wilkens, S. J.; Xia, B.; Weinhold, F.; Markley, J. L.; Westler, W. M. *J. Am. Chem. Soc.* **1998**, *120*, 4806–4814.

[115] Rinkevicius, Z.; Vaara, J.; Telyatnyk, L.; Vahtras, O. *J. Chem. Phys.* **2003**, *118*, 2550–2561.

[116] Wilkens, S. J.; Xia, B.; Volkman, B. F.; Weinhold, F.; Markley, J. L.; Westler, W. M. *J. Phys. Chem. B* **1998**, *102*, 8300–8305.

[117] Moon, S.; Patchkovskii, S. *First-principles calculations of paramagnetic NMR shifts, in* M. Kaupp, M. Bühl, and V. G. Malkin, (editors)*, Calculation of NMR and EPR parameters. Theory and applications*; Wiley-VCH, Weinheim, 2004.

[118] Autschbach, J.; Patchkovskii, S.; Pritchard, B. *J. Chem. Theory Comput.* **2011**, *7*, 2175–2188.

[119] Hrobárik, P.; Hrobáriková, V.; Meier, F.; Repiský, M.; Komorovský, S.; Kaupp, M. *J. Phys. Chem. A* **2011**, *115*, 5654–5659.

[120] Van den Heuvel, W.; Soncini, A. *Phys. Rev. Lett.* **2012**, *109*, 073001.

[121] Soncini, A.; den Heuvel, W. V. *J. Chem. Phys.* **2013**, *138*, 021103.

[122] Martin, B.; Autschbach, J. *J. Chem. Phys.* **2015**, *142*, 054108.

[123] Vaara, J.; Rouf, S. A.; Mareš, J. *J. Chem. Theory Comput.* **2015**, *11*, 4840–4849.

[124] Gendron, F.; Sharkas, K.; Autschbach, J. *J. Phys. Chem. Lett.* **2015**, *6*, 2183–2188.

[125] Gendron, F.; Autschbach, J. *J. Chem. Theory Comput.* **2016**, *12*, 5309–5321.

[126] Martin, B.; Autschbach, J. *Phys. Chem. Chem. Phys.* **2016**, *18*, 21051–21068.

[127] Rouf, S. A.; Mareš, J.; Vaara, J. *J. Chem. Theory Comput.* **2017**, *13*, 3731–3745.

[128] Pennanen, T. O.; Vaara, J. *J. Chem. Phys.* **2005**, *123*, 174102.

[129] Hrobárik, P.; Reviakine, R.; Arbuznikov, A. V.; Malkina, O. L.; Malkin, V. G.; Köhler, F. H.; Kaupp, M. *J. Chem. Phys.* **2007**, *126*, 024107.

[130] Pritchard, B.; Autschbach, J. *Inorg. Chem.* **2012**, *51*, 8340–8351.

[131] Gohr, S. Fully relativistic calculations of EPR and paramagnetic NMR parameters for heavy atom compounds. Ph.D. thesis, Technischen Universität Berlin, 2018.

[132] Giannozzi, P. et al. *J. Phys.: Condens. Matter* **2009**, *21*, 395502.

[133] Lippert, G.; Hutter, J.; Parrinello, M. *Theor. Chem. Acc.* **1999**, *103*, 124–140.

[134] Iannuzzi, M.; Chassaing, T.; Wallman, T.; Hutter, J. *Chimia* **2005**, *59*, 499–503.

[135] Lippert, G.; Hutter, J.; Parrinello, M. *Mol. Phys.* **1997**, *92*, 477–488.

[136] Del Ben, M.; Hutter, J.; VandeVondele, J. *J. Chem. Theory Comput.* **2012**, *8*, 4177–4188.

[137] Weber, V.; Iannuzzi, M.; Giani, S.; Hutter, J.; Declerck, R.; Waroquier, M. *J. Chem. Phys.* **2009**, *131*, 014106.

[138] Pauwels, E.; Asher, J.; Kaupp, M.; Waroquier, M. *Phys. Chem. Chem. Phys.* **2011**, *13*, 18638–18646.

[139] Slichter, C. P. *Principles of magnetic resonance*; Springer Science & Business Media, 2013; Vol. 1.

[140] Pound, R. V. *Phys. Rev.* **1950**, *79*, 685–702.

[141] Atkins, P. W.; Friedman, R. S. *Molecular quantum mechanics*, 5th ed.; Oxford University Press, USA, 2010.

[142] Odom, B.; Hanneke, D.; D'Urso, B.; Gabrielse, G. *Phys. Rev. Lett.* **2006**, *97*, 030801.

[143] Levitt, M. H. *Spin dynamics: basics of nuclear magnetic resonance*; Wiley, 2001.

[144] Aucar, I. A.; Gomez, S. S.; Giribet, C. G.; Aucar, G. A. *Phys. Chem. Chem. Phys.* **2016**, *18*, 23572–23586.

[145] Jensen, F. *Introduction to Computational Chemistry*, 2nd ed.; Wiley, 2006.

[146] Bleaney, B. *J. Magn. Reson.* **1972**, *8*, 91 – 100.

[147] McGarvey, B. R. *Inorg. Chem.* **1995**, *34*, 6000–6007.

[148] Mondal, A.; Gaultois, M. W.; Pell, A. J.; Iannuzzi, M.; Grey, C. P.; Hutter, J.; Kaupp, M. *J. Chem. Theory Comput.* **2018**, *14*, 377–394.

[149] Blundell, S. *Magnetism in condensed matter (Oxford master series in physics)*, 1st ed.; Oxford University Press, USA, 2001.

[150] Chernova, N. A.; Nolis, G. M.; Omenya, F. O.; Zhou, H.; Li, Z.; Whittingham, M. S. *J. Mater. Chem.* **2011**, *21*, 9865–9875.

[151] Mondal, A.; Kaupp, M. *J. Phys. Chem. Lett.* **2018**, *9*, 1480–1484.

[152] Petit, S.; Borshch, S. A.; Robert, V. *J. Am. Chem. Soc.* **2003**, *125*, 3959–3966.

[153] Petit, S.; Borshch, S. A.; Robert, V. *Inorg. Chem.* **2004**, *43*, 4210–4215.

[154] Hairie, T.; Robert, V.; Petit, S. *Phys. Rev. B* **2006**, *74*, 052408.

[155] Bertini, I.; Luchinat, C. *Coord. Chem. Rev.* **1996**, *150*, 77 – 110.

[156] Szabo, A.; Ostlund, N. S. *Modern quantum chemistry: introduction to advanced electronic structure theory*; Dover Publications Inc., 2012.

[157] Helgaker, T.; Jorgensen, P.; Olsen, J. *Molecular electronic-structure theory*; John Wiley & Sons, 2014.

[158] Roos, B. O.; Taylor, P. R.; Siegbahn, P. E. M. *Chem. Phys.* **1980**, *48*, 157–173.

[159] Knowles, P.; Sexton, G.; Handy, N. *Chem. Phys.* **1982**, *72*, 337 – 347.

[160] Olsen, J. *Int. J. Quantum Chem.* **2011**, *111*, 3267–3272.

[161] Andersson, K.; Malmqvist, P.; Roos, B. O. *J. Chem. Phys.* **1992**, *96*, 1218–1226.

[162] Andersson, K.; Malmqvist, P. A.; Roos, B. O.; Sadlej, A. J.; Wolinski, K. *J. Phys. Chem.* **1990**, *94*, 5483–5488.

[163] Angeli, C.; Cimiraglia, R.; Evangelisti, S.; Leininger, T.; Malrieu, J.-P. *J. Chem. Phys.* **2001**, *114*, 10252–10264.

[164] Angeli, C.; Cimiraglia, R.; Malrieu, J.-P. *Chem. Phys. Lett.* **2001**, *350*, 297 – 305.

[165] Angeli, C.; Cimiraglia, R.; Malrieu, J.-P. *J. Chem. Phys.* **2002**, *117*, 9138–9153.

[166] Havenith, R. W. A.; Taylor, P. R.; Angeli, C.; Cimiraglia, R.; Ruud, K. *J. Chem. Phys.* **2004**, *120*, 4619–4625.

[167] Angeli, C.; Pastore, M.; Cimiraglia, R. *Theor. Chem. Acc.* **2007**, *117*, 743–754.

[168] Angeli, C.; Borini, S.; Cestari, M.; Cimiraglia, R. *J. Chem. Phys.* **2004**, *121*, 4043–4049.

[169] Angeli, C.; Bories, B.; Cavallini, A.; Cimiraglia, R. *J. Chem. Phys.* **2006**, *124*, 054108.

[170] Møller, C.; Plesset, M. S. *Phys. Rev.* **1934**, *46*, 618–622.

[171] Koch, H.; Jørgensen, P. *J. Chem. Phys.* **1990**, *93*, 3333–3344.

[172] Siegbahn, P. E. M. *J. Chem. Phys.* **1980**, *72*, 1647–1656.

[173] Roos, B. O.; Andersson, K.; Fülscher, M. P. *Chem. Phys. Lett.* **1992**, *192*, 5–13.

[174] Koch, W.; Holthausen, M. C. *A chemist's guide to density functional theory*; John Wiley & Sons, 2015.

[175] Hohenberg, P.; Kohn, W. *Phys. Rev.* **1964**, *136*, B864–B871.

[176] Jensen, F. *Introduction to computational chemistry*; John wiley & sons, 2017.

[177] Perdew, J. P.; Ruzsinszky, A.; Tao, J.; Staroverov, V. N.; Scuseria, G. E.; Csonka, G. I. *J. Chem. Phys.* **2005**, *123*, 062201.

[178] Kohn, W.; Sham, L. J. *Phys. Rev.* **1965**, *140*, A1133–A1138.

[179] Goedecker, S. *Rev. Mod. Phys.* **1999**, *71*, 1085–1123.

[180] Dunlap, B. I.; Connolly, J. W. D.; Sabin, J. R. *J. Chem. Phys.* **1979**, *71*, 4993–4999.

[181] Chen, X.; Langlois, J.-M.; Goddard, W. A. *Phys. Rev. B* **1995**, *52*, 2348–2361.

[182] Ordejón, P.; Artacho, E.; Soler, J. M. *Phys. Rev. B* **1996**, *53*, R10441–R10444.

[183] Goringe, C.; Hernndez, E.; Gillan, M.; Bush, I. *Comput. Phys. Commun.* **1997**, *102*, 1 – 16.

[184] Kenny, S. D.; Horsfield, A. P.; Fujitani, H. *Phys. Rev. B* **2000**, *62*, 4899–4905.

[185] Mostofi, A. A.; Skylaris, C.-K.; Haynes, P. D.; Payne, M. C. *Comput. Phys. Commun.* **2002**, *147*, 788 – 802.

[186] Liu, Y.; Yarne, D. A.; Tuckerman, M. E. *Phys. Rev. B* **2003**, *68*, 125110.

[187] Jr., T. H. D. *J. Chem. Phys.* **1989**, *90*, 1007–1023.

[188] Iannuzzi, M.; Hutter, J. *Phys. Chem. Chem. Phys.* **2007**, *9*, 1599–1610.

[189] Declerck, R.; Pauwels, E.; Van Speybroeck, V.; Waroquier, M. *Phys. Rev. B* **2006**, *74*, 245103.

[190] Perdew, J. P.; Burke, K.; Ernzerhof, M. *Phys. Rev. Lett.* **1996**, *77*, 3865–3868.

[191] VandeVondele, J.; Krack, M.; Mohamed, F.; Parrinello, M.; Chassaing, T.; Hutter, J. *Comput. Phys. Commun.* **2005**, *167*, 103–128.

[192] Goedecker, S.; Teter, M.; Hutter, J. *Phys. Rev. B* **1996**, *54*, 1703–1710.

[193] VandeVondele, J.; Hutter, J. *J. Chem. Phys.* **2007**, *127*, 114105.

[194] Weigend, F.; Ahlrichs, R. *Phys. Chem. Chem. Phys.* **2005**, *7*, 3297–3305.

[195] Weigend, F. *Phys. Chem. Chem. Phys.* **2006**, *8*, 1057–1065.

[196] Lee, C.; Yang, W.; Parr, R. G. *Phys. Rev. B* **1988**, *37*, 785–789.

[197] Becke, A. D. *J. Chem. Phys.* **1993**, *98*, 5648–5652.

[198] Vosko, S. H.; Wilk, L.; Nusair, M. *Can. J. Phys.* **1980**, *58*, 1200–1211.

[199] Krishnan, R.; Binkley, J. S.; Seeger, R.; Pople, J. A. *J. Chem. Phys.* **1980**, *72*, 650–654.

[200] Blaudeau, J.-P.; McGrath, M. P.; Curtiss, L. A.; Radom, L. *J. Chem. Phys.* **1997**, *107*, 5016–5021.

[201] Van Yperen-De Deyne, A.; Pauwels, E.; Van Speybroeck, V.; Waroquier, M. *Phys. Chem. Chem. Phys.* **2012**, *14*, 10690–10704.

[202] Munzarová, M.; Kaupp, M. *J. Phys. Chem. A* **1999**, *103*, 9966–9983.

[203] Becke, A. D. *Phys. Rev. A* **1988**, *38*, 3098–3100.

[204] Adamo, C.; Barone, V. *J. Chem. Phys.* **1999**, *110*, 6158–6170.

[205] Pederson, M. R.; Khanna, S. N. *Phys. Rev. B* **1999**, *60*, 9566–9572.

[206] Schmitt, S.; Jost, P.; van Wüllen, C. *J. Chem. Phys.* **2011**, *134*, 194113.

[207] Ganyushin, D.; Neese, F. *J. Chem. Phys.* **2006**, *125*, 024103.

[208] Malmqvist, P.-A.; Roos, B. O. *Chem. Phys. Lett.* **1989**, *155*, 189–194.

[209] Kutzelnigg, W.; Fleischer, U.; Schindler, M. In *NMR basic principles and progress*; Diehl, P., Fluck, E., Günther, H., Kosfeld, R., Seelig, J., Eds.; Springer: Berlin, 1991.

[210] Mackenzie, K. J. D.; Smith, M. E. *Multinuclear solid-state NMR of inorganic materials*; Elsevier Science: Oxford, U.K., 2002.

[211] Vaara, J. In *In high resolution NMR spectroscopy*; Contreras, R. H., Ed.; Elsevier: Amsterdam, 2013.

[212] Kubica, A.; Kowalewski, J.; Kruk, D.; Odelius, M. *J. Chem. Phys.* **2013**, *138*, 064304.

[213] Carlier, D.; Ménétrier, M.; Grey, C. P.; Delmas, C.; Ceder, G. *Phys. Rev. B* **2003**, *67*, 174103.

[214] Zhang, Y.; Castets, A.; Carlier, D.; Ménétrier, M.; Boucher, F. *J. Phys. Chem. C* **2012**, *116*, 17393–17402.

[215] Blöchl, P. E. *Phys. Rev. B* **1994**, *50*, 17953–17979.

[216] Yazyev, O. V.; Tavernelli, I.; Helm, L.; Röthlisberger, U. *Phys. Rev. B* **2005**, *71*, 115110.

[217] Bahramy, M. S.; Sluiter, M. H. F.; Kawazoe, Y. *Phys. Rev. B* **2007**, *76*, 035124.

[218] Marsman, M.; Kresse, G. *J. Chem. Phys.* **2006**, *125*, 104101.

[219] Dovesi, R.; Orlando, R.; Civalleri, B.; Roetti, C.; Saunders, V. R.; Zicovich-Wilson, C. M. *Z. Kristallogr.* **2005**, *220*, 571–573.

[220] Pennanen, T. O.; Machacek, J.; Taubert, S.; Vaara, J.; Hnyk, D. *Phys. Chem. Chem. Phys.* **2010**, *12*, 7018–7025.

[221] Kruck, M.; Sauer, D. C.; Enders, M.; Wadepohl, H.; Gade, L. H. *Dalton Trans.* **2011**, *40*, 10406–10415.

[222] Mareš, J.; Liimatainen, H.; Pennanen, T. O.; Vaara, J. *J. Chem. Theory Comput.* **2011**, *7*, 3248–3260.

[223] Bühl, M.; van Mourik, T. *Wiley Interdiscip. Rev. Comput. Mol. Sci.* **2011**, *1*, 634–647.

[224] Gohr, S.; Hrobárik, P.; Repiský, M.; Komorovský, S.; Ruud, K.; Kaupp, M. *J. Phys. Chem. A* **2015**, *119*, 12892–12905.

[225] Mehring, M. *Principles of High Resolution NMR in Solids*; Springer-Verlag Berlin Heidelberg, 1983.

[226] Haeberlen, U. *High resolution NMR in solids*; Academic Press, New York, 1976.

[227] Blöchl, P. E. *Phys. Rev. B* **2000**, *62*, 6158–6179.

[228] Blügel, S.; Akai, H.; Zeller, R.; Dederichs, P. H. *Phys. Rev. B* **1987**, *35*, 3271–3283.

[229] Neese, F. *J. Chem. Phys.* **2005**, *122*, 034107.

[230] Malkina, O. L.; Vaara, J.; Schimmelpfennig, B.; Munzarov, M.; Malkin, V. G.; ; Kaupp, M. *J. Am. Chem. Soc.* **2000**, *122*, 9206–9218.

[231] Schimmelpfenning, B. AMFI - an atomic mean field integral program, University of Stockholm, Stockholm, Sweden. 1996.

[232] Schreckenbach, G.; Ziegler, T. *J. Phys. Chem. A* **1997**, *101*, 3388–3399.

[233] Slater, J. C. *Phys. Rev.* **1951**, *81*, 385–390.

[234] Ditchfield, R. *Mol. Phys.* **1974**, *27*, 789–807.

[235] Keith, T.; Bader, R. *Chem. Phys. Lett.* **1992**, *194*, 1–8.

[236] Keith, T. A.; Bader, R. F. *Chem. Phys. Lett.* **1993**, *210*, 223–231.

[237] Cheeseman, J. R.; Trucks, G. W.; Keith, T. A.; Frisch, M. J. *J. Chem. Phys.* **1996**, *104*, 5497–5509.

[238] Kacprzak, S.; Reviakine, R.; Kaupp, M. *J. Phys. Chem. B* **2007**, *111*, 811–819.

[239] Kaupp, M.; Gress, T.; Reviakine, R.; Malkina, O. L.; Malkin, V. G. *J. Phys. Chem. B* **2003**, *107*, 331–337.

[240] Sheldrick, G. M. *Acta Crystallogr. Sect. C* **2015**, *71*, 3–8.

[241] Clough, S.; Poldy, F. *J. Phys. C: Solid State Phys.* **1973**, *6*, 1953.

[242] Schäfer, A.; Horn, H.; Ahlrichs, R. *J. Chem. Phys.* **1992**, *97*, 2571–2577.

[243] Stoll, H.; Paulus, B.; Fulde, P. *J. Chem. Phys.* **2005**, *123*, 144108.

[244] Allolio, C.; Salas-Illanes, N.; Desmukh, Y. S.; Hansen, M. R.; Sebastiani, D. *J. Phys. Chem. B* **2013**, *117*, 9939–9946.

[245] Wang, X.; Hou, Z.; Ikeda, T.; Terakura, K. *J. Phys. Chem. C* **2014**, *118*, 13929–13935.

[246] Koseki, S.; Schmidt, M. W.; Gordon, M. S. *J. Phys. Chem. A* **1998**, *102*, 10430–10435.

[247] Koseki, S.; Schmidt, M. W.; Gordon, M. S. *J. Phys. Chem.* **1992**, *96*, 10768–10772.

[248] Koseki, S.; Gordon, M. S.; Schmidt, M. W.; Matsunaga, N. *J. Phys. Chem.* **1995**, *99*, 12764–12772.

[249] Kaupp, M.; Reviakine, R.; Malkina, O. L.; Arbuznikov, A.; Schimmelpfennig, B.; Malkin, V. G. *J. Comput. Chem.* **2002**, *23*, 794–803.

[250] Jack, K. H.; Gutmann, V. *Acta Crystallogr.* **1951**, *4*, 246–249.

[251] Hepworth, M. A.; Jack, K. H. *Acta Crystallogr.* **1957**, *10*, 345–351.

[252] Hoppe, R.; Becker, S. *Z. Anorg. Allg. Chem.* **1989**, *568*, 126–135.

[253] Smith, R. I.; Jørgensen, J.-E. *Acta Crystallogr. Sect. B* **2006**, *62*, 987–992.

[254] Onoda, M.; Hirose, H. *J. Phys. Soc. Jpn.* **2012**, *81*, 094801.

[255] Yin, S.-C.; Grondey, H.; Strobel, P.; Anne, M.; Nazar, L. F. *J. Am. Chem. Soc.* **2003**, *125*, 10402–10411.

[256] Krzystek, J.; Ozarowski, A.; Telser, J.; Crans, D. C. *Coord. Chem. Rev.* **2015**, *301*, 123 – 133, The ninth international symposium on the chemistry and biological chemistry of vanadium.

[257] Patoux, S.; Wurm, C.; Morcrette, M.; Rousse, G.; Masquelier, C. *J. Power Sources* **2003**, *119-121*, 278–284.

[258] Yin, S.-C.; Strobel, P. S.; Grondey, H.; Nazar, L. F. *Chem. Mater.* **2004**, *16*, 1456–1465.

[259] Gong, C.; Xue, Z.; Wen, S.; Ye, Y.; Xie, X. *J. Power Sources* **2016**, *318*, 93 – 112.

[260] Wu, H.; Liu, Q.; Guo, S. *Nano-Micro Letters* **2014**, *6*, 316–326.

[261] Yi, T.-F.; Li, X.-Y.; Liu, H.; Shu, J.; Zhu, Y.-R.; Zhu, R.-S. *Ionics* **2012**, *18*, 529–539.

[262] Satyavani, T.; Kumar, A. S.; Rao, P. S. *Eng. Sci. Technol. Int J.* **2016**, *19*, 178 – 188.

[263] Nicolas, D.; Marine, C.; Jean-Frederic, M.; Dominique, G. *ChemPhysChem* **2014**, *15*, 1922–1938.

[264] Yu, F.; Zhang, L.; Li, Y.; An, Y.; Zhu, M.; Dai, B. *RSC Adv.* **2014**, *4*, 54576–54602.

[265] Deng, S.; Wang, H.; Liu, H.; Liu, J.; Yan, H. *Nano-Micro Letters* **2014**, *6*, 209–226.

[266] Yuan, L.-X.; Wang, Z.-H.; Zhang, W.-X.; Hu, X.-L.; Chen, J.-T.; Huang, Y.-H.; Goodenough, J. B. *Energy Environ. Sci.* **2011**, *4*, 269–284.

[267] Zhang, Y.; yuan Huo, Q.; pei Du, P.; zhen Wang, L.; qin Zhang, A.; hua Song, Y.; Lv, Y.; yin Li, G. *Synth. Met.* **2012**, *162*, 1315 – 1326.

[268] Jin, C.; Zhang, X.; He, W.; Wang, Y.; Li, H.; Wang, Z.; Bi, Z. *RSC Adv.* **2014**, *4*, 15332–15339.

[269] Chung, S.-Y.; Bloking, J. T.; Chiang, Y.-M. *Nat. Mater.* **2002**, *1*, 123–128.

[270] Padhi, A. K.; Nanjundaswamy, K. S.; Goodenough, J. B. *J. Electrochem. Soc.* **1997**, *144*, 1188–1194.

[271] Kang, B.; Ceder, G. *Natur.* **2009**, *458*, 190.

[272] Woo, O. S.; Seung-Taek, M.; Seung-Min, O.; Hwan, O. K.; Khalil, A.; Bruno, S.; Yang-Kook, S. *Adv. Mater.* **2010**, *22*, 4842–4845.

[273] Yonggang, W.; Yarong, W.; Eiji, H.; Kaixue, W.; Haoshen, Z. *Angew. Chem. Int. Ed.* **2008**, *47*, 7461–7465.

[274] HoChun, Y.; MinKi, J.; Bong-Soo, J.; Hyun-Soo, K.; Jaephil, C. *Adv. Energy Mater.* **2011**, *1*, 347–351.

[275] Eftekhari, A. *J. Power Sources* **2017**, *343*, 395 – 411.

[276] Yu, C.; Ganapathy, S.; Van Eck, E. R.; Wang, H.; Basak, S.; Li, Z.; Wagemaker, M. *Nat. Commun.* **2017**, *8*, 1086.

[277] Kervern, G.; Pintacuda, G.; Zhang, Y.; Oldfield, E.; Roukoss, C.; Kuntz, E.; Herdtweck, E.; Basset, J.-M.; Cadars, S.; Lesage, A.; Copéret, C.; Emsley, L. *J. Am. Chem. Soc.* **2006**, *128*, 13545–13552.

[278] Blanc, F.; Leskes, M.; Grey, C. P. *Acc. Chem. Res.* **2013**, *46*, 1952–1963.

[279] Cerofolini, L.; Staderini, T.; Giuntini, S.; Ravera, E.; Fragai, M.; Parigi, G.; Pierattelli, R.; Luchinat, C. *J. Biol. Inorg. Chem.* **2018**, *23*, 71–80.

[280] Herchel, R.; Váhovská, L.; Potočňák, I.; Trávníček, Z. *Inorg. Chem.* **2014**, *53*, 5896–5898.

[281] de Graaf, C.; Sousa, C. *Int. J. Quantum Chem.* **2006**, *106*, 2470–2478.

[282] Neese, F. *Wiley Interdiscip. Rev. Comput. Mol. Sci.* **2012**, *2*, 73–78.

[283] Neese, F. *Int. J. Quantum Chem.* **2001**, *83*, 104–114.

[284] Maganas, D.; Sottini, S.; Kyritsis, P.; Groenen, E. J. J.; Neese, F. *Inorg. Chem.* **2011**, *50*, 8741–8754.

[285] Sundararajan, M.; Ganyushin, D.; Ye, S.; Neese, F. *Dalton Trans.* **2009**, 6021–6036.

[286] Ruamps, R.; Batchelor, L. J.; Maurice, R.; Gogoi, N.; Jiménez-Lozano, P.; Guihéry, N.; de Graaf, C.; Barra, A.-L.; Sutter, J.-P.; Mallah, T. *Chem. Eur. J.* **2013**, *19*, 950–956.

[287] van Wüllen, C. *Phys. Chem. Chem. Phys.* **2000**, *2*, 2137–2144.

[288] Ievină, A.; Straumanis, M.; Karlsons, M. *Z. Phys. Chem.* **1938**, *40B*, 146.

[289] Hou, X.; Kirkpatrick, R. J. *Inorg. Chem.* **2001**, *40*, 6397–6404.

[290] Wizent, N.; Behr, G.; Lipps, F.; Hellmann, I.; Klingeler, R.; Kataev, V.; Löser, W.; Sato, N.; Büchner, B. *J. Cryst. Growth* **2009**, *311*, 1273 – 1277.

[291] Liang, G.; Park, K.; Li, J.; Benson, R. E.; Vaknin, D.; Markert, J. T.; Croft, M. C. *Phys. Rev. B* **2008**, *77*, 064414.

[292] Vaknin, D.; Zarestky, J. L.; Miller, L. L.; Rivera, J.-P.; Schmid, H. *Phys. Rev. B* **2002**, *65*, 224414.

[293] Vaknin, D.; Zarestky, J. L.; Ostenson, J. E.; Chakoumakos, B. C.; Goñi, A.; Pagliuso, P. J.; Rojo, T.; Barberis, G. E. *Phys. Rev. B* **1999**, *60*, 1100–1110.

[294] Song, Y.; Zavalij, P. Y.; Suzuki, M.; Whittingham, M. S. *Inorg. Chem.* **2002**, *41*, 5778–5786.

[295] Ehrenberg, H.; Bramnik, N. N.; Senyshyn, A.; Fuess, H. *Solid State Sci.* **2009**, *11*, 18–23.

[296] Kosova, N. V.; Slobodyuk, A. B.; Podgornova, O. A. *J. Struct. Chem.* **2016**, *57*, 345–353.

[297] Geller, S.; Durand, J. L. *Acta Crystallogr.* **1960**, *13*, 325–331.

[298] Janssen, Y.; Santhanagopalan, D.; Qian, D.; Chi, M.; Wang, X.; Hoffmann, C.; Meng, Y. S.; Khalifah, P. G. *Chem. Mater.* **2013**, *25*, 4574–4584.

[299] Kubel, F. *Z. Kristallogr.* **1994**, *209*, 755.

[300] Warda, S. A.; Lee, S.-L. *Z. Kristallogr. - New Cryst. Struct.* **1997**, *212*, 319.

[301] Roberts, M.; Biendicho, J. J.; Hull, S.; Beran, P.; Gustafsson, T.; Svensson, G.; Edström, K. *J. Power Sources* **2013**, *226*, 249 – 255.

[302] Singh, V.; Gershinsky, Y.; Kosa, M.; Dixit, M.; Zitoun, D.; Major, D. T. *Phys. Chem. Chem. Phys.* **2015**, *17*, 31202–31215.

[303] Toft-Petersen, R.; Reehuis, M.; Jensen, T. B. S.; Andersen, N. H.; Li, J.; Le, M. D.; Laver, M.; Niedermayer, C.; Klemke, B.; Lefmann, K.; Vaknin, D. *Phys. Rev. B* **2015**, *92*, 024404.

[304] Goñi, A.; Lezama, L.; Barberis, G.; Pizarro, J.; Arriortua, M.; Rojo, T. *J. Magn. Magn. Mater.* **1996**, *164*, 251 – 255.

[305] Ait-Salah, A.; Dodd, J.; Mauger, A.; Yazami, R.; Gendron, F.; Julien, C. M. *Z. Anorg. Allg. Chem.* **2006**, *632*, 1598–1605.

[306] Li, J.; Tian, W.; Chen, Y.; Zarestky, J. L.; Lynn, J. W.; Vaknin, D. *Phys. Rev. B* **2009**, *79*, 144410.

[307] Jensen, T. B. S.; Christensen, N. B.; Kenzelmann, M.; Rønnow, H. M.; Niedermayer, C.; Andersen, N. H.; Lefmann, K.; Jiménez-Ruiz, M.; Demmel, F.; Li, J.; Zarestky, J. L.; Vaknin, D. *Phys. Rev. B* **2009**, *79*, 092413.

[308] Pigliapochi, R.; Seymour, I. D.; Merlet, C.; Pell, A. J.; Murphy, D. T.; Schmid, S.; Grey, C. P. *Chem. Mater.* **2018**, *30*, 817–829.

[309] Kaus, M.; Issac, I.; Heinzmann, R.; Doyle, S.; Mangold, S.; Hahn, H.; Chakravadhanula, V. S. K.; Kübel, C.; Ehrenberg, H.; Indris, S. *J. Phys. Chem. C* **2014**, *118*, 17279–17290.

[310] Wittmann, T.; Mondal, A.; Tschense, C. B. L.; Wittmann, J. J.; Klimm, O.; Siegel, R.; Corzilius, B.; Weber, B.; Kaupp, M.; Senker, J. *J. Am. Chem. Soc.* **2018**, *140*, 2135–2144.

[311] Rowsell, J. L. C.; Millward, A. R.; Park, K. S.; Yaghi, O. M. *J. Am. Chem. Soc.* **2004**, *126*, 5666–5667.

[312] Qiu, S.; Xue, M.; Zhu, G. *Chem. Soc. Rev.* **2014**, *43*, 6116–6140.

[313] Li, Q.; Zhang, W.; Miljanić, O. Š.; Sue, C.-H.; Zhao, Y.-L.; Liu, L.; Knobler, C. B.; Stoddart, J. F.; Yaghi, O. M. *Science* **2009**, *325*, 855–859.

[314] Cai, H.; Li, M.; Lin, X.-R.; Chen, W.; Chen, G.-H.; Huang, X.-C.; Li, D. *Angew. Chem. Int. Ed.* **2015**, *54*, 10454–10459.

[315] Seo, J. S.; Whang, D.; Lee, H.; Im Jun, S.; Oh, J.; Jeon, Y. J.; Kim, K. *Natur.* **2000**, *404*, 982.

[316] Lee, J.; Farha, O. K.; Roberts, J.; Scheidt, K. A.; Nguyen, S. T.; Hupp, J. T. *Chem. Soc. Rev.* **2009**, *38*, 1450–1459.

[317] Czaja, A. U.; Trukhan, N.; Muller, U. *Chem. Soc. Rev.* **2009**, *38*, 1284–1293.

[318] Ma, L.; Abney, C.; Lin, W. *Chem. Soc. Rev.* **2009**, *38*, 1248–1256.

[319] Horcajada, P. et al. *Nat. Mater.* **2010**, *9*, 172.

[320] Horcajada, P.; Gref, R.; Baati, T.; Allan, P. K.; Maurin, G.; Couvreur, P.; Frey, G.; Morris, R. E.; Serre, C. *Chem. Rev.* **2012**, *112*, 1232–1268.

[321] McKinlay, A.; Morris, R.; Horcajada, P.; Frey, G.; Gref, R.; Couvreur, P.; Serre, C. *Angew. Chem. Int. Ed.* **2010**, *49*, 6260–6266.

[322] Hong, B. H.; Bae, S. C.; Lee, C.-W.; Jeong, S.; Kim, K. S. *Science* **2001**, *294*, 348–351.

[323] Wack, J.; Siegel, R.; Ahnfeldt, T.; Stock, N.; Mafra, L.; Senker, J. *J. Phys. Chem. C* **2013**, *117*, 19991–20001.

[324] Wittmann, T.; Siegel, R.; Reimer, N.; Milius, W.; Stock, N.; Senker, J. *Chem. Eur. J.* **2015**, *21*, 314–323.

[325] Van de Voorde, B.; Bueken, B.; Denayer, J.; De Vos, D. *Chem. Soc. Rev.* **2014**, *43*, 5766–5788.

[326] Samokhvalov, A. *Chem. Eur. J.* **2015**, *21*, 16726–16742.

[327] Li, J.-R.; Kuppler, R. J.; Zhou, H.-C. *Chem. Soc. Rev.* **2009**, *38*, 1477–1504.

[328] Batten, S. R.; Robson, R. *Angew. Chem. Int. Ed.* **1998**, *37*, 1460–1494.

[329] Estermann, M.; McCusker, L.; Baerlocher, C.; Merrouche, A.; Kessler, H. *Natur.* **1991**, *352*, 320.

[330] Maes, M. et al. *Angew. Chem.* **2011**, *123*, 4296–4300.

[331] Nuzhdin, A. L.; Kovalenko, K. A.; Dybtsev, D. N.; Bukhtiyarova, G. A. *Mendeleev Commun.* **2010**, *20*, 57 – 58.

[332] Ahmed, I.; Khan, N. A.; Hasan, Z.; Jhung, S. H. *J. Hazard. Mater. 250-251*.

[333] Dai, J.; McKee, M. L.; Samokhvalov, A. *J. Porous Mater.* **2014**, *21*, 709–727.

[334] Alaerts, L.; Maes, M.; van der Veen, M. A.; Jacobs, P. A.; De Vos, D. E. *Phys. Chem. Chem. Phys.* **2009**, *11*, 2903–2911.

[335] Van de Voorde, B.; Boulhout, M.; Vermoortele, F.; Horcajada, P.; Cunha, D.; Lee, J. S.; Chang, J.-S.; Gibson, E.; Daturi, M.; Lavalley, J.-C.; Vimont, A.; Beurroies, I.; De Vos, D. E. *J. Am. Chem. Soc.* **2013**, *135*, 9849–9856.

[336] Devautour-Vinot, S.; Martineau, C.; Diaby, S.; Ben-Yahia, M.; Miller, S.; Serre, C.; Horcajada, P.; Cunha, D.; Taulelle, F.; Maurin, G. *J. Phys. Chem. C* **2013**, *117*, 11694–11704.

[337] Čendak, T.; Žunkovič, E.; Godec, T. U.; Mazaj, M.; Logar, N. Z.; Mali, G. *J. Phys. Chem. C* **2014**, *118*, 6140–6150.

[338] Chui, S. S.-Y.; Lo, S. M.-F.; Charmant, J. P. H.; Orpen, A. G.; Williams, I. D. *Science* **1999**, *283*, 1148–1150.

[339] Achmann, S.; Hagen, G.; Hmmerle, M.; Malkowsky, I. M.; Kiener, C.; Moos, R. *Chem. Eng. Technol.* **2010**, *33*, 275–280.

[340] Jeremias, F.; Khutia, A.; Henninger, S. K.; Janiak, C. *J. Mater. Chem.* **2012**, *22*, 10148–10151.

[341] Férey, G.; Mellot-Draznieks, C.; Serre, C.; Millange, F.; Dutour, J.; Surblé, S.; Margiolaki, I. *Science* **2005**, *309*, 2040–2042.

[342] Bertini, I.; Luchinat, C.; Parigi, G. *Eur. J. Inorg. Chem.* **2000**, *2000*, 2473–2480.

[343] Bertini, I.; Turano, P.; Vila, A. J. *Chem. Rev.* **1993**, *93*, 2833–2932.

[344] Wicholas, M.; Mustacich, R.; Jayne, D. *J. Am. Chem. Soc.* **1972**, *94*, 4518–4522.

[345] Walker, F. A. *Inorg. Chem.* **2003**, *42*, 4526–4544.

[346] Banci, L.; Bertini, I.; Luchinat, C.; Pierattelli, R.; Shokhirev, N. V.; Walker, F. A. *J. Am. Chem. Soc.* **1998**, *120*, 8472–8479.

[347] Ishii, Y.; Wickramasinghe, N. P.; Chimon, S. *J. Am. Chem. Soc.* **2003**, *125*, 3438–3439.

[348] Wickramasinghe, N. P.; Shaibat, M. A.; Ishii, Y. *J. Phys. Chem. B* **2007**, *111*, 9693–9696.

[349] Wickramasinghe, N. P.; Shaibat, M. A.; Jones, C. R.; Casabianca, L. B.; de Dios, A. C.; Harwood, J. S.; Ishii, Y. *J. Chem. Phys.* **2008**, *128*, 052210.

[350] Grimme, S.; Antony, J.; Ehrlich, S.; Krieg, H. *J. Chem. Phys.* **2010**, *132*, 154104.

[351] Sinnecker, S.; Neese, F.; Noodleman, L.; Lubitz, W. *J. Am. Chem. Soc.* **2004**, *126*, 2613–2622.

[352] Senker, J. *Unpublished results, personal communication to the author* **XXX**,

[353] Welo, L. A. *Philos. Mag.* **1928**, *6*, 481–509.

[354] Honda, M.; Morita, M.; Date, M. *J. Phys. Soc. Jpn.* **1992**, *61*, 3773–3785.

[355] Tadros, A. M.; Royko, M. M.; Kelley, S. P.; Belmore, K.; Rogers, R. D.; Vincent, J. B. *Polyhedron* **2015**, *100*, 17 – 27.

[356] Dawson, D. M.; Ke, Z.; Mack, F. M.; Doyle, R. A.; Bignami, G. P. M.; Smellie, I. A.; Buhl, M.; Ashbrook, S. E. *Chem. Commun.* **2017**, *53*, 10512–10515.

[357] Bhl, M.; Ashbrook, S. E.; Dawson, D. M.; Doyle, R. A.; Hrobrik, P.; Kaupp, M.; Smellie, I. A. *Chem. Eur. J.* **2016**, *22*, 15328–15339.

[358] Novotn, J.; Sojka, M.; Komorovsky, S.; Neas, M.; Marek, R. *J. Am. Chem. Soc.* **2016**, *138*, 8432–8445.

[359] Rouf, S. A.; Jakobsen, V. B.; Mare, J.; Jensen, N. D.; McKenzie, C. J.; Vaara, J.; Nielsen, U. G. *Solid State Nucl. Magn. Reson.* **2017**, *87*, 29–37.

[360] Chavan, S.; Vitillo, J. G.; Groppo, E.; Bonino, F.; Lamberti, C.; Dietzel, P. D. C.; Bordiga, S. *J. Phys. Chem. C* **2009**, *113*, 3292–3299.

[361] Gavrilenko, K. S.; Addison, A.; Thompson, L.; Pavlishchuk, V. V. *Theor. Exp. Chem.* **2004**, *40*, 214–219.

[362] Lim, H.; Lee, J.; Jin, S.; Kim, J.; Yoon, J.; Hyeon, T. *Chem. Commun.* **2006**, 463–465.

[363] Calleja, G.; Melero, J.; Martnez, F.; Molina, R. *Water Res.* **2005**, *39*, 1741 – 1750.

[364] Crowther, N.; Larachi, F. *Appl. Catal., B* **2003**, *46*, 293 – 305.

[365] McDaniel, M. P. In *Chapter 3 - A Review of the Phillips supported chromium catalyst and its commercial use for ethylene polymerization*; Gates, B. C., Knzinger, H., Eds.; Advances in Catalysis; Academic Press, 2010; Vol. 53; pp 123 – 606.

[366] Eisch, J. J. *Organometallics* **2012**, *31*, 4917–4932.

[367] Abedi, S.; Abdouss, M. *Appl. Catal., A* **2014**, *475*, 386 – 409.

[368] Hesemann, P. *Curr. Opin. Green Sustainable Chem.* **2018**, *10*, 21 – 26, Green Catalysis.

[369] Pelletier, J. D. A.; Basset, J.-M. *Acc. Chem. Res.* **2016**, *49*, 664–677.

[370] Gawande, M. B.; Monga, Y.; Zboril, R.; Sharma, R. *Coord. Chem. Rev.* **2015**, *288*, 118 – 143.

[371] Pintacuda, G. *Unpublished results, personal communication to the author* **XXX**,

[372] Luber, S.; Iannuzzi, M.; Hutter, J. *J. Chem. Phys.* **2014**, *141*.

[373] Schfer, A.; Huber, C.; Ahlrichs, R. *J. Chem. Phys.* **1994**, *100*, 5829–5835.

[374] Bussi, G.; Donadio, D.; Parrinello, M. *J. Chem. Phys.* **2007**, *126*, 014101.